AEROTHERMODYNAMIC INVESTIGATION OF THE TURBINE BLADE FILM COOLING WITH LARGE EDDY SIMULATION METHOD

Lianfeng Yang

Supervisor: Prof. Pietro Zunino

Co-Supervisor: Prof. Francesca Satta, Prof. Dario Barsi, Prof. Yigang Luan

Department of Mechanical Engineering, Energy, Management and Transports

University of Genova

This dissertation is submitted for the degree of

Doctor of Philosophy

January 2022

Declaration

I hereby declare that except where specific reference is made to the work of others, the contents of this dissertation are original and have not been submitted in whole or in part for consideration for any other degree or qualification in this, or any other university. This dissertation is my own work and contains nothing which is the outcome of work done in collaboration with others, except as specified in the text and acknowledgements.

Lianfeng Yang

January 2022

Abstract

Gas turbines have been widely used in the aviation, marine, power plant, etc., which plays an indispensable role in modern industries. Nowadays, higher efficiency and larger output power is demanded, consequently, the turbine inlet temperature (TIT) has to be increased to up to 2260K in some turbofan engines. The turbine blades or vanes operate in a harsh environment and the operating temperature significantly surpasses the melting point of the turbine blade material. Therefore, the turbine cooling technology is of vital importance aiming to guarantee the lifespan of the turbine blades and the safe operation. Apart from the internal cooling methods, the external film cooling is a necessary and effective solution to protect the outer surface of the blades against the extreme high temperature mainstream from the combustion chamber.

In this thesis, the thermal performance of the laidback fan-shaped film hole structure was numerically studied, which is known as 7-7-7 laidback fan-shaped film hole proposed by Thole [1]. Large eddy simulation (LES) method was implemented to investigate the thermal performance of the shaped film hole, and the LES result was compared with the RANS simulation with various turbulent models and verified by the experimental data from Thole. Besides, a comparative study was conducted between the conventional cylindrical film hole and the 7-7-7 shaped film hole. The results show the better cooling effectiveness with sufficient spread in spanwise direction as the blowing ratio increases, and proper orthogonal decomposition (POD) method was employed to present the coherent structure in flow field. Additionally, the effects of the blowing ratios M on the shaped film hole were simulated with LES in the range of M=0.5-3.0. Three different mainstream inlet turbulence intensities included between Tu=0.5% and Tu=20% were chosen to research the effects on the cooling effectiveness. Three mainstream inlet velocity profiles were applied for the LES calculation. The convex curved bottom surface was also investigated and compared with the flat bottom wall. The results show that M=1.5 can obtain a relative better performance for the same turbulence intensity of 0.5%. The cooling effectiveness deteriorates as the mainstream turbulence intensity increases from 0.5% to 20%. The mainstream inlet velocity profile causes less effects on the effectiveness relative to the blowing ratio and inlet turbulence intensity. The effectiveness of the convex curved bottom

surface decays at higher blowing ratio condition. In addition, aerothermal performance of film cooled C3X vane was analyzed, and a comparison between the cylindrical and shaped film hole cases was presented. The effects of the two different film hole structures on the pressure and temperature distributions were studied.

The present work evaluated the LES accuracy through a comparison with the experimental data and presented the reason of the different predictions between the LES and RANS. The numerical research on the film cooling can be considered as a baseline for further comparison and investigation of the film cooling in turbine blades or vanes.

Key Word: gas turbine, film cooling, large eddy simulation, C3X vane

Contents

List of figures

List of tables

Nomenclature

d	distance to the closest wall m
e	internal energy J
f	body forces
h	enthalpy J
k	turbulent kinetic energy J/kg
p	absolute pressure Pa
p_s	static pressure Pa
p_t	absolute total pressure Pa
$\dot{q}$	heat flux W/m^2
q_R	radiative heat flux W/m^2
t	time s
u	velocity m/s
u_τ	friction velocity m/s
A	area m^2
C	true chord length m
C_x	axial chord length m
C_d	discharge coefficient
D	diameter of the film hole m
D_h	hydraulic diameter of freestream inlet m
F	force N
H	height of blades or vanes m
H_{12}	shape factor $H_{12}= \delta^*/\theta$
I_m	identity matrix
L	the total length of the film hole m
L_{curve}	the length of the curved surface m
L_{arc}	arc length along the blade m
$L_{arc\ max}$	maximum arc length along the blade m
Ma	Mach number
P	pitch between two holes m

R_s	Reynolds stress
S	spacing between two holes m
T	static temperature K
T_t	total temperature K
T_{non}	non-dimensional temperature
V	volume of the cell m^3

Greek Symbols

γ	heat capacity ratio
δ	boundary layer thickness m
δ^*	displacement thickness m
ε	dissipation rate of turbulent kinetic energy $J/(kg \cdot s)$
η	adiabatic cooling effectiveness
θ	momentum thickness m
κ	Von Kármán constant
λ	thermal conductivity $W/(m \cdot K)$
μ	dynamic viscosity Pa·s
ρ	density kg/m^3
$\vec{\sigma}$	stress tensor
$\vec{\tau}$	shear tensor
ω_x	streamwise vorticity 1/s
ω_a	axial vorticity 1/s

Superscripts

$-$	time-averaged
$\sim$	spatially filtered

Subscripts

c	coolant
∞	free stream
aw	adiabatic wall
cl	centerline

in	inlet
out	outlet
ave	area-averaged
lat	lateral-averaged
1	inlet
2	outlet
is	isentropic

Abbreviations

DR	density ratio
VR	velocity ratio
M	blowing ratio or mass flux
I	momentum flux ratio
Tu	turbulence intensity
PSP	pressure-sensitive paint
IRT	infrared thermography
CFD	computational fluid dynamics
RANS	Reynolds-averaged Navier–Stokes
LES	large eddy simulation
DNS	direct numerical simulation
Re	Reynolds number
Re_θ	Reynolds number based on momentum thickness $\mathrm{Re}_\theta = \rho u_\infty \theta/\mu$
CRVP	counter-rotating vortex pair
anti-CRVP	anti-counter-rotating vortex pair
K-H vortex	Kelvin-Helmholtz vortex
POD	Proper orthogonal decomposition
SVD	Singular value decomposition

Chapter 1

Introduction

1.1 Background and motivation

The gas turbine is one of the types of internal combustion engines, which is mainly composed of compressor, combustor and turbine, and operates on the Brayton cycle. It has been commonly used for the aircraft propulsion, land-based power plants, ships, tanks and other industrial applications [2], because of its compactness, low weight and multiple fuel choices [3]. And it includes the technological innovation, new materials development and the cutting-edge manufacturing technologies. Hence, there is no denying the fact that gas turbines are the heart of most modern industries.

In recent decades, the gas turbine has been found increasing service and the demands of the high efficiency and output power also have been growing rapidly for modern gas turbines. The last 20 years witnessed the development of the gas turbine technology, the simple cycle gas turbine thermal efficiency shows a great boost from 15% to 45% accompanied by the increase of the compressor pressure ratio from 7:1 to up to 45:1 [3], and the reason behind this is improvement of the turbine inlet temperature (TIT) thanks to the evolution of the single crystal material, thermal barrier coating (TBC), new internal and external cooling schemes, etc.

Fig. 1.1 depicts that in the past 60 years the turbine inlet temperature has shown an increasing growth trend. In 1960s, due to the limitation of the melting point of the blade material, the turbine inlet temperature has to be constrained under about 1300K. Some simple internal cooling structures were applied, for instance the straight tube inner channels, which is thought to be an important evolution of the turbine blade. Thus, the maximum metal temperature has no longer been the constraint of the operating temperature of the turbine blade. And these simple cooling passages provide about 100K reduction of the blade. In 1970s and 1980s [4], the internal cooling method was gradually switched from the simple cooling channels to the sophisticated cooling structures. As a result, the thermal

resistance of the turbine blade improved, and the turbine inlet temperature reached as high as about 1400K in 1990. Moreover, with the development of the impingement cooling and film cooling as well as the thermal barrier coating and single crystal techniques, the blade has achieved about 400K temperature drop [5]. It allows the maximum hot gas temperature to reach 1800K approximately. In addition, the US Department of Defense and NASA launched a program called integrated high-performance turbine engine technology (IHPTET) aiming to double the output power of the engine in the next decade in three ways: 1) improved cooling effectiveness, 2) high-temperature materials with TBC and 3) increased flow path efficiency with reducing leakage [2]. In 2011, Mitsubishi Heavy Industries has announced that their advanced J-series gas turbine achieved 1873K (1600℃) with the power output of 320MW, which was the highest turbine inlet temperature at that time [6].

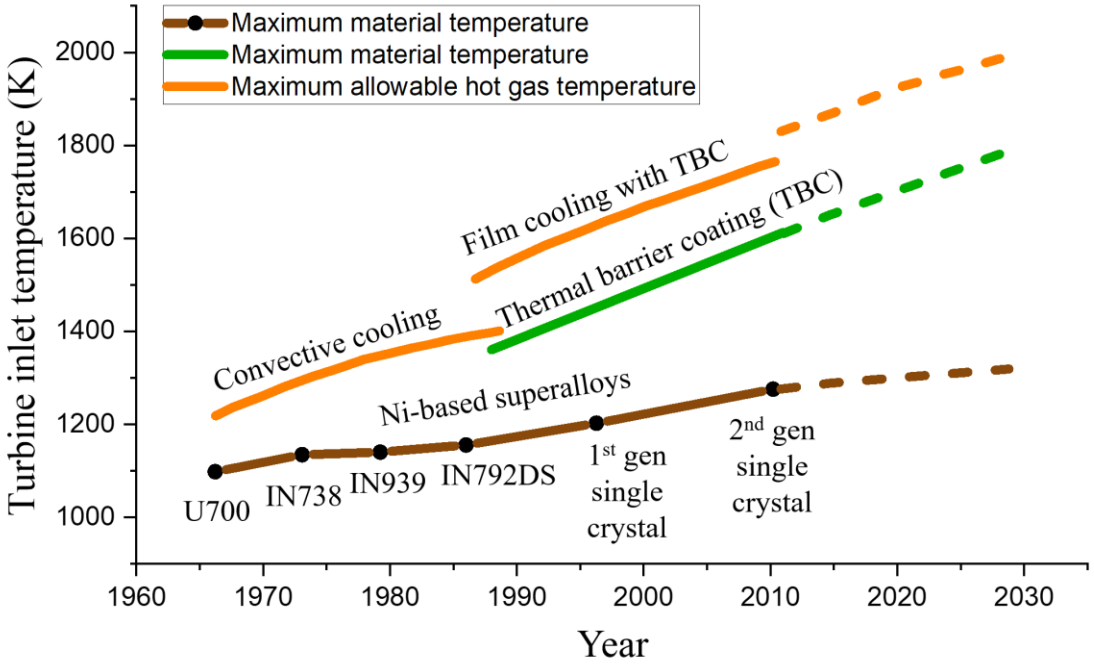

Fig. 1.1 The improvement of turbine inlet temperature in recent decades [7, 8]

Tab. 1.1 presents the specifications of several well-known turbofan engines. According to the data, the turbine inlet temperature has been raising from near 1400K to 2300K continuously since 1970s. Correspondingly, from 1970s to 2000s the Maximum thrust almost doubled as well as the thrust with afterburner. Therefore, the turbine inlet

temperature affects the performance deeply. Note that the turbine inlet temperature of F135-PW-100 is over 2200K [9], which has exceeded the metal operating temperature even though the single crystal turbine blade technology coupled with thermal barrier coating (TBC) are utilized. To maintain the blade expectation of life, it is necessary that the cooling technique has to be employed.

Tab. 1.1 The specification of modern gas turbine engines

Engine / Parameter	F100-PW-100	D-30F-6	M53-P2	Al-31F	M88-2	F119-PW-100	WS-10	F135-PW-100
Turbine inlet temperature K	1399	1387	1600	1665	1850	1977	1747	2260
Maximum thrust KN	55.2	93	64	74.6	50	116	76.2	128
Thrust with afterburner KN	106.4	152	95	122.6	75	156	147	191
Pressure Ratio	25	21.2	9.8	23	24.5	35	32	28
Air mass flow kg/s	101.1	150	85	112	65	-	118	-
Program launched	-	-	1967	1973	1983	1983	1987	-
In service	1974	1979	1980	1985	1990	1997	2007	2006
Manufacturer	P&W	Soloviev Design Bureau	Safran Aircraft Engines	Lyulka	Safran Aircraft Engines	P&W	Shenyang Aeroengine Research Institute	P&W
Applications	F-15 A/B	MiG-31	Dassault Mirage 2000	Su-27	Dassault Rafale	F-22	Chengdu J-20	F-35

Meanwhile, the growth of the new materials makes a substantial contribution to the improvement of the heat resistance as well. The nickel-based superalloys are currently used, which begin to melt at 1260℃-1371℃ and thereby can guarantee the safe operations under about 1090℃ (2000℉) [2]. As for the higher strength single crystal blade materials, Pratt

& Whitney is deemed to be the pioneer. This new technology was first used in 1969 in the J58 engine for the SR-71 Blackbird, the super spy plane that operated at the edge of space at fantastic speeds [10]. And in the late 1970s Cannon Muskegon Corporation released their 3rd generation single crystal superalloys technology CMSX-4 plus, which has the capability of the thermal resistance at 1200℃ [11, 12].

The public literature shows that the turbine inlet temperature raises about 15K-20K every year on average [13]. The heat resistance of the material usually makes a steady progress and improves 8K each year, therefore, the cooling technology is indispensable to offset gap between the increase of the turbine inlet temperature and the capability of the material.

Fig. 1.2 illustrates the relationship between the turbine rotor inlet temperature and the specific output power. The ideal Brayton cycle performance line represents the gas turbine engine operateing with 100% efficiency and without any losses. For various kinds of gas turbine engines, the scatter shows a similar upward trend along with the ideal performance

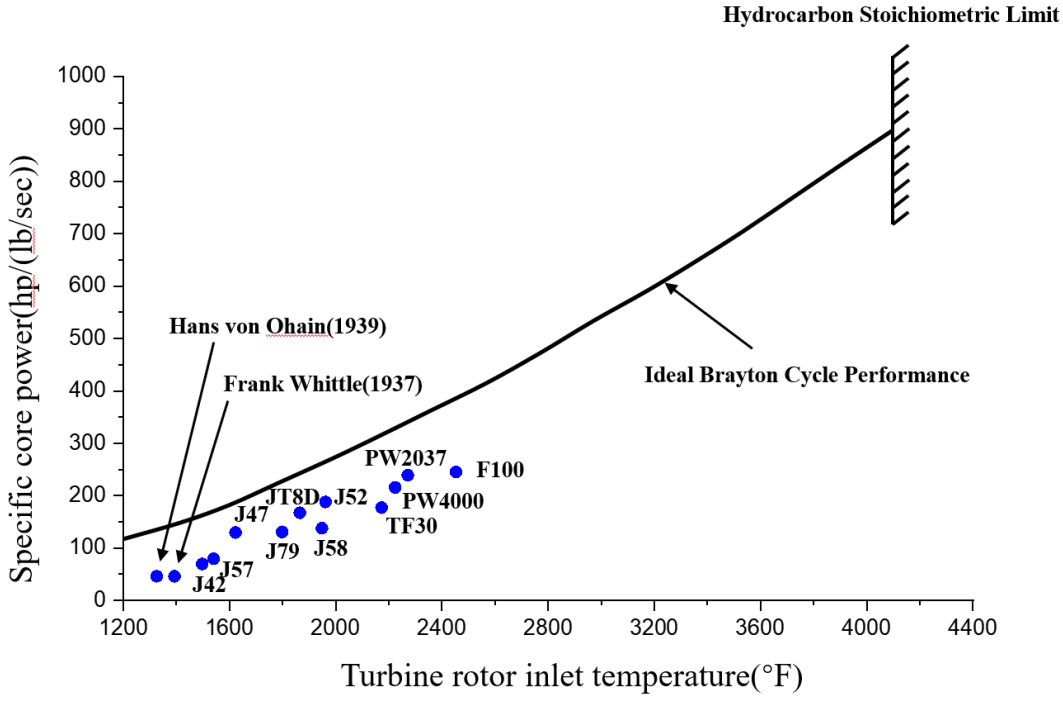

Fig. 1.2 The increase of the cycle output power with respect to the turbine inlet temperature [14]

curve. Since Frank Whittle and Hans von Ohain conceived the idea for the jet engine in 1930s, the turbine inlet temperature has nearly doubled, and in the meanwhile the specific output power has improved roughly four times. Therefore, the turbine inlet temperature has a significant effect on the turbine output power. An increase of 56℃ in the turbine inlet temperature has the potential to gain an improvement of 8%-13% in output power and 2%-4% in simple cycle efficiency correspondingly [3]. Thereby, raising the turbine inlet temperature is of vital importance to the performance of the whole engine and it is also one of the most significant research orientations according to the history of the gas turbine development.

1.2 Objectives of this study

In this paper, the present investigation is mainly focused on numerical simulation of the aerothermal performance of the turbine blade film cooling mainly with large eddy simulation (LES) method. The verification of the large eddy simulation was conducted referring to the thermal experimental data of previous public literature, and the evaluation of the numerical simulation was compared between the Reynolds-averaged Navier-Stokes (RANS) method with various turbulence models and large eddy simulation method with different subgrid models. The characterization of the flow field can reveal the effects on the thermal effectiveness thanks to the advantages of the LES method. Meanwhile, the mechanisms of the flow and heat transfer in turbine blade can shed new light on the design and optimization of the turbine blade in the future. Additionally, the film cooled NASA C3X turbine vane with the conventional cylindrical and laidback fan-shaped film holes were investigated using LES method to analyze the effects of two types of the film holes on the thermal performance in the cascade under the realistic engine conditions. The comparative study can present the performance advantages of the fan-shaped film holes and the effects of the film cooling holes on the temperature distributions of the turbine cascade.

Chapter 2

Turbine blade cooling technology

2.1 Turbine blade internal cooling

The turbine blade cooling methods can be classified into two main categories: the internal cooling and the external cooling methods. As mentioned above, the internal cooling technology was applied in the turbine blade prior to the other cooling schemes, for instance, the external film cooling. The improvement and optimization of the internal cooling structure never stop developing in the past years and various types and solutions have occurred corresponding to the development of the modern gas turbine. Fig. 2.1 is a typical case that presents the average radial temperature profile of the annular burner outlet. Because of the position of the first-stage nozzle vane and blade, they always need to suffer from the high-temperature mainstream exhausting from the combustion chamber. The air temperature in the first-stage nozzle vanes can reach 1149℃-1260℃, and the major challenges for the vanes and blades are not only the high temperature, but also the thermal stress. The operating environment of the first-stage blades or vanes is absolutely harsh, and in many cases, they are the bottleneck component of the entire engine. Therefore, the internal cooling is very important to the life expectancy and safe operation of blades and vanes.

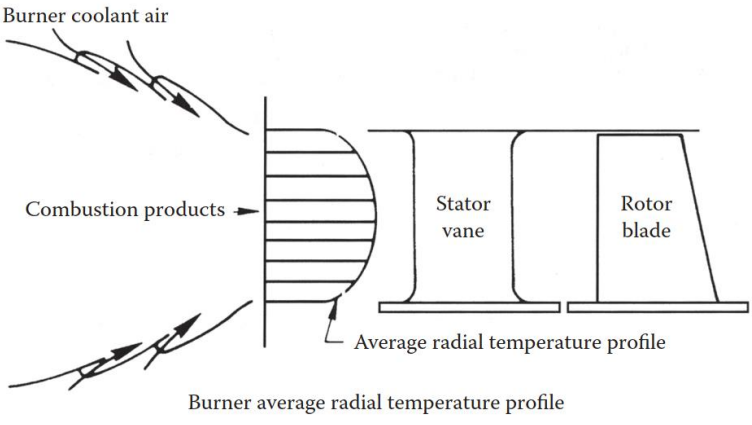

Fig. 2.1 The temperature distribution of the annular burner outlet

The internal cooling scheme includes the jet impingement cooling, serpentine cooling passage, rib-roughened channels, pin fin channels, dimple and protrusion channels, matrix cooling channels and so on. Fig. 2.2 exhibits the insides of the first-stage blades of five different gas turbines. The top row belongs to the heavy-duty gas turbine, while the bottom row comes from the turbofan engines. The AL-31 turbine blade is cooled with matrix channels in the middle region. Except for the AL-31 turbine blades, the rest use the rib-roughened and 180-degree serpentine cooling passages.

Fig. 2.2 The internal cooling structures of the first-stage blades [15]

In the area of trailing edge, pin fin can be seen in GE CF6. All the internal cooling schemes are designed for the purpose of enhancing the heat transfer inside the blades or vanes. In addition, the usage amount of the coolant and the pressure loss also needs to be considered, aiming at using the minimum coolant and obtaining the maximum cooling effect. The blade can be controlled under an appropriate temperature and the thermal stress sustains within a safe range.

Fig. 2.3 is a schematic diagram of a modern fully cooled turbine blade. As it can be seen in the leading edge, the gas flows through the tiny impingement holes into the front plenum and impinges on the inside wall of the leading edge. The high-speed impingement jets can lead to a very high local heat transfer coefficient. The principle is that near the stagnation point the turbulence fluctuation is much stronger and the boundary layer is thinner. Because the heat load is the highest in the leading edge, the jet impingement cooling is considered as a very effective way to exchange the heat between the turbine blade wall and the coolant. However, the jet impingement cooling can be only used for the leading edge of the rotor blades, because the variance in temperature between the impingement stagnation point and the other leading-edge region is huge, thus, the high thermal stress is found on the leading-edge region. In addition, the impingement holes need to be laid out on the inner wall, which causes that the structure strength deteriorates to some extent, but the high rotational speed of the rotor needs higher strength of the structure to keep the structure integration. The effects on the performance of the jet impingement mainly result from the geometric dimension, including the diameter of the impingement holes, the airflow direction [16], layout of the holes [17], jet-to-target plate distance [18], the target surface curvature ratio [19, 20], target surface roughness [21, 22], etc.

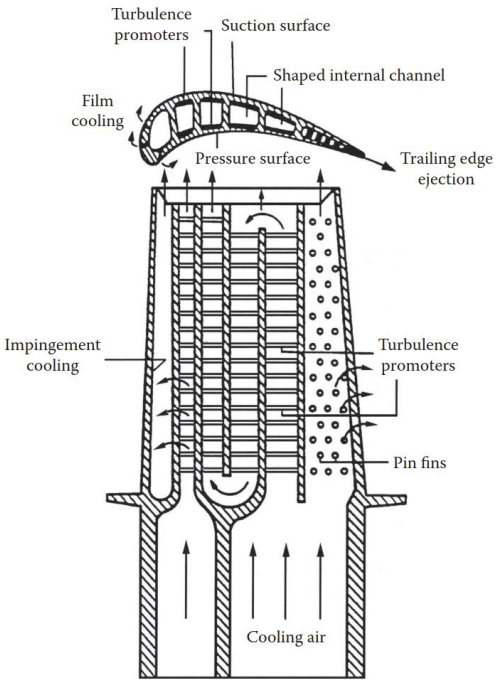

Fig. 2.3 Typical internal cooling concepts of modern turbine blade [23]

The 180-degree rib-roughened channels are employed in the mid-chord region. The horizontal ribs are arrayed perpendicular to the cooling passages, which can cause the boundary layer separation and reattachment on the inner wall. The secondary flow can improve the heat transfer performance and increase the pressure loss inevitably. The effects on the thermal performance involve pitch-to-height ratio [24], rib angle [25] and inline or staggered rib configurations [26, 27] and so on.

Pin fin turbulator layout is often applied in the trailing-edge region [15], because it's difficult to array the ribs in the confined spaces, whereas pin fins can fulfil the requirements for space saving and structural strength. The airflow bumps against the pin fin, and the heat transfer improves due to the horseshoe vortex and boundary layer separation [28]. The main performance parameters of the pin fin contain the pin fin layout patterns [29], the shape of the pins [30], height-to-diameter ratios [31].

Apart from the ribs, pin fins and serpentine cooling schemes, dimple, protrusion and matrix cooling channel are also frequently used. The arrays of dimples, shallow indentations or depressions are another kind of turbulators on the inner wall of the turbine blade, which can generate vortices and increase the flow turbulence. As illustrated in Fig. 2.4, the inside surface of the dimple can be divided into two main zones, one is the recirculation zone with lower heat transfer, and the other is called reattachment zone where the heat transfer is higher. The vortex shedding results in an enhancement in heat transfer on the downstream surface of the dimple, but also causes the increase of the pressure loss [32]. The turbulence intensity of the freestream[33], the shape of the concavity [34] and the ratio of dimple depth to dimple print diameter [35] affect the thermal performance.

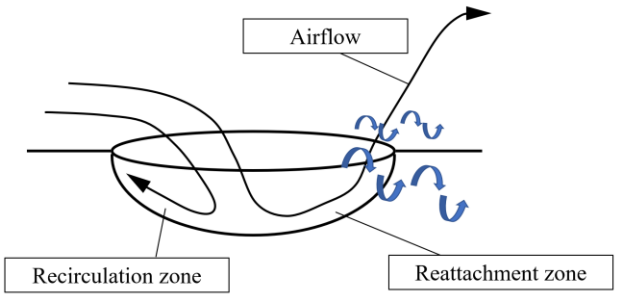

Fig. 2.4 Schematic of the dimple vertex generator

Matrix cooling, also known as latticework or vortex cooling, is a novel cooling structure for the internal cooling of the turbine blade [36]. The matrix cooling channel can be simplified as a two-layer structure as shown in Fig. 2.5. The top and bottom surfaces represent the pressure side and the suction side of the blade. The rib height is half of the channel height, and the angle of all the ribs are β with respect to the mainflow streamwise direction. The turning angle of the air is equal to 2β through the side region. Due to the turning structure, secondary vortices are generated, and air impingement occurs on the side walls, which contributes to the increase of the heat transfer. Because of its extraordinary hear transfer enhancement, it can be used to solve the overheating region effectively without sacrificing the structure strength, but inevitably the cost of the pressure drop is higher than the other internal cooling schemes. Saha [37] investigated the matrix cooling channels under Re=24,000, 40,000, 60,000. Thermal performance factor (defined as $TPF=(Nu/Nu_0)\times(f/f_0)^{-1/3}$) of the matrix channel is 1-1.3, compared with the pin fins of 0.70-0.85 [38]. The average heat transfer enhancement is in the range of 4-5 and as high as 7-8 in the turning areas. Research has been undertaken to investigate the effects of the rotation [39], Reynolds number [40], sidewall slots [41], bleed holes [42], etc.

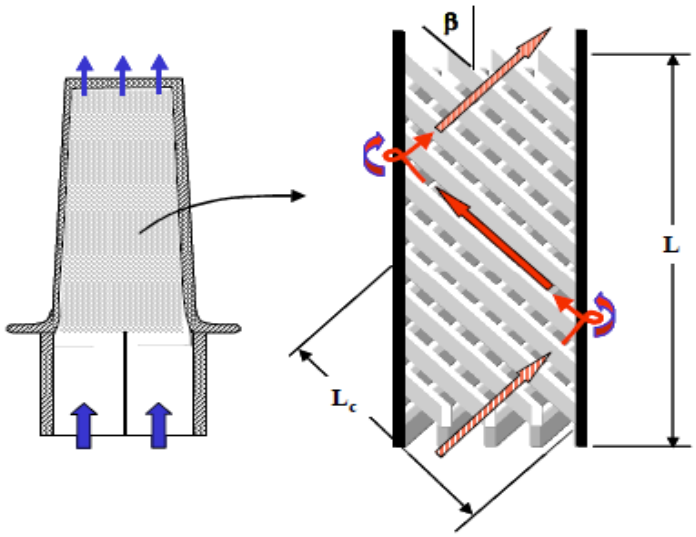

Fig. 2.5 Schematic of the simplified matrix cooling channel [43]

2.2 Turbine blade film cooling

2.2.1 Development of film cooling

Film cooling is an evolutionary innovation in the history of the turbine blades or vanes cooling. In 1970s, film cooling started to be widely applied in the gas turbine [44]. This type of cooling solution depends on ejecting the coolant gas from the internal cooling passages through multiple smaller shaped film cooling holes that are laid out on the outer surface of the turbine blades or vanes, and the coolant can attach the surface of the blades and form an insulating layer between the hot mainstream and the blade wall [45]. The design of the film cooling has been optimizing to reduce the detachment and improve the cooling effectiveness with less coolant.

The film cooling technology was first investigated for the combustor liners of the gas turbine or the rocket engine in preference to the turbine blades or nozzle vanes. Dating back to as early as 1954 [46], before the applications of the conventional film cooling holes, the so-called stepdown slot has been studied by R. A. Seban [47-49], Eckert and Birkebak [50], Chin et al.[51] and Hartnett et al. [52] in 1960s. As shown in Fig. 2.6, the conventional film cooling configuration is reported in Fig. 2.6(a), while the earlier stepdown slot geometry is presented in Fig. 2.6(b). Both types of the film cooling aim at using the low temperature coolant through the slots or holes as an envelope of film and protecting the blade wall from the freestream at high temperature. Later, film cooling was used for the turbine blades as well, which has been gradually becoming a research topic of growing interest in recent decades.

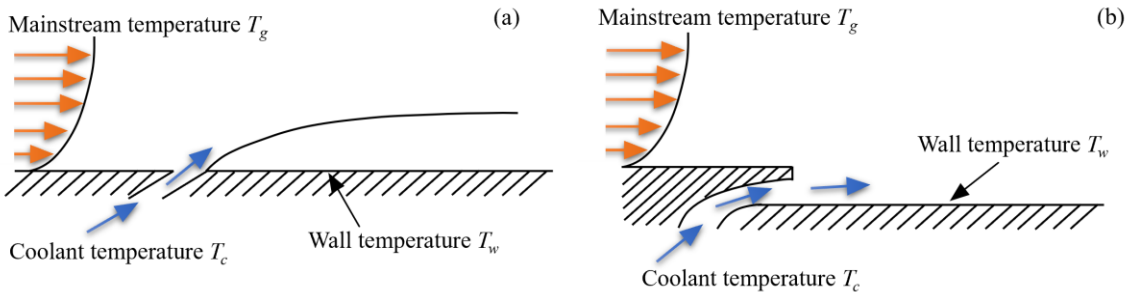

Fig. 2.6 Various types of film cooling: (a) conventional film cooling (b) stepdown slot [53]

2.2.2 Fundamentals of film cooling

The conditions of the mainstream and coolant gas are intimately tied to the thermal performance of the film cooling and the flow field schemes. The main parameters include the density ratio (DR), velocity ratio (VR), blowing ratio or mass flux (M) and momentum flux ratio (I) [54]. These definitions of the ratios are given by equations 1.1.

$$\begin{gathered} \mathrm{DR}=\frac{\rho_c}{\rho_\infty} \quad \mathrm{VR}=\frac{u_c}{u_\infty} \\ \mathrm{M}=\frac{\rho_c u_c}{\rho_\infty u_\infty}=\frac{\dot{m}_c/\mathrm{A}_{in}}{\rho_\infty u_\infty} \quad \mathrm{I}=\frac{\rho_c u_c^2}{\rho_\infty u_\infty^2} \end{gathered} \tag{1.1}$$

where the subscripts c and ∞ stand for the coolant and free stream respectively. A_{in} is the inlet area of the film hole and $\dot{m}_c$ is the mass flow of the coolant.

The non-dimensional temperature T_{non} is depicted in Fig. 2.7 as a measurement of the temperature profile. It shows the thermal profile of the centerline of cylindrical film cooling rectangular passage. The normalized temperature equation is defined as [45]:

$$T_{non}=\frac{T_\infty - T}{T_\infty - T_c} \tag{1.2}$$

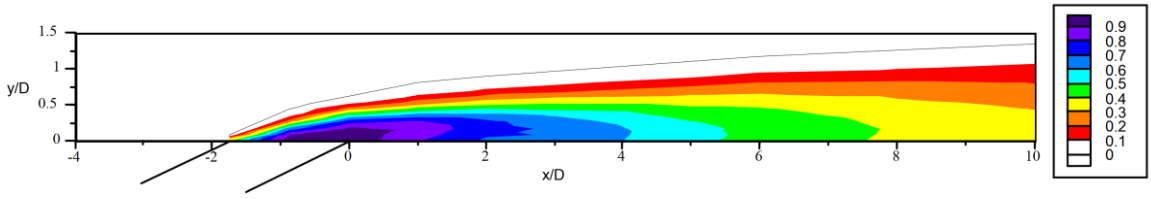

Fig. 2.7 Thermal profiles of the coolant temperature distribution

where T_∞ is the mainstream temperature, T_c is the coolant gas temperature and T is the local temperature. T_{non} is zero when the local temperature is equal to the mainstream temperature, and T_{non} equals unity if the local temperature is the coolant temperature. On the adiabatic wall, the coolant temperature T_c becomes the adiabatic wall temperature T_{aw}. And the mainstream temperature T_∞ can be normalized by the adiabatic wall temperature T_{aw} referred to as the adiabatic cooling effectiveness η, defined as:

$$\eta=\frac{T_\infty - T_{aw}}{T_\infty - T_c} \tag{1.3}$$

When the adiabatic wall temperature is equal to the coolant temperature, the value of the adiabatic effectiveness η is unity, while adiabatic effectiveness η is zero, when the adiabatic wall temperature is the mainstream temperature, which also means the film cooling have no effects on the wall temperature reduction.

A new term, heat flux q, is introduced to represent the heat load to the surface, which is defined as:

$$q = h(T_{ref} - T_w) \tag{1.4}$$

where T_{ref} is the reference temperature (also called driving temperature), and T_w is the wall temperature. The heat fluxes q_0'' and q_f'' indicate that the surface is without and with the film cooling respectively, given as:

$$\begin{aligned} q_0'' &= h_0 (T_\infty - T_w) \\ q_f'' &= h_f (T_{aw} - T_w) \end{aligned} \tag{1.5}$$

where h_0 and h_f are represented as the convective heat transfer coefficients without and with the film cooling respectively. T_{ref} is substituted by free stream temperature T_∞ for the non-film cooling scheme. As for the surface with film cooling, usually the adiabatic wall temperature T_{aw} is presumed to be the driving temperature potential for the heat flux into the wall. The ratio of the q_f'' and q_0'' is called the heat load ratio as follows [2]:

$$\begin{aligned} \frac{q_f''}{q_0''} &= \frac{h_f}{h_0} \frac{T_{aw} - T_w}{T_\infty - T_w} \\ &= \frac{h_f}{h_0} \left(1 - \eta \frac{T_\infty - T_c}{T_\infty - T_w}\right) \end{aligned} \tag{1.6}$$

In equation 1.6, the heat transfer coefficient ratio h_f/h_0 is larger than 1, due to the enhancement of the mixing of the mainstream and the coolant. The adiabatic film cooling effectiveness multiplied by $\frac{T_\infty - T_c}{T_\infty - T_w}$ is less than 1. Therefore, the heat load ratio should be smaller than 1.

Equation 1.6 contains three variables that can be obtained from the separate experiments, one is the case where the surface is not heated and the coolant flows through the film cooling hole mixing with the mainstream, where the T_{aw} is obtained. And another one is the coolant and mainstream remain unchanged as the former one, but the cooling passage is heated at a certain temperature, thus the film cooling heat transfer coefficient h_f is gained. The last one is to measure the heat transfer coefficient without film cooling h_0

The discharge coefficient C_d can be used to evaluate the thermal performance of the film cooling holes as well, which can assess the flow losses quantitatively. The discharge coefficient C_d is defined as the ratio of the actual mass flow rate to the ideal mass flow rate through film cooling holes, shown in equation 1.7:

$$C_d = \frac{\dot{m}_c}{\dot{m}_{c,is}} = \frac{\dot{m}_c}{\rho_{c,is} u_{c,is} A_{in}} \tag{1.7}$$

Where $\dot{m}_c$ denotes the actual mass flow of the coolant and $\dot{m}_{c,is}$ is calculated with the assumption of the isentropic one-dimensional expansion from the total pressure in the coolant plenum $p_{t,c1}$ to the static pressure in the mainstream channel p_{c2}, which can be calculated as follows:

$$\dot{m}_{c,is} = A_{in}\, p_{t,c1} \left(\frac{p_{c2}}{p_{t,c1}}\right)^{\frac{\lambda+1}{2\lambda}} \sqrt{\frac{2\lambda}{(\lambda-1) R T_{t,c1}} \left[\left(\frac{p_{t,c1}}{p_{c2}}\right)^{\frac{\lambda-1}{\lambda}} - 1\right]} \tag{1.8}$$

Where A_{in} is the cross-sectional area for the cylindrical hole and the cross-sectional area of the cylindrical section for the shaped film hole respectively.

2.2.3 Geometry of film cooling holes

The geometry of film cooling holes has been developing and evolving from simple to complex. As mentioned before, the slot and round holes were studied and researched at the beginning. One of the aims is to optimize the film cooling structure and use less coolant to obtain better thermal cooling effectiveness. Hence, slot was changed into the discrete film holes. Sinha et al. [54] investigated the cylindrical film cooling hole experimentally at DR=1.2-2.0, M=0.25-1.0. The centerline film effectiveness distributions are compared to study the effects of the blowing ratio, velocity ratio and momentum flux ratio. For lower blowing ratios, the injection can stay attached to the surface and film effectiveness scales

with mass flux ratio. For higher blowing ratios, the detachment and reattachment affect the film cooling effectiveness significantly. Pietrzyk et al. [55] measured the velocity profiles of the cylindrical hole passage along the streamwise direction at lower blowing ratios M=0.25-1.0. Good correspondence can be found between the large velocity gradient, the turbulence level and *uv* shear stress component. Large positive shear is generated at the interface between the mainstream and coolant corresponding to the peaks of the *uv* shear stress component. For the further downstream region, the shear layer is indistinguishable. Pietrzyk et al. [56] also studied the cylindrical film hole at unit and two density ratios and blowing ratio of M=0.5, the results show that the dense jet has lower velocity at near wall region and near field than the unit density jet, and further downstream the velocity field is similar to each other. Thole et al. [57] obtained the non-dimensional temperature of the cylindrical holes at different streamwise positions under M=0.5-2.0, DR=1.2-2.0 and I=0.125-2.0. They proved the momentum flux ratio as the scaling parameter which dictates the attached and or detached state of the coolant injection.

The shaped film hole was also studied and applied later. Bunker [58] summarized four types of the shaped film holes shown in Fig. 2.8. The expansion in lateral direction is called fan-shaped (also known as flared holes), the expansion in forward direction is known as laidback. Geometry A is commonly applied in practice that is composed of the conventional cylindrical section and both lateral and forward expansion section. Geometry B only has the lateral exit expansion. Geometry C only contains the laidback exit expansion. Geometry D is the conical film hole throughout the structure with the same expansion in each direction around the centerline.

Gritsch et al. [59] studied the shaped film cooling holes and measured the adiabatic wall cooling effectiveness shown in Fig. 2.9. The three geometries are inclined with the angle of 30°. Geometry B and C expand both in lateral direction with the angle of 14°. While Geometry C is the laidback fan-shaped hole with 15° forward expansion angle. The results show that the flared shaped and laidback fan-shaped holes both improve the laterally averaged film cooling effectiveness compared with the cylindrical film hole, especially at higher blowing ratios.

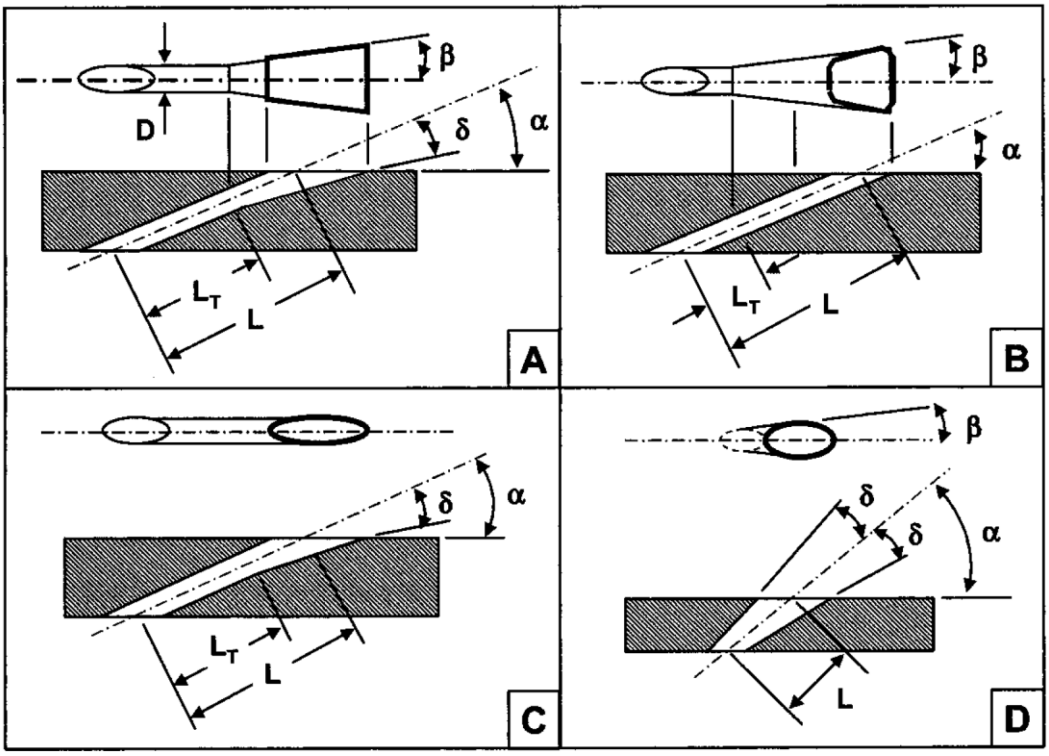

Fig. 2.8 Geometries of four types of shaped film cooling holes [58]

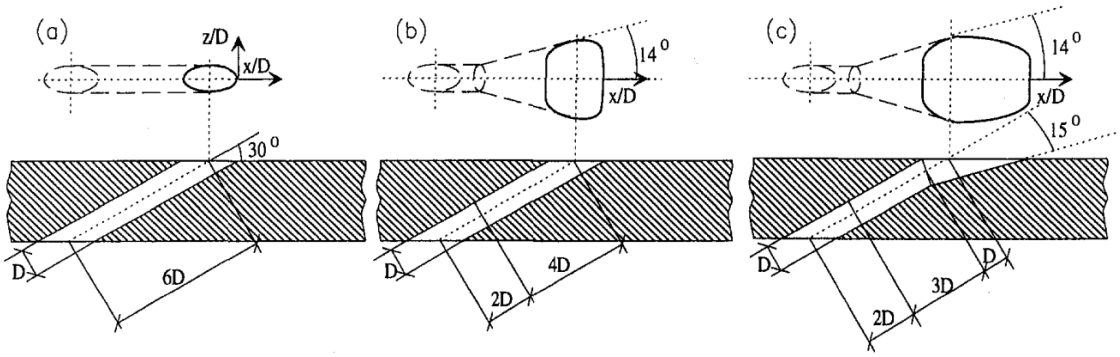

Fig. 2.9 Schematic of shaped film cooling holes [59]

Schroeder and Thole [1] proposed the 7-7-7 shaped hole as a baseline solution based on the large number of data from the previous public literature. The 7-7-7 film hole arrangement is a type of laidback fan-shaped film cooling hole with the same 7 degree in both two lateral and forward expansion. The results show the best cooling effectiveness for various density ratio when blowing ratio is roughly equal to 1.5.

2.2.4 Applications of film cooling

As mentioned above, film cooling was used for the combustion chamber at the beginning. Later, film cooling technology has been applied into not only the turbine blades

or nozzle vanes, but also the blade tip and endwall regions. A film cooled blade often has the leading-edge film cooling holes (showerhead), pressure and suction side film cooling hole arrays [44].

2.2.4.1 Tip film cooling

Fig. 2.10 presents the film cooled rotor turbine blade of GE CF6. The squealer tip hole and tip-cap hole can be found in the tip region, since the tip of the blade suffers from a high heat load and the high-temperature clearance leakage flow from the pressure side to the suction side through the space between the tip and the shroud, and it may damage the blade tip. Hence, film cooled tip can prevent the blade from the failure.

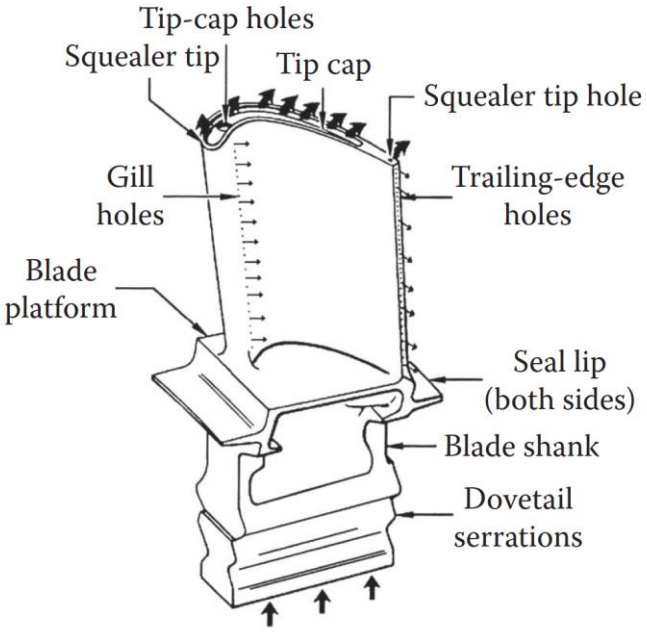

Fig. 2.10 High pressure turbine rotor blade for GE CF6 [60]

In 1955, Kim and Metzger et al. [61, 62] studied three blade tip film cooling configurations presented in Fig. 2.11. The coolant is ejected through the tip, pressure side and the grooved-tip surface, and the types of the film cooling hole shape include the discrete slots, round holes, flared holes on pressure side and round holes on the grooved-tip surface (squealer). The distribution of the Nusselt number and film cooling effectiveness are presented under different mass flow ratios of the coolant to the mainstream. The discrete slot shows a higher film effectiveness and better protection capability.

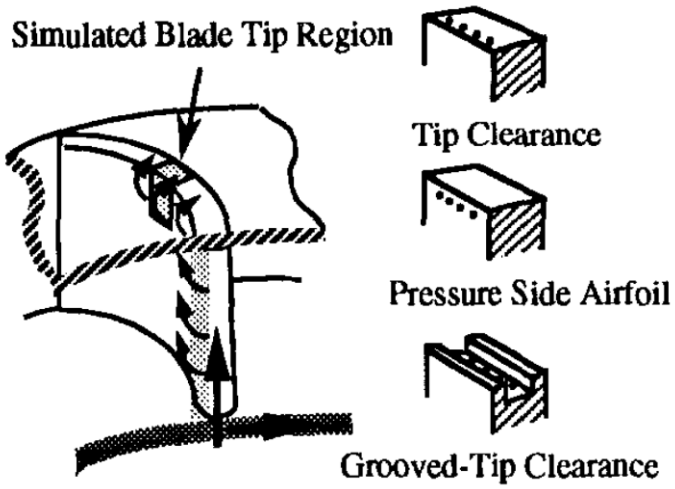

Fig. 2.11 Various configurations of the tip film cooling [61]

Bunker [63] conducted the experiment and showed the distribution of the heat transfer coefficient of the tip surface for the sharp and rounded edge tips. Jae Su Kwak and J C Han [64] used transient liquid crystal technique to measure the heat transfer coefficient and the film effectiveness on the squealer tip surface of a linear turbine blade cascade. The heat transfer coefficient increases with the increase of the tip clearance. The heat transfer coefficient decreases, and the overall film effectiveness increases for the grooved tip compared with the plane tip. Mhetras et al. [65] measured the film cooling effectiveness on the squealer rim walls and the squealer cavity floor under M=0.5, 1.0, 2.0. The injection from only near tip pressure side causes the cooling effectiveness to deteriorate on the cavity floor and inner rim walls. Aha et al. [66] conducted the experiment with the pressure-sensitive paint to study the effects of the presence of squealer, the locations of the holes and the tip clearance on the film cooling effectiveness. Yan, He et al. investigated a series of squealer tip film cooling configurations with numerical simulations [67-70]. The effects of the tip gaps and blowing ratios on the heat transfer coefficient and the film cooling effectiveness are studied. A lower heat transfer coefficient area can be found near the pressure side of the cavity floor when the blowing ratio raises.

2.2.4.2 Endwall film cooling

For the low-aspect ratio and low-solidity turbine designs, the film cooled endwall plays an important role [2]. Low speed experiments were carried out by Dunn and Stoddard [71]. The Reynolds number ahead of the stator is about 1.3×10^5 based on the mid annular chord

length and the Mach number is 0.8. The heat flux was measured by the thin-film heat-transfer gages that were installed on the endwall and airfoil pressure side.

In Fig. 2.12, Takeishi et al. [72] studied a low speed, low aspect ratio (H/C=0.5) and fully annular turbine nozzle vane cascade at M=0.5-2.5. The inlet velocity is 15m/s and the outlet velocity is 64m/s. Three positions of the film cooling holes were tested on the endwall. The results show that the secondary flows strongly affect the heat transfer and film cooling on the endwall and the suction side, while have almost no influence on the pressure side. The horseshoe vortex increases the heat transfer and decreases the film cooling effectiveness near the leading edge on the endwall.

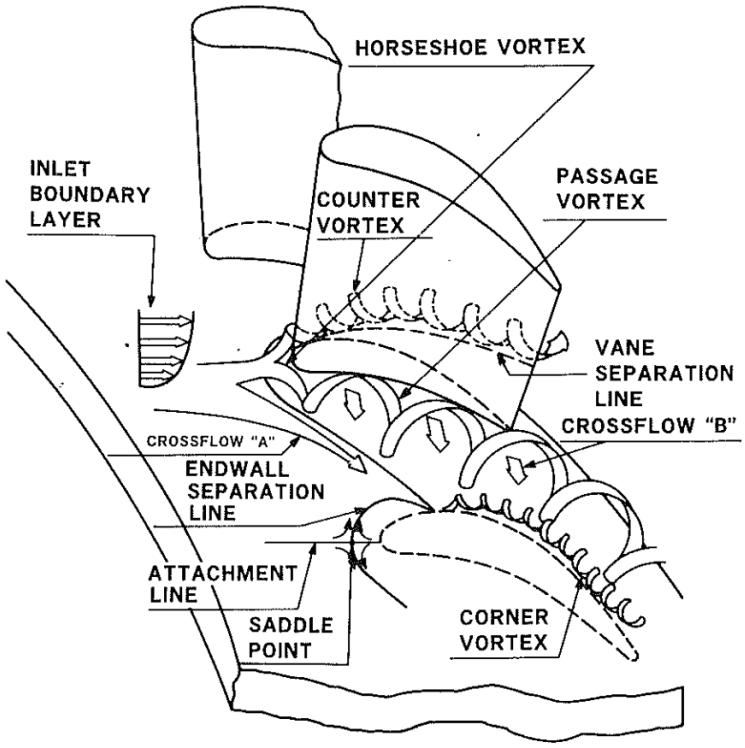

Fig. 2.12 The flow scheme of the nozzle vane cascade [72]

Friedrichs et al. [73] investigated a large-scale low-speed linear turbine cascade using the ammonia and diazo technique to measure the film cooling effectiveness distribution. As illustrated in Fig. 2.13, the coolant below the lift-off lines (the dash line) is inefficient, because the coolant is ejected through the film holes and detached from the endwall surface, then it mixes with the freestream. While the ejection far away from the lift-off lines provide effective film cooling capability to the endwall.

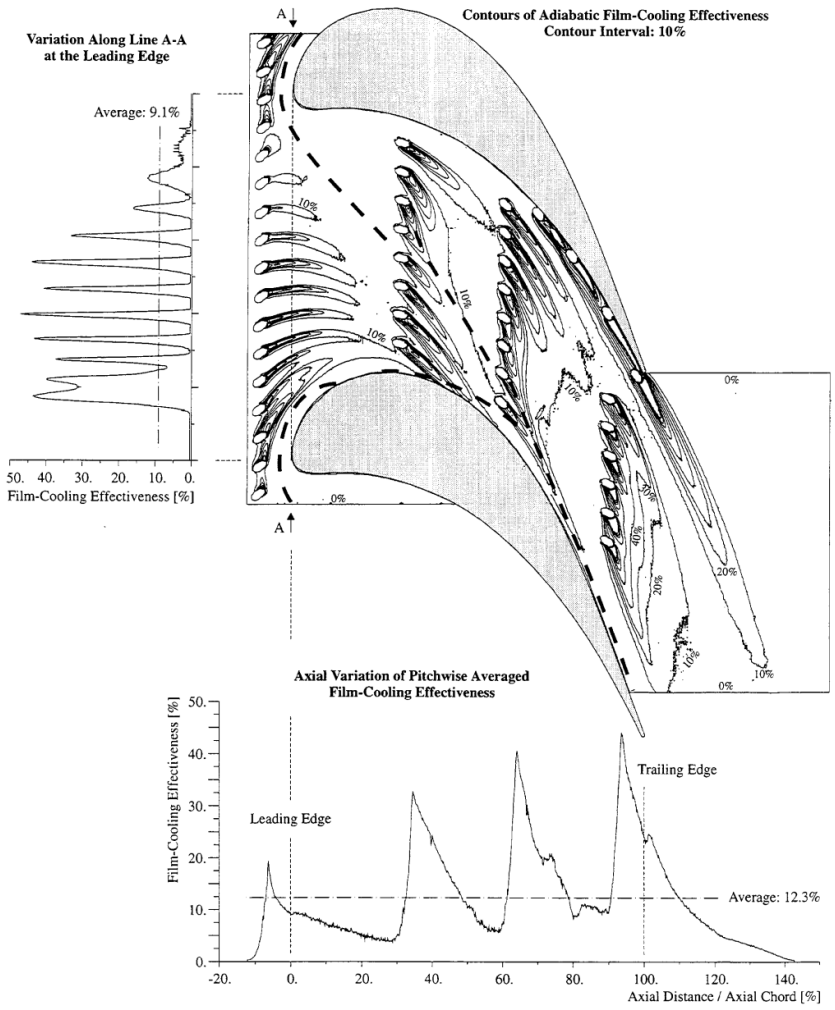

Fig. 2.13 Distribution of the endwall film cooling effectiveness [73]

Satta and Tanda [74] carried out the experiments on two endwall film cooling configurations. It was found that the film hole array that are aligned in the pitchwise direction provides an over-cooled and under-cooled regions, which is efficient for the coolant to cover the endwall surface and causes a lower effectiveness region between adjacent rows of holes. Lynch, Mensch, Thole et al. [75, 76] also conducted the experiments on the contoured endwall film cooling with the flush slot that simulated the leakage. Results show that the heat transfer coefficient increases when the net leakage increases from zero to 0.6% of the mainstream rate, but the heat flux to the contoured endwall surface decreases due to the high cooling effectiveness of the leakage flow. The endwall film cooling results in the increase of the passage vortex, secondary velocity and exit plane turbulent kinetic energy, whereas the contoured endwall reduces all of them.

2.2.4.3 Turbine blades or vanes film cooling

Fig. 2.14 illustrates three real turbine blade or vane with the external film cooling, which are the first-stage rotor of MTU RB199 used in the aircraft Panavia Tornado, the first-stage nozzle guide vane of IAE V2500 applied in Airbus A320 and the first stage stator of Pratt & Whitney F100 in F16 fighter jet respectively. A vast array of film cooling holes is set at the leading edge, trailing edge and mid-chord regions.

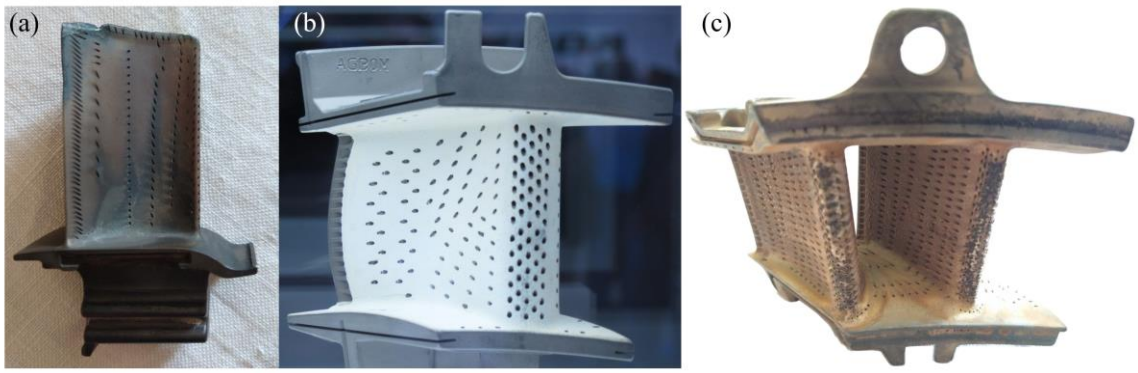

Fig. 2.14 Turbine blade or vane with film cooling arrangement (a) MTU RB199 (b) IAE V2500 (c) Pratt & Whitney F100

Because of the high temperature mainstream from the combustion chamber, the leading edge of the first-stage nozzle vane has to withstand a high heat load. Hence, it is necessary to apply the film cooling to the leading-edge region. According to the review of Kercher [77], there were at least 35 years since the film cooling is used for the leading edge. Gary et al. [78] experimentally studied the leading-edge film cooling with two angled film holes at 18° and 35° with respect to the spanwise direction as depicted in Fig. 2.15. The smaller angled film cooling configuration presents a better thermal performance for the highly accelerated mainstream. Kim et al. [79] conducted the experiment with five different laidback shaped holes at M=0.7-1.7, and studied the effect of the holes on the film cooling effectiveness distribution. Elnady et al. [80] carried out an experimental investigation on the shaped film holes on the leading edge region. The injection angle is 60° and 90° relative to the spanwise at M=1-2 and DR=0.9. The suction side shows a lower cooling effectiveness than the pressure side. Coolant injected at 90° can hardly keep attached to the highly curved leading-edge surface, therefore, the 60° angled film holes show a better film cooling effectiveness compared with the steep inclination angled holes.

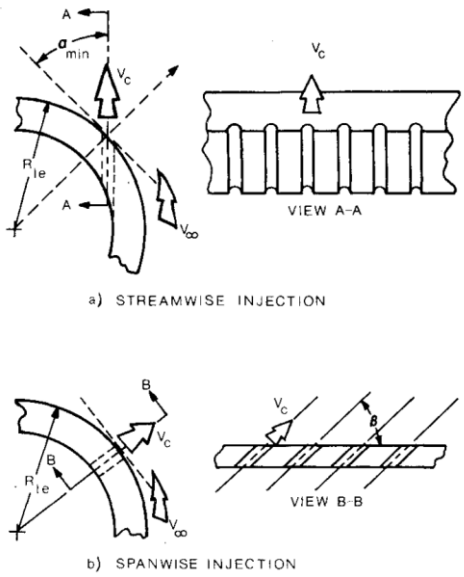

Fig. 2.15 Schematic of the film cooled leading edge configuration [78]

In 1988, Hylton et al. [81] from NASA researched the C3X and Mark II vanes with not only internal cooling tube passages but also leading-edge, downstream pressure-side and suction-side film cooling. And earlier in 1983, Hylton et al. [82] also carried out the experiment on the C3X and Mark II vanes with another configuration of internal cooling passage. The metallic film cooled linear vane cascade was made with the installation of the thermocouples on all surfaces. The film cooled part was separated from the rear part of the vanes by cutting the vane into two segments and creating a sealed air gap. The large number of the heat transfer coefficient data were measured under the real engine condition of the nozzle vane.

2.2.5 Film cooling investigation methods

2.2.5.1 Experimental investigations

Dating from 1969, experiments have been carried out as the main investigation method in earlier stage of the research. The main purpose is to obtain the surface temperature distribution and calculate the heat transfer coefficient. Thus, the thermocouple can be found in many papers, due to its cheaper price, easy operation and convenient acquisition. In 1969, Goldstein et al. [83] conducted the experiment with the thermocouples in the test plate downstream of the five-hole injection arrays. Hylton et al. [81, 82] used thermocouples to measure the pressure and suction side temperature distributions of C3X and Mark II vanes

at midspan. Thole et al. [57], Sinha et al. [54], and Pietrzyk et al. [84] used the thermocouples to measure the coolant temperature.

Since 1970s, the thin-film heat flux gage was employed to measure the heat flux rate of the turbine blades or vanes under real engine simulated condition. Abhari and Epstein [85] measured the effect of the unsteadiness on the heat transfer using the heat flux gage. Doorly and Oldfield et al. [86, 87] used thin-film heat flux gage to investigate the transient turbine cascade heat transfer.

Infrared thermography (IRT) is a non-intrusive method to obtain the heat transfer performance. It can provide the temperature maps in a certain area, which depends on the IR resolution of the IR camera. Blair and Lander [88] introduced the application of this technique to testing the leading-edge film cooling effectiveness as early as 1975. Eberly [89] also used the infrared camera to measure the flat plate adiabatic film cooling effectiveness.

Pressure-sensitive paint (PSP) is a newer measurement technique. The fundamental principle is the oxygen quenching of luminescence from the paint [90]. Since 1990s, the PSP was used in aerodynamic testing. McLachlan and Bell [91] measured the pressure distribution of the airfoil surface. Zhang et al. [92], Wang [93] and Li et al.[94] employed the PSP to measure the film cooling effectiveness on the turbine nozzle vane surface in a high speed wind tunnel. Abdeh, Ravelli and Barigozzi et al. [95-97] investigated the leading edge film cooling system of a nozzle guide vane equipped with cylindrical film holes by PSP technique and analyzed the aerothermal performance with N_2 or CO_2 coolant.

Liquid crystal technique is also commonly used in the film cooling investigation. Drost et al. [98] used the transient liquid crystal technique to measure the film cooling effectiveness and heat transfer on a flat plate and a linear turbine cascade. The maximum lateral averaged effectiveness is about 0.3 behind the injection on suction side, and the film cooling effectiveness is constant at around 0.05 further downstream on pressure side. Lutum et al. [99] determined the film cooling effectiveness and heat transfer coefficients of the cylindrical and shaped film holes in a converging channel. Results show the converging channel causes the freestream acceleration and the decrease of film cooling effectiveness. Barigozzi et al. [100] studied the cylindrical and fan-shaped film holes with

and without the upstream ramp with the transient liquid crystal measurement technique, results show that the cylindrical hole with ramp improves the thermal protection only at M=0.3, while the upstream ramp results in the detrimental effect to the fan-shaped film hole at M=0.3-1.0. Satta and Tanda [74, 101] conducted the experiment using liquid crystal thermography to measure the local heat transfer coefficient and cooling effectiveness of a turbine cascade endwall. The re-design of discrete-hole configuration was proposed and obtained better coolant coverage, based on knowledge of the heat transfer coefficient.

2.2.5.2 Reynolds-averaged Navier–Stokes (RANS) simulations

Because of the application and development of the computer in the past decades, the computational fluid dynamics (CFD) becomes a commonly used method. Depending on the high performance computing, an increasing number of researchers choose the numerical simulation method to evaluate the thermal performance of the film cooling structures.

Chen et al. [102] tested the k-ε EARSM turbulence model with a curved cylindrical film hole. Compared with the k-ε RNG model and SST model, k-ε EARSM turbulence model shows a relative better prediction than the other two models, because it contains a nonlinear relation between Reynolds stress and strain rate. Li et al. [103] investigated the 7-7-7 shaped film hole under the endwall cross flow condition. Realisable k-ε model shows the most accurate trend of film cooling effectiveness, compared with the Standard k-ε, SST and Transitional SST turbulence model.

For some cases without film cooling, the RANS method could be the better choice for its high efficiency and less expensive computational cost. However, for the film cooling cases, the RANS method has the limitation. For instance, the normal spreading of the coolant is underestimated by 20%-50% [104]. The conventional eddy viscosity model assumes isotropic flow field, while the vortices are generated and the flow is unsteady and anisotropic [102].

2.2.5.3 Large eddy simulation

Large eddy simulation is a numerical technique for integrating spatially filtered equations of motion, which can describe the details of three-dimensional turbulence in the

flow field [105]. Large eddy simulation is increasingly employed in not only the academia but industry gradually, thanks to the computer technological advances.

Rozati and Tafti [106] studied the leading-edge cylindrical film cooling hole with large eddy simulation at density ratio DR=1 and low blowing ratio M=0.4. The simulation presents the asymmetric counter-rotating vortex pair in the immediate wake of the injection driven by the lower pressure zone in the wake.

Li et al. [107] studied the axial and compound angle cylindrical film holes with various length-diameter ratios (L/D=0.5-5) using large eddy simulation. The non-compound film hole shows the best film cooling effectiveness, and as for the compound angle holes, L/D=2 has better cooling effectiveness than L/D=5.

Zamiri et al. [108] used LES to investigate a type of laidback fan-shaped film cooling hole. A comparison of the LES, DES, SAS and hybrid RANS/LES has been made, and LES shows the best results in terms of the film cooling effectiveness prediction.

2.2.5.4 Direct Numerical Simulation

Direct Numerical Simulation (DNS) can simulate the whole range of spatial and temporal scales of turbulence, which indicates that the Navier-Stokes equations are numerically solved without the turbulence model used in the RANS simulation or the subgrid model in LES. Therefore, DNS needs expensive computational resources under a limited lower Reynolds number, compared with the RANS and LES.

Muldoon and Acharya [109, 110] numerically studied the single film hole with DNS method at Reynolds number 3,068. The exact k and ε were solved by DNS and compared with these terms obtained by standard k-ε model. Results show that the eddy viscosity in standard k-ε model shows large errors, and two damping functions were proposed to improve the accuracy. The appropriate eddy viscosity can minimize the error between the DNS and standard k-ε model. Besides, they also researched the effect of the pulsed coolant on the film effectiveness at Re=8,000 [111]. The recirculation region behind the coolant is reduced and enhances the film cooling effectiveness. Fu et al. [112] also investigated the vortices in the single film cooling channel at Re=480 and 3,200 with 0% and 5% turbulence intensity of the freestream.

2.3 Other cutting-edge cooling solutions

2.3.1 Novel cooling schemes

Transpiration cooling is seen to be one of the most efficient methods in the next generation, which is also shown in Fig. 1.1. It is a thermodynamic process where the heat from the porous wall is absorbed by the gas coolant through the wall and the convective and radiative heat flux loads are relieved simultaneously in order to prevent the blades from the serious heavy heat load damage. While the tough challenge is that the porous material needs to tolerate the required process of the oxidation, otherwise, it will result in the blockage of the tiny holes in the Swiss cheese-like porous wall.

There are several examples with this novel cooling scheme, and two of the best-known applications are called Transply and Lamilloy [113, 114].

Transply was developed by Rolls Royce in the 1970s as illustrated in Fig. 2.16. It is like a sandwich by brazing two or more laminates of a high-temperature alloy together. In the middle of the layers contains the interconnecting flow channels that allow the low-temperature gas to flow through porous structure, and the heat is taken by the gas coolant from the wall.

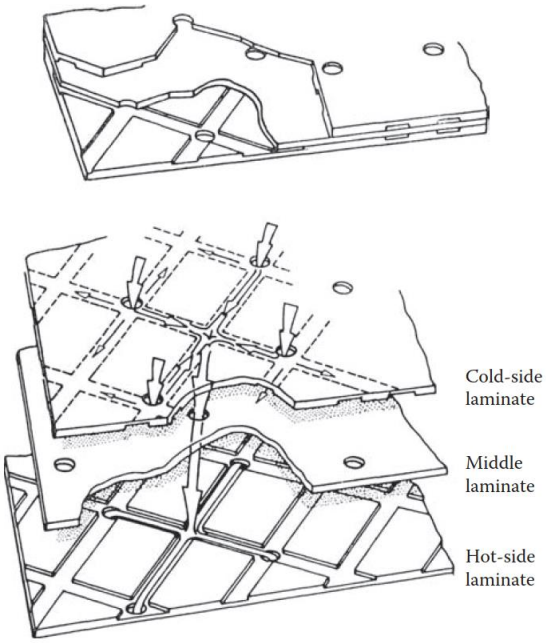

Fig. 2.16 Constructional features of Rolls Royce Transply [115]

This cooling method is firstly customized for the combustor chamber wall. The air goes through the evenly spaced holes and forms a large number of small jet flows on the hot gas side of the liner. Then lots of tiny air jets insulate the liner wall from the hot stream. Later dual-wall cooling was proposed by Rolls Royce, which is a collection of these advanced novel cooling schemes including the Transply cooling technology. The casting laminates are applied as the inner and outer wall of the turbine blades. Since then, Rolls Royce has submitted several patents about turbine blade cooling with the dual-wall cooling technology [116, 117].

Another application is the Lamilloy technology created by the American Allison Engine Company. Fig. 2.17 shows the constructure of this kind of cooling scheme. It is very similar to Rolls Royce's Transply, which means it has the same deficiencies and limitations as the Transply.

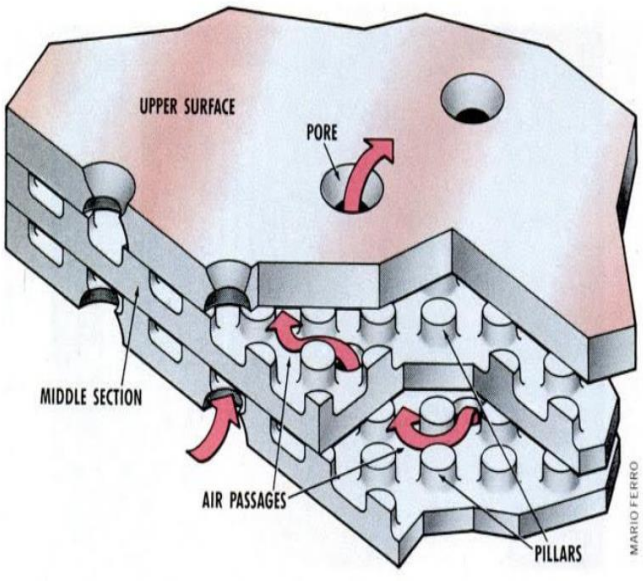

Fig. 2.17 Lamilloy construction transpiration cooling schematic diagram from Allison [118]

Besides, Allison proposed the concept of Castcool, casting the complicated internal cooling system as well as the tiny exits on the outer surface of the blades as shown in Fig. 2.18. With the combination of the Castcool technology and the Lamilloy laminates wall constructure and the help of CMSX-4 single crystal technology, Allison employed the dual-wall Lamilloy quasi-transpiration cooling technology to the airfoil, which facilitates a further 222℃ improvement of the turbine inlet temperature [119].

Fig. 2.18 The turbine blade with Castcool technology

Apart from that, Supercool were also proposed for the advanced turbine blade manufacturing by Pratt & Whitney during the second stage of the IHPTET program. The internal cooling passages are designed the same as the traditional blades, while the casting and laser hole drilling techniques are applied to make the holes small enough. This technology has been verified on F119 turbofan engine and employed on F135 with a 20% increase of the cooling efficiency. Additionally, the high pressure turbine blades of PW800 are also equipped with this technology.

2.3.2 Thermal barrier coating

Due to the enormous demands on the performance of the gas turbine, the turbine inlet temperature continues to increase to satisfy the requirements for the power output and high efficiency. The nozzle vanes have to face the problems of the extreme high operating temperature, though turbine internal cooling passages and external film cooling are well designed for addressing this intractable problem. Consequently, engineers begin to think of adding a coating on the outside surface of the turbine blades or nozzle vans, which is so-called thermal barrier coating.

Usually, the thickness of the coatings is in the range of 100μm-2 mm [120], serving to insulate components from prolonged mainstream with high temperature. Because of the protection of the TBC, the turbine blade or vanes can sustain an acceptable temperature

between the load-bearing alloys and the coating surface and keep the material operating with enough strength [121].

The thermal barrier coatings are composed of four layers between the hot gas and the internal cooling air, which are the ceramic topcoat, thermally grown oxide layer, metallic bond coat and metal substrate as shown in Fig. 2.19.

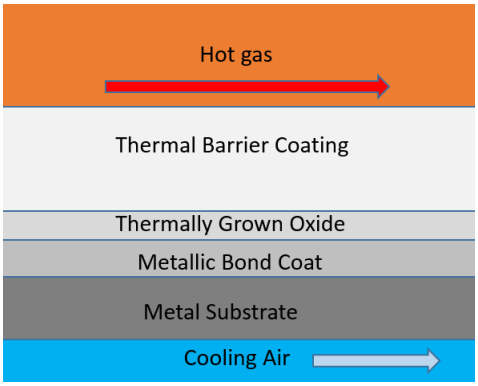

Fig. 2.19 Schematic of the TBC and associated layers

Atmospheric plasma spray and electron beam physical vapour deposition methods are two types of techniques that are the most widely used for thermal barrier coatings nowadays [122]. Thanks to the use of the TBC, it allows for about 5℃-10℃ reduction per mil of the coating[3] and the turbine inlet temperature can increase by 93℃-149℃ (200℉–300℉) [2].

Chapter 3

Numerical methodology

Thanks to the technical progress of the computation resource, the performance of the computer has been greatly increased according to the Moore's law. The evaluation of the computer in return makes a substantial contribution to the rapid development of the computational fluid dynamics, which can not only significantly save computing time and provide the simulation results to the engineers or researchers, but also make the large-scale calculation possible, such as the large eddy simulation or even the direct numerical simulation.

3.1 Governing equations of fluid dynamics

The governing equations of fluid dynamics are the essential of the computational fluid dynamics, which are composed of the continuity, momentum and energy equations. These equations can mathematically characterize the physics of the three dimensional flow field [123].

Based on physical principle that the mass is conserved, the model of the finite control volume can be used to obtain the mass equation. The continuity equation in conservation form is defined as:

$$\frac{\partial \rho}{\partial t} + \nabla \cdot (\rho \vec{u}) = 0 \tag{1.9}$$

Momentum equation can be derived with the Newton's second law that *F*=ma. It is initially named as Navier-Stokes equation in memory of Frenchman M. Navier and Englishmen G. Stokes, which is given in conservation form as follows:

$$\frac{\partial (\rho \vec{u})}{\partial t} + \nabla \cdot (\rho \vec{u} \vec{u}) = \nabla \cdot (\rho \vec{\sigma}) + \rho \vec{f} \tag{1.10}$$

where $\vec{\sigma}$ is stress tensor, $\vec{f}$ is the body forces. The stress tensor can be written as:

$$\vec{\sigma} = - pI_m + \vec{\tau} \tag{1.11}$$

where I_m represents the identity matrix, $\vec{\tau}$ is the shear tensor.

Thus, equation 1.10 can be rewritten as:

$$\frac{\partial(\rho\vec{u})}{\partial t} + \nabla\cdot(\rho\vec{u}\vec{u}) = \nabla\cdot[\rho(- pI_m + \vec{\tau})] + \rho\vec{f} \tag{1.12}$$

Energy equation in conservation form is defined as:

$$\begin{aligned}\rho\frac{\partial}{\partial t}\left(e + \frac{1}{2}|\vec{u}|^2\right) + \frac{\partial\rho}{\partial t}\left(e + \frac{1}{2}|\vec{u}|^2\right) &= \rho\vec{f}\cdot\vec{u} + \nabla\cdot(\rho\vec{\sigma}\cdot\vec{u}) \\ &+ \rho(\dot{q} + q_R) + \nabla\cdot(\lambda\nabla T) \\ &- \left(e + \frac{1}{2}|\vec{u}|^2\right)\nabla\cdot(\rho\vec{u}) - \rho\vec{u}\cdot\nabla\left(e + \frac{1}{2}|\vec{u}|^2\right)\end{aligned} \tag{1.13}$$

where λ is thermal conductivity, e is the internal energy, $\frac{1}{2}|\vec{u}|^2$ is the kinetic energy, $\dot{q}$ is the heat flux and q_R is the radiative heat flux if the radiation problem is concerned.

For the ideal gas, ideal gas equation of state is also employed.

$$p = \rho RT \tag{1.14}$$

where R represents specific ideal gas constant. T is the temperature of the fluid. In Ansys Fluent, the pressure is equal to the operating pressure plus the gauge pressure for the ideal gas.

In terms of the incompressible flow and constant density, the continuity, momentum and energy equations can be rearranged as:

$$\begin{gathered}\nabla\cdot\vec{u} = 0 \\ \frac{\partial\vec{u}}{\partial t} + (\vec{u}\cdot\nabla)\vec{u} = \nabla\cdot(- pI_m + \vec{\tau}) + \vec{f} \\ \frac{\partial}{\partial t}\left(e + \frac{1}{2}|\vec{u}|^2\right) = \vec{f}\cdot\vec{u} + \nabla\cdot(\vec{\sigma}\cdot\vec{u}) + (\dot{q} + q_R) + \nabla\cdot(\lambda\nabla T) - \vec{u}\cdot\nabla\left(e + \frac{1}{2}|\vec{u}|^2\right)\end{gathered} \tag{1.15}$$

3.2 RANS simulation

The Reynolds-averaged Navier–Stokes simulation method can date back to 1985 when Reynolds first proposed the idea of the time average. Using the Reynolds decomposition, the instantaneous quantity is decomposed into the time averaged value and the fluctuating value. The Navier-Stokes equations can be rearranged as:

$$\begin{aligned} &\frac{\partial \rho}{\partial t} + \nabla \cdot (\rho \bar{u}) = 0 \\ &\frac{\partial \rho \bar{u}}{\partial t} + \nabla \cdot (\rho \bar{u} \bar{u}) = -\nabla \bar{p} + \nabla \cdot \left\{ \mu \left[\nabla \bar{u} + (\nabla \bar{u})^T - \frac{2}{3} (\nabla \cdot \bar{u}) I_m \right] \right\} + \nabla \cdot R_s \end{aligned} \tag{1.16}$$

Where R_s is the Reynolds stress, and the Reynolds equation 1.16 can be rearranged as equation 1.18 with the Boussinesq eddy viscosity assumption in equation 1.17.

$$\begin{aligned} R_s &= -\rho u_i' u_j' \\ &= \mu_t \left[\nabla \bar{u} + (\nabla \bar{u})^T - \frac{2}{3} (\nabla \cdot \bar{u}) I_m \right] - \frac{2}{3} \rho k I_m \end{aligned} \tag{1.17}$$

$$\begin{aligned} &\frac{\partial \rho}{\partial t} + \nabla \cdot (\rho \bar{u}) = 0 \\ &\frac{\partial \rho \bar{u}}{\partial t} + \nabla \cdot (\rho \bar{u} \bar{u}) = -\nabla \left(\bar{p} + \frac{2}{3} \rho k \right) + \nabla \cdot \left\{ (\mu + \mu_t) \left[\nabla \bar{u} + (\nabla \bar{u})^T - \frac{2}{3} (\nabla \cdot \bar{u}) I_m \right] \right\} \end{aligned} \tag{1.18}$$

After the decomposition, the nonlinearity of the N-S equation induces the generation of the Reynolds stress term. To obtain the solution of the time averaged Reynolds equation with the additional unknown quantity, four main categories of the turbulence models have been developed since 1950s, which are zero-equation, one-equation, two-equation and second-order closure models. The original and variety of the *k*-ε and *k*-ω turbulence models belong to the two-equation turbulence model.

3.2.1 Standard *k*-ε turbulence model

The standard *k*-ε turbulence model is one of the most well-known models commonly used in practical engineering numerical simulation, due to the stability, appropriate accuracy and low request for the computation resource. It is capable of describing the flow field and heat transfer for various fluids proposed by Launder and Spalding [124].

The transport equations for standard *k*-*ε* turbulence model are given as follows, where *k* and *ε* is calculated.

$$\begin{aligned}\frac{\partial(\rho k)}{\partial t}+\frac{\partial(\rho k u_i)}{\partial x_i}&=\frac{\partial}{\partial x_j}\left[\left(\frac{\mu_t}{\sigma_k}+\mu\right)\frac{\partial k}{\partial x_j}\right]+G_k+G_b-\rho\varepsilon-Y_M+S_k\\ \frac{\partial(\rho\varepsilon)}{\partial t}+\frac{\partial(\rho\varepsilon u_i)}{\partial x_i}&=\frac{\partial}{\partial x_j}\left[\left(\frac{\mu_t}{\sigma_\varepsilon}+\mu\right)\frac{\partial\varepsilon}{\partial x_j}\right]+C_{1\varepsilon}\frac{\varepsilon}{k}(G_k+C_{3\varepsilon}G_b)-C_{2\varepsilon}\rho\frac{\varepsilon^2}{k}+S_\varepsilon\end{aligned} \tag{1.19}$$

where G_k is the generation of turbulence kinetic energy due to the velocity gradient. G_b is the generation of turbulence kinetic energy due to the buoyancy. Y_M represents the contribution of the fluctuating dilatation in compressible turbulence to the overall dissipation rate. $C_{1\varepsilon}$ and $C_{2\varepsilon}$ are constants given in equation 1.21. σ_k and σ_ε are the turbulent Prandtl numbers. S_k and S_ε are user-defined source terms.

The turbulent viscosity can be obtained by *k* and *ε* in equation 1.19.

$$\mu_t=\rho C_\mu\frac{k^2}{\varepsilon} \tag{1.20}$$

where C_μ is a constant.

In Ansys Fluent, the constants in transport equations and turbulence viscosity equation are prescribed as:

$$C_{1\varepsilon}=1.44\ C_{2\varepsilon}=1.92\ C_\mu=0.09\ \sigma_k=1.0\ \sigma_\varepsilon=1.3 \tag{1.21}$$

3.2.2 RNG *k*-*ε* turbulence model

RNG *k*-*ε* turbulence model was proposed by Yakhot and Orzag [125]. Based on the standard *k*-*ε* turbulence model, RNG *k*-*ε* turbulence model was derived by a statistical technique called renormalization group, which is more suitable for rapidly strained flows and swirling flows.

The transport equations for RNG *k*-*ε* turbulence model in high Reynolds number case are given as [126]:

$$\frac{\partial(\rho k)}{\partial t}+\frac{\partial(\rho k u_i)}{\partial x_i}=\left[\frac{\partial}{\partial x_j}\left(\mu+\frac{\mu_t}{\sigma_k}\right)\frac{\partial k}{\partial x_j}\right]+G_k+G_b-\rho\varepsilon-Y_M+S_k$$
$$\frac{\partial(\rho\varepsilon)}{\partial t}+\frac{\partial(\rho\varepsilon u_i)}{\partial x_i}=\left[\frac{\partial}{\partial x_j}\left(\mu+\frac{\mu_t}{\sigma_\varepsilon}\right)\frac{\partial\varepsilon}{\partial x_j}\right]+C_{1\varepsilon}\frac{\varepsilon}{k}(G_k+C_{3\varepsilon}G_b)-C_{2\varepsilon}\rho\frac{\varepsilon^2}{k}-R_\varepsilon+S_\varepsilon \quad (1.22)$$

where R_ε, $C_{1\varepsilon}$ and $C_{2\varepsilon}$ are defined as:

$$C_{1\varepsilon}=1.42\ C_{2\varepsilon}=1.68 \quad (1.23)$$

$$R_\varepsilon=\frac{C_\mu\rho\eta^3\left(1-\frac{\eta}{\eta_0}\right)}{1+\beta\eta^3}\frac{\varepsilon^2}{k}$$
$$\eta=\frac{Sk}{\varepsilon}\ \eta_0=4.38\ \beta=0.012\ S=\sqrt{2S_{ij}S_{ij}} \quad (1.24)$$

For high Reynolds number cases, turbulence viscosity is defined the same as the standard *k*-*ε* turbulence model, however, the constant C_μ equals 0.0845 which is different but very close to C_μ=0.09.

3.2.3 Realizable *k*-*ε* turbulence model

Realizable *k*-*ε* turbulence model was proposed by Shih et al. [127], which is suitable for the separated flows and complex secondary flows according to the initial studies, Compared with standard *k*-*ε* turbulence model, both realizable *k*-*ε* model and RNG *k*-*ε* model show good capability in flow field with strong streamline curvature, vortices and rotation, but it is not clear in which instance realizable *k*-*ε* model performs better than RNG *k*-*ε* model. Two main differences relative to the standard *k*-*ε* model are shown as follows: one is that C_μ is not a constant but defined as the following equation:

$$C_\mu=\frac{1}{A_0+A_s\frac{kU^*}{\varepsilon}} \quad (1.25)$$

The other is the modified transport equation for the dissipation rate in equation 1.26:

$$\frac{\partial(\rho k)}{\partial t}+\frac{\partial(\rho k u_i)}{\partial x_i}=\frac{\partial}{\partial x_j}\left[\left(\frac{\mu_t}{\sigma_k}+\mu\right)\frac{\partial k}{\partial x_j}\right]+G_k+G_b-\rho\varepsilon-Y_M+S_k$$
$$\frac{\partial(\rho\varepsilon)}{\partial t}+\frac{\partial(\rho\varepsilon u_i)}{\partial x_i}=\frac{\partial}{\partial x_j}\left[\left(\frac{\mu_t}{\sigma_\varepsilon}+\mu\right)\frac{\partial\varepsilon}{\partial x_j}\right]+\rho C_1 S\varepsilon-\rho C_2\frac{\varepsilon^2}{k+\sqrt{\nu\varepsilon}}+C_{1\varepsilon}\frac{\varepsilon}{k}C_{3\varepsilon}G_b+S_\varepsilon \quad (1.26)$$

Where

$$C_{1\varepsilon}=1.44\ C_2=1.9\ \sigma_k=1.0\ \sigma_\varepsilon=1.2$$
$$C_1=\max\left[0.43,\frac{\eta}{\eta+5}\right]\ \eta=S\frac{k}{\varepsilon}\ \ S=\sqrt{2S_{ij}S_{ij}} \tag{1.27}$$

3.2.4 Standard *k-ω* turbulence model

The standard *k-ω* turbulence model was firstly proposed by Kolmogorov in 1942 [128]. Kolmogorov modeled the governing equations with the specific rate of dissipation of the turbulence kinetic energy. Later, Wilcox et al. focused on the improvement of the *k-ω* turbulence model. The transport equations are as follows [129]:

$$\begin{aligned}\frac{\partial(\rho k)}{\partial t}+\frac{\partial(\rho k u_i)}{\partial x_i}&=\frac{\partial}{\partial x_j}\left[\left(\mu+\frac{\mu_t}{\sigma_k}\right)\frac{\partial k}{\partial x_j}\right]+G_k-Y_k+S_k\\ \frac{\partial(\rho\omega)}{\partial t}+\frac{\partial(\rho\omega u_i)}{\partial x_i}&=\frac{\partial}{\partial x_j}\left[\left(\mu+\frac{\mu_t}{\sigma_\omega}\right)\frac{\partial\omega}{\partial x_j}\right]+G_\omega-Y_\omega+S_\omega\end{aligned} \tag{1.28}$$

where G_ω is the generation of the specific rate of dissipation. Y_k and Y_ω represents the dissipation of k and ω.

The turbulent viscosity is calculated as:

$$\mu_t=\rho\alpha^*\frac{k}{\omega} \tag{1.29}$$

where for high Reynolds number, α^* is equal to unity.

3.2.5 SST *k-ω* turbulence model

The refinements of the SST *k-ω* turbulence model are the gradual change from the boundary layer region near walls to the outer high Reynolds number region and the modified turbulent viscosity, which shows better performance in various flows. Besides, when the wall shear stress is too high, the standard *k-ω* turbulence model doesn't separate the flow correctly from the wall, while SST *k-ω* model can give better separation prediction. In SST *k-ω* turbulence model, the only difference is that a cross-diffusion term D_ω is added in ω equation.

$$\frac{\partial(\rho k)}{\partial t}+\frac{\partial(\rho k u_i)}{\partial x_i}=\frac{\partial}{\partial x_j}\left[\left(\mu+\frac{\mu_t}{\sigma_k}\right)\frac{\partial k}{\partial x_j}\right]+G_k-Y_k+S_k$$
$$\frac{\partial(\rho \omega)}{\partial t}+\frac{\partial(\rho \omega u_i)}{\partial x_i}=\frac{\partial}{\partial x_j}\left[\left(\mu+\frac{\mu_t}{\sigma_\omega}\right)\frac{\partial \omega}{\partial x_j}\right]+G_\omega-Y_\omega+D_\omega+S_\omega \quad (1.30)$$

where D_ω is given as $D_\omega=2(1-F_1)\rho\frac{1}{\omega\sigma_{\omega 2}}\frac{\partial k}{\partial x_j}\frac{\partial \omega}{\partial x_j}$ and $\sigma_{\omega 2}=1.168$, F_1 represents the blending function.

3.2.6 Transition model

Two types of transition model are used in this thesis, which are the SST k-ω with γ transition model and the SST k-ω with γ-Re_θ transition model. In Ansys Fluent, the Transition SST model is known as the SST k-ω with γ-Re_θ transition model. For the purpose of preventing confusion, the Transition SST model will be written as the SST k-ω with γ-Re_θ transition model. The γ transition model is developed based on the γ-Re_θ transition model. The γ transition model reduces the computational resources and has provisions for crossflow instability.

For SST k-ω with γ-Re_θ transition model, the transport equations for intermittency γ and transition momentum thickness Reynolds number Re_θ are defined as:

$$\frac{\partial(\rho \gamma)}{\partial t}+\frac{\partial(\rho \gamma u_i)}{\partial x_i}=P_{\gamma 1}-E_{\gamma 1}+P_{\gamma 2}-E_{\gamma 2}+\frac{\partial}{\partial x_j}\left[\left(\mu+\frac{\mu_t}{\sigma_\gamma}\right)\frac{\partial \gamma}{\partial x_j}\right]$$
$$\frac{\partial(\rho Re_\theta)}{\partial t}+\frac{\partial(\rho Re_\theta u_i)}{\partial x_i}=P_{\theta t}+\frac{\partial}{\partial x_j}\left[\sigma_{\theta t}(\mu+\mu_t)\frac{\partial Re_\theta}{\partial x_j}\right] \quad (1.31)$$

For SST k-ω with γ transition model, the intermittency γ is defined as:

$$\frac{\partial(\rho \gamma)}{\partial t}+\frac{\partial(\rho \gamma u_i)}{\partial x_i}=P_\gamma-E_\gamma+\frac{\partial}{\partial x_j}\left[\left(\mu+\frac{\mu_t}{\sigma_\gamma}\right)\frac{\partial \gamma}{\partial x_j}\right] \quad (1.32)$$

3.3 LES

With the help of the large eddy simulation, the flow field can be characterized with much more details where the large scale eddies are computed directly, and the small scale eddies are modeled by subgrid-scale models. LES was first proposed by Joseph

Smagorinsky in 1963 [130] to simulate the atmospheric air currents. In 1970, LES was developed by Deardorff [131].

LES is applied in a wide range of the practical engineering applications. Because LES finds a balance between the accuracy of the results and the cost of the computation as shown in Tab. 3.1. Approximately, for DNS the mesh cell number, non-dimensional time step size and number of time steps are directly proportional to $Re^{9/4}$, $Re^{-3/4}$ and $Re^{3/4}$, therefore the total computation is cubic of Reynolds number [132]. Therefore, DNS is usually applied for the investigations that reveal and study the details and mechanisms as a baseline of the CFD turbulence model calibrations with a limited much lower Reynolds number condition. As for the LES, since the small scale vortices are filtered out, the spatial and temporal resolution can be scaled up relative to the DNS method, and the cost of the computational resource is reduced. According to the estimation of Rogallo and Moin and Yang and Ferziger [128], the grid number relationship between the LES and DNS required for channel flow scheme is given by equation 1.33. Thus, LES can be more realistic for the research or engineering practice with higher Reynolds number cases.

$$N_{LES} \approx \left(\frac{0.4}{Re_{\tau}^{1/4}} \right) N_{DNS} \tag{1.33}$$

Considering the large number of simulation data and the extremely high computation cost, DNS is not feasible for the current calculation, due to the limitation of the computer. Hence, LES and RANS are more applicable to be used, which can maintain the computational resources at manageable levels.

Tab. 3.1 Difference among the RANS, LES and DNS [132]

	DNS	LES	RANS
Resolution	entire	only large eddies	only averaged flow
Turbulence model	without models	subgrid-scale models	turbulence models
Storage	huge	intermediate	small
Computational resources	huge	intermediate	small

Fig. 3.1 presents the schematic of the spatial filter used in LES. $u(x)$ denotes the instantaneous velocity in red line and $\bar{u}(x)$ is the filtered velocity in black line. The filter variable is defined by equation 1.34.

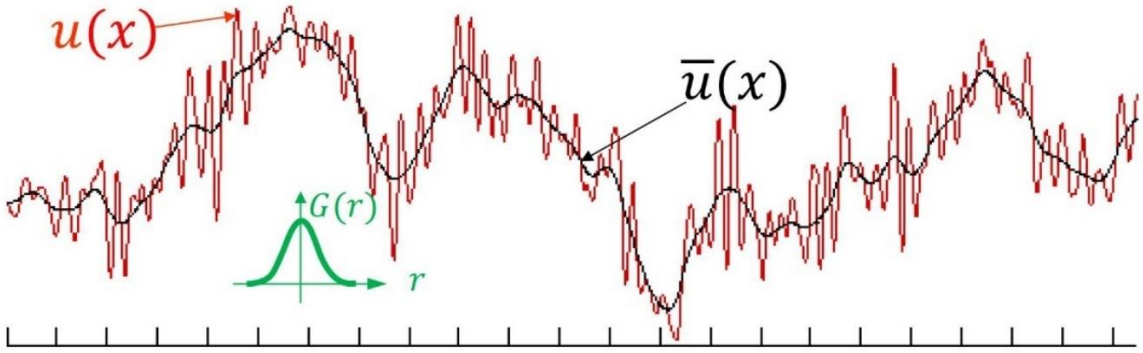

Fig. 3.1 Schematic of the instantaneous and spatial filtered velocity in LES

$$\bar{\phi}(x) = \int \phi(x') G(x,x') dx' \tag{1.34}$$

where G is the filter function. There are three filters that are commonly used in LES: the box filter, Gaussian filter and sharp cutoff filter. [133] In Fluent, the function G is given as equation 1.35.

$$G(x,x') = \begin{cases} 1/V & x' \in v \\ 0 & x' \; otherwise \end{cases} \tag{1.35}$$

For LES the governing equations should be filtered spatially as follows.

$$\begin{gathered} \frac{\partial \rho}{\partial t} + \frac{\partial \rho \tilde{u}_i}{\partial x_i} = 0 \\ \frac{\partial \rho \tilde{u}_i}{\partial t} + \frac{\partial \rho \widetilde{u_i u_j}}{\partial x_j} = -\frac{\partial \tilde{p}}{\partial x_i} + \frac{\partial}{\partial x_j}\left[\mu\left(\frac{\partial \tilde{u}_i}{\partial x_j} + \frac{\partial \tilde{u}_j}{\partial x_i}\right) - \frac{2}{3}\frac{\partial \tilde{u}_k}{\partial x_k}\delta_{ij}\right] + \frac{\partial \tau_{ij}}{\partial x_j} + \tilde{f} \\ \frac{\partial \rho \tilde{h}}{\partial t} + \frac{\partial \rho \tilde{u}_i \tilde{h}}{\partial x_i} - \frac{\partial \tilde{p}}{\partial t} - \tilde{u}_j \frac{\partial \tilde{p}}{\partial x_i} - \frac{\partial}{\partial x_i}\left(\lambda \frac{\partial \tilde{T}}{\partial x_i}\right) = -\frac{\partial}{\partial x_j}\left[\rho\left(\widetilde{u_i h} - \tilde{u}_i \tilde{h}\right)\right] \end{gathered} \tag{1.36}$$

where h is the enthalpy and subgrid-scale turbulent stress τ_{ij} is calculated by equation 1.37, whose form is similar to the Boussinesq eddy viscosity assumption. $\widetilde{S}_{ij}$ is the strain rate tensor for the resolved scale eddies.

$$\begin{aligned}\tau_{ij} &= \widetilde{\rho uu} - \rho\tilde{u}\tilde{u} \\ &= -2\mu_t \tilde{S}_{ij} + \frac{1}{3}\tau_{kk}\delta_{ij} \\ &= -2\mu_t \frac{1}{2}\left(\frac{\partial \tilde{u}_i}{\partial x_j} + \frac{\partial \tilde{u}_j}{\partial x_i}\right) + \frac{1}{3}\tau_{kk}\delta_{ij}\end{aligned} \tag{1.37}$$

The subgrid-scale turbulent stress is split into the deviatoric part and the isotropic part respectively as follows:

$$\tau_{ij} = \left(\tau_{ij} - \frac{1}{3}\tau_{kk}\delta_{ij}\right) + \frac{1}{3}\tau_{kk}\delta_{ij} \tag{1.38}$$

where μ_t in the deviatoric part is solved by the subgrid-scale model.

In this paper three types of subgrid-scale models were evaluated, which are the Smagorinsky-Lilly model, Wall-Adapting Local Eddy-Viscosity (WALE) model and algebraic Wall-Modeled LES (WMLES) model.

For Smagorinsky-Lilly model, turbulent viscosity is calculated by:

$$\begin{aligned}\mu_t &= \rho L_s^2 \left|\tilde{S}\right| \\ \left|\tilde{S}\right| &= \sqrt{2\tilde{S}_{ij}\tilde{S}_{ij}} \\ L_s &= \min\left(\kappa d,\ C_s \triangle\right) \\ \triangle &= V^{1/3}\end{aligned} \tag{1.39}$$

where d is the distance to the closest wall, C_s is the Smagorinsky constant. V is the volume of the cell. $\triangle$ is known as the cutoff length scale. For large scale vortices, the length scale is larger than the threshold and resolved by N-S equations. If the vortices are smaller than the length scale, the unresolved smaller vortices are modeled by the subgrid model.

In WALE model, turbulent eddy viscosity is modeled by:

$$\begin{aligned}\mu_t &= \rho L_s^2 \frac{\left(S_{ij}^d S_{ij}^d\right)^{3/2}}{\left(\tilde{S}_{ij}\tilde{S}_{ij}\right)^{5/2} + \left(S_{ij}^d S_{ij}^d\right)^{5/4}} \\ L_s &= \min\left(\kappa d,\ C_w V^{1/3}\right) \\ S_{ij}^d &= \frac{1}{2}\left[\left(\frac{\partial \tilde{u}_i}{\partial x_j}\right)^2 + \left(\frac{\partial \tilde{u}_j}{\partial x_i}\right)^2\right] - \frac{1}{3}\left(\frac{\partial \tilde{u}_k}{\partial x_k}\right)^2 \delta_{ij}\end{aligned} \tag{1.40}$$

where C_w is a constant of 0.325.

As for WMLES model, eddy viscosity is given by:

$$\mu_t = \rho \min\left[(\kappa d_w)^2,\ (C_{smag}\triangle)^2\right] \cdot S \cdot \left\{1 - \exp\left[-\left(\frac{y^+}{25}\right)^3\right]\right\}$$
$$\triangle = \min\left(\max\left(C_w \cdot d_w;\ C_w \cdot h_{\max},\ h_{wn}\right);\ h_{\max}\right) \tag{1.41}$$

where h_{max} is the maximum edge length for a rectilinear hexahedral cell, h_{wn} is the wall-normal grid spacing, and C_w is 0.15.

3.4 Wall treatment and y^+ value

y^+ is a non-dimensional value that indicates the distance from the first cell center to the solid wall, which is important for the selection of the turbulence model and wall function. The non-dimensional wall distance y^+ and non-dimensional velocity u^+ are defined as follows:

$$y^+ = \frac{y u_\tau}{\nu} = \frac{y}{\nu}\sqrt{\frac{\tau_w}{\rho}}$$
$$u^+ = \frac{u}{\sqrt{\frac{\tau_w}{\rho}}} \tag{1.42}$$

where τ_w is the wall shear stress, u_τ is the friction velocity. Fig. 3.2 represents the non-dimensional velocity u^+ with respect to the non-dimensional wall distance y^+. The near wall region, namely the boundary layer region, is divided into four segments, depending on y^+: the viscous sublayer, the buffer layer, the log-law region and the outer layer. The first three layers are collectively known as the inner layer.

For the viscous sublayer, y^+ is usually less than 5 where u^+ is linear to y^+ ($u^+ = y^+$). The flow can be considered as laminar flow. For the log-law region, y^+ is in the range of 5-30 approximately. And the relationship between y^+ and u^+ is:

$$u^+ = \frac{1}{\kappa}\ln y^+ + C \tag{1.43}$$

where κ is the Von Kármán constant of 0.41 and C is a constant of about 5.2. The flow scheme becomes turbulent.

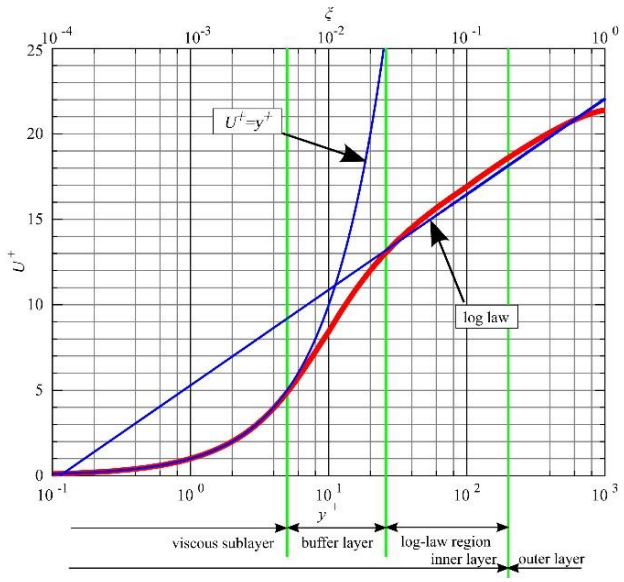

Fig. 3.2 Law of the wall

As for the buffer layer, it is the transition region where the flow changes from laminar to turbulent. The relation could be complex and no longer satisfy equation 1.43. In the buffer layer, the velocity profile cannot be well described, compared with the other aforementioned two layer regions. Hence, the wall functions usually request that the mesh should avoid the first cell center being located in the buffer layer.

In RANS simulation, enhanced wall function is used for all the *k*-ε turbulence models and the Reynolds stress model. The viscous sublayer can be resolved if the near-wall mesh is fine enough, which means y^+ should be in the order of 1. For the *k*-ω turbulence models, it is insensitive to the y^+ value, accordingly, if y^+ is about 1, the viscous sublayer is resolved. If y^+ is larger than 30 in the log-law region, an empirical assumption will be used to characterize the boundary layer.

Chapter 4

Numerical simulation of film cooling holes

4.1 Geometry and mesh

Fig. 4.1 depicts the geometry of the 7-7-7 shaped film hole and conventional cylindrical film hole channels. Both channels are 44.7*D* long and 6*D* wide. The plenum of the coolant is a cube of 6*D* for both geometries. The distance between the inlet of the mainstream and the trailing edge of the shaped hole is 4.7*D* in order to satisfy the inlet boundary layer characteristics and the turbulence intensity and reproduce the mainstream velocity profile in the experiment conveniently, and that of the cylindrical film hole is 3.3*D*. The origin of the geometry is located at the midpoint of the film hole exit trailing edge.

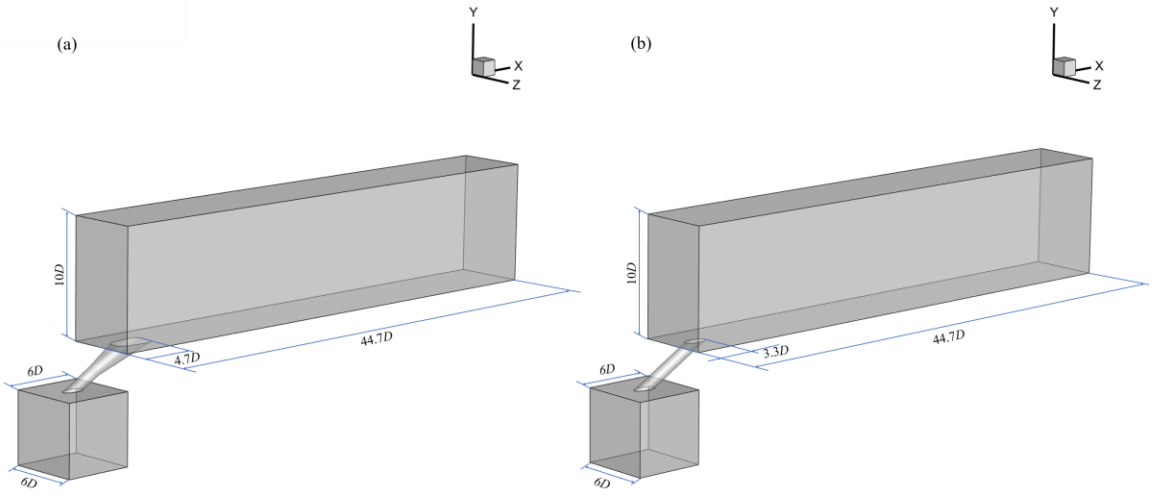

Fig. 4.1 Schematic of the cooling channels (a) 7-7-7 shaped film hole (b) cylindrical film hole

Fig. 4.2 illustrates the top view and side view of the two types of film holes. The diameter *D* of the film hole in two configurations is 0.00775m (7.75mm), which equals to the one in the experiment from Thole and can keep the error or difference as low as possible. The length *L* of the cylindrical film hole is 6*D*. The inclination is 30 degrees. The 7-7-7

shaped film hole was proposed by Thole's group, which can be used as a baseline for various kinds of shaped holes and benchmark the thermal performance comparatively [1].

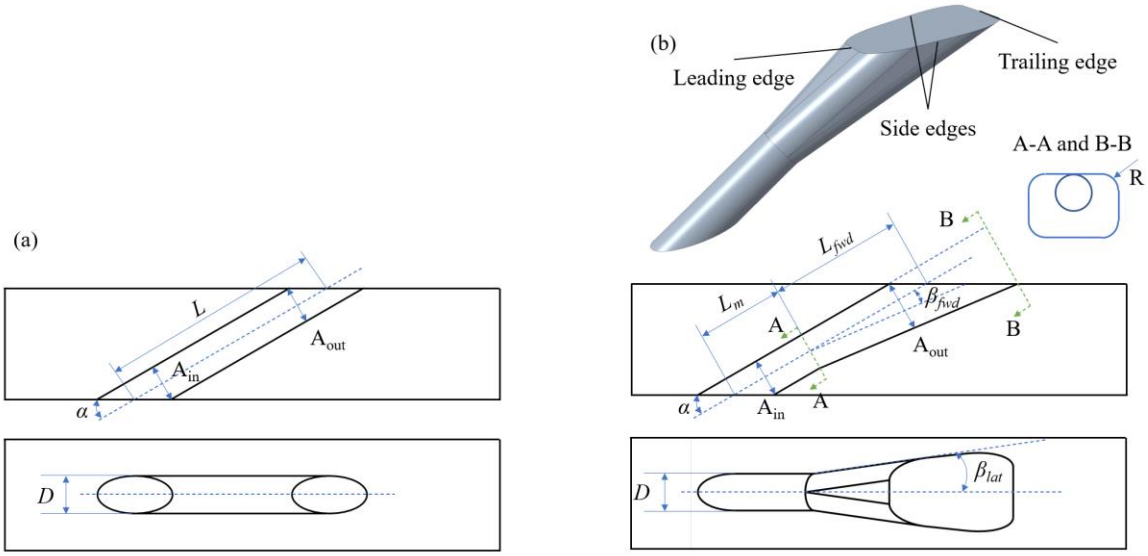

Fig. 4.2 Schematic of (a) cylindrical film hole and (b) 7-7-7 shaped film hole

There are two parts of most shaped film holes, one is the cylindrical part the same as the traditional film hole (plane A-A), and the other is the expansion part in lateral and forward directions (Between plane A-A and plane B-B) with a fillet radius of 0.5*D*. The triple seven in the name indicates all the expansion angles in two lateral and one forward directions are 7°. According to the researcher, 7 degrees expansion angle are widely investigated by researchers, for example, Fawcett et al. [134] tested shaped hole similar to 7-7-7 baseline hole with 7° lateral and forward expansion angles, and Gritsch et al. [135] studied 7° laidback shaped film hole as well as 7° lateral and 15° forward expansion angles [59]. For the 7-7-7 shaped film hole, the length of the cylindrical and expansion segments are respectively 2.5*D* and 3.5*D*. The lateral pitch distance between two holes is 6*D*, and the inclined angle is 30°. The area ratio of film hole inlet to outlet A_{out}/A_{in} is 2.5. More details are shown in Tab. 4.1.

Tab. 4.1 Parameters of 7-7-7 shaped film hole

Parameters	Values
Injection angle α	30°
L (L_m +L_{fwd})	6D

L_m	2.5D
L_{fwd}	3.5D
P	6D
Area ratio A_{out}/A_{in}	2.5

The energy spectrum with respect to the inverted length scale is shown in Fig. 4.3 [133]. L_0 and l denotes the integral length scale and the smallest resolved length scale. The integral length scale l_0 is given as:

$$l_0 = \frac{k^{3/2}}{\varepsilon} \; or \; l_0 = \frac{k^{1/2}}{C_\mu \omega} \tag{1.44}$$

where C_μ is equal to 0.09.

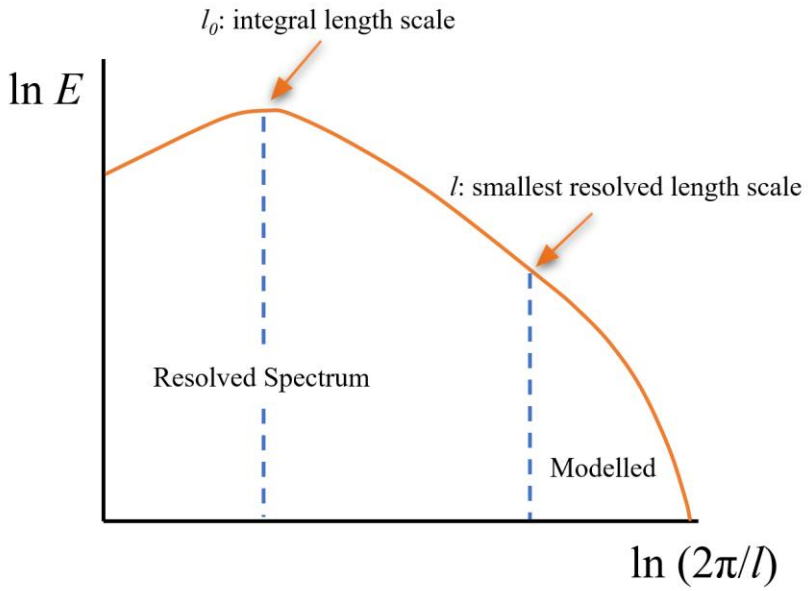

Fig. 4.3 Energy spectrum against the inverted length scale

The turbulent kinetic energy peaks at the integral length scale and the integral length scale should be sufficiently resolved. As the length scale decreases, the size of the vortices become smaller. The finer the mesh is, the more vortices can be resolved. To guarantee that over 80% of the turbulent kinetic energy is resolved, l/l_0 should be less than 0.42 in the region of interest. In large eddy simulation, the cutoff length scale $\triangle$ is half of the smallest resolved length scale l. Thus, $l_0/\triangle$ should be larger than 4.8 to make sure at least

80% large scale vortices can be resolved. After the trail, 11.4 million fine mesh can keep the $l_0/\triangle$ value higher than 4.8 in the initial steady simulation, which is used for the large eddy simulation in current work.

The mesh of the 7-7-7 shaped film cooling hole is depicted in Fig. 4.4. The structured mesh is generated by ICEM CFD and hexahedral meshes are used. The refinement is made near the wall. The mesh cell number for large eddy simulation is about 11.4 million in the present work. The refined mesh used in LES provides a higher resolution that Δx^+ is equal to about 26, Δy^+ is in the range of 0.18-15, due to the boundary layer refinement near the bottom wall and the slip upper wall, and Δz^+ equals about 16.

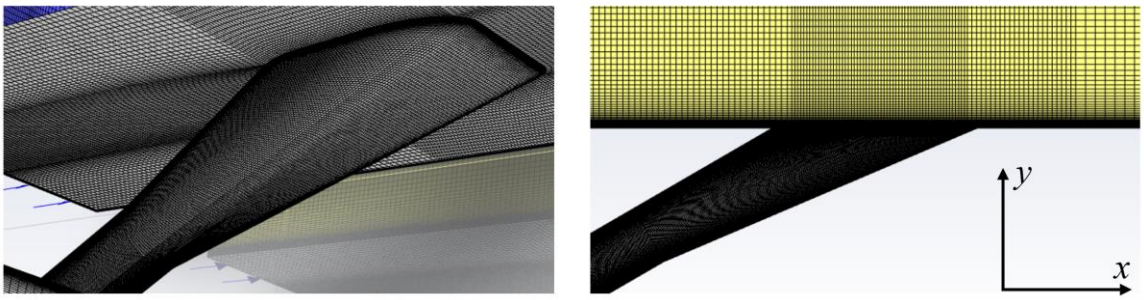

Fig. 4.4 grids of the shaped film cooling hole with near-wall refinement

For the RANS simulation, the regions near walls are refined to fulfil $y^+<1$ requirement for all *k-ε* turbulence models with enhanced wall function, *k-ω* turbulence models with or without transition models, Reynolds stress model with enhanced wall function. Fig. 4.5 presents the distributions of y^+ on the bottom wall with various turbulence models. The y^+ is in the range of about 0.1-0.2 in the whole RANS simulations. It indicates that for *k-ε* turbulence models and Reynolds stress model with enhanced wall function and *k-ω* turbulence models, the viscous sublayer is resolved.

Mesh independence study for the shaped film hole was conducted with four meshes from 2.3 million to 11.4 million, as shown in Fig. 4.6.

Since the 11.4 million mesh can be used for large eddy simulation, it is the baseline for the comparison. For the coarsest mesh with 2.3 million cells, the lateral averaged film cooling effectiveness is significantly underestimated. 4.0 million mesh reduces the error

further downstream, but the discrepancies are still too large to be used for the simulation. When the mesh cell reaches to about 7.1 million, the trend of the lateral averaged effectiveness shows an agreement with the benchmark. Thus, 7.1 million mesh can be employed in the RANS simulation for balancing the calculation efficiency and computational cost, according to the mesh independence study.

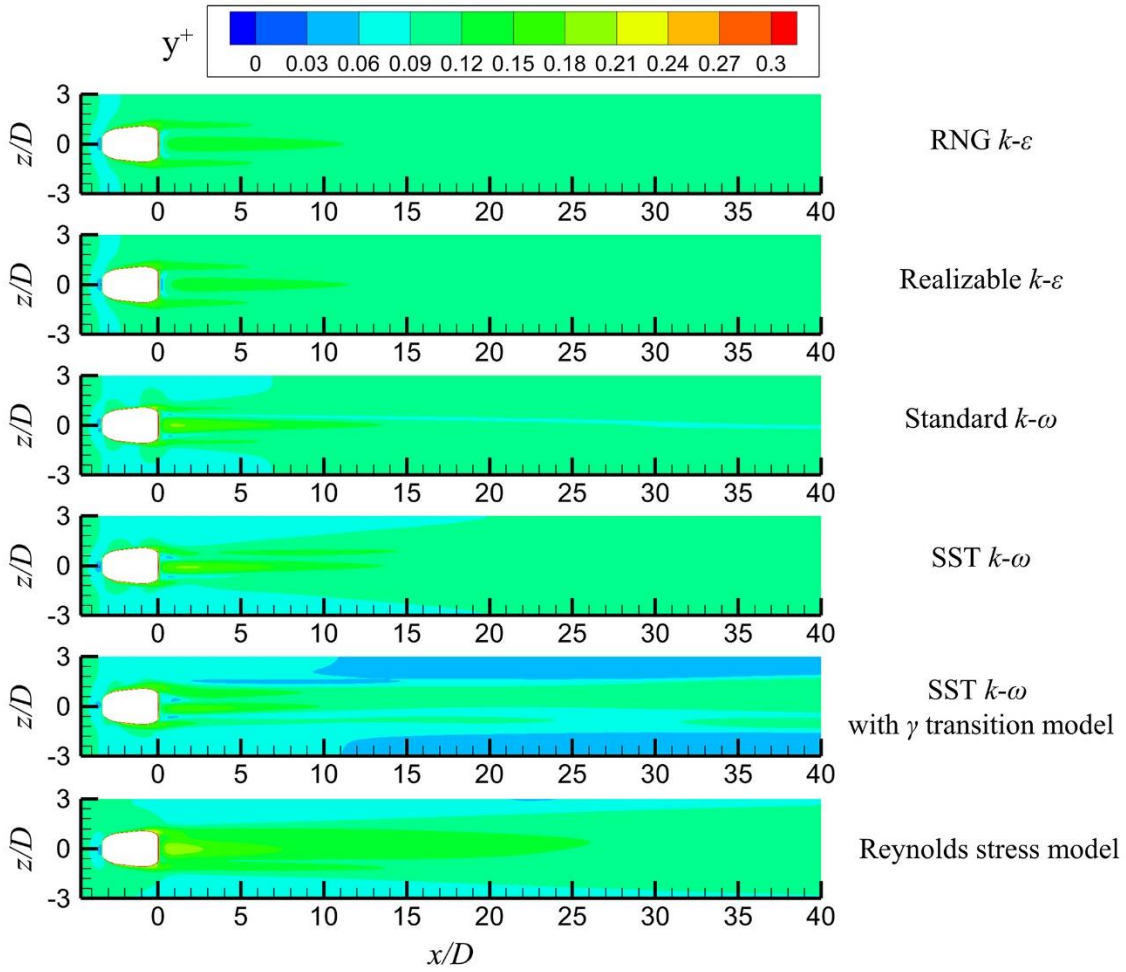

Fig. 4.5 Distributions of y^+ with various turbulence models in RANS simulation at M=1.5 DR=1.5

For the cylindrical film hole, since the geometry is much simpler than the shaped film hole, the mesh used in both RANS and LES calculations are about 7.4 million. Because LES with 7.4 million mesh can satisfy the aforementioned requirements, 7.4 million mesh should be enough for RANS as well.

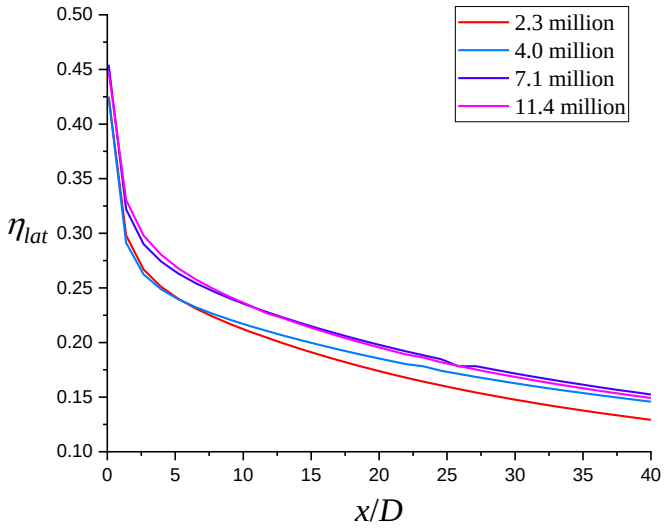

Fig. 4.6 Mesh independence of shaped film hole with various meshes at M=1.5 DR=1.5 Tu=0.5%

4.2 Boundary conditions

All the calculations were conducted with the commercial software Ansys Fluent. Fig. 4.7 presents the boundary conditions employed in the numerical simulation. The velocity inlet is used as the inlet boundary condition and the freestream is fixed at 10m/s with the spectral synthesizer fluctuating velocity algorithm. The spectral synthesizer was proposed by Kraichnan [136] and modified by Smirnov et al. [137] based on the random flow generation technique to generate non-homogeneous anisotropic flow field. The velocity profile is imposed to mimic the boundary layer in the experiment. The outlet is connected to the atmosphere where the outlet gauge pressure is equal to zero in Fluent. Two side walls are set as periodic boundary condition. The bottom surface is no slip adiabatic wall, while the top surface is slip wall which indicates that the boundary layer is only generated on the bottom surface. The coolant is supplied from the plenum, and the coolant velocity is adjusted as the change of the blowing ratio. The mainstream turbulence intensity is set in the range of 0.5%-20%, and the coolant turbulence intensity is equal to zero, which means there are no perturbations at the inlet of the coolant plenum.

The Reynolds number based on film hole diameter D and the mainstream inlet velocity is 5,102, and Re_θ based on the momentum boundary layer thickness is 670 in the verification test. The mainstream temperature is 295K and the surface is cooled by the

coolant of 196K. The blowing ratio M is in the range of 0.5-3.0 in the cases of this thesis, and the density ratio DR is constant at 1.5.

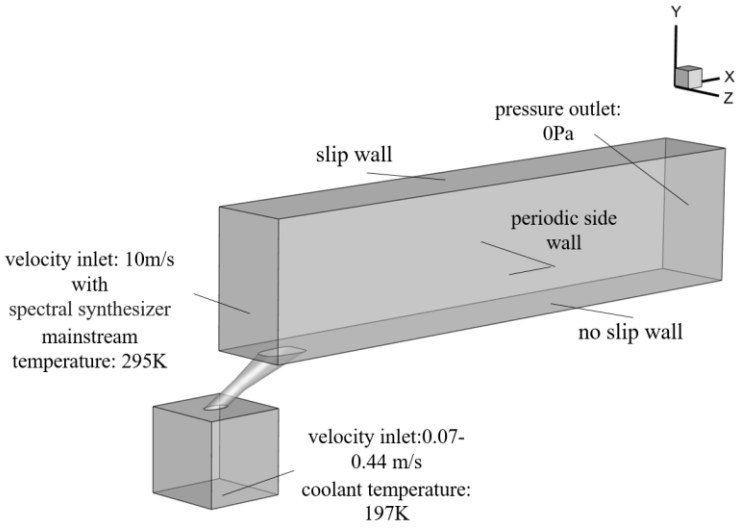

Fig. 4.7 Boundary conditions of film cooling on a flat plate surface

The time step size is set to 5×10^{-5}s with maximum iterations of a time step of 15 to guarantee CFL courant number is less than one shown in equation 1.45.

$$\mathrm{CFL} = \frac{u\triangle t}{\triangle x} \tag{1.45}$$

A steady simulation is calculated as the initial value of the LES, and about 10 flow-through time, defined as the time that the mainstream flows from the mainstream inlet to the outlet of the passage, is carried out before starting to sample the statistics data, to make sure the transient solution has achieved convergence. To keep the averaged results accurate enough, the sampling period is about 10 flow-through time as well.

The simulation is conducted with SIMPLEC pressure-based solver for high accuracy and fidelity. The filtered N-S equations are resolved with bounded second order implicit time discretization and bounded central differencing spatial discretization.

The LES is simulated with the help of the powerful server. The server is equipped with 104 cores and 128GB memory, and about 12,480 core hours are needed for 10 flow-through time using 48 cores with a better efficiency.

4.3 Evaluation and verification

The large eddy simulation has been proven with the experimental data from Thole. In the experiment of Thole [1, 138], a closed loop wind tunnel is powered by an axial or centrifugal fan. The freestream is continuously heated at 295K by a bank heater, and the coolant is cooled by liquid nitrogen and dried by solid desiccant. The surface temperature is measured by the infrared camera.

For the purpose of reproducing the inlet boundary condition of the experiment, the velocity profile is applied to match the experimental condition in the LES simulation, and inlet velocity profile is extracted from a flat plate steady simulation with RNG k-ε turbulence model and enhanced wall function. The velocity profile and normalized velocity profile used in the unsteady LES simulation are shown in Fig. 4.8.

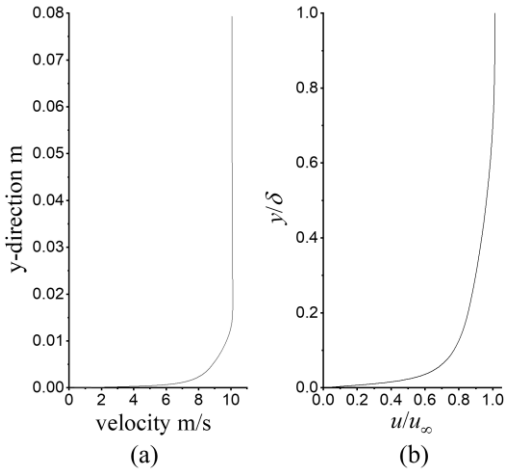

Fig. 4.8 Inlet boundary condition of LES (a) velocity profile (b) normalized velocity profile

The boundary layer characteristics are presented in Tab. 4.2, compared with that of the experiment. Δ^*/D is deduced from θ/D and H_{12} provided in public literature, all the other parameters in the flat plate steady simulation show great agreement with the measurement in the experiment.

Tab. 4.2 Boundary layer parameters of mainstream inlet in CFD and EXP

	Tu	δ^*/D	θ/D	H_{12}	Re_θ	u_τ m/s
LES	0.5%	0.20	0.14	1.45	671	0.5
EXP	0.5%	0.20	0.14	1.45	670	0.5

Fig. 4.9 presents the centerline and lateral averaged film cooling effectiveness with respect to the streamwise direction on the bottom surface of the cooling channel. The blowing ratio is 1.5 and the density ratio is 1.5. The mainstream inlet turbulence intensity is 0.5%. Comparing with the experiment, the capability of LES with three different subgrid-scale models can be evaluated intuitively. For centerline cooling effectiveness, LES with WMLES model shows a good agreement from x/D=10 to x/D=40, while it overestimates the film cooling effectiveness in the range of x/D=0-10 where the error exists mainly in upstream region. On the contrary, Smagorinsky-Lilly subgrid-scale model shows a better prediction at x/D=0-7 roughly, however, the cooling effectiveness in downstream region from x/D=7 to x/D=40 is underestimated. Corresponding to the centerline cooling effectiveness, the contours of adiabatic film cooling effectiveness is comparatively shown in Fig. 4.10. The overestimate of the effectiveness by WMLES subgrid-scale model is reflected in the area downstream the trailing edge, where the color in the contour differs from the others. For lateral averaged film cooling effectiveness, WMLES model shows wider discrepancies than the other ones, WALE and Smagorinsky-Lilly subgrid-scale model are much close to each other with the same trend. The prediction shows a good agreement upstream of the channel, but the effectiveness is overestimated further downstream of the channel.

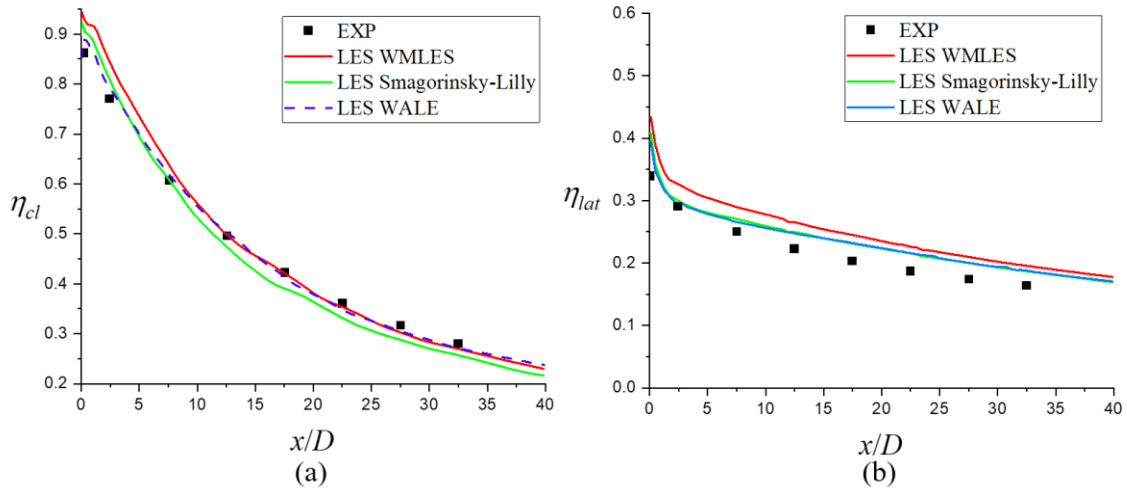

Fig. 4.9 comparison between the LES calculation and experimental data (a) centerline cooling effectiveness (b) lateral averaged film cooling effectiveness

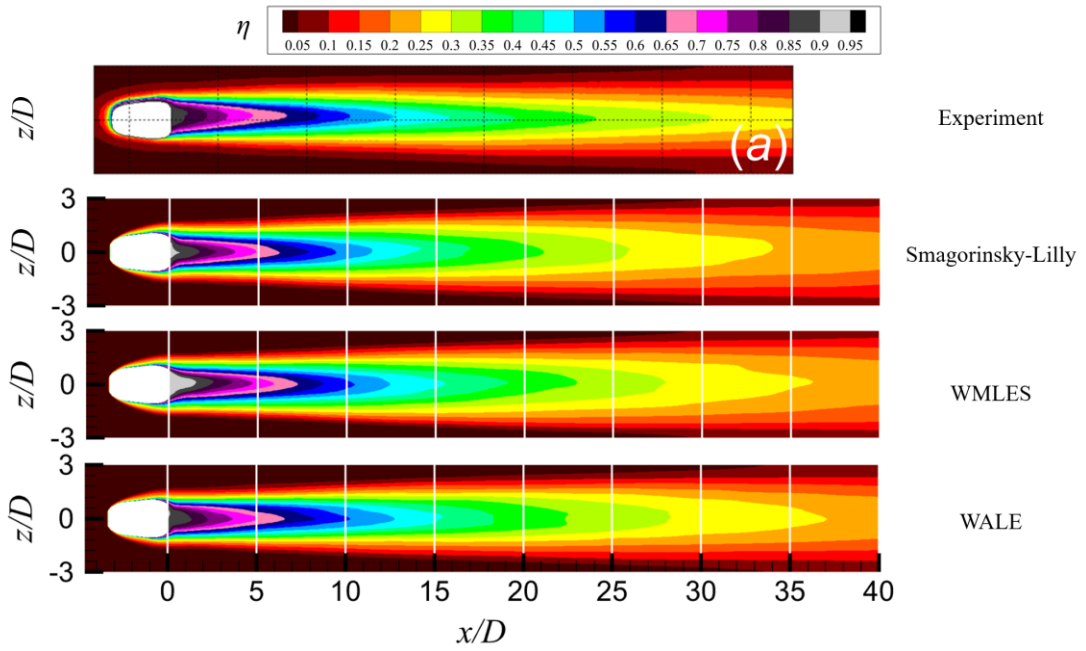

Fig. 4.10 Contours of time-averaged adiabatic effectiveness of the bottom surface with various subgrid-scale model

As for the WALE model, the minimum error is 1.2% and the maximum error is 3.5% shown in Tab. 4.3, compared with the experimental data. Smagorinsky-Lilly model presents the largest discrepancy at x/D=27.5 with 9.3% error, and WMLES model gives 6.8% error in the vicinity of x/D=0.2 region. The averaged errors of Smagorinsky-Lilly, WMLES and WALE subgrid-scale models are 5.9%, 3.8% and 2.6% respectively.

Tab. 4.3 Error of centerline film cooling effectiveness in streamwise direction

x/D	Exp	Smagorinsky-Lilly	Error	WMLES	Error	WALE	Error
0.2	0.86	0.90	4.7%	0.92	6.8%	0.89	2.8%
2.4	0.77	0.81	4.7%	0.83	7.5%	0.79	2.4%
7.6	0.61	0.61	0.1%	0.63	4.6%	0.62	1.8%
12.6	0.50	0.47	4.3%	0.50	0.0%	0.50	1.2%
17.6	0.42	0.39	7.7%	0.42	0.3%	0.41	2.3%
22.5	0.36	0.33	8.3%	0.35	2.1%	0.35	3.5%
27.5	0.32	0.29	9.3%	0.30	5.0%	0.31	3.5%
32.5	0.28	0.26	8.4%	0.27	4.2%	0.27	3.1%

On balance, WALE subgrid-scale model shows the best performance in the whole range of the surface. Because the WALE subgrid-scale model can return the correct wall asymptotic behavior for wall bounded flows and a zero turbulent viscosity for laminar shear flows. Therefore, LES with WALE model is selected in current work. The spreading of the coolant is well predicted with all subgrid-scale models, which also indicates the high fidelity of the large eddy simulation in film cooling issues.

In addition, RANS simulation has also been carried out to evaluate the difference between the RANS and LES. Fig. 4.11 illustrates the distributions of film cooling effectiveness with various turbulence models as well as LES with WALE subgrid-scale model. As can be seen, the lateral spreading of the coolant is much inadequate to a varying extent with RANS simulation in contrast to the LES calculation. Besides, the decrease of the film cooling effectiveness along the streamwise direction is insufficient on the bottom surface. Note that k-ω turbulence models generally show further extension in streamwise direction than k-ε turbulence models, which results in large errors in the effectiveness prediction. All three types of k-ω turbulence models cannot predict the lateral distribution of the film cooling effectiveness correctly. For the k-ε turbulence model with enhance wall treatment, RNG k-ε turbulence model provides a better adiabatic effectiveness distribution than Realizable k-ε turbulence model.

Fig. 4.12 depicts the centerline adiabatic film cooling effectiveness with respect to the x direction normalized by the diameter of the film hole D at M=1.5 and DR=1.5. SST k-ω and Realizable k-ε turbulence models show similar trends, and SST k-ω with γ transition model gives the highest adiabatic effectiveness at x/D=0-15. The Reynolds stress model shows a moderate value of film cooling effectiveness, but it still overestimates the adiabatic film cooling effectiveness than RNG k-ε turbulence model, which gives a marked bias of 32%. The averaged error of various turbulence models is 23%-47%, illustrated in Tab. 4.4. RNG k-ε turbulence model has the minimum error, while SST k-ω with γ transition model shows the largest discrepancies, followed by SST k-ω, Realizable k-ε and Standard k-ω models. All the RANS simulations overestimate the adiabatic film cooling effectiveness in centerline.

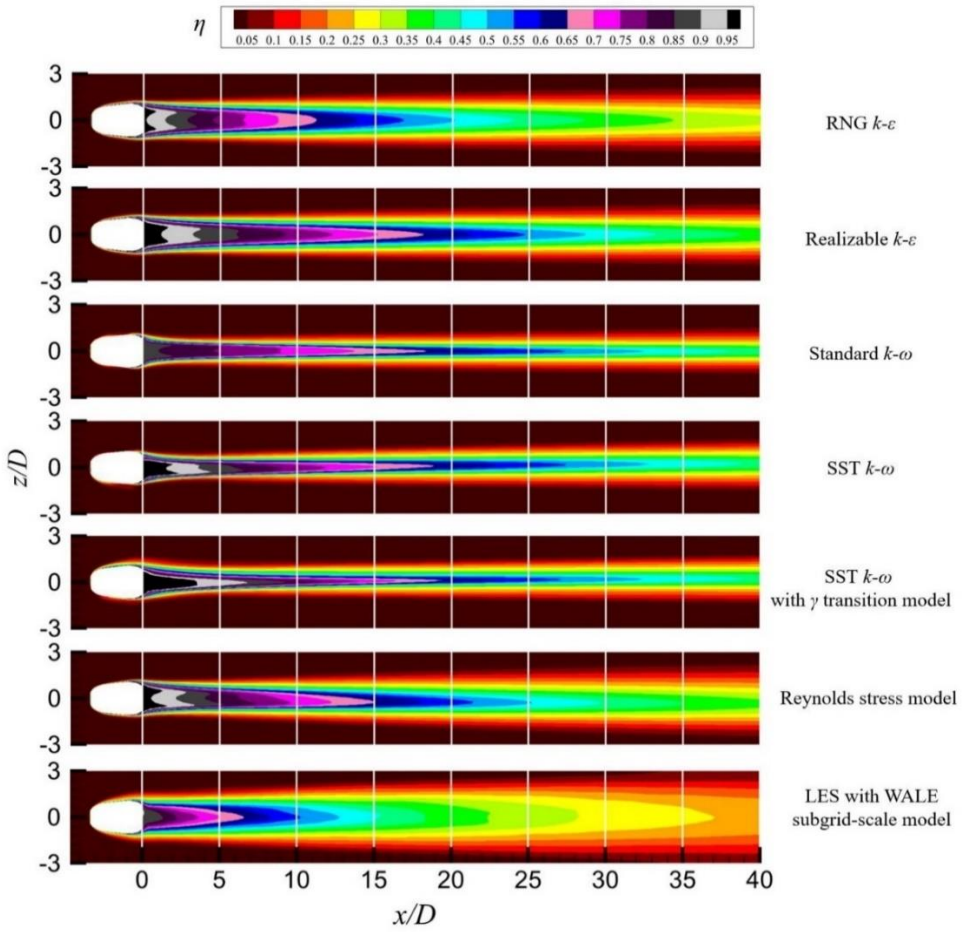

Fig. 4.11 Time-averaged adiabatic film cooling effectiveness with different turbulence models

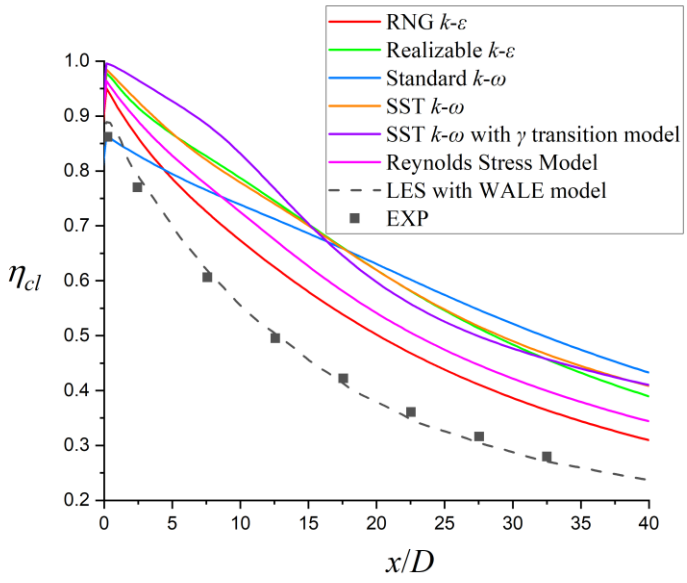

Fig. 4.12 Time-averaged centerline adiabatic film cooling effectiveness given by RANS and LES at M=1.5 and DR=1.5 Tu=0.5%

Tab. 4.4 Averaged error of adiabatic film cooling effectiveness with various turbulence models

	RNG k-ε	Realizable k-ε	Standard k-ω	SST k-ω	SST k-ω with γ transition model	Reynolds stress model
Averaged error	23.0%	45.8%	44.0%	46.1%	47.0%	32.0%

Generally speaking, for RANS simulation RNG k-ε turbulence model provides the best distribution of the cooling effectiveness. Because the cooling effectiveness in the region near the downstream trailing edge of the film hole is close to LES in not only streamwise direction but lateral direction, however, the limitation of the coolant spreading still exists in all RANS turbulence model. RANS simulation can only provide the thermal results qualitatively.

Hence, LES is much more suitable to the film cooling quantitative analysis than the RANS method, due to the three-dimensional complex and strong anisotropic flow field. And the advantages of the high fidelity in LES far outweigh the relative expensive computation.

4.4 Results and discussion

All the cases of the 7-7-7 laidback fan-shaped film cooling hole and the conventional cylindrical film cooling hole are listed in Tab. 4.5 and Tab. 4.6. Note that L for the shaped film hole is equal to the sum of the cylindrical section length L_m and expansion part length L_{fwd}. And L represents the whole length between the inlet and outlet cross sections for conventional cylindrical film hole. α represents the inclined angle with respect to the streamwise direction. The detailed information of three mainstream inlet velocity profiles is shown in section 4.4.4.

Tab. 4.5 List of the 7-7-7 shaped film hole cases with various parameters

Case	P/D	L/D	α °	M	DR	I	Tu %	Bottom surface	Inlet profile
1	6	6	30	**0.5**	1.5	0.17	0.5	flat	profile1
2	6	6	30	**1.0**	1.5	0.67	0.5	flat	profile1
3	6	6	30	**1.5**	1.5	1.50	0.5	flat	profile1
4	6	6	30	**2.0**	1.5	2.67	0.5	flat	profile1

5	6	6	30	**3.0**	1.5	6.00	0.5	flat	profile1
6	6	6	30	1.5	1.5	1.50	**10**	flat	profile1
7	6	6	30	1.5	1.5	1.50	**20**	flat	profile1
8	6	6	30	2.0	1.5	2.67	**10**	flat	profile1
9	6	6	30	2.0	1.5	2.67	**20**	flat	profile1
10	6	6	30	1.5	1.5	1.50	0.5	flat	**profile2**
11	6	6	30	1.5	1.5	1.50	0.5	flat	**profile3**
12	6	6	30	1.5	1.5	1.50	0.5	**curved**	profile1
13	6	6	30	2.0	1.5	2.67	0.5	**curved**	profile1
14	6	6	30	3.0	1.5	6.00	0.5	**curved**	profile1

Apart from the cases in the lists simulated with large eddy simulation, the RANS simulation with various turbulent models was also carried out at M=1.5 and DR=1.5 Tu=0.5% for the evaluation shown in the previous chapter.

Tab. 4.6 List of the conventional cylindrical film hole cases with various parameters

Case	*P*/*D*	*L*/*D*	α °	M	DR	I	Tu %	Bottom surface	Inlet profile
15	6	6	30	**0.5**	1.5	0.17	0.5	flat	profile1
16	6	6	30	**1.0**	1.5	0.67	0.5	flat	profile1
17	6	6	30	**1.5**	1.5	1.50	0.5	flat	profile1

4.4.1 Shaped film hole vs cylindrical film hole

A comparison has been conducted between the laidback fan-shaped film cooling hole and the conventional cylindrical film cooling hole. As mentioned in previous section, for the purpose of controlling the variable of the film hole geometry, the diameter *D* of the inlet cross section is the same for both cases and the pitch *P* between the centerline of two film holes is equal to 6*D* for two film hole structures. The inclined angle of the film hole equals 30°. Besides, the size of the film cooling channel is the same. Consequently, the thermal performance can be evaluated under the same condition. The 7-7-7 laidback fan-shaped film hole is referred to as the shaped film hole unless otherwise specified. The density ratio is equal to 1.5 and mainstream inlet turbulence intensity is 0.5% for the cases in the comparison.

The discharge coefficient can be used as the means of evaluating the flow losses of the coolant through the film cooling hole quantitively. The isentropic mass flow rate is defined based on the inlet cross-sectional area perpendicular to the film hole axis for the cylindrical hole and the inlet cross-sectional area of the cylindrical section perpendicular to the axis of the cylindrical section for the shaped film hole.

Fig. 4.13 presents the comparison of the discharge coefficient between the cylindrical and shaped film holes with respect to the pressure ratio and the blowing ratio. According to equation 1.8, the total pressure in the coolant plenum is measured at the center location 3*D* below the film tube inlet cross section, and the static pressure in the mainstream channel is monitored 3*D* above the midpoint of the trailing edge of the film tube exit.

According to the LES results, both film hole structures show an upward trend with the increase of the pressure ratio and blowing ratio. Note that for the cylindrical film hole, the discharge coefficient grows sharply at M=0.25-1.0 corresponding to $p_{t,c1}/p_{c2}$=1.0001-1.0003, while the growth rate of C_d becomes slower as the pressure ratio or blowing ratio increases. It can be implied that the loss is significant at lower blowing ratio conditions. The discharge coefficient trend calculated by LES is similar to these measured by Mensch and Thole [139] and Burd and Simon [140] shown in Fig. 4.13a, though the *L*/*D* in LES is slightly different from the ones used in the experiments. In Fig. 4.13b, all the experimental data is measured by Liu et al. [141]. The length-to-diameter ratios of the cylindrical film hole are *L*/*D*=3 in all three experimental cases. The discharge coefficient of 135° ribbed crossflow channels is lower than that of the coolant plenum case at roughly M=0.5-1.0, then the case of 135° ribbed crossflow channels surpasses the case of the coolant plenum since M=1.0. The discharge coefficients in the experiment with coolant plenum and LES show the same trend in the range of M=0.25-2.0.

For the fan-shaped film hole, the discharge coefficient increases as the pressure ratio or blowing ratio rises. Note that at M=1.5 the discharge coefficient is slightly lower than the expected value indicating that the loss goes up, which results from the separation zone in the expansion part of the film tube. In addition, the discharge coefficient of shaped hole increases by about 19%-27% at M=0.5-2.0, compared with the cylindrical hole. Thus, the

fan-shaped film hole reduces the flow losses obviously compared to the cylindrical film hole.

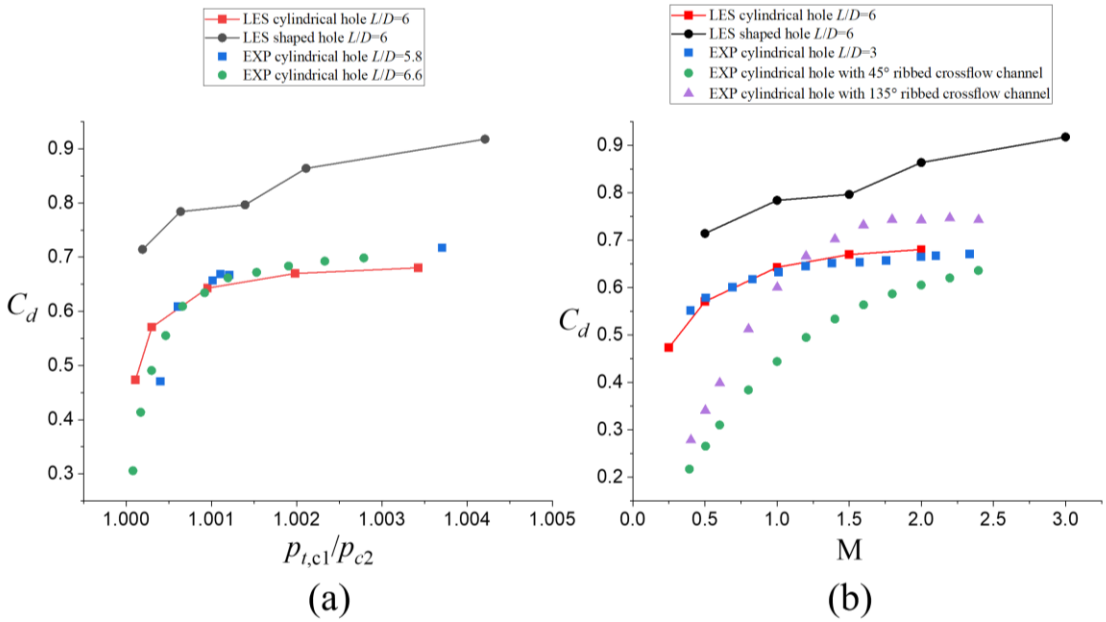

Fig. 4.13 Discharge coefficients of cylindrical and shaped film holes with respect to (a) pressure ratio (b) blowing ratio (LES at DR=1.5 Tu=0.5%)

Fig. 4.14 shows the pressure difference between the film tube inlet and outlet normalized by the mainstream dynamic pressure, which can reflect the pressure loss at various blowing ratio conditions due to the effects of the film hole geometry. The pressure loss difference is smaller at lower blowing ratios, and the difference of the losses increases as the blowing ratio becomes higher.

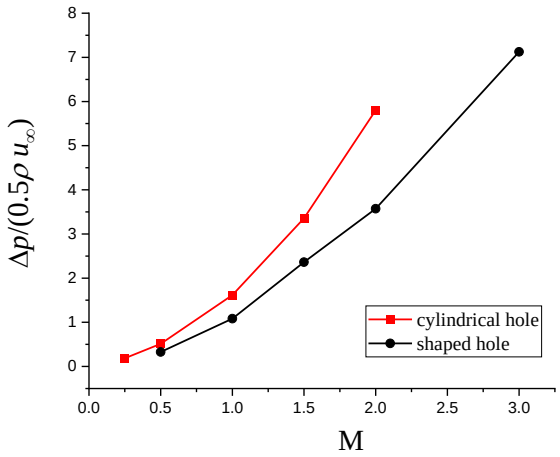

Fig. 4.14 Pressure loss of cylindrical and shaped film holes with varying blowing ratios at DR=1.5 Tu=0.5%

The turbulence intensity of cylindrical and shaped film holes at *x/D*=2.5 is illustrated in Fig. 4.15. The cross sections are located where the mixing process takes place. Tu at core regions of the cylindrical hole is as high as about 20% at M=1.5, while Tu is only up to about 11% for the shaped hole at M=0.5-1.5. High Tu region indicates the flow field in cylindrical hole is unsteady with intense velocity fluctuation. Lower Tu region for shaped hole is evenly distributed between z/D=-2 and +2, which implies that the flow field in the expansion part of the shaped hole is steadier with less velocity fluctuation.

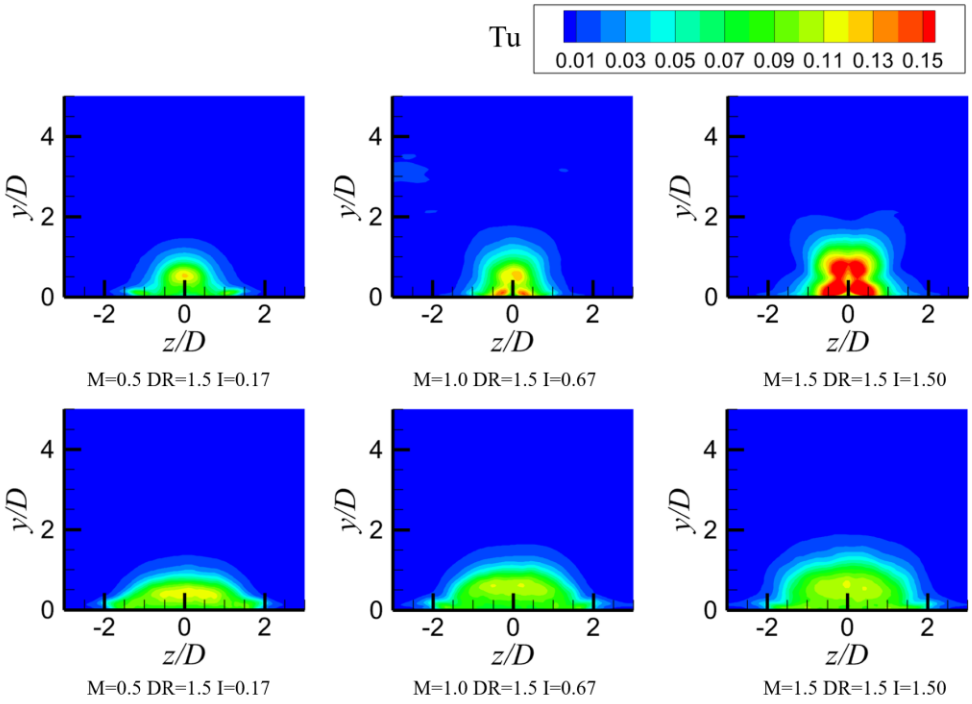

Fig. 4.15 Turbulence intensity of cylindrical and shaped film holes with varying blowing ratios at *x/D*=2.5 (top row: cylindrical hole, bottom row: shaped hole)

Fig. 4.16 compares cooling effectiveness of the shaped film hole and cylindrical film hole along the centerline. The solid lines represent the typical cylindrical hole, and the dash lines denote the 7-7-7 shaped film hole. For the shaped film hole, the centerline cooling effectiveness increases as the blowing ratio increases, and the growth rate is larger from M=0.5 to M=1.0 than that from M=1.0 to M=1.5. For the cylindrical film hole, when the blowing ratio is M=0.5, there is no separation along the streamwise direction, and the coolant remains attached to the bottom surface. Note that the centerline cooling effectiveness surpasses the shaped film hole for the same blowing ratio. As the blowing ratio increases from M=1.0 to M=1.5, the centerline cooling effectiveness is decayed

significantly. At M=1.0-1.5, separations occur at x/D=2 approximately, and at higher blowing ratio of M=1.5, the coolant with higher momentum causes the detachment more intensively and the coolant jet is lifted further away from bottom surface, which leads to the undesired effects on the centerline film cooling effectiveness even though there is a reduction of the difference between M=1.0 and M=1.5 at far field. At M=1.0, the reattachment occurs after the detachment, which leads to the recovery of the centerline film cooling effectiveness at about x/D=6. The centerline cooling effectiveness at M=1.0 overtakes the one at M=0.5.

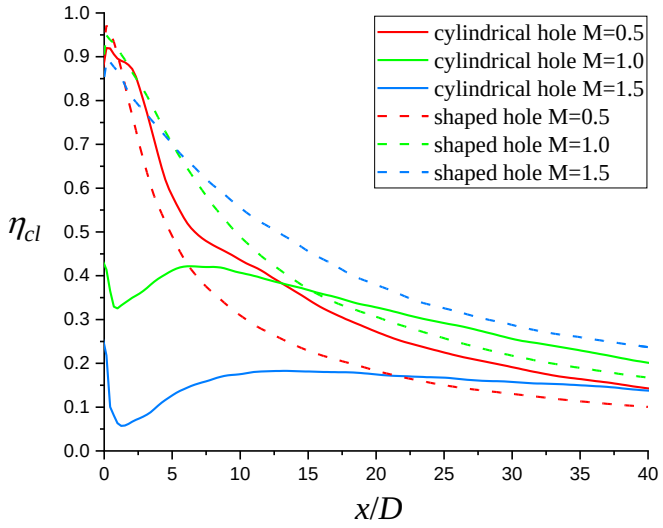

Fig. 4.16 Time-averaged centerline adiabatic film cooling effectiveness distributions of shaped film hole and cylindrical film hole at DR=1.5 Tu=0.5%

According to the study from Thole et al. [57], with the length to diameter ratio of 3.5 and injection angle of 35°, when momentum flux ratio I is less than 0.4, the coolant jet can still keep attached to the bottom surface. At 0.4<I<0.8, the separation occurs, and the coolant then reattaches to the bottom surface. when I is larger than 0.8 the injection remains detached from the surface. In current work, results show that no separation occurs for the lower momentum flux ratio of I=0.17, the detachment and attachment are observed for the moderate I=0.67. For the higher I=1.50, the coolant jet has already detached from the surface at near field followed by a slight and negligible reattachment subsequently.

The lateral averaged time resolved film cooling effectiveness distributions of shaped film hole and cylindrical film hole are depicted in Fig. 4.17. For the shaped film hole, the

lateral averaged film cooling effectiveness is improved as the blowing ratio increases from M=0.5 to M=1.5 at further downstream regions. Note that the effectiveness of M=1.5 is lower than M=1.0 at x/D=0-10. Corresponding to Fig. 4.18, the injection at M=1.5 doesn't spread as sufficiently as the one at M=1.0. The reason is that the recirculation occurs near the laidback side at M=1.5 shown in Fig. 4.35, which affects the spread of the coolant at near field. In addition, the coolant containing more momentum can delay the process of the penetration, thus, the lateral averaged film cooling effectiveness at M=1.5 surpasses that at M=1.0. For the cylindrical film hole, the lateral averaged effectiveness is worsened dramatically at near field, because the coolant jet contains higher momentum, and the separation occurs as soon as the injection enters the cooling channel. Since the detached coolant is pushed by the mainstream and then reattaches to the surface at M=1.0, the lateral averaged effectiveness begins to increase. Whereas at M=1.5 the strong separation directly results in the significant drop to nearly zero. Overall, the shaped film hole has the advantage over the cylindrical film hole at higher blowing ratio (M>1.0), while the cylindrical film hole obtains higher centerline and lateral averaged effectiveness than the shaped film hole at M<1.0.

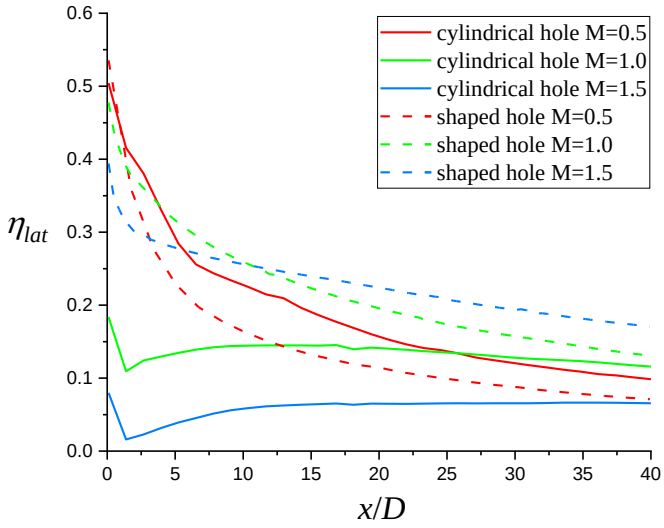

Fig. 4.17 Lateral averaged mean film cooling effectiveness distributions of shaped film hole and cylindrical film hole at DR=1.5 Tu=0.5%

The contours plot of the time-averaged film cooling effectiveness of the bottom surface are shown in Fig. 4.18. The marked difference of the effectiveness is detected according to

the contrast. For blowing ratio of M=0.5, both film hole structures present a good film and the protection against the high temperature mainstream. The distribution of the effectiveness shows that in cylindrical hole the coolant covers less in spanwise direction and is concentrated in the centerline regions, compared with the shaped film hole. The high effectiveness of the cylindrical hole remains to further downstream of the bottom surface as compared with the shaped film hole, but the coolant coverage is not as uniform as the shaped hole.

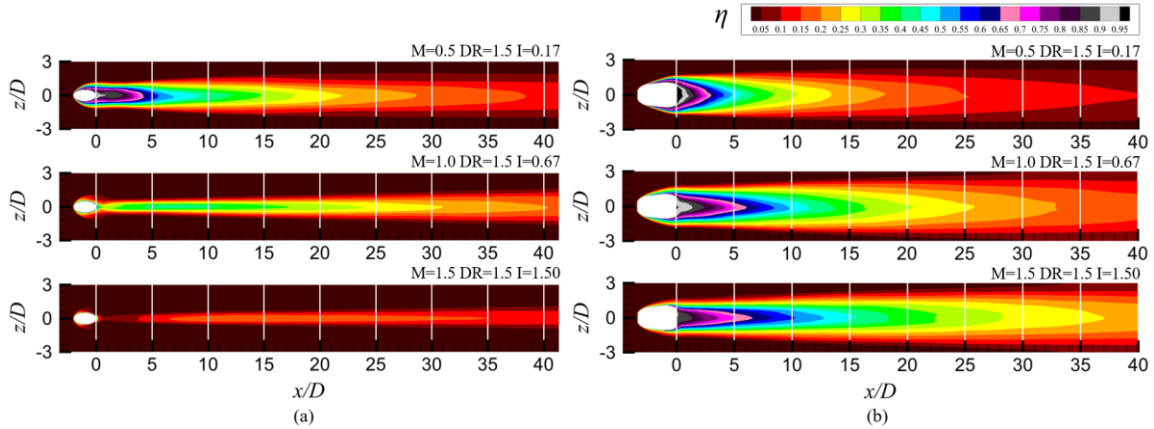

Fig. 4.18 Time-averaged film cooling effectiveness contours of (a) cylindrical film hole and (b) shaped film hole at M=0.5-1.5 DR=1.5 Tu=0.5%

The coolant coverage in spanwise direction is manifestly inadequate for higher momentum flux ratio cases of the cylindrical hole where the separation occurs at near field. However, the laidback fan-shaped film hole still presents a good thermal performance even the momentum flux ratio increases to 1.50, because the fan-shaped structure can expand the shape of coolant with 7° lateral expansion and enlarge the size of the hole exit in spanwise direction, which causes the improvement of the lateral spread of the coolant. Additionally, due to the 7° forward expansion, the issue of the separation at near field is resolved at high blowing ratio condition, which can also improve the effectiveness sharply at near field.

In Fig. 4.19, the contours of the time-averaged non-dimensional temperature is presented. The center planes show the position of the coolant in *xy* plane and the shift of the temperature normalized by the mainstream temperature. It is found that for the

cylindrical film hole in Fig. 4.19a, the core region of the coolant can nearly remain unchanged, then T_{non} declines at outer layers due to the penetration of mainstream.

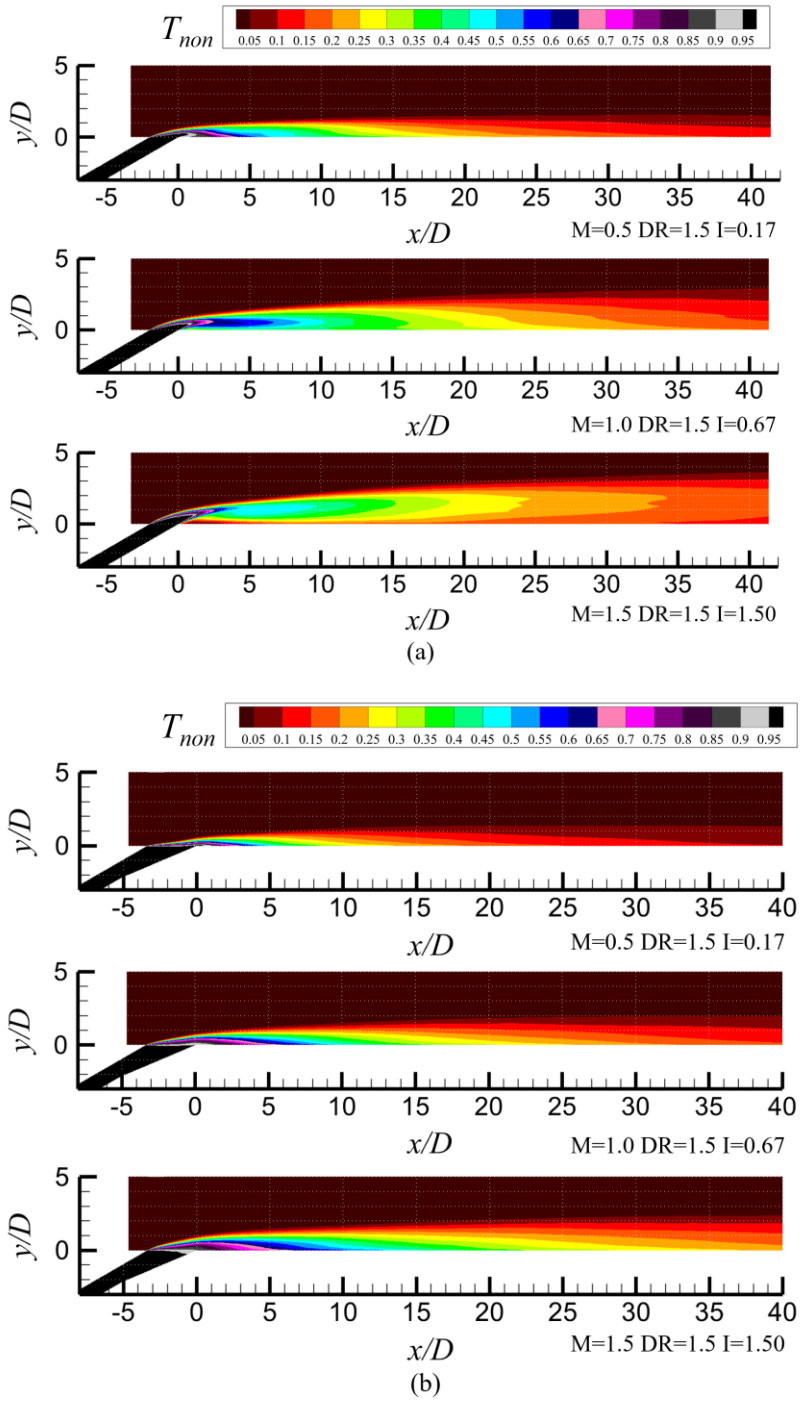

Fig. 4.19 Time-averaged non-dimensional temperature distributions of (a) cylindrical film hole and (b) shaped film hole at M=0.5-1.5 DR=1.5 Tu=0.5%

While for the shaped film hole in Fig. 4.19b, the coolant is diffused and expanded in lateral and spanwise directions, which reduces the momentum in the jet. And the coolant T_{non} decreases immediately when it is mixed with the mainstream at near field, as clearly shown especially at the trailing edge of the shaped hole exit at M=1.5. For M=0.5-1.5 conditions, the coolant jet remains attached to the surface at both near and far field for the shaped film hole. However, for the cylindrical film hole, the coolant can stay attached at the bottom surface without the separation only at M=0.5. Once the blowing ratio increases to 1.0 or even higher, the separation is formed at near field in cylindrical hole, as demonstrated in Fig. 4.16. Though the coolant is pushed by freestream towards the downstream, high momentum coolant at M=1.5 cannot reattach to the surface completely as the M=1.0 condition. And the injection shows an upward trajectory flowing along the streamwise direction, which causes the further deterioration downstream of the surface.

The distinct difference between the conventional cylindrical film hole and shaped film hole structures can be found in the distributions of the time averaged non-dimensional temperature along the streamwise direction at z/D=0, as shown in Fig. 4.20. The blowing ratio increases from M=0.5 to M=1.5 corresponding to Fig. 4.20a to Fig. 4.20c. For lower blowing ratio case of M=0.5, the normalized temperature shows a significant increase when the normal wall distance reduces at x/D=5-15, indicating the concentration of the coolant at near field in the centerline. The coolant distribution is similar for two film hole structures in wall-normal direction, because the coolant ends at almost the same distance to the bottom wall for the same streamwise position, as T_{non} decreases to nearly zero.

When the blowing ratio increases to M=1.0 in Fig. 4.20b, it is noticed that T_{non} of the cylindrical film hole shows a sharp decrease at near wall region (red solid line), which indicates that the coolant jet separates at near field. The injection with higher momentum detaches from the bottom surface causing the decay of the T_{non} and the worsened cooling effectiveness on the bottom wall in this area. At x/D=15 in the middle region of the channel, the coolant has reattached to the surface though a light separation still exists at near wall region. Since the coolant is lifted from the bottom wall at middle and far field regions, the T_{non} is higher for cylindrical film hole than the shaped film hole at the same y/D location.

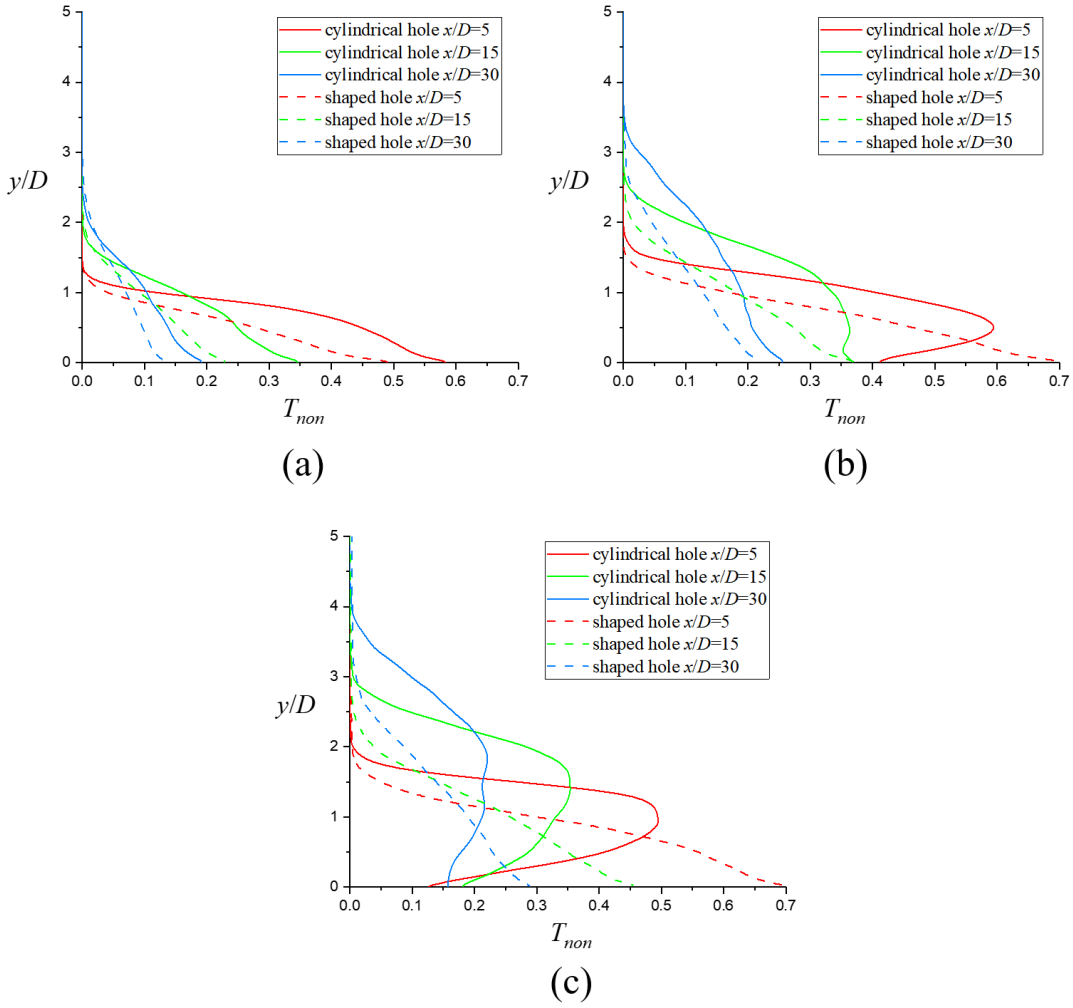

Fig. 4.20 Time averaged non-dimensional temperature at near, middle and far fields along wall-normal direction (a) M=0.5 (b) M=1.0 (c) M=1.5 at DR=1.5 Tu=0.5%

As the blowing ratio is equal to M=1.5, the high momentum in the coolant results in the intensive separation at near field and the coolant jet detaches from the surface from near field to far field. Because the coolant is lifted from the bottom wall, the maximum of T_{non} is located at about y/D=1 at near field for cylindrical film hole. And the T_{non} decreases sharply as the distance reduces to the bottom wall due to the detachment. However, for the shaped film hole, the coolant can remain attached to the surface along the streamwise direction. Accordingly, the cooling effectiveness maintains a higher value at the bottom surface for the same streamwise location.

Fig. 4.21 depicts the root mean square of the temperature fluctuation in the center plane. T_{RMS} contours can locate the interface of the mainstream and the coolant highlighted by the

dash line. T_{RMS} is higher at the windward side because the mainstream strikes and push the coolant. At M=0.5, the angle between the dash line at the leading edge and the bottom wall remains smaller for both two film hole structures. When M=1.0, the mix for cylindrical film hole is more intensive and durable along the streamwise direction. The angle between the interface and the *x*-axis is slightly larger than the shaped film hole. At M=1.5, the clear detachment of the coolant can be observed directly after the film hole exit for cylindrical hole. While the interface still remains close to the bottom surface without separation at near field for shaped hole.

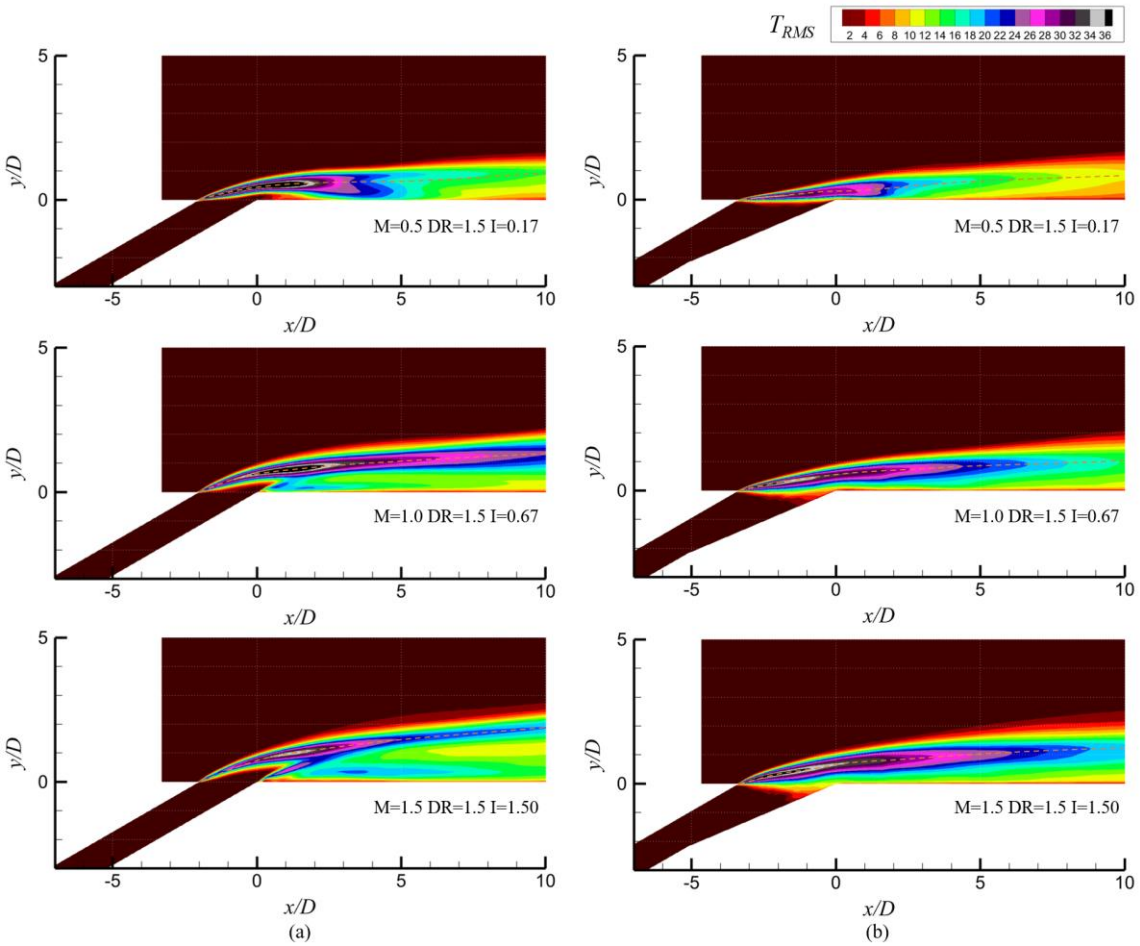

Fig. 4.21 T_{RMS} contours of (a) cylindrical film hole (b) shaped film hole at DR=1.5 Tu=0.5%

Fig. 4.22 presents the distributions of adiabatic film cooling effectiveness at near, middle and far fields along the spanwise direction from M=0.5-1.5. For lower blowing ratio of M=0.5, the cylindrical film hole leads to a higher distribution between z/D=-1 and z/D=1 region, compared with the shaped film hole. While the effectiveness falls dramatically

when the areas exceed the z/D= ±1, which implies the insufficient spread in spanwise direction for the cylindrical film hole. For higher blowing ratio of M=1.0, the reattachment is followed by the detachment of the coolant at x/D=5. Note that the cooling effectiveness of the cylindrical film hole is much lower than the shaped film hole in spanwise direction. At further downstream, the coolant spreads slightly in spanwise direction, but the effectiveness is still worse than the shaped film hole. The film cooling effectiveness deteriorates further at M=1.5, where the coolant detaches from the bottom surface. The shaped film cooling structure shows the benefits of the lateral coolant expansion without the separation at near field.

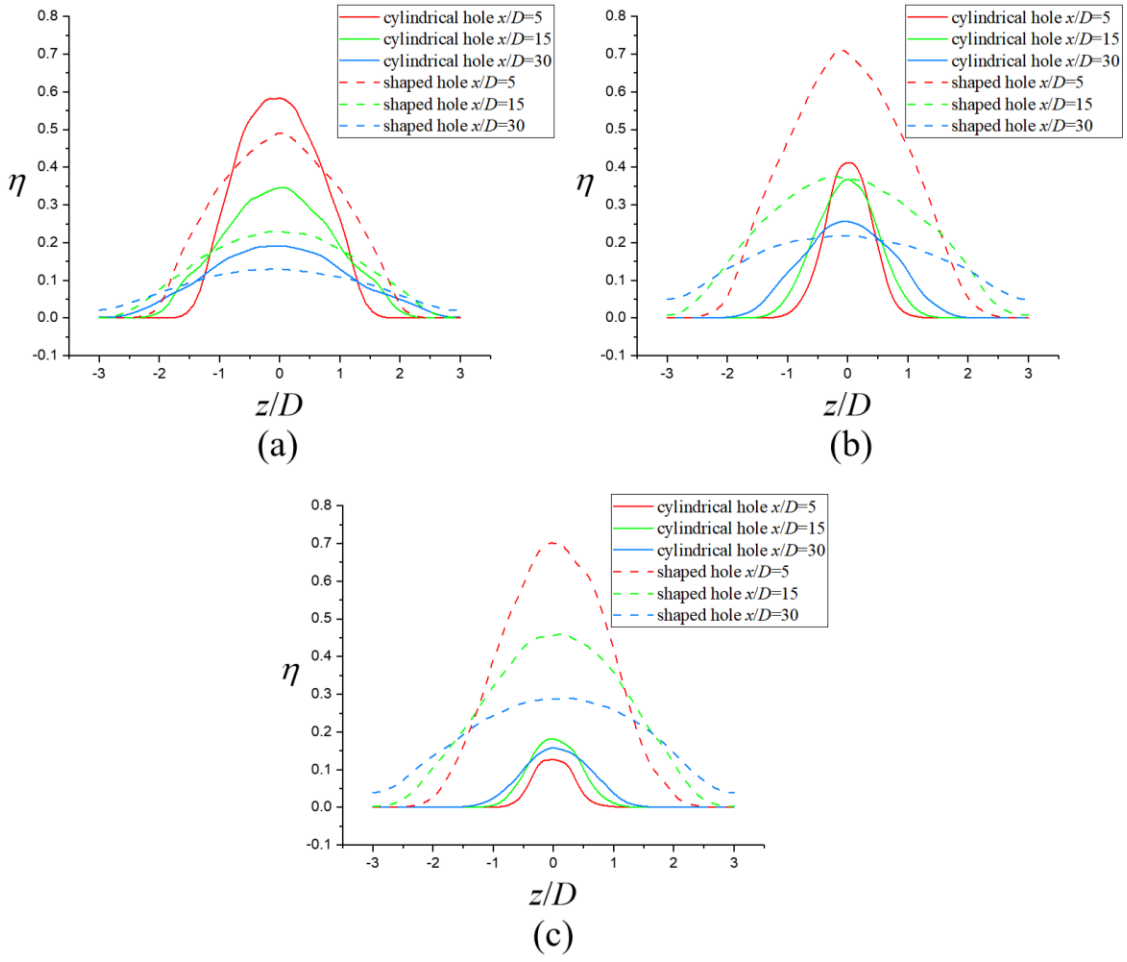

Fig. 4.22 Spanwise distributions of adiabatic film cooling effectiveness at near, middle and far fields (a) M=0.5 (b) M=1.0 (c) M=1.5 at DR=1.5 Tu=0.5%

Fig. 4.23 illustrates the comparison of area-averaged adiabatic film cooling effectiveness in the range of M=0.5-2.0 and the experimental data from Saumweber et al.

[142]. In the study of Saumweber et al., the injection angle is equal to 30° and the pitch to film hole diameter is 4. The laidback fan-shaped film hole in the experiment has the similar structure but the larger expansion angles: 14° and 15° in two lateral and forward expansion respectively. The effectiveness is averaged over an area of one pitch in width and 20*D* length in streamwise direction. It can be seen that the LES results show a similar trend with the experiment for two different film hole structures. The shaped film hole can obtain much higher area-averaged film cooling effectiveness than the cylindrical film hole at M=0.5-2.5.

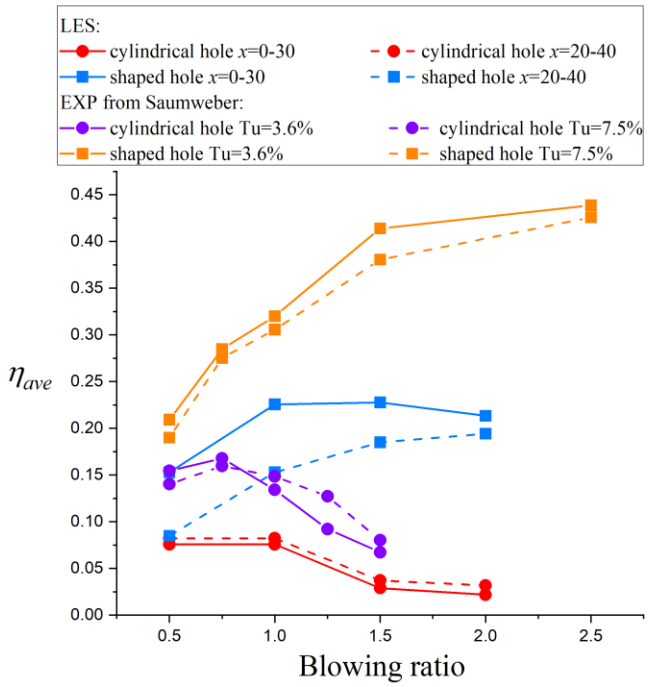

Fig. 4.23 Area-averaged adiabatic film cooling effectiveness distributions of LES at M=0.5-2.0 DR=1.5 Tu=0.5% and EXP at M=0.5-2.5 DR=1.7 Tu=3.6%, 7.5%

The area used for the average of LES is 6*D* in width and 20*D* or 30*D* in length. The red and blue solid line represents LES results in the area range of *x*/*D*=0-30 which can reflect the temperature distribution at upstream and middle regions of the channel, and the red and blue dash line denotes the region of *x*/*D*=20-40 that shows thermal performance in the middle and downstream of the cooling channel.

The area-averaged effectiveness at both *x*/*D*=0-30 and *x*/*D*=20-40 regions surpasses the conventional cylindrical film hole at the blowing ratios from M=0.5 to M=2.0. The shaped film hole shows an upward trend for the area-averaged effectiveness in the range of

x/D=20-40. In the range of x/D=0-30, the area-averaged effectiveness of shaped film hole becomes stable at M=1.0-1.5 and decrease at M=2.0. However, for the cylindrical film hole, the area-averaged effectiveness can be sustained only at M=0.5-1.0 in both x/D=0-30 and x/D=20-40 regions. And when the blowing ratio raises to M=1.5, the detachment results in the sharp decrease by about 61.9% and 54.9% for x/D=0-30 and x/D=20-40 respectively, compared with the M=1.0 condition.

The Proper orthogonal decomposition (POD) is a numerical method which is commonly used for the analysis of the turbulent flows and the detection of the coherent structure. The POD method was proposed by Lumley [143] in 1967. The POD modes can be calculated by Singular value decomposition (SVD). The data matrix A is arranged as follows:

$$A=\begin{bmatrix} T(x_1,y_1,t_1) & T(x_1,y_1,t_2) & \cdots & T(x_1,y_1,t_n) \\ T(x_2,y_1,t_1) & T(x_2,y_1,t_2) & \cdots & T(x_2,y_1,t_n) \\ \vdots & \vdots & \ddots & \vdots \\ T(x_m,y_1,t_1) & T(x_m,y_1,t_2) & \cdots & T(x_m,y_1,t_n) \\ T(x_1,y_1,t_1) & T(x_1,y_1,t_2) & \cdots & T(x_1,y_1,t_n) \\ T(x_1,y_2,t_1) & T(x_1,y_2,t_2) & \cdots & T(x_1,y_2,t_n) \\ \vdots & \vdots & \ddots & \vdots \\ T(x_1,y_m,t_1) & T(x_1,y_m,t_2) & \cdots & T(x_1,y_m,t_n) \end{bmatrix}$$

The data matrix A is decomposed into the form of $A=U\Sigma V^T$ where U and V is an M×M and N×N orthogonal matrices respectively and Σ is an M×N rectangular diagonal matrix with ordered eigenvalues on the diagonal. The rank of A is equal to the total number of the nonzero singular values in the diagonal matrix Σ.

Fig. 4.24 and Fig. 4.25 depict the POD results on the central plane for cylindrical and shaped film cooling holes at M=0.5 and 1.5. For the cylindrical film hole, the POD temperature distributions between mode1 and mode2 are similar to each other for both blowing ratios. The energy consists in the vortices generated since the leading edge of the film hole, and the high value regions lie at the interface between the coolant and the mainstream. At M=0.5 there is not separation at near field downstream of the cylindrical film hole, thus, the convection patterns are distributed at lower vertical position near the bottom wall. However, separation occurs at near field at M=1.5, so the POD peak value is

located at higher vertical position. In addition, for mode2 the higher POD value area can be found at *x*/*D*=3 where the injection reattaches to the surface.

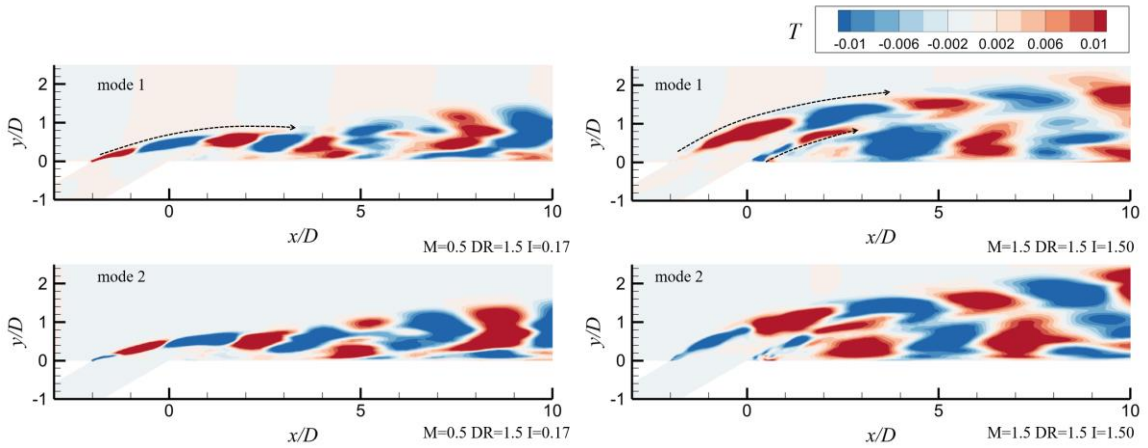

Fig. 4.24 POD modes of temperature on the center plane of cylindrical film hole at M=0.5 and 1.5

For the shaped film cooling hole, the patterns of mode1 and mode2 are quite different from the cylindrical film hole, especially at M=1.5. The strong temperature region is closer to *y*/*D*=0 and located above the film hole exit and near field downstream at M=0.5 and 1.5, which means that the expansion segment of the shaped film hole can reduce velocity of the coolant and keep the coolant attached to the bottom wall. At M=1.5 the high value region exists at higher *y*/*D* location corresponding to the location of the shear layer between the coolant and mainstream.

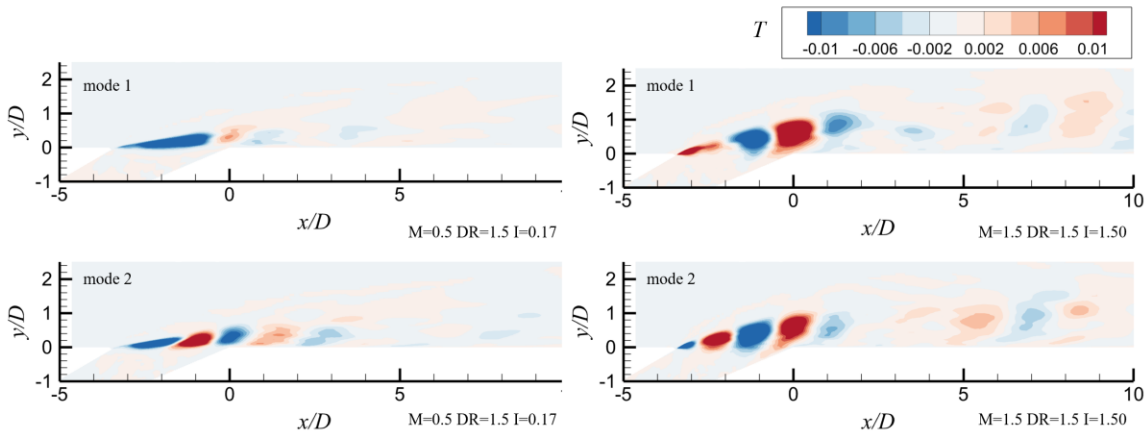

Fig. 4.25 POD modes of velocity magnitude on the center plane of shaped film hole at M=0.5 and 1.5

Fig. 4.26 shows the velocity power spectral density at three bowing ratios of cylindrical film hole. Four monitor points are set at the exit of the film hole to collect the instantaneous

velocity data for a period. The average frequencies for blowing ratios of 0.5, 1.0 and 1.5 are 139Hz, 251Hz and 249Hz respectively. The frequency of M=0.5 is nearly half of M=1.0 and 1.5, and higher blowing ratios of M=1.0 and 1.5 give close frequencies. It can be inferred that smaller scale vortices are generated and dominated in the vicinity of film hole exit region for higher blowing ratios and larger size vortices for lower blowing ratio.

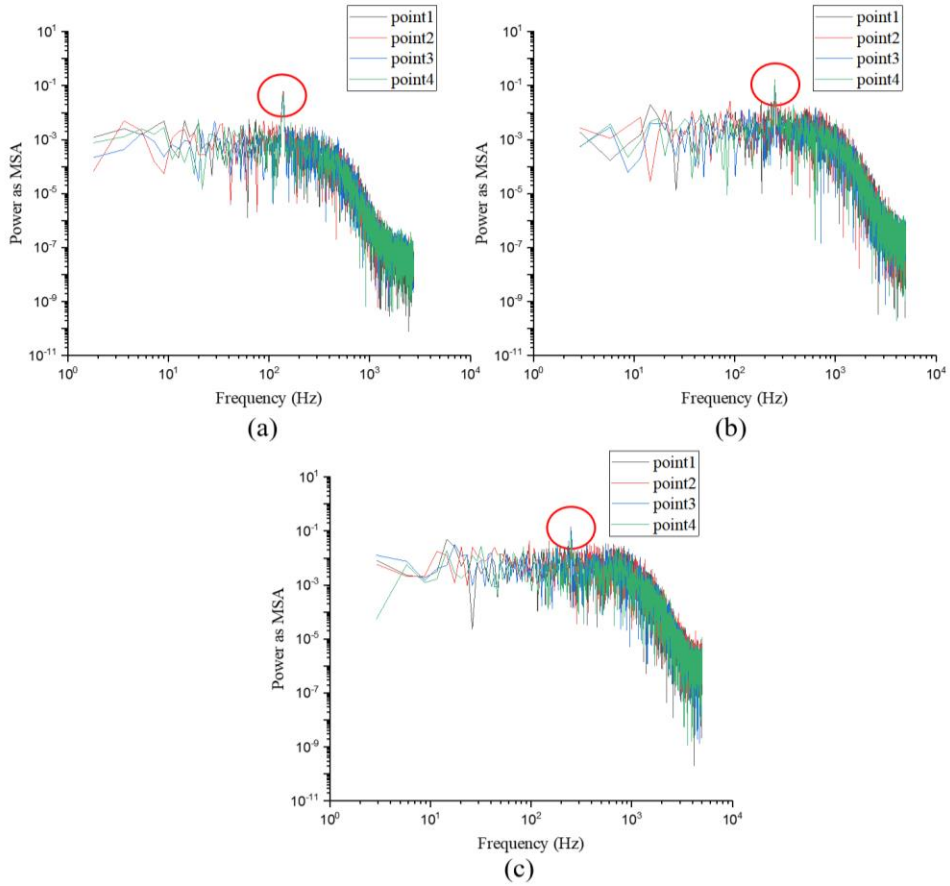

Fig. 4.26 Instantaneous velocity power spectral density (PSD) (a) M=0.5 (b) M=1.0 (c) M=1.5 at DR=1.5 Tu=0.5%

4.4.2 Effects of blowing ratios on shaped film hole

Based on the 7-7-7 laidback fan-shaped film hole geometry, the Effects of blowing ratios on the shaped film hole was studied in this section. The blowing ratio is from M=0.5 to 3.0, corresponding to the momentum flux ratio in the range of I=1.17-6.00. The density ratio is equal to 1.5 and the mainstream inlet turbulence intensity is kept at 0.5% for all cases.

Fig. 4.27 shows the adiabatic film cooling effectiveness of the 7-7-7 shaped hole with the blowing ratio from 0.5 to 3.0 at lower turbulence intensity of 0.5%. And the mainstream inlet velocity profile in section 4.3 is employed in the simulation. The cooling effectiveness increases distinctly in the streamwise direction as the blowing ratio grows from M=0.5 to M=1.5. Note that the area covered by the coolant becomes narrow when the blowing ratio is higher than M=1.5, which results in the lower adiabatic effectiveness in transverse direction and the concentration near the centerline. As shown in Fig. 4.28, the centerline cooling effectiveness curves of M=1.5-3.0 are close to each other at x/D=0-20, but for the lower blowing ratio of M=0.5 and M=1.0, the centerline effectiveness decreases sharply at first and the decay rate is reduced since approximately x/D=10 downstream. From x/D=0 to x/D=10 the blowing ratios in range of 1.5-3.0 show a similar trend with the same decay rate roughly. After x/D=20 cooling effectiveness of M=2.0 and 3.0 surpasses that of M=1.5.

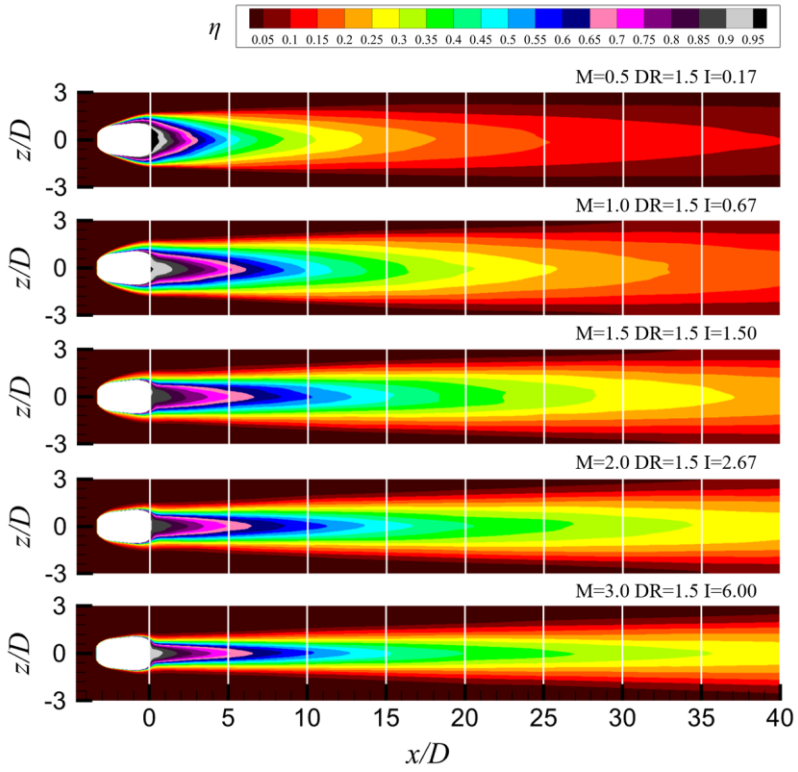

Fig. 4.27 Time-averaged film cooling effectiveness contours of shaped film hole with various blowing ratios at DR=1.5 Tu=0.5%

Fig. 4.29 illustrates the lateral averaged film cooling effectiveness of 7-7-7 shaped hole at DR=1.5 Tu=0.5%. η_{lat} decreases sharply at the beginning of the downstream area of the film hole. η_{lat} at M=0.5 gives a quicker drop than M=1.5-3.0. Because the velocity at the

exit of the shaped hole is relatively slower than the high blowing ratio cases, the coolant is heated by the mainstream as soon as it flows through film hole. The coolant is mixed into the mainstream, therefore, there is not enough coolant to cover the further area downstream and η_{lat} is the lowest from x/D=10 to x/D=40 in comparison. For M=2.0 and 3.0, the lateral averaged effectiveness slowly decreases along the passage. η_{lat} at M=1.5 is higher than M=2.0 and 3.0 at x/D=0-20, which indicates a better spread of the coolant laterally at M=1.5. Considering the whole range of the channel, M=1.0 and M=1.5 provide the best performance in the range of x/D=0-12 and x/D=12-25 respectively due to the appropriate velocity and momentum of the coolant.

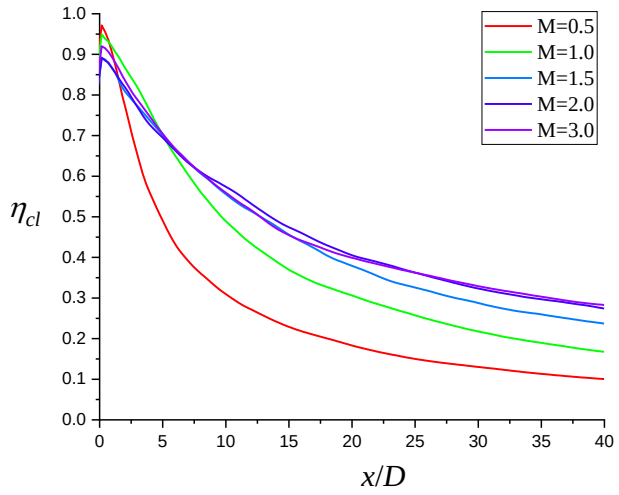

Fig. 4.28 Time-averaged centerline adiabatic film cooling effectiveness of shaped hole at DR=1.5 Tu=0.5%

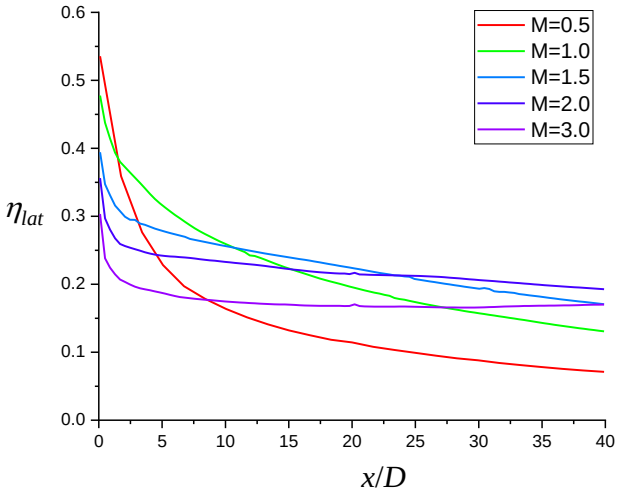

Fig. 4.29 Lateral averaged mean film cooling effectiveness of shaped hole at DR=1.5 Tu=0.5%

Fig. 4.30 illustrates the distributions of the time-averaged non-dimensional temperature in wall-normal direction at z/D=0. Three streamwise locations are chosen representative of the near, middle and far field of the cooling channel. As can be seen, the normalized temperature decreases as the distance from the wall increases. As the coolant develops from near to far field, the rate of T_{non} decay is reduced, and the T_{non} declines from about 0.7 to 0.3. In addition, when the blowing ratio grows from 1.5 to 3.0, the non-dimensional temperature of the coolant raises at the same distance to the bottom wall, which implies that the coolant can resist the penetration of the mainstream at high blowing ratio condition. And no separation is observed near the bottom surface at higher blowing ratio condition for shaped film hole.

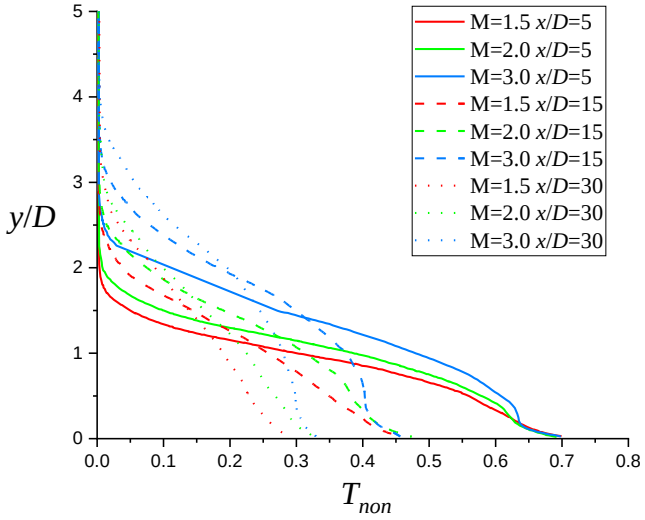

Fig. 4.30 Time-averaged non-dimensional temperature T_{non} distributions along wall-normal direction at M=1.5-3.0 DR=1.5 Tu=0.5%

The time-averaged non-dimensional temperature T_{non} in cross section is presented in Fig. 4.31. Lower blowing ratio indicates the coolant contains less momentum as the coolant is injected into the mainstream channel, and the spread of the coolant is limited in wall-normal direction. The coolant is pressed by the mainstream near the surface. In the downstream part of the channel x/D=20-40 at the lower blowing ratio M=0.5, most coolant is absorbed into the high temperature gas due to the low momentum in the coolant (I=1.17), hence, the cooling effectiveness is poor in this area. For the higher blowing ratio M=1.5-3.0, the low temperature coolant is diffused in the middle region of the channel, because the high momentum (I=1.50-6.00) of the coolant postpones the mixture of the coolant and

the freestream, which can protect a larger area of the surface and resist the mainstream penetrating through the coolant.

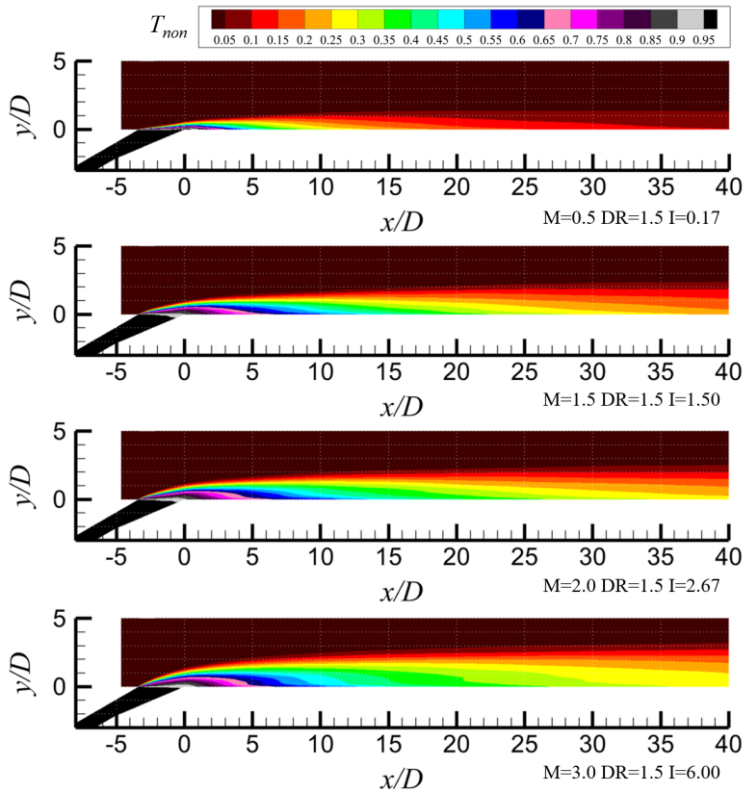

Fig. 4.31 Time-averaged non-dimensional temperature T_{non} distributions of shaped film hole with various blowing ratios in cross section at DR=1.5 Tu=0.5%

Fig. 4.32 depicts the contours of the root mean square temperature normalized by the time-averaged temperature at blowing ratios of 0.5-3.0, corresponding to the non-dimensional temperature in Fig. 4.31. The interface of the coolant and the mainstream can be located by temperature fluctuation, and the interface line is defined by the maximum of T_{RMS}/T_{ave}, presented with the dash line. Note that the higher the blowing ratio is, the larger the angle that the interface line shows is at the film hole exit region.

For low blowing ratio M=0.5, the temperature fluctuation keeps high in the range of x/D=0-10 at only near field. Far downstream of the channel, the T_{RMS}/T_{ave} level drops sharply. As the increase of the blowing ratio, the T_{RMS}/T_{ave} expands in both streamwise and wall-normal directions. A strong mix of the mainstream and the coolant occurs in the vicinity of the leading edge of the film hole. The mixing layer can be seen from the leading edge of the film hole to the downstream until the coolant merges into the mainstream. Due

to the high momentum in the coolant at high blowing ratio of M=2.0 and 3.0, the coolant can suspend the penetration into the mainstream and the mixing process lasts longer with the extent to the further downstream, relative to the low blowing ratio.

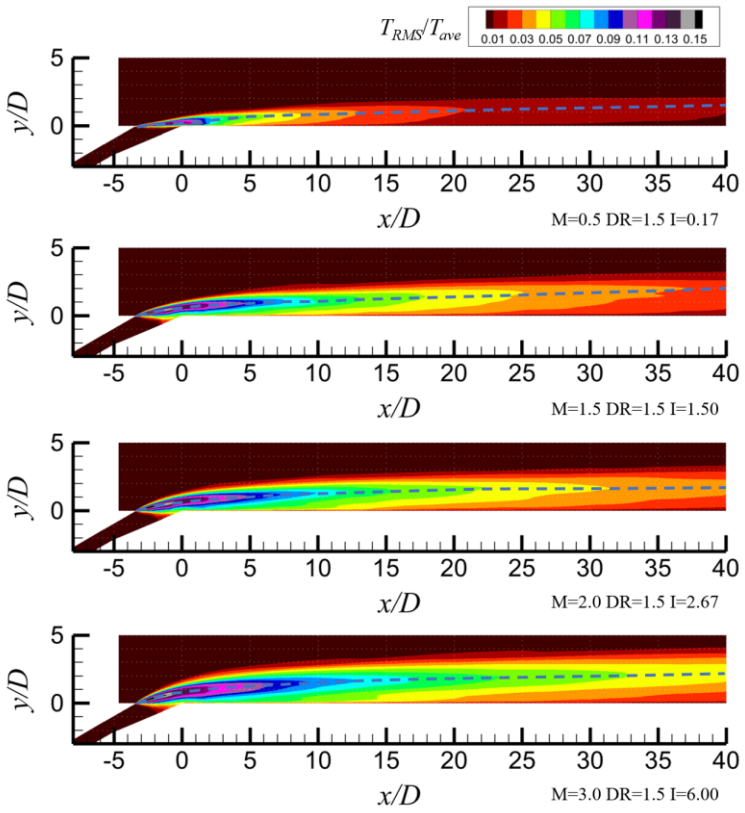

Fig. 4.32 T_{RMS}/T_{ave} distributions of shaped film hole with various blowing ratios in cross section at DR=1.5 Tu=0.5%

Corresponding to Fig. 4.31 and Fig. 4.32, Fig. 4.33 and Fig. 4.34 illustrate the T_{non} and T_{RMS}/T_{ave} cross-section distributions along various streamwise positions with much detailed thermal information. Compared with the other three higher blowing ratio cases, for M=0.5 the coolant jet is much flatter and closer to the bottom surface showing an arched shape distribution. T_{RMS}/T_{ave} distribution represents the penetration of the coolant into the mainstream, the coverage of the coolant at M=0.5 is only from x/D=0 to x/D=15 approximately, because at x/D=15 T_{RMS}/T_{ave} has already decreased to a relative lower value and there is rarely coolant left. As the blowing ratio increases, the coolant jet T_{non} distribution is plumper like a semicircle shape. T_{non} in the core region of coolant jet decreases slowly at M=1.5-3.0, compared with M=0.5 case. T_{non} can still keep as high as

about 0.45 at x/D=10, and the low temperature coolant dominates most of the channel in spanwise direction.

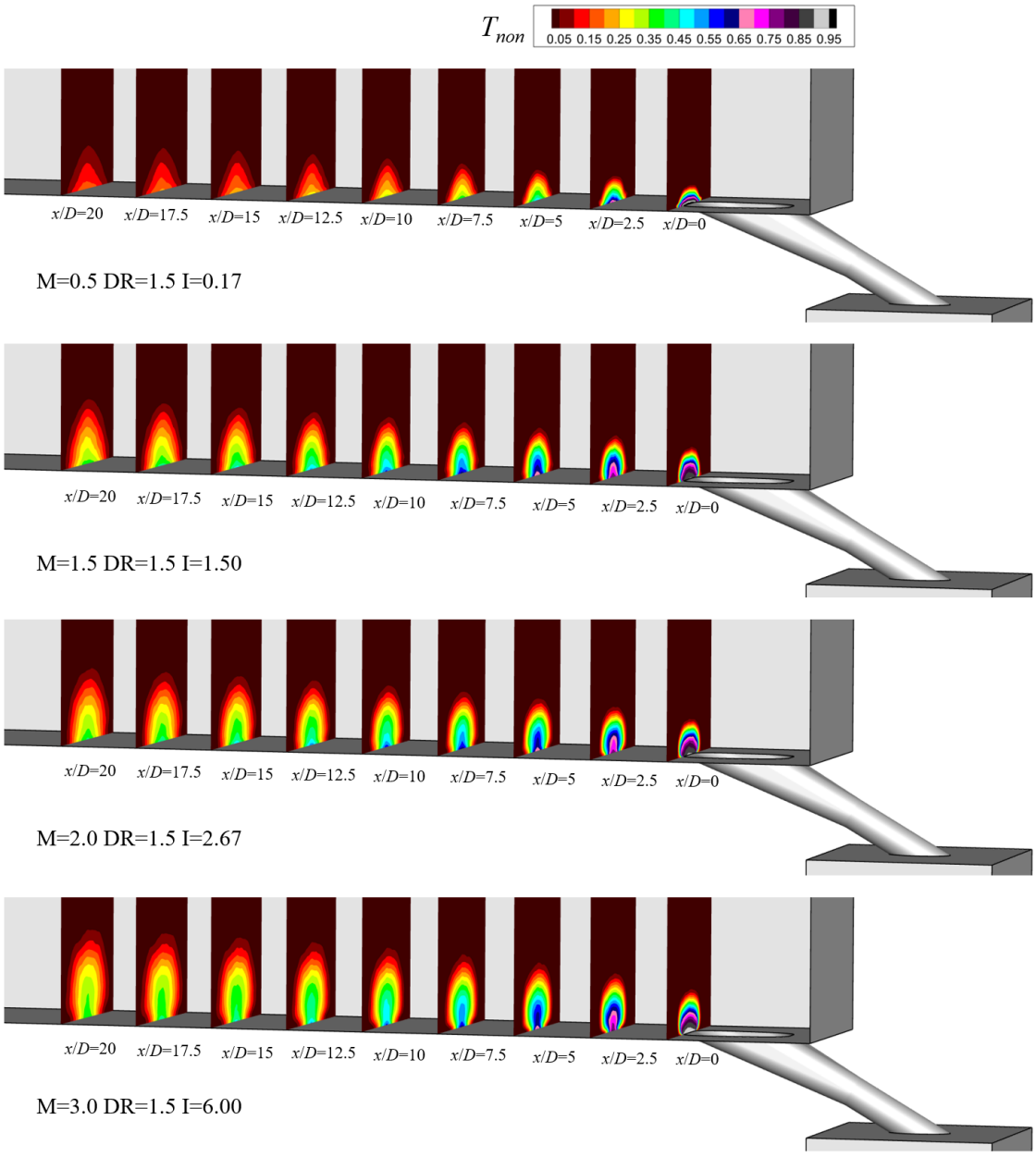

Fig. 4.33 Time-averaged non-dimensional temperature T_{non} distributions of shaped film hole with various blowing ratios along streamwise direction at DR=1.5 Tu=0.5%

As depicted in Fig. 4.34, for higher blowing ratio of M=1.5-3.0, the mix occurs from the outside of the coolant injection at near field. Because of the CRVP discussed in the following sections, the CRVP begins to absorb the high temperature mainstream around the coolant through the edge of coolant near the bottom surface, therefore, the T_{non} drops

on the two sides of the coolant near the bottom surface, and the coolant is also strongly mixed with the mainstream where T_{RMS}/T_{ave} is higher on the two sides of the coolant.

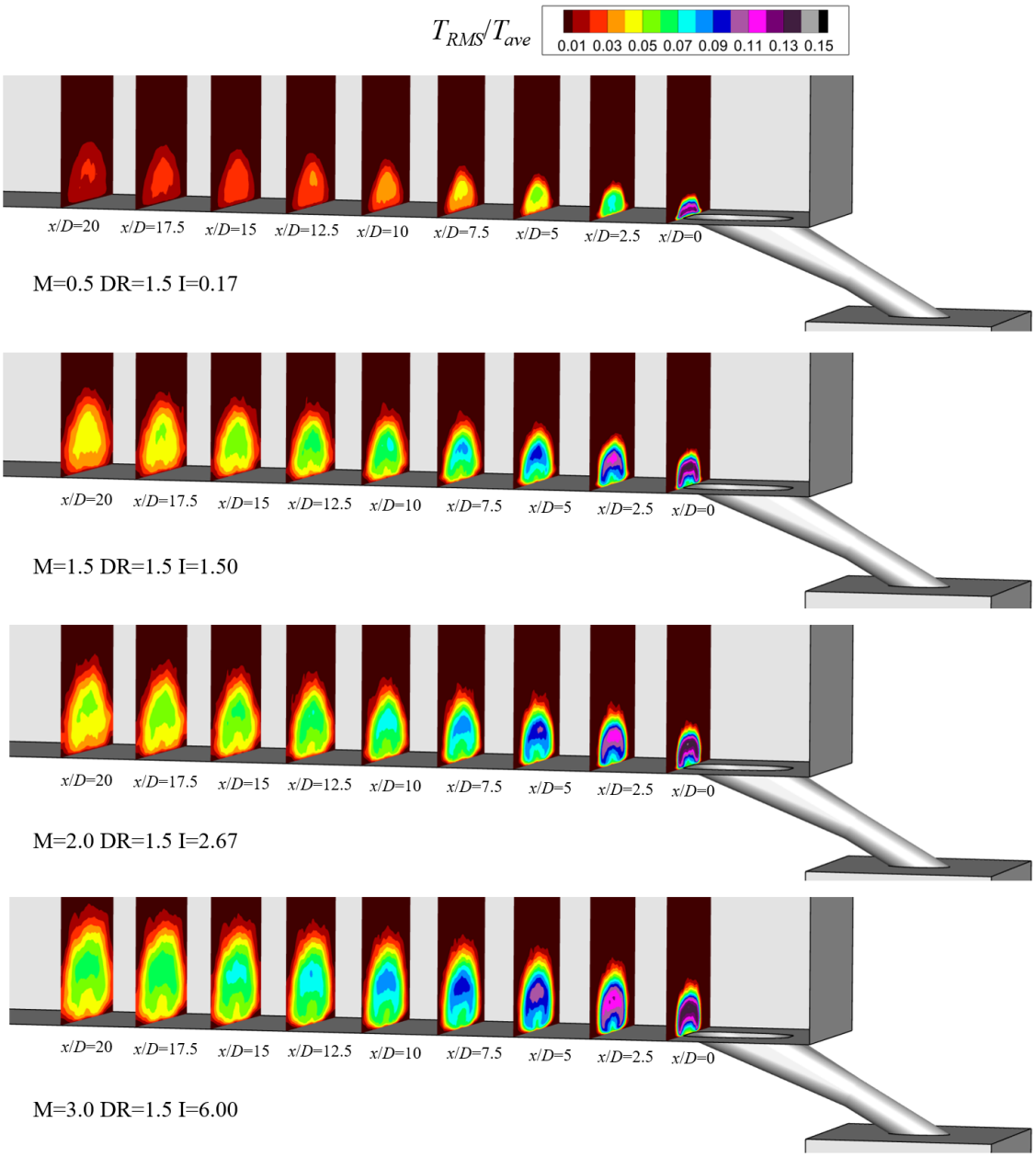

Fig. 4.34 T_{RMS}/T_{ave} distributions of shaped film hole with various blowing ratios along streamwise direction at DR=1.5 Tu=0.5%

Fig. 4.35 presents the time-averaged velocity of the shaped hole at various blowing ratios conditions. The high velocity is shown in the upper region of the cylindrical part of the shaped film hole, and the low velocity occurs at the back side of the tube inlet and the

laidback region, because there is a sudden reduction in cross sectional area when the coolant flows from the plenum to the film tube. The coolant is pushed to the upper side of tube with higher momentum. As the coolant reaches the end of the cylindrical part of the tube, the coolant begins to decelerate on account of the expansion in forward and lateral directions. Note that a low velocity recirculation occurs near the laidback side at M=1.5, which causes the velocity to be lower near the leading edge of the film hole exit.

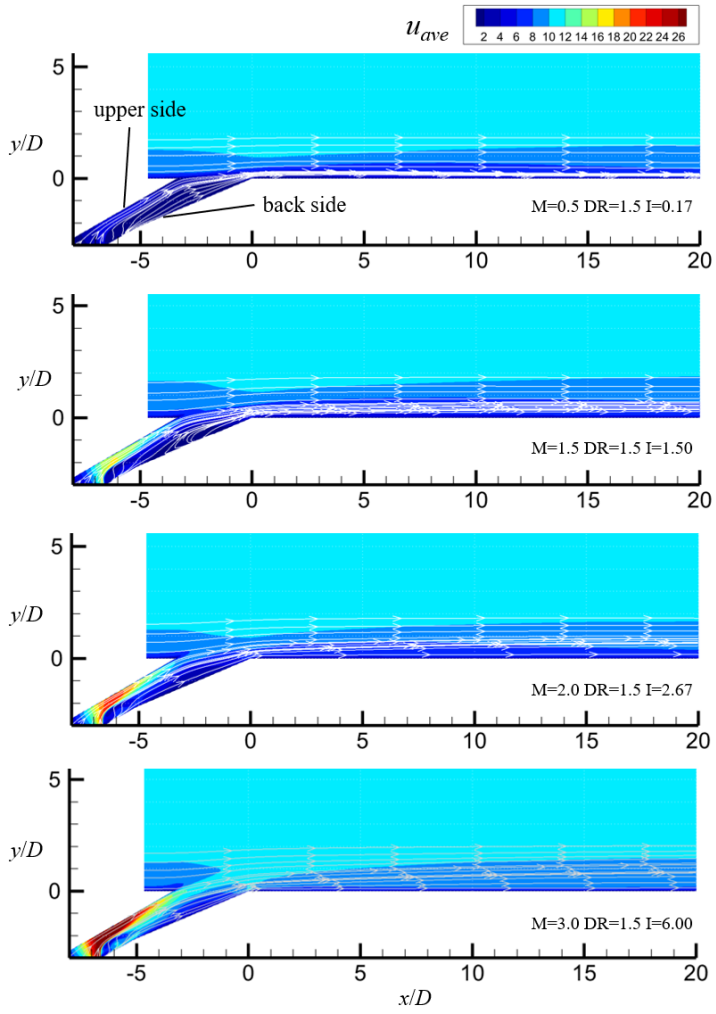

Fig. 4.35 Time-resolved velocity distribution of shaped film hole with various blowing ratios in cross section at DR=1.5 Tu=0.5%

Corresponding to Fig. 4.35, Fig. 4.36 shows the u_{RMS}/u_{ave} distribution of shaped film hole with various blowing ratios, which also can be known as the turbulence intensity. A pronounced velocity fluctuation is presented from the back of the tube inlet to the laidback side of the expansion part. The mixing shear layer interface of different velocities can be

seen between the mainstream and the coolant. For lower blowing ratios, the mixing layer is much closer to the bottom surface of the cooling channel. The low momentum coolant is mixed with the mainstream at the exit of the film tube until about x/D=5, which means the further downstream region loses the protection of the low temperature film. For higher blowing ratios, the velocity fluctuation decreases along the streamwise direction with higher descent rate, which indicates that higher momentum suppresses the mixing process, and the coolant can last further downstream.

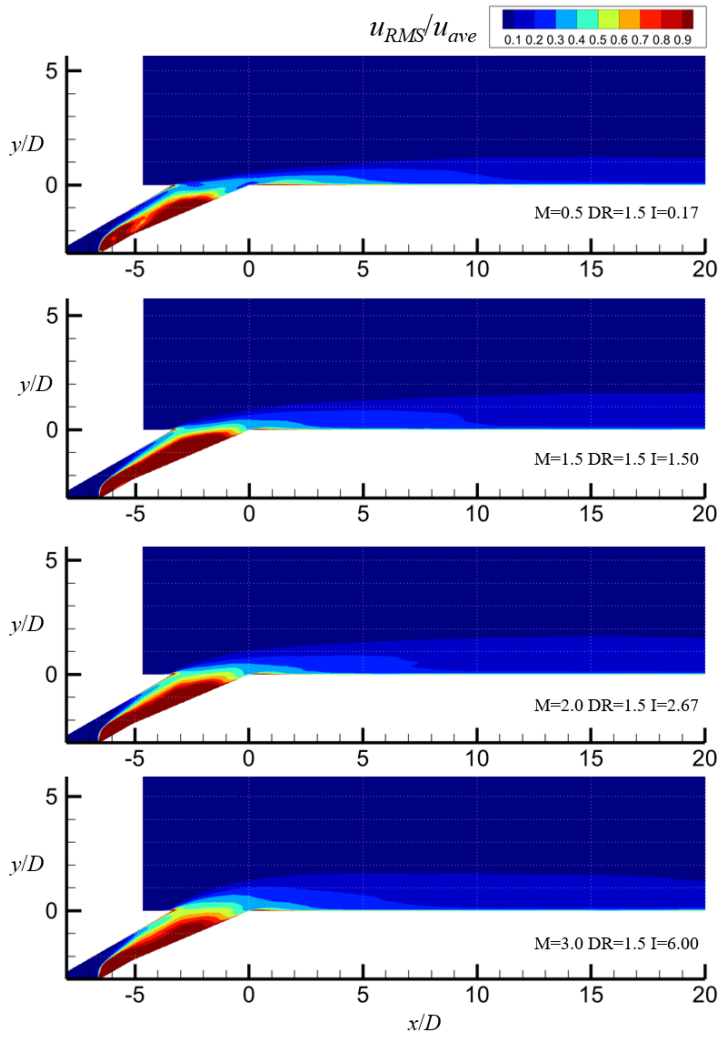

Fig. 4.36 u_{RMS}/u_{ave} distributions of shaped film hole with various blowing ratios in cross section at DR=1.5 Tu=0.5%

Fig. 4.37-Fig. 4.40 present the cross-sectional distributions of the axial vorticity ω_a and the axial velocity u_a normalized by mainstream velocity u_∞ along the cylindrical axis of the film hole shown in Fig. 4.37a and Fig. 4.37b. The distance between the inlet and exit of the

film hole tube is divided equally into 10 parts. The planes C1-C4 are located in the cylindrical part of the tube, and the planes C5-C9 lie in the expansion part. The positive axial vorticity ω_a value represents the clockwise rotating direction looking from the inlet to the outlet of the tube and vice versa. Since the axial velocity in the film hole tube at M=0.5 is much lower than the other cases, therefore, the scale in Fig. 4.37d is reduced to present more details.

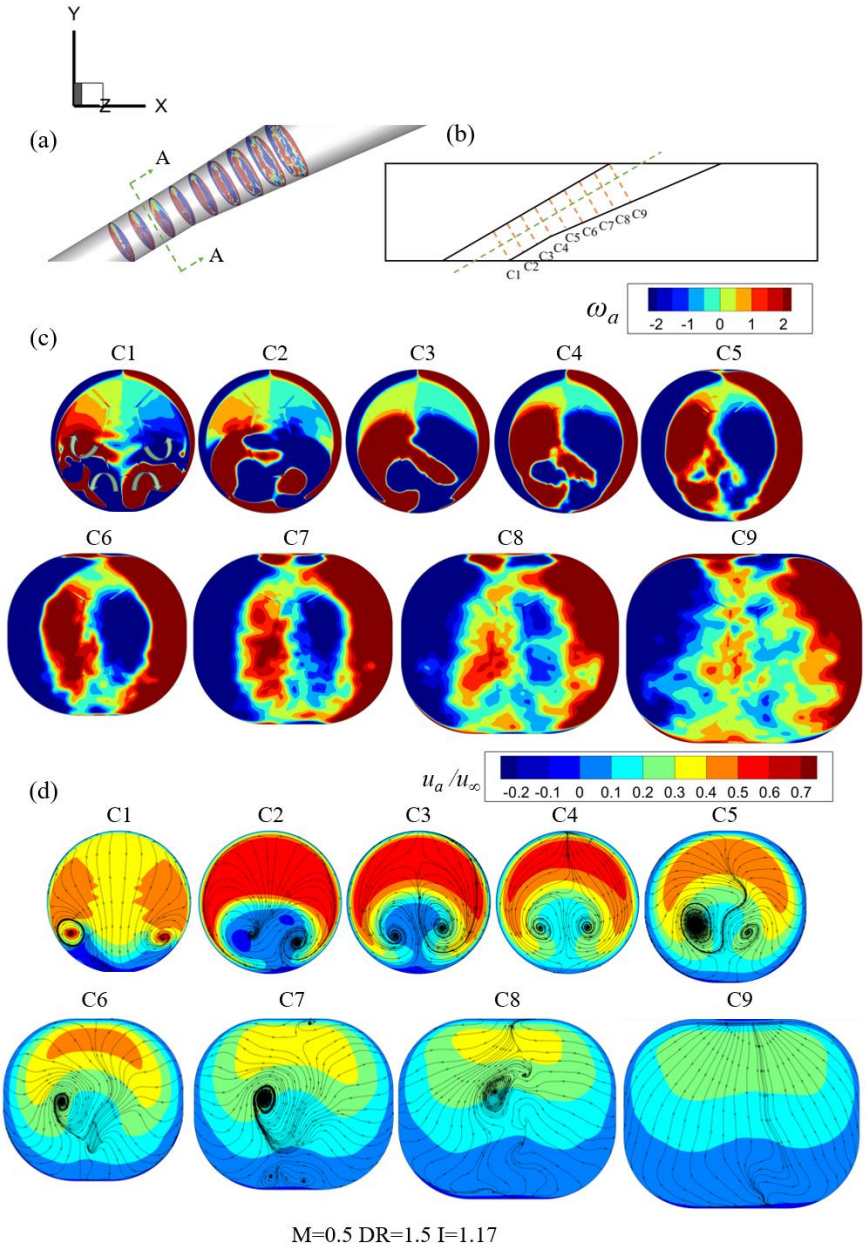

M=0.5 DR=1.5 I=1.17

Fig. 4.37 Cross-sectional distributions in tube axial direction (a) locations of planes (c) time-averaged axial vorticity ω_a (d) time-averaged u_a/u_∞ and streamlines at M=0.5 Tu=0.5%

Due to the sudden contraction of the film hole tube, the coolant interacts with the in-tube wall near the film hole inlet. For M=0.5 shown in Fig. 4.37, a vortex pair generates at the two sides of the C1 plane, and high axial velocity region is near the two sides of the cross section. In the C2-C4 planes, high axial velocity region is concentrated in the upper half-plane surrounding the low axial velocity region. Then, the high axial velocity region begins to reduce, and the downward streamlines result in the axial velocity increase. In the expansion part of the shaped film hole, the vortex pair formed in the cylindrical part is weakened and only one main vortex core is found in C6-C8 planes, the other is weakened and dissipates between the C5 and C6 planes. In C9 plane, the vortex almost dissipates, and the flow field is much steadier. In the side walls of expansion part, the axial vorticity is positive in +z region and negative in -z region along the in-tube side walls. And the core area with opposite axial vorticity pair starts to be weakened and reduced at the beginning of the expansion segment. At the exit of the tube, the axial vorticity in the center area is close to zero, and the two side areas of the cross section are strengthened. Thus, the shear vortices can be generated at two side edges of the film hole exit.

For M=1.5 depicted in Fig. 4.38, the vortex cores in C1 plane are lower and closer to each other, compared with M=0.5. Due to the higher velocity of the coolant, the vortex pair is strengthened from C1 to C3. Note that more high velocity coolant is forced to rotate and drawn into the bottom of the pair of vortices. The vortex pair located in low velocity region moves close to each other from C1 plane to C5 plane. The high velocity area decreases, and the vortex pair begins to be weakened at the transition location of the cylindrical and expansion parts illustrated in C4 and C5 planes, where the axial vorticity distribution becomes symmetric about the vertical centerline in C5 plane, but the sign of the vorticity is opposite. It can be found that some new and small vortices are formed at the bottom of the C6 plane in Fig. 4.38b, and in C7 plane a new vortex pair is presented and strengthened in the C8 plane. The coolant at the bottom of the tube channel flows upwards, which corresponds to the recirculation zone in Fig. 4.35. The area of the negative and positive axial vorticity at the two sides of the channel enlarges from C6 to C9 in Fig. 4.38a. In the recirculation zone, a low velocity zone can be observed at the bottom, and the area increases from C7 plane to C8 plane and then slightly decreases from C8 plane to C9 plane.

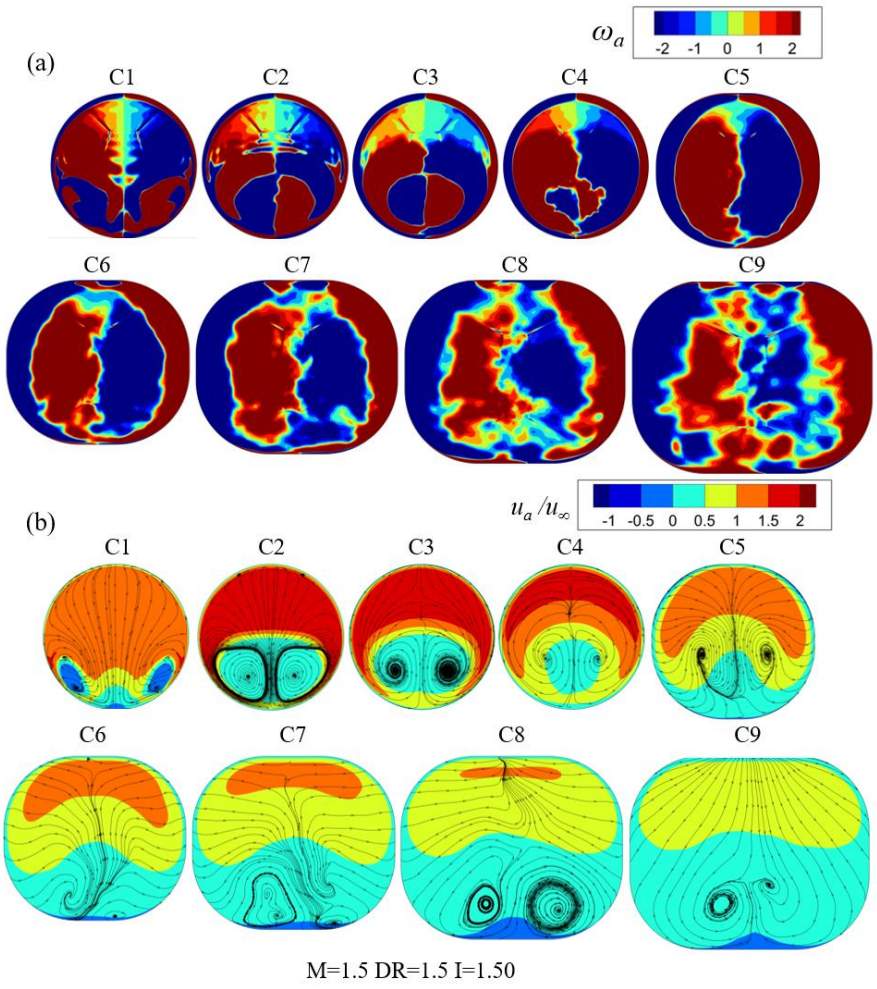

Fig. 4.38 Cross-sectional distributions in tube axial direction (a) time-averaged axial vorticity ω_a (b) time-averaged u_a/u_∞ and streamlines at M=1.5 Tu=0.5%

When blowing ratios are equal to 2.0 and 3.0 shown in Fig. 4.39 and Fig. 4.40, the flow field in the film tube is similar to each other. As the blowing ratio increases, the high velocity regions increase especially in C5-C9 planes. At the inlet of the tube the coolant flows towards the upper wall, which results in the high pressure and velocity region. The vortex pair dominates the whole lower half-plane in C2 and C3. And the distance between the two vortices becomes smaller in the range of C2-C5 and the vortex pair interacts with each other and dissipates at the transition position. The lateral expansion and laidback structure cause the velocity decrease which stabilizes the flow field. The streamline direction is from the middle top to bottom and two sides, which implies the coolant in the expansion diffuses to the side walls. And the axial vorticity is distributed chaotically in the center of the cross section.

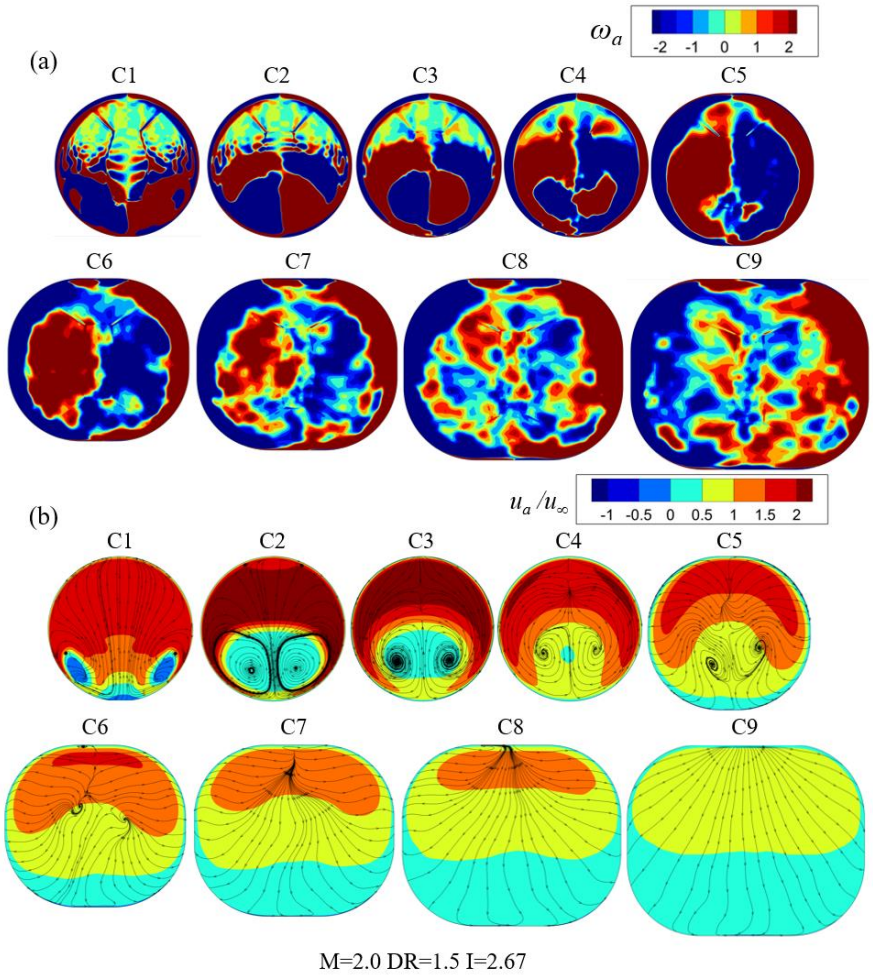

Fig. 4.39 Cross-sectional distributions in tube axial direction (a) time-averaged axial vorticity ω_a (b) time-averaged u_a/u_∞ and streamlines at M=2.0 Tu=0.5%

Fig. 4.41-Fig. 4.44 illustrate the time-average T_{RMS} and streamlines along streamwise direction at different blowing ratios, which penetrate the relationship between the RMS of the temperature fluctuation and the flow field with the effects of the blowing ratio. The streamwise direction (x direction) points to the contours perpendicularly. Compared with the four different blowing ratios, the streamlines and the T_{RMS} at M=0.5 are distinctly different from the others. Because of the lower blowing ratio and lower momentum flux ratio, the coolant at M=0.5 has already penetrated deep into the mainstream since x/D=15, and the penetration consumes most of the coolant from x/D=0 to x/D=15, which explains the reason why the cooling effectiveness at M=0.5 is much lower than the other cases with higher blowing ratios in Fig. 4.28.

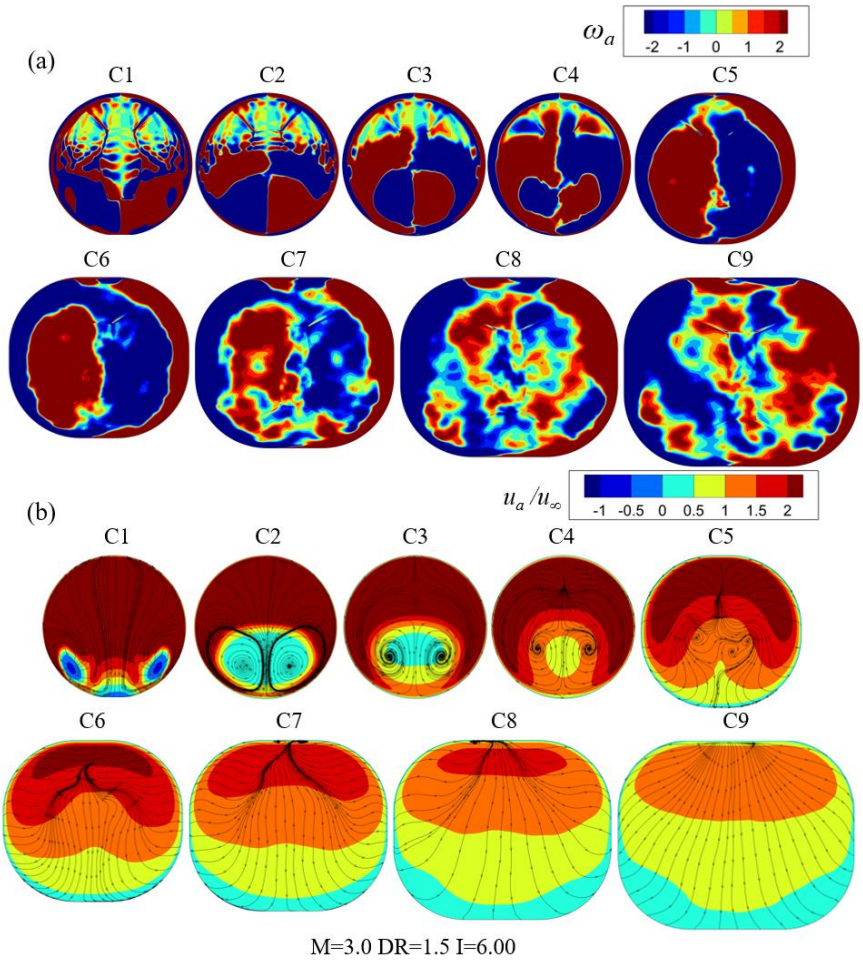

Fig. 4.40 Cross-sectional distributions in tube axial direction (a) time-averaged axial vorticity ω_a (b) time-averaged u_a/u_∞ and streamlines at M=3.0 Tu=0.5%

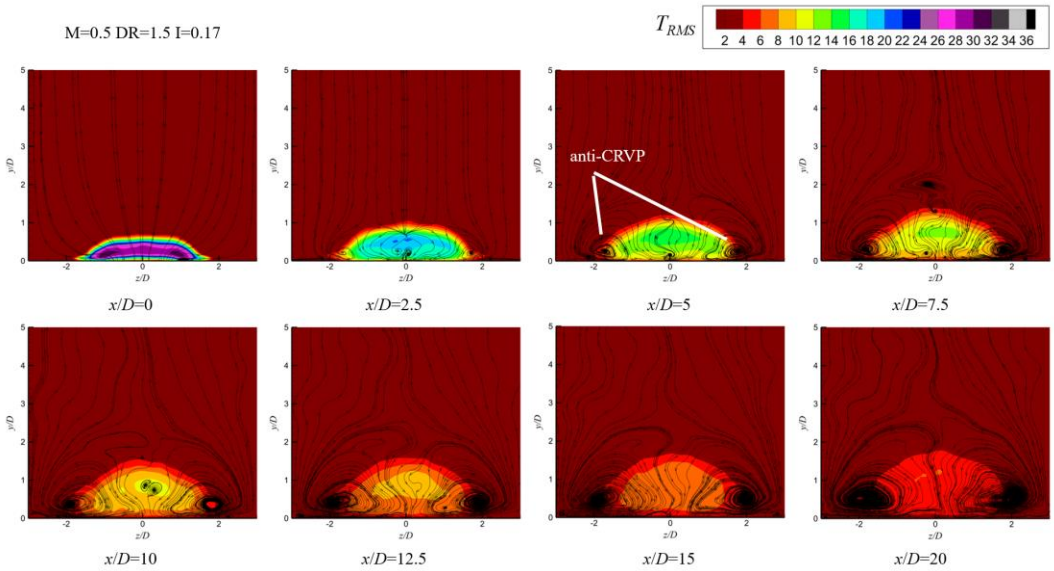

Fig. 4.41 T_{RMS} distributions and streamlines along streamwise direction at M=0.5 DR=1.5 Tu=0.5%

In addition, the counter-rotating vortex pair (CRVP) cannot form as marked as the cases with the high blowing ratio conditions, note that only some tiny vortices occur at z/D=0, y/D=0.5 and x/D=2.5, while bold streamlines show a counter-rotating vortex pair generates at the same position as the blowing ratio increases over 0.5. Bunker [58] pointed out that the formation of this type of counter-rotating vortices results from the interaction of the coolant with the mainstream. And the vortices tend to draw the mainstream to the bottom surface, which can reduce the cooling effectiveness seriously. For blowing ratio of 0.5, though the CRVP doesn't form near the centerline in streamwise direction, an anti-CRVP occurs at two corners of the high temperature fluctuation region near the side of the channel since x/D=5.

When the blowing ratio reaches 1.5 shown in Fig. 4.42, the small CRVP initially generates at the edge of the coolant close to the bottom surface, then the CRVP grows into two large scale main vortices in the center of the low temperature coolant jet until x/D=10. After that the CRVP starts to diminish and almost disappears at x/D=15. On the other hand, the anti-CRVP generates on both sides of the CRVP with the opposite rotating directions to the CRVP at x/D=5. According to Haven [144], the anti-CRVP is also known as the anti-kidney vortex pair, and it can reduce the undesirable effects of the CRVP, because the anti-CRVP mitigates the coolant detachment and enhances the spreading of the coolant on the bottom surface, which delays the high temperature mainstream into the coolant jet [145].

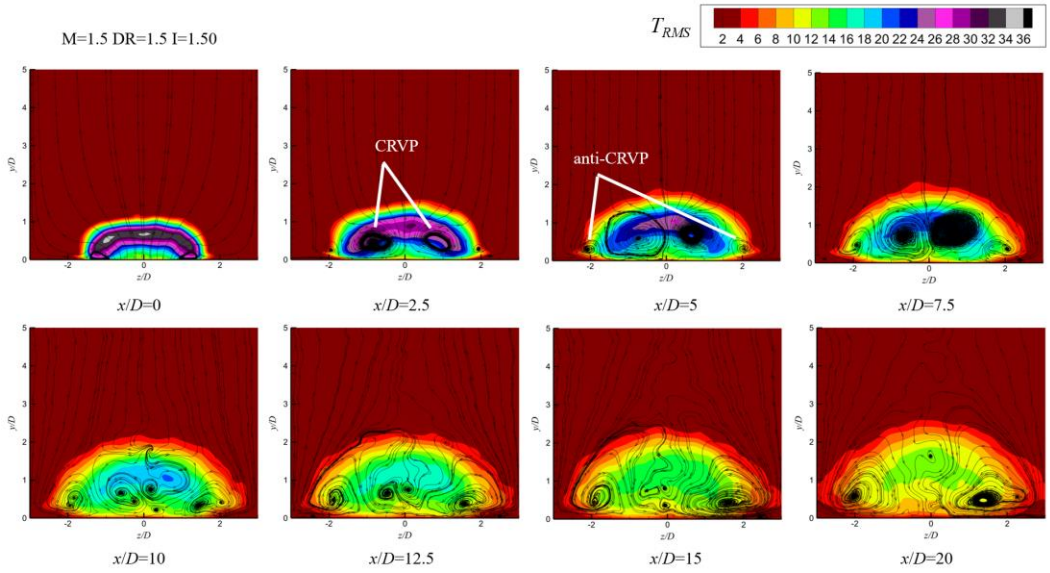

Fig. 4.42 T_{RMS} distributions and streamlines along streamwise direction at M=1.5 DR=1.5 Tu=0.5%

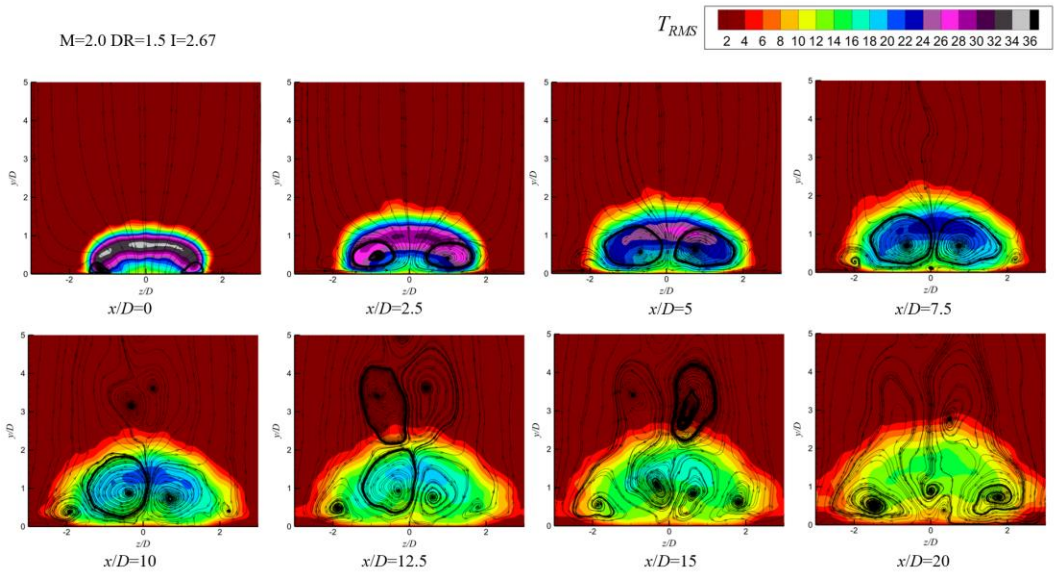

Fig. 4.43 T_{RMS} distributions and streamlines along streamwise direction at M=2.0 DR=1.5 Tu=0.5%

For M=2.0 and 3.0 in Fig. 4.43 and Fig. 4.44, there are subtle differences between the development of the coolant at the beginning. Both cases have high momentum in the coolant, hence, the coolant is detached from the bottom surface when it is injected into the mainstream channel. As can be seen at x/D=0, the CRVP is formed obviously at two sides of the coolant. Along the cooling passage, the coolant can be preserved longer than the low blowing ratio cases from the ingestion of the mainstream. However, the high blowing ratio doesn't contribute much to the improvement of cooling effectiveness, because for M=2.0 the large scale and strong CRVP is formed and leads to the separation of the coolant from the bottom surface, even though the anti-CRVP tries to restrain the detachment of the coolant.

When the blowing ratio goes as high as M=3.0, the anti-CRVP cannot generate on the side of the CRVP, which means without the help of the anti-CRVP, more high temperature mainstream is sucked through the two sides of the CRVP near the bottom wall and deteriorates the cooling effectiveness to some extent. Additionally, a pair of vortices is formed at x/D=10 above the CRVP with the opposite rotating direction at M=2.0 and 3.0.

Corresponding to the T_{RMS} distributions at different cross sections shown in Fig. 4.41-Fig. 4.44, Fig. 4.45 depicts the root mean square of the temperature fluctuation at the bottom surface at different blowing ratios conditions. For low blowing ratio of M=0.5, high

temperature fluctuation region is mainly found around the film hole exits and the near downstream areas. And the temperature fluctuation declines dramatically and vanishes at x/D=20 approximately, indicating that the coolant has been ingested by the mainstream.

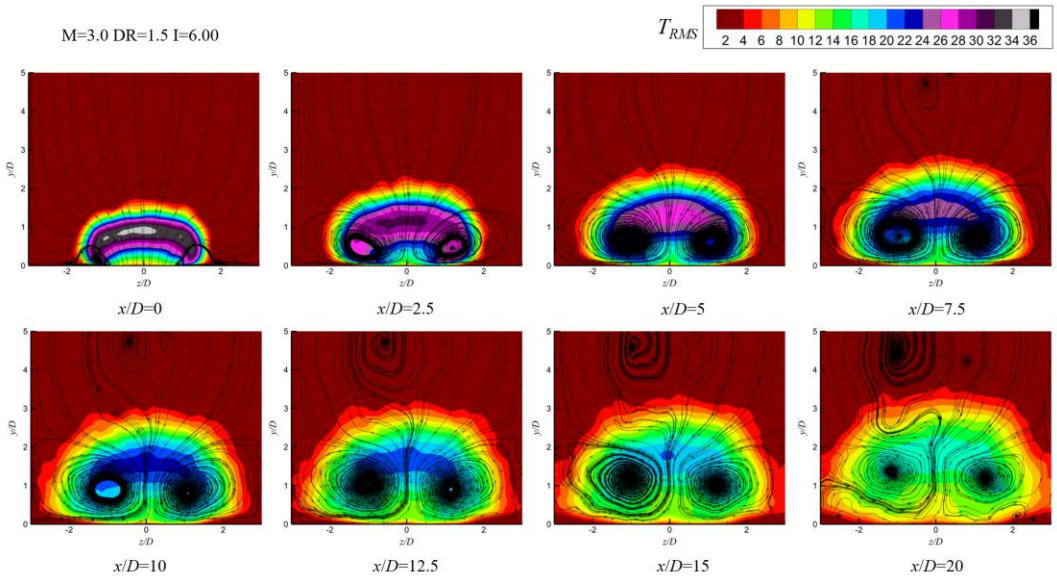

Fig. 4.44 T_{RMS} distributions and streamlines along streamwise direction at M=3.0 DR=1.5 Tu=0.5%

With respect to higher blowing ratios M=1.0-3.0, the significant difference is that the two stripes of high T_{RMS} occur downstream of the film hole. When the momentum of the coolant jet increases with the blowing ratio, the high T_{RMS} stripes can sustain further downstream. However, the lateral T_{RMS} distributions of the bottom surface becomes smaller and narrower at higher blowing ratios, especially the trailing edge region of the film hole at M=3.0, compared with M=1.0-2.0. The reason is that at M=3.0, the CRVP dominates the cooling channel, and the anti-CRVP doesn't generate, which means more high temperature mainstream draws into the bottom. Besides, the core region of the coolant is lifted from the bottom surface and the mainstream penetrates deeper beneath the coolant.

Fig. 4.46 presents the centerline and the lateral averaged T_{RMS} distributions at bottom surface along the streamwise direction with different blowing ratios. When the blowing ratio increases from 0.5 to 1.5, the lateral averaged T_{RMS} grows at the same position downstream. Besides, the lateral averaged temperature fluctuation at M=0.5 drops with a rapid decline rate from x/D=0-10, compared with the other cases, and the decline rate begins to slow from x/D=15 to x/D=40.

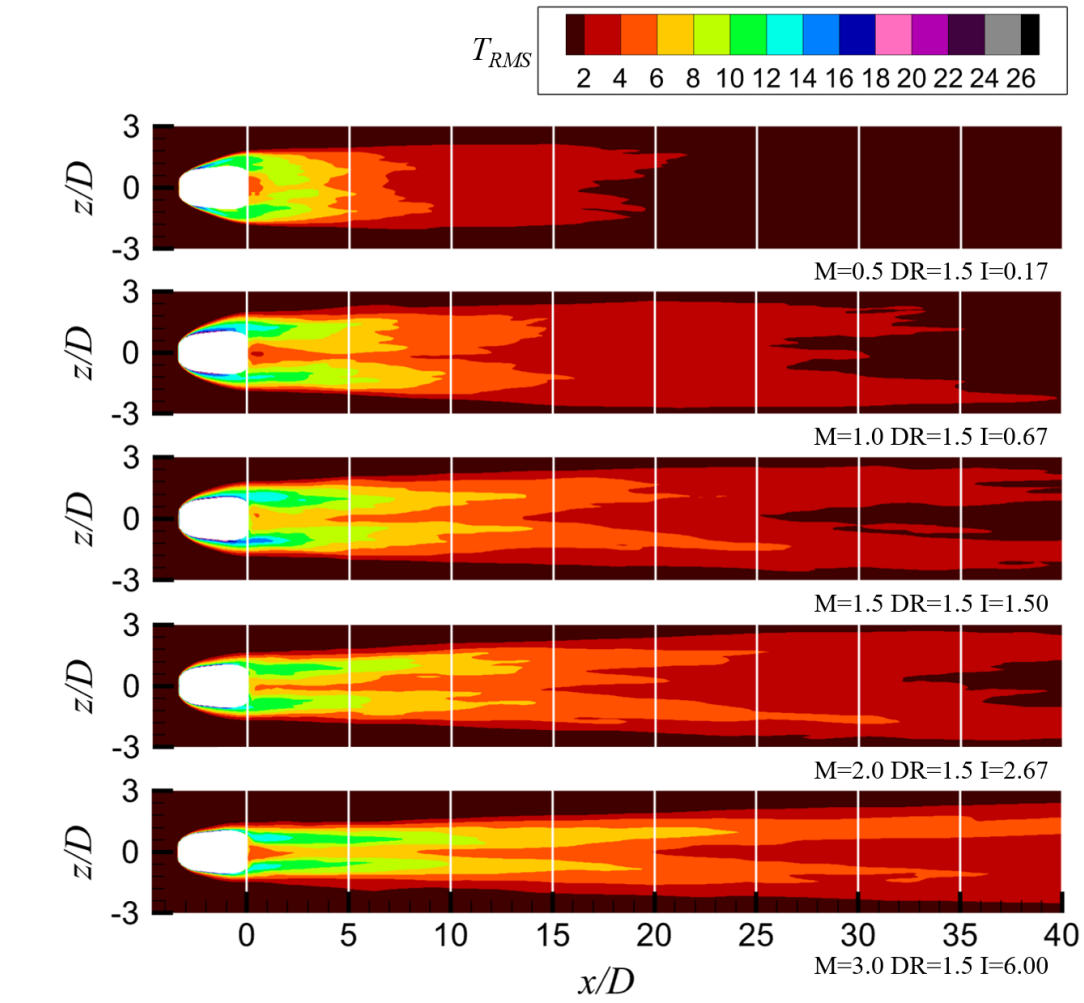

Fig. 4.45 T_{RMS} distributions of the bottom surface with various blowing ratios at DR=1.5 Tu=0.5%

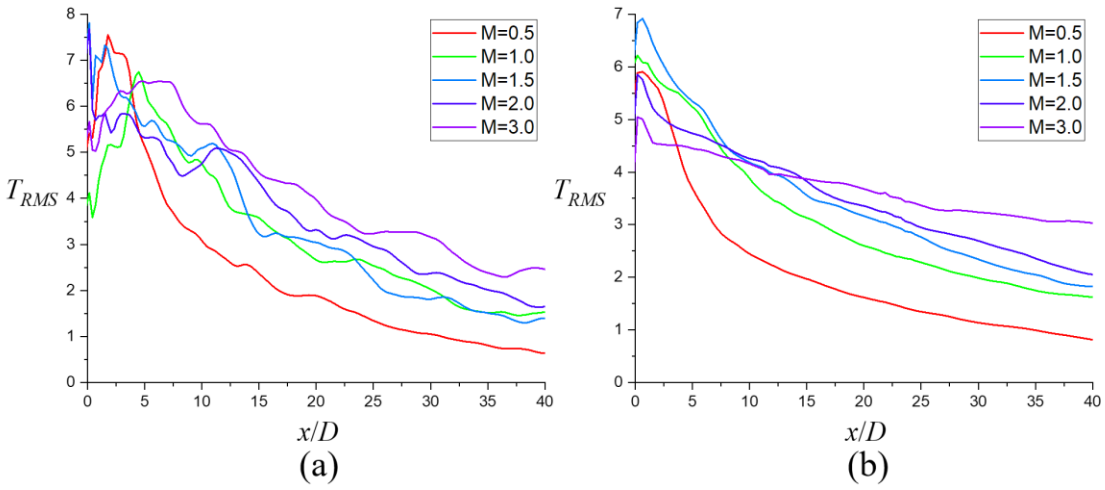

Fig. 4.46 T_{RMS} distributions at bottom surface at DR=1.5 Tu=0.5% (a) along the centerline (b) lateral-averaged

As for M=2.0 and 3.0, the temperature fluctuation becomes more violent at further downstream regions. As shown in Fig. 4.46, the temperature fluctuates more widely along the centerline with the increase of the blowing ratio. It can be inferred that strong separation occurs in the coolant jet. Note that there is a relatively lower T_{RMS} region just behind the trailing edge of the film cooling hole at higher blowing ratio, where the coolant is steady and rarely affected by the CRVP.

Hunt [146] proposed a method called Q-criterion in 1988. Q-criterion identifies vortices in the flow field, because the region with vortices usually satisfies that second invariant of $\nabla\vec{u}$ is positive. Q is defined as:

$$\mathrm{Q} = \frac{1}{2}\left[(\nabla \cdot \vec{u})^2 - \left(\|\mathrm{S}\|^2 - \|\Omega\|^2\right)\right] \tag{1.46}$$

where the symmetric component S and the anti-symmetric component Ω are defined as follows:

$$\begin{aligned} \mathrm{S} &= \frac{1}{2}\left(\nabla\vec{u} + (\nabla\vec{u})^T\right) \\ \Omega &= \frac{1}{2}\left(\nabla\vec{u} - (\nabla\vec{u})^T\right) \end{aligned} \tag{1.47}$$

For impressible flow, the gradient of the velocity is equal to zero, so equation 1.46 can be rewritten as:

$$\mathrm{Q} = \frac{1}{2}\left(\|\Omega\|^2 - \|\mathrm{S}\|^2\right) \tag{1.48}$$

Fig. 4.47 presents time-averaged streamwise vorticity ω_x distributions and Q-criterion iso-surface. The iso-value of Q equals 1 for four cases with various blowing ratios. For low blowing ratio of M=0.5, small scale horseshoe vortices are formed on the edge of the leading edge of the film hole exit. The streamwise vorticity ω_x of the horseshoe vortices is positive in the negative-z region and negative in the positive-z region. And the horseshoe vortices extend along the two side edges of the film hole exit, where the shear vortices are also formed. Since the momentum of the injection is lower, the shear vortices cannot be remarkably observed and merge with the leading-edge horseshoe vortices. As can be

observed, the leading-edge horseshoe vortices and the side-edge shear vortices have an opposite streamwise vorticity in the positive and negative-z regions. Therefore, it can be inferred that the shear vortices don't contain enough energy in the low momentum coolant jet, and the relatively more intense horseshoe vortices weaken the shear vortices, which is the reason why the CRVP doesn't appear and generate from the shear vortices at lower momentum case.

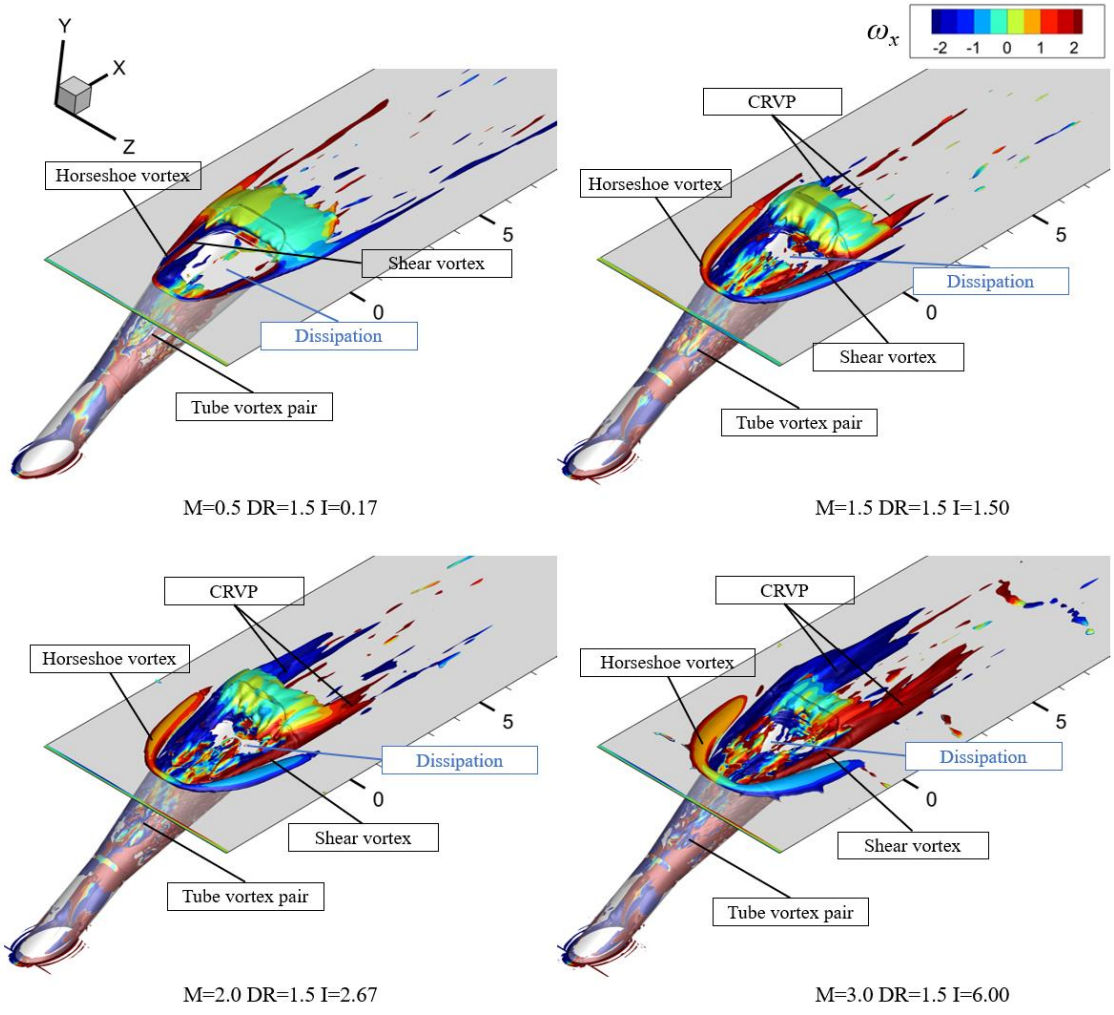

Fig. 4.47 Time-averaged streamwise vorticity ω_x distributions and Q-criterion iso-surface with various blowing ratios at DR=1.5 Tu=0.5%

There is a pair of vortices generated in the film hole tube, however, this pair of vortices dissipates at near exit region and the CRVP can hardly form downstream of the film hole exit, which can also be demonstrated from Fig. 4.41. The mixture of horseshoe vortices

and shear vortices develops from leading edge region and converts into an anti-CRVP on two sides of the center area where the CRVP is formed in higher blowing ratio cases.

When blowing ratio reaches 1.5, the leading-edge horseshoe vortices are enhanced, compared with M=0.5. The horseshoe vortices in positive and negative-z regions form a larger angle between each other, which results in a larger distance between the leading-edge horseshoe vortices and the side-edge shear vortices. Therefore, the negative ω_x horseshoe vortices and positive shear ω_x vortices don't yield much interaction with each other. And the CRVP generates from the shear vortices from two side edges, and the anti-CRVP develops from the outside of the horseshoe vortices. Note that the pair of vortices from the film hole tube dissipates at the center exit area with a lower dissipation rate relative to M=0.5, while still maintains in near side edge areas. Hence, higher momentum coolant jet tends to form CRVP downstream of the shaped film hole.

When M=2.0 and M=3.0, the horseshoe vortices continue to be more intense and distance between the horseshoe vortices and the shear vortices increases along the streamwise direction. The vortex pair in the tube only dissipates at the film hole exit small region, and the tube vortex pair is stronger than the low blowing ratio cases. The shear vortices are larger and stronger along the two side edges than the horseshoe vortices. Thus, the outside horseshoe vortices exert less effects on the shear vortices. Far downstream of the channel, the CRVP develops from the intense shear vortices and can be found obviously at the near field downstream.

The main difference between M=2.0 and M=3.0 lies in the further downstream region. At M=3.0 the high momentum of the coolant causes the shear vortices to be stronger and the CRVP dominates the channel rapidly. The horseshoe vortices dissipate downstream and anti-CRVP cannot be generated, but a pair of vortices occurs above the CRVP due to the strong disturbance of the CRVP to the flow field.

Fig. 4.48 and Fig. 4.49 illustrate the side view and top view of film cooling channel with instantaneous Q-criterion iso-surface at DR=1.5 Tu=0.5%. The Q value is set to 1 for cases with various blowing ratios. The harpin vortices develop from small scale size to large scale size along the streamwise direction. For low blowing ratios of M=0.5-1.0, the hairpin vortices are pressed very close to the bottom surface by the mainstream. The core

region of the injection is flatter shown in Fig. 4.41 and Fig. 4.42, compared with the high blowing ratio cases at the same location in Fig. 4.43 and Fig. 4.44. From the top view, the hairpin vortices spread and cover the cooling passage laterally since x/D=10 and x/D=5 roughly for M=0.5 and M=1.0 respectively which occurs at near field compared with high blowing ratio cases. It is also found that the vortices from the coolant dissipate quickly according to the T_{RMS} distributions. The dissipation is enhanced by the interaction between the coolant and the mainstream. Moreover, the vortices in the film hole tube begin to be generated in the rear position of cylindrical section of the shaped film hole at low blowing ratio. With the growth of the blowing ratios, the vortices in the tube are formed at the entrance of the film hole earlier.

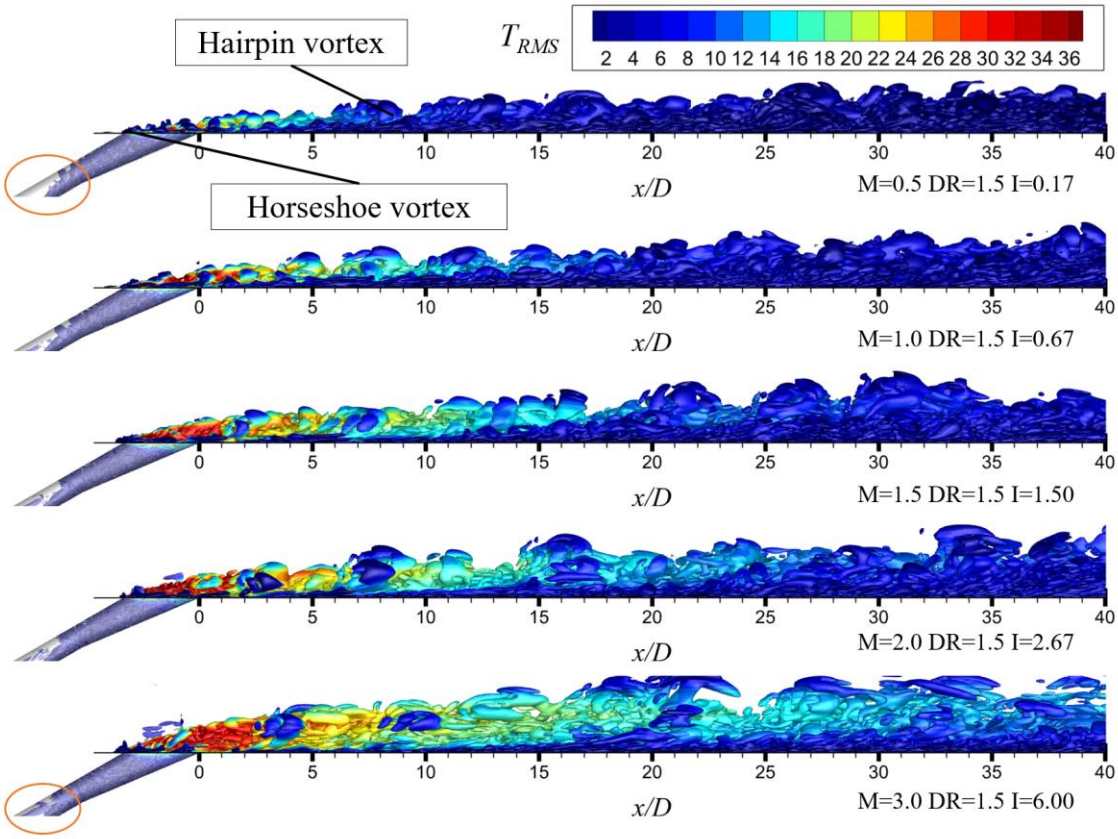

Fig. 4.48 Side view of film cooling channel with instantaneous Q-criterion iso-surface and T_{RMS} distributions at DR=1.5 Tu=0.5%

When blowing ratio increases, larger scale horseshoe vortices can be seen at the leading edge from the top view in Fig. 4.49, and the horseshoe vortices become discontinuous at M=2.0 and M=3.0. Note that for M=3.0 the horseshoe vortices dissipate and disappear at

near field, corresponding to the absence of the anti-CRVP downstream. And the lateral spread of the coolant is inadequate because the high momentum coolant jet leads to the lift of the injection in wall-normal direction. The top view manifests the location of the jet and mainstream interaction. As the blowing ratio increases, the coverage of the coolant is narrower in spanwise direction and longer in streamwise direction. In addition, the Kelvin-Helmholtz vortices are generated at the interface of the coolant and the mainstream, which are caused by the Kelvin-Helmholtz instabilities. The velocity of the jet differs from the mainstream, thus, there is a velocity shear near the interface.

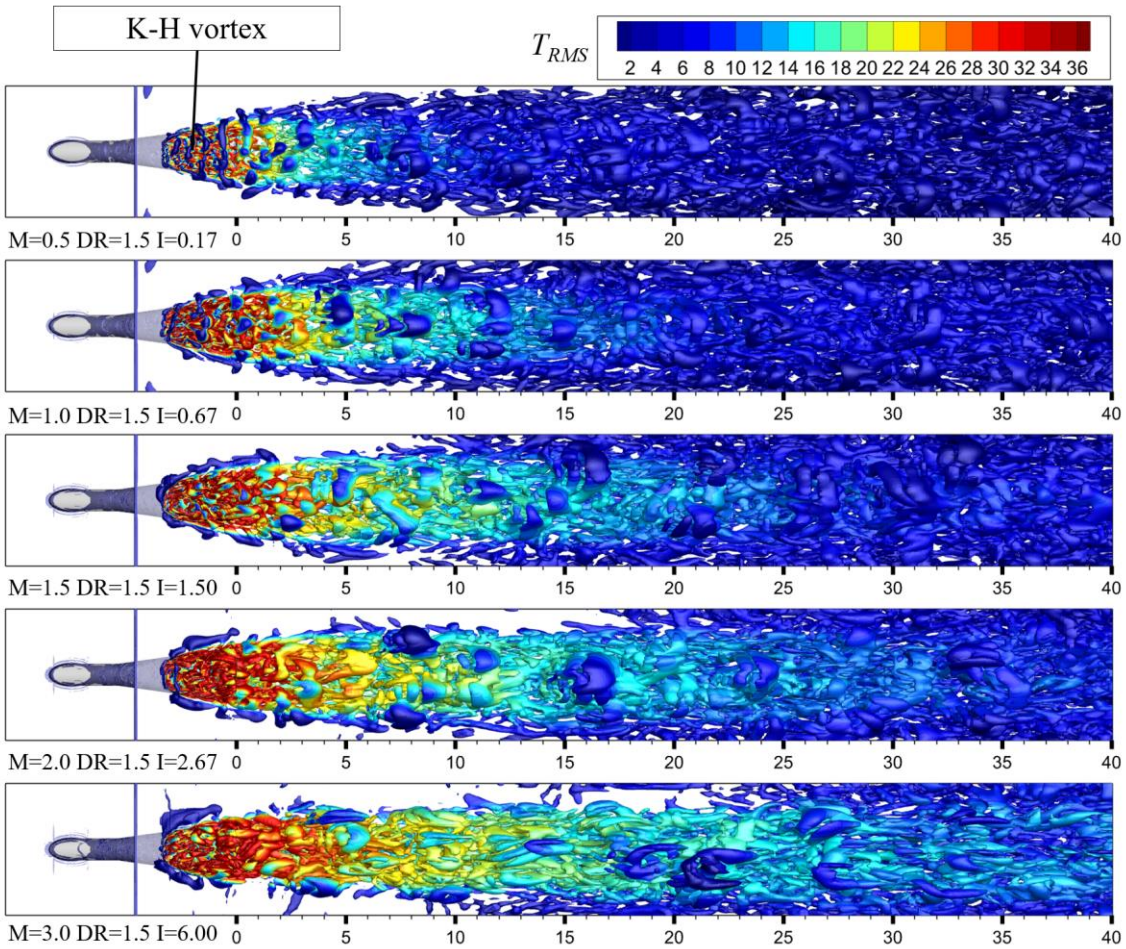

Fig. 4.49 Top view of film cooling channel with instantaneous Q-criterion iso-surface and T_{RMS} distributions at DR=1.5 Tu=0.5%

Fig. 4.50 presents the time-averaged Reynolds shear stresses in three directions at M=1.5. -*u*'*v*', -*v*'*w*' and -*u*'*w*' denote the different components of the Reynolds shear stress. In order to present the details of the distributions, the scale is adjusted for each contour.

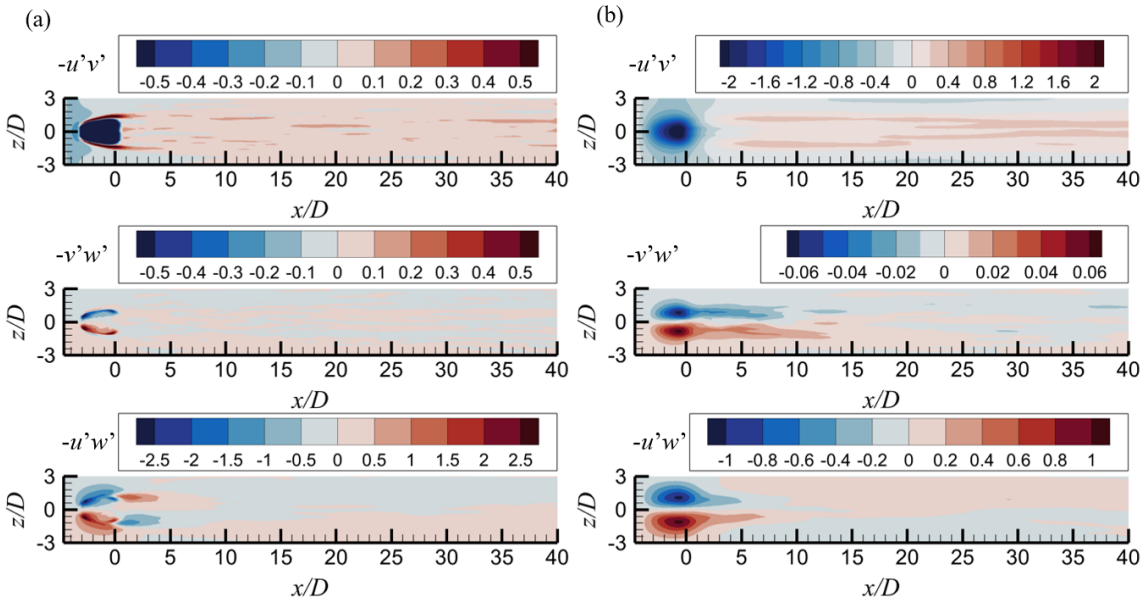

Fig. 4.50 Time-averaged -*u*'*v*', -*v*'*w*' and -*u*'*w*' Reynolds shear stresses at M=1.5 DR=1.5 Tu=0.5% (a) *y*/*D*=0.1 (b) *y*/*D*=1

For the plane of *y*/*D*=0.1 which is very close to the bottom wall, the -*u*'*v*' Reynolds shear stress is more concentrated in the two side edges area of the film hole exit, where the shear vortices are generated. And the negative -*u*'*v*' value consists in the location of the film hole exit. The -*u*'*v*' is reduced along the streamwise direction, and some stripe areas still contain higher shear stress. At *y*/*D*=1 shown in Fig. 4.50b, the negative -*u*'*v*' Reynolds shear stress is diffused centered in the film hole exit position. Two main high value shear stress stripes occur from *x*/*D*=5-40. Corresponding to Fig. 4.52, the negative -*u*'*v*' Reynolds shear stress reaches the maximum when the coolant is injected into the coolant channel. The -*u*'*v*' begins to decay in the wall-normal direction. Note that there are two positive -*u*'*v*' stress areas at two sides of the exit of film hole, where the anti-CRVP is formed. For the Reynolds shear stresses -*v*'*w*', it is enhanced due to the coolant jet with the inclined angle to the mainstream. -*v*'*w*' is positive in -z region near the side of the film hole exit and negative in +z region.

In Fig. 4.51, -*u*'*v*', -*v*'*w*' and -*u*'*w*' Reynolds shear tensor components are illustrated at *x*/*D*=-3.5 upstream of the film hole. a high value area of -*u*'*v*' shear stress is shown in the center near the bottom wall. -*v*'*w*' and -*u*'*w*' Reynolds shear components is symmetric with respect to the center cross section plane.

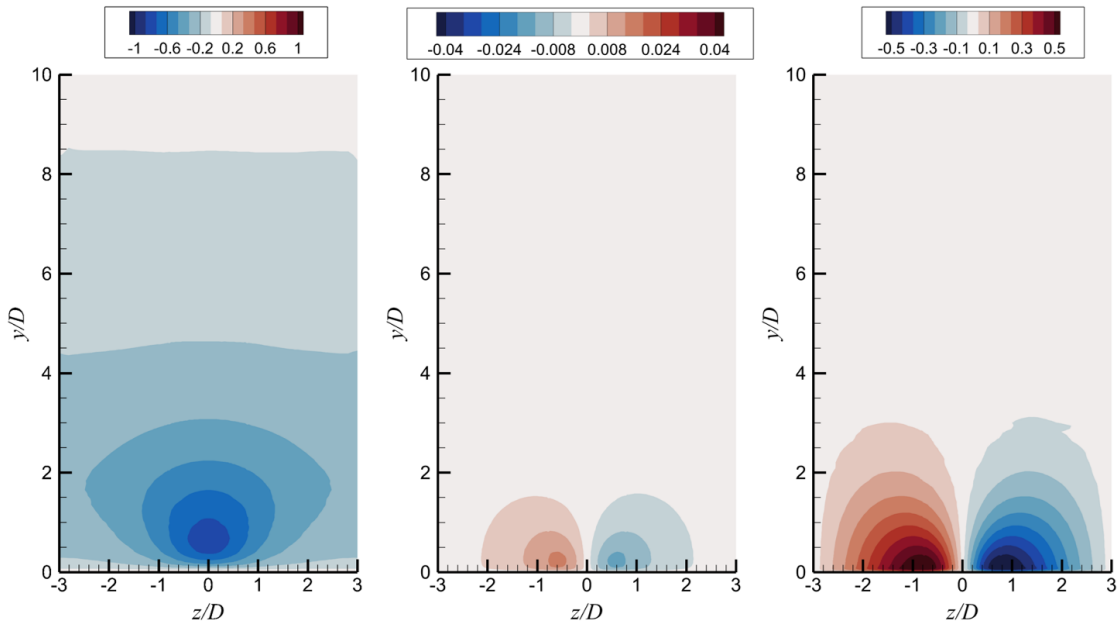

Fig. 4.51 Cross sections of time-averaged -*u*'*v*', -*v*'*w*' and -*u*'*w*' Reynolds shear stresses at *x*/*D*=-3.5 M=1.5 DR=1.5 Tu=0.5%

Fig. 4.52 shows the wall normal cross sections downstream of the film hole at *x*/*D*=0. As the distance to the bottom wall increases from *y*/*D*=0.1 to *y*/*D*=1, the -*v*'*w*' shear stress decreases but spreads around the injection illustrated Fig. 4.52b. For the -*u*'*w*' Reynolds shear stress, the distribution shows an intimate connection between the -*u*'*w*' value and the CRVP location. Because the CRVP is generated downstream of the film hole exit, the value of -*u*'*w*' is distributed inversely in the cross section of *x*/*D*=0 and symmetric about the *z*/*D*=0. The -*u*'*w*' Reynolds shear stress is also symmetric with respect to the centerline from the top view at *y*/*D*=0.1 and *y*/*D*=1. Near the bottom surface at *y*/*D*=0.1, because of the inverse rotating direction of the shear vortices and the CRVP, the -*u*'*w*' value is opposite for -z and +z regions.

Film cooling contains the process of the mix between the injection and the mainstream, which shows strong anisotropic characteristics in flow field. However, for RANS simulation method, the Boussinesq eddy viscosity assumption is used to calculate the turbulent viscosity μ_t. Therefore, the turbulence model based on the isotropic eddy viscosity causes the unrealistic or even unphysical results. The errors or discrepancies are much

glaring in terms of the film cooling issue. This is the reason why RANS presents large differences with the experimental data, compared with LES shown in Fig. 4.12.

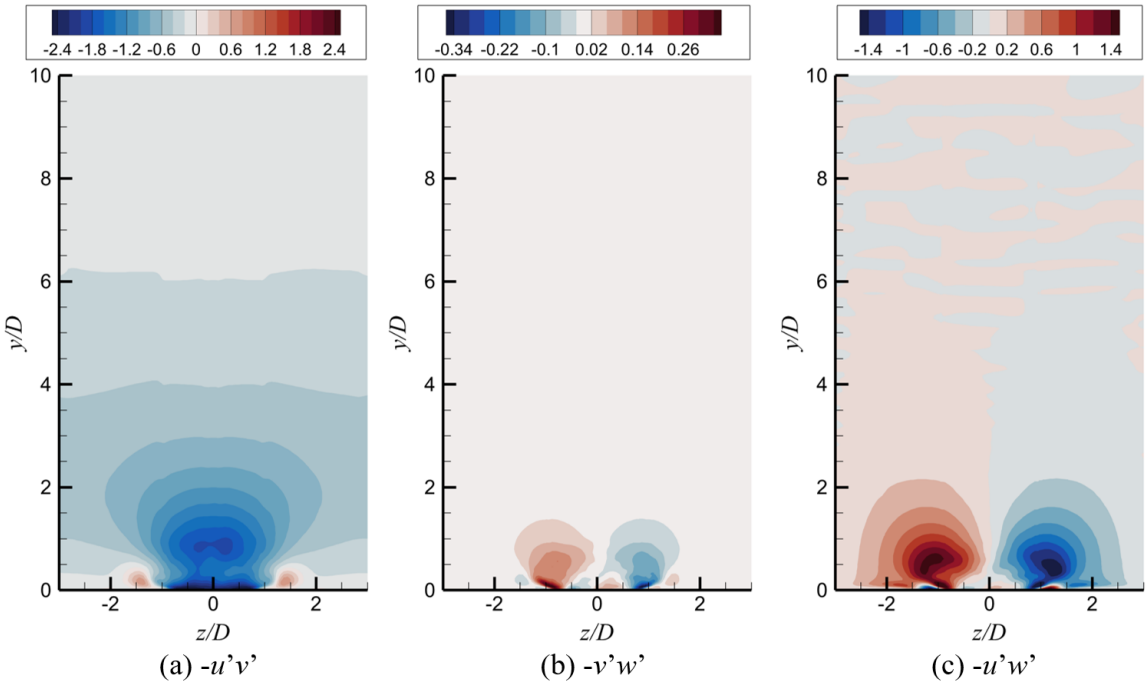

Fig. 4.52 Cross sections of time-averaged -*u*'*v*', -*v*'*w*' and -*u*'*w*' Reynolds shear stresses at *x*/*D*=0 M=1.5 DR=1.5 Tu=0.5%

For LES, it can resolve over 80% large scale eddies directly by the N-S equation depending on the refined mesh, which means higher accuracy of the results can be obtained without the eddy viscosity turbulence model. Though the rest 20% small-size vortices are modeled by the subgrid models in LES, the prediction of LES is still much closer to the experimental data, compared with the RANS methods. In Fluent, the variables at each time step can be sampled during the simulation, such as the filtered velocity $\widetilde{u}_i$. Referring to the approach for calculating the anisotropic eddy viscosity used in the LES [147], the turbulent viscosity in spanwise and wall-normal directions can be derived as follows by time averaging u_iu_j firstly.

$$\begin{aligned}\overline{u_i u_j} &= \overline{(\bar{u}_i + u_i')(\bar{u}_j + u_j')} \\ &= \overline{\bar{u}_i \bar{u}_j + \bar{u}_i u_j' + \bar{u}_j u_i' + u_i' u_j'} \\ &= \bar{u}_i \bar{u}_j + \overline{u_i' u_j'}\end{aligned} \tag{1.49}$$

Therefore, the Reynolds stress can be written as:

$$\overline{u_i' u_j'} = \overline{u_i u_j} - \bar{u}_i \bar{u}_j \tag{1.50}$$

To determine the Reynolds stress $\overline{u_i' u_j'}$, the sampling instantaneous variables u_i and u_j can be averaged to calculate $\overline{u_i u_j}$ and $\bar{u}_i \bar{u}_j$. Thus, the Reynolds stress can be rearranged as:

$$\overline{u_i' u_j'} = \frac{\sum_{t=0}^{t} u_i u_j dt}{\sum_{t=0}^{t} dt} - \frac{\sum_{t=0}^{t} u_i dt \sum_{t=0}^{t} u_j dt}{\left(\sum_{t=0}^{t} dt\right)^2} \tag{1.51}$$

The turbulent viscosities in wall-normal and spanwise directions are defined as the following equations:

$$\begin{aligned} -\overline{u'v'} &= \nu_{t\_y}\left(\frac{\partial \bar{u}}{\partial y} + \frac{\partial \bar{v}}{\partial x}\right) \\ -\overline{u'w'} &= \nu_{t\_z}\left(\frac{\partial \bar{u}}{\partial z} + \frac{\partial \bar{w}}{\partial x}\right) \end{aligned} \tag{1.52}$$

where υ_{t_y} and υ_{t_z} represent the wall-normal and spanwise turbulent viscosities respectively. $\left(\frac{\partial \bar{u}}{\partial y} + \frac{\partial \bar{v}}{\partial x}\right)$ and $\left(\frac{\partial \bar{u}}{\partial z} + \frac{\partial \bar{w}}{\partial x}\right)$ are the strain rate.

The ratio of the spanwise to the wall-normal turbulent viscosity $\upsilon_{t\_z}/\upsilon_{t\_y}$ is also applied to measure the anisotropy in film cooling.

Fig. 4.53 illustrates the turbulent viscosity in spanwise and wall-normal directions at M=1.5. According to the comparison between the υ_{t_y} and υ_{t_z} contours, it's clearly seen that the distinct differences of the turbulent viscosity in *z* and *y* directions, note that the scale of υ_{t_y} is 20 times as high as the υ_{t_z}. The υ_{t_y} at *y*/*D*=1 increases from *x*/*D*=5 to *x*/*D*=40 relative to *y*/*D*=0.1. The υ_{t_z} at *y*/*D*=1 grows in the negative-*x* regions. The viscosity in spanwise direction is much higher at *x*/*D*=0 and *z*/*D*=±3 where the horseshoe vortex generates. The υ_{t_z} is negative when *x*/*D* is negative, and υ_{t_z} is positive in the region of *x*/*D*>0 except the area in the vicinity of the centerline downstream of the channel.

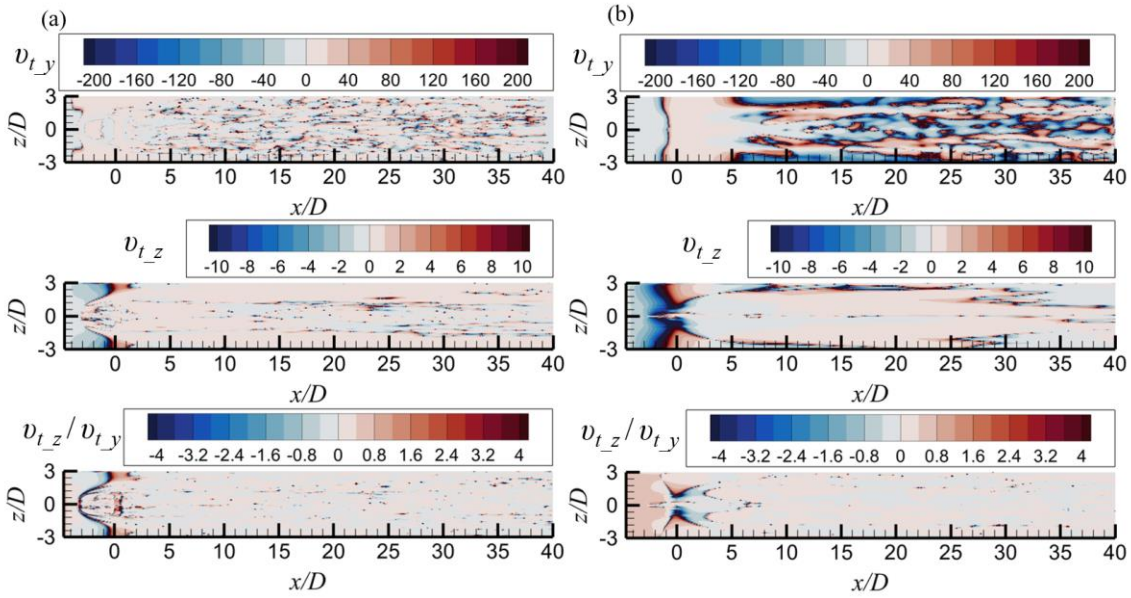

Fig. 4.53 Time-averaged turbulence viscosity in wall-normal (top row) and spanwise (middle row) directions and the ratio of υ_{t_y} to υ_{t_z} (bottom row) at M=1.5 DR=1.5 Tu=0.5% (a) y/D=0.1 (b) y/D=1

The ratio $\upsilon_{t\_z}/\upsilon_{t\_y}$ implies the anisotropy in turbulent viscosity for film cooling. The strong anisotropy occurs in the film hole exit regions where the mainstream and the coolant interact with each other intensively. Thus, for RANS simulation the Reynolds stress in three-dimensional complex flow with strong mixing cannot be simulated accurately enough from the mean rate of strain, especially the high ratio $\upsilon_{t\_z}/\upsilon_{t\_y}$ areas. For LES, the anisotropy in Reynolds stresses of three directions can be physically predicted.

4.4.3 Effects of inlet turbulence intensity on shaped film hole

Polanka [148] studied a turbine vane with film cooling holes and generated a 18% turbulence level at the leading edge of the airfoil. Thole et al. [149] innovated a new turbulence generator to provide high freestream turbulence intensity as high as 20%. The main idea is to inject the high velocity gas vertically into the mainstream crossflow, which overcomes the limitation turbulence intensity level generated by the grid arrays. Therefore, according to previous public research, three different turbulence intensity values can be considered as low, moderate and high, namely Tu=0.5%, Tu=10% and Tu=20% respectively.

Fig. 4.54 and Fig. 4.55 present the time-averaged adiabatic effectiveness on bottom surface at M=1.5 and 2.0 with the effects of various turbulence intensity values. The

mainstream inlet velocity profile is the same as the previous calculation. With the increase of the mainstream inlet turbulence intensity, the film cooling effectiveness decreases along the streamwise direction for both blowing ratios. The high turbulence intensity gives undesirable effects on the coverage of the coolant on the bottom surface downstream. As

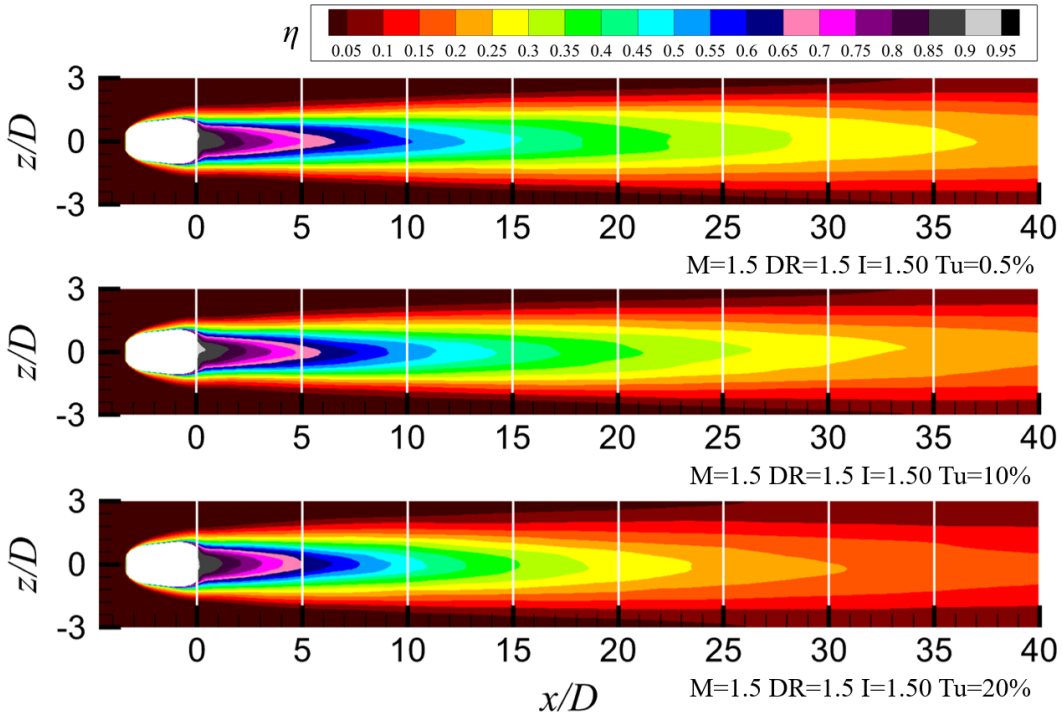

Fig. 4.54 Contours of time-averaged adiabatic effectiveness contours of the bottom surface with various turbulence intensity at M=1.5 DR=1.5

shown in the contours, the spreading of the coolant jet core region, where η is larger than 0.7, is reduced to about x/D=5 in streamwise direction at two blowing ratios of 1.5 and 2.0 as the turbulence intensity increases, which also indicates that the mixing process between the coolant jet and mainstream becomes stronger and the coolant is absorbed by the mainstream in the near downstream of the trailing edge of the film hole.

In Fig. 4.56, the effects of three different levels are shown on the centerline adiabatic film cooling effectiveness distributions of the bottom surface along the streamwise direction. As can be seen, both blowing ratios show the same downward trend with the increase of the downstream distance. Note that as the mainstream inlet turbulence intensity increases, the effects on the centerline adiabatic film cooling effectiveness become more obvious, and the difference between the moderate and high turbulence intensities is greater

than that of the low and moderate turbulence intensities in the further downstream areas (x/D=10-40). Note that this distinguish is clearer for the case of M=1.5, which could be deduced that low blowing ratio cases of M=1.5 is more sensitive to the high freestream turbulence intensity.

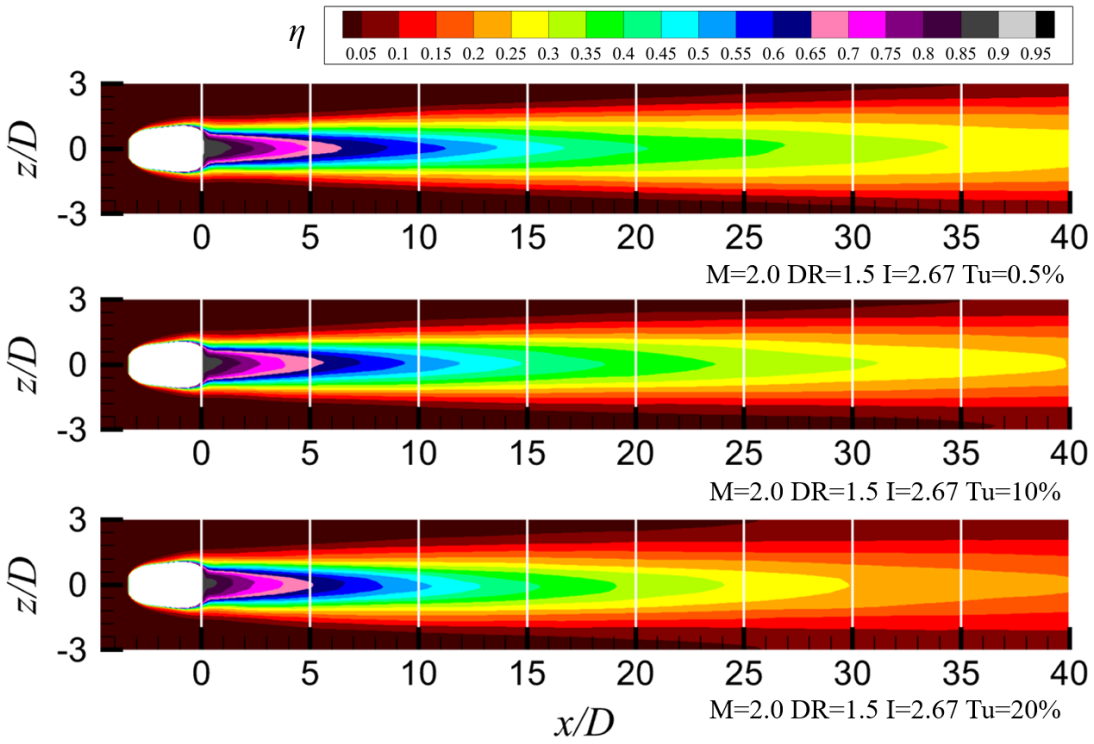

Fig. 4.55 Contours of time-averaged adiabatic effectiveness contours of the bottom surface with various turbulence intensity at M=2.0 DR=1.5

Fig. 4.57 presents the lateral-averaged adiabatic film cooling effectiveness distributions at different turbulence intensity levels. For blowing ratio of 1.5, the film cooling effectiveness is compound by the increase of the turbulence intensity. Note that when Tu reaches 20%, the deterioration occurs and gradually increases since x/D=10 approximately. There is negligible impact of the high turbulence intensity on the lateral-averaged film cooling effectiveness in the range of x/D=0-5, which implies that the coolant spreading in the lateral direction is similar to each other near the film hole trailing edge region. However, at further downstream of the channel, the lateral averaged film cooling effectiveness of high turbulence intensity shows significant reduction at x/D=20-40, and the negative effects of the high turbulence intensity is more manifest on the lateral averaged effectiveness from Tu=10% to Tu=20% than that from Tu=0.5% to Tu=10%.

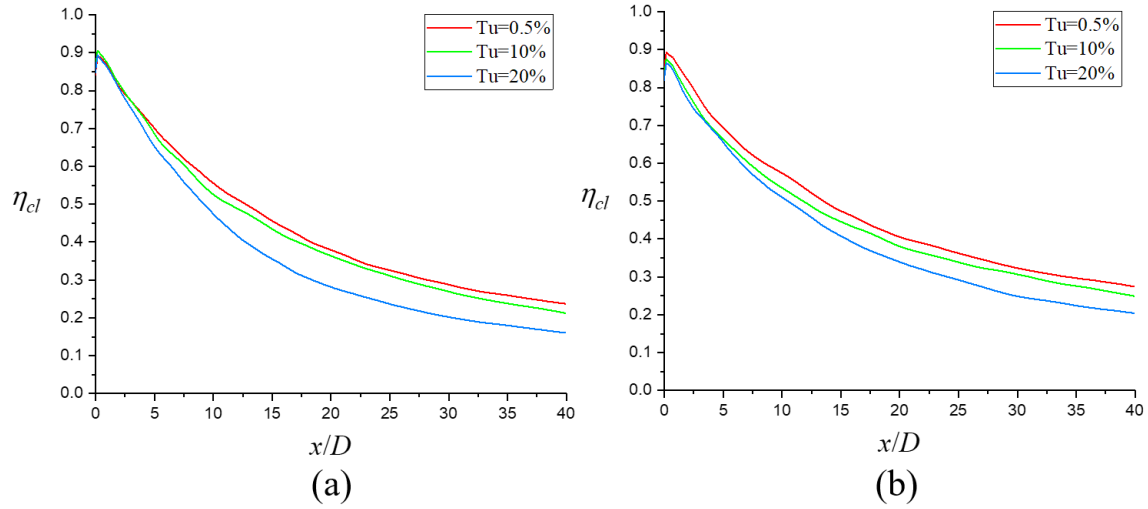

Fig. 4.56 Time-averaged centerline adiabatic film cooling effectiveness distributions (a) M=1.5 DR=1.5 (b) M=2.0 DR=1.5

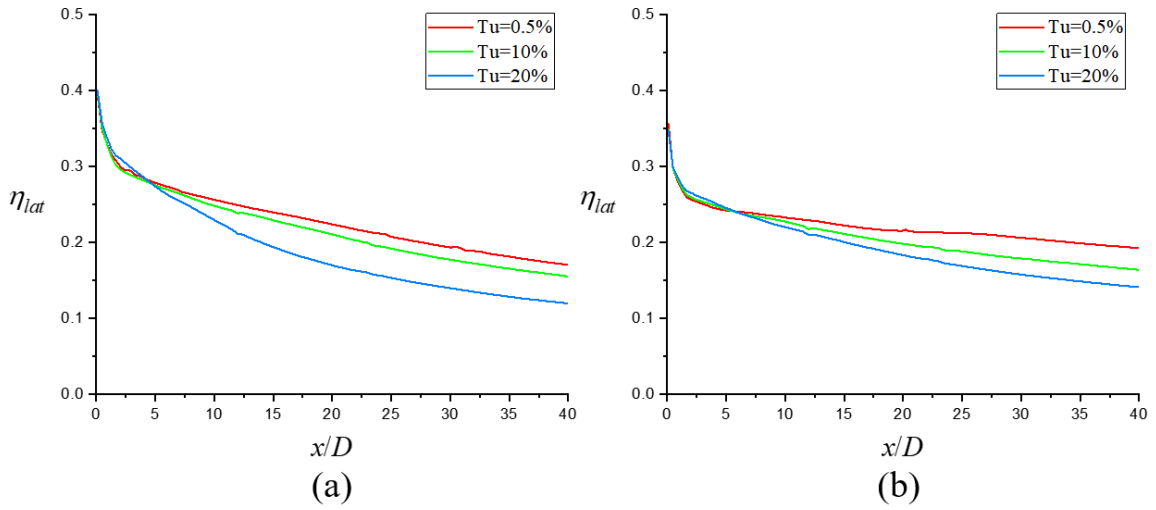

Fig. 4.57 Lateral-averaged adiabatic film cooling effectiveness distributions (a) M=1.5 DR=1.5 (b) M=2.0 DR=1.5

When the blowing ratio increases to M=2.0, there is a downward tendency for the film cooling effectiveness at Tu=10% and 20%. At low turbulence intensity 0.5%, note that a small fluctuation occurs between *x*/*D*=25-30. From *x*/*D*=20 to *x*/*D*=40, the decrease is about 7.6%-14.8% at Tu=10% and 14.6%-26.8% at Tu=20%. And the maximum drop occurs at the end of the channel *x*/*D*=40 for both blowing ratios conditions. Hence, high turbulence intensity has more undesired effects on the cooling effectiveness at further downstream of the cooling channel.

Fig. 4.58 illustrates the area-averaged adiabatic film cooling effectiveness distributions from Tu=0.5% to Tu=20% for shaped film hole. The solid line represents the area range of x/D=0-30, and the dash line denotes the region of x/D=20-40. As can be seen, the increasing mainstream inlet turbulence intensity provides more influence on the low blowing ratio case (M=1.5) relative to high blowing ratio of M=2.0. The decay rate of area-averaged adiabatic film cooling effectiveness grows as the turbulence intensity increases from 10% to 20% for the low blowing ratio case, while the high blowing ratio of M=2.0 falls much more mildly. It can be inferred that the mixing between the coolant and the mainstream is stronger for low blowing ratio conditions at high turbulence intensity, thereby, the coolant is consumed more upstream, and the further downstream of the bottom surface cannot be covered sufficiently by the coolant. Because the dash line reflects the cooling effectiveness at a further distance downstream.

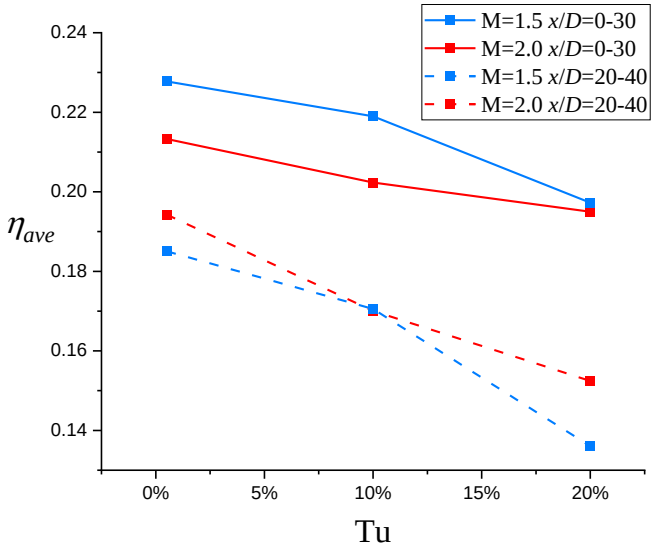

Fig. 4.58 Area-averaged adiabatic film cooling effectiveness distributions at various turbulence intensity conditions

As for the low blowing ratio, the cooling effectiveness is exacerbated by the high turbulence intensity. Tu=20% results in a 13.4% and an 8.6% decrease of the area-averaged film cooling effectiveness for M=1.5 and M=2.0 from x/D=0 to x/D=30, and also causes a reduction of 26.5% and 21.5% for M=1.5 and M=2.0 in the area of x/D=20-40 respectively. These results are also consistent with investigations from Bons et al. [150], who studied the cylindrical film holes with the turbulence intensity up to 17% and the blowing ratios

from 0.55 to 1.85. For the cylindrical film hole, the high freestream turbulence intensity drastically reduces the centerline cooling effectiveness directly behind the coolant jet hole at about M=0.7.

Fig. 4.59 illustrate the spanwise distributions of adiabatic film cooling effectiveness at M=1.5 and M=2.0. Both blowing ratio conditions show similar distributions at the same streamwise position. For the region directly downstream the film hole in Fig. 4.59a and Fig. 4.59d, the cooling effectiveness is reduced near two sides of the center with the increase of the turbulence intensity. While the cooling effectiveness shows a slower drop far spanwise from the center at high turbulence intensity, hence, the shape of high turbulence intensity curve becomes flatter compared with the low turbulence intensity, which means more coolant spreads in spanwise direction, and the effectiveness is enhanced laterally. And the CRVP dominates wider the spanwise direction.

In the middle of the channel as shown in Fig. 4.59b and Fig. 4.59e, the cooling effectiveness decays more markedly at Tu=20%, and the effects on the low blowing ratio are more serious relative to the high blowing ratio. At further downstream locations presented in Fig. 4.59c an Fig. 4.59f, the cooling effectiveness decreases further. The difference on the sides of the channel is negligible, however, the center region still shows an obvious decline. The spanwise distributions of adiabatic film cooling effectiveness at three streamwise locations demonstrate that the high turbulence intensity enhances the mixing process, which results in a large effectiveness degradation at far field downstream of the channel.

Fig. 4.60 presents the instantaneous Q-criterion iso-surface with the temperature contours. The Q value is set to 0.01 for M=1.5 and M=2.0, and the temperature above 285K is cut off, which means the vortex structures of the mainstream is removed whereas the vortices from coolant are preserved. The hairpin vortices can be found along the bottom surface covered by the outside high temperature mainstream. And the hairpin vortices develop and scale up along the channel.

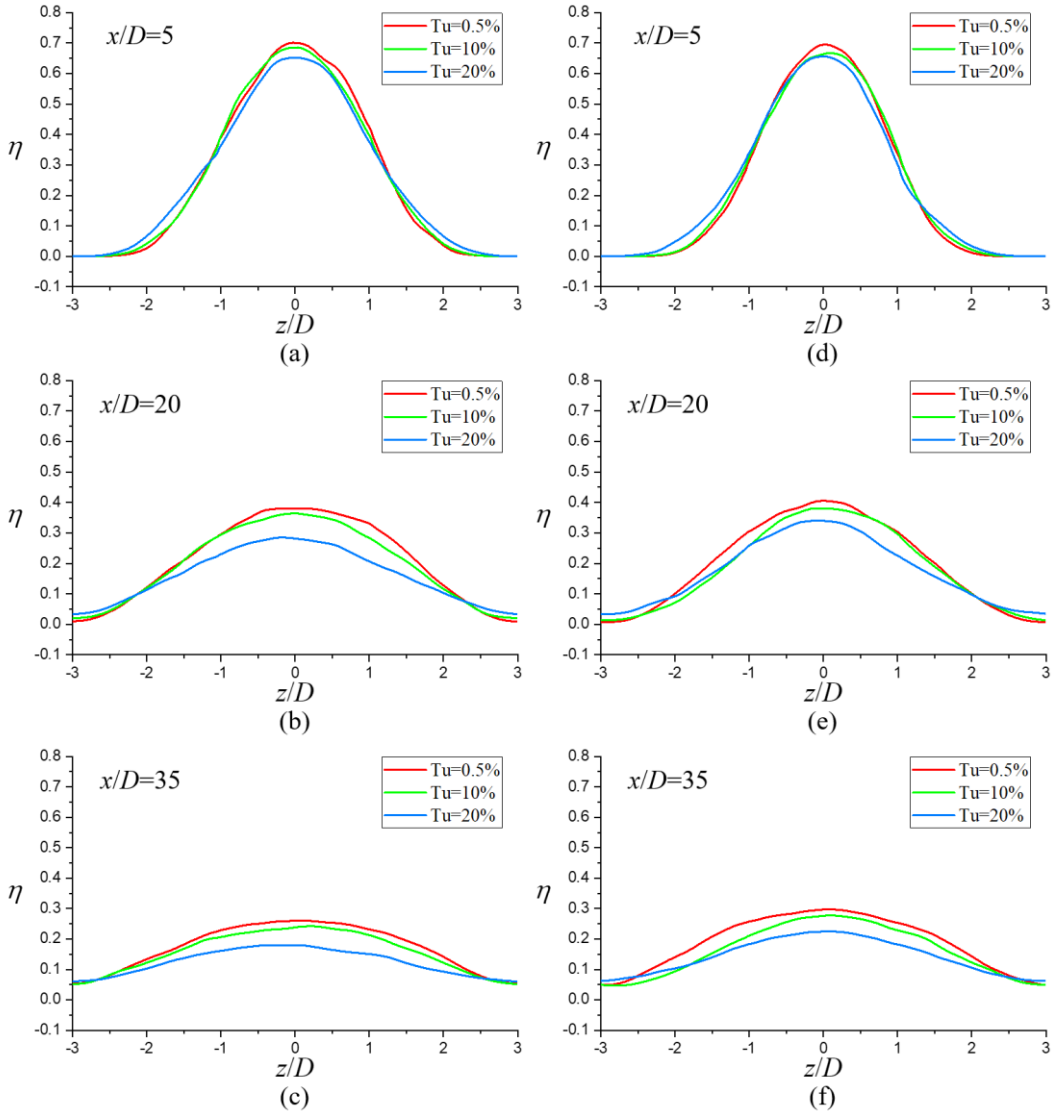

Fig. 4.59 Spanwise distributions of adiabatic film cooling effectiveness (a-c) M=1.5 DR=1.5 (d-f) M=2.0

The instantaneous Q-criterion iso-surface can reveal the process where the coolant is mixed with the mainstream. For both cases with different blowing ratios, as the mainstream inlet turbulence intensity increases, the coolant jet is diffused in spanwise and wall-normal directions. And the lateral diffusion increases with higher turbulence intensity, which can be inferred that the mix is stronger near the downstream of the film hole exit. The coolant distributions of the vortices at the middle part of the channel are wider in spanwise direction at M=1.5 and Tu=20%, compared with the further downstream of the channel. At lower Tu, the spread of the CRVP and anti-CRVP in the coolant is limited in the lateral and wall-

normal directions, however, at higher Tu, the vortices dominate more cooling channel in both spanwise and wall-normal directions.

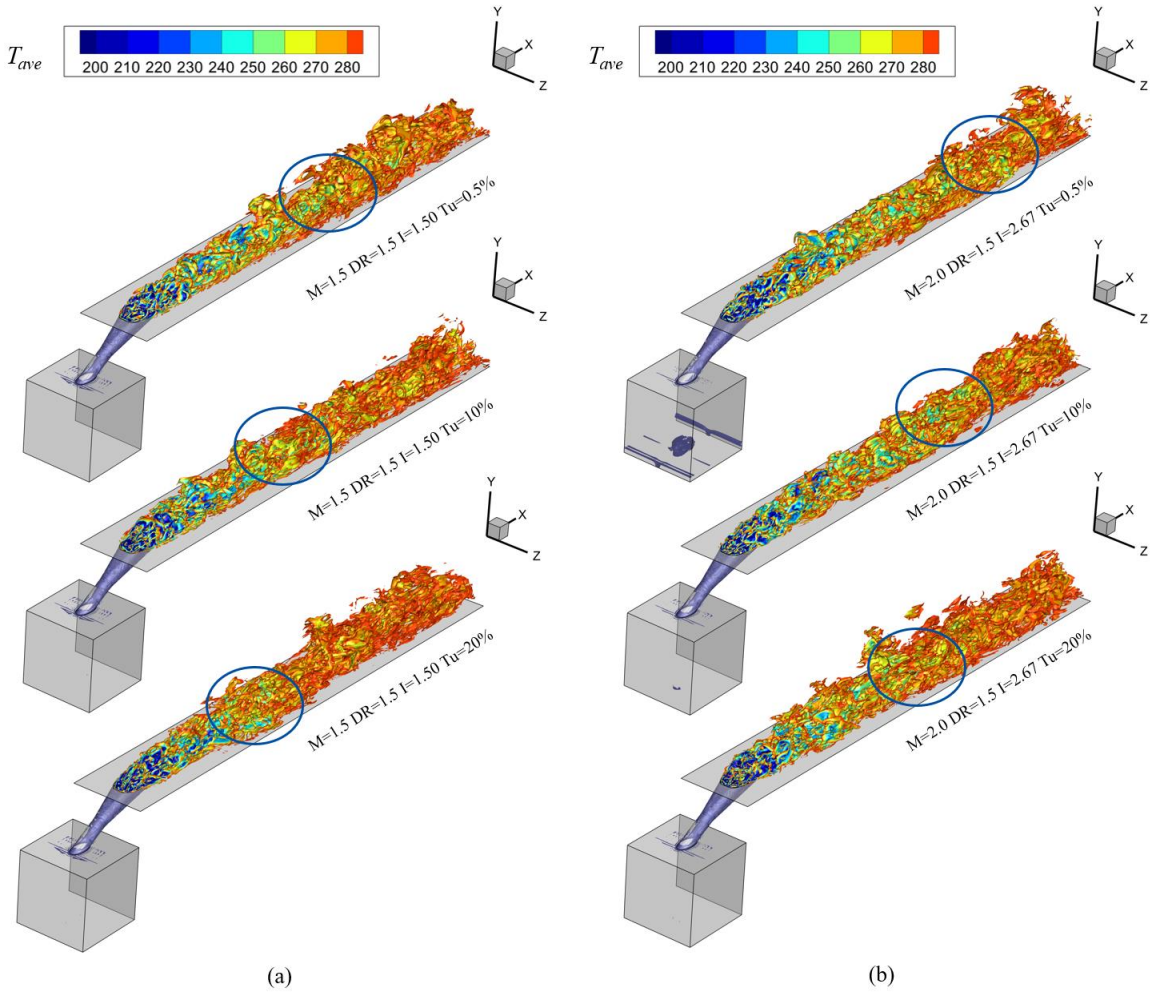

Fig. 4.60 Instantaneous Q-criterion iso-surface colored by mean temperature (a) M=1.5 DR=1.5 (b) M=2.0 DR=1.5

In addition, from the change of the color along the streamwise direction, it's clear that the temperature of the coolant increases from the outside and the volume of the coolant becomes less, which reflects the cooling effectiveness is worsen. And the coolant interacts closely with the mainstream in the far field downstream, note that the high temperature has already penetrated into the low temperature coolant, due to the absorption effects of the CRVP.

4.4.4 Effects of inlet boundary layer parameters on shaped film hole

In order to investigate the effects of the inlet boundary conditions on the film cooling performance, three different velocity profiles are used as the mainstream inlet boundary conditions, shown in Fig. 4.61. velocity profile 1 is same as the velocity profile used in the previous sections, velocity profile 2 and 3 are employed to study the effects of the mainstream inlet boundary condition.

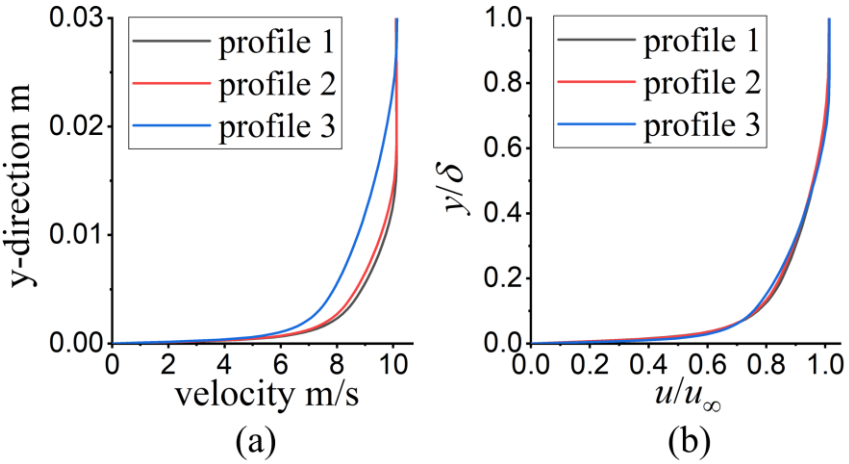

Fig. 4.61 Three velocity profiles of the mainstream inlet (a) velocity profile (b) normalized velocity profile

Since the upstream flow condition of the turbine blade is fully turbulent, three turbulent velocity profile was chosen. The detailed boundary layer parameters are listed in Tab. 4.7. Note that due to the increase of θ/D from 0.14 to 0.29, the Re_θ increases from 671 to 1401, and the friction velocity varies from 0.5 to 0.44. The mainstream inlet turbulence intensity remains constant at 0.5%.

Tab. 4.7 Boundary layer parameters of three different velocity profiles

	Tu	δ^*/D	θ/D	H_{12}	Re_θ	u_τ m/s
Profile 1	0.5%	0.20	0.14	1.45	671	0.5
Profile 2	0.5%	0.23	0.16	1.43	779	0.48
Profile 3	0.5%	0.41	0.29	1.40	1401	0.44
EXP	0.5%	0.20	0.14	1.45	670	0.5

Fig. 4.62 depicts the time-averaged film cooling effectiveness with three mainstream inlet velocity profiles. The differences of the cooling effectiveness contours are not manifest generally. The main distinction consists in the streamwise distributions. With the increase of the displacement and momentum thickness as well as Re_θ, the cooling effectiveness shows a mild decay at far field downstream. Considering the centerline distributions in Fig. 4.63a, a slight decrease occurs at about x/D=0-10, and in the region of x/D=20-40, cooling effectiveness with velocity profile 3 surpasses the other two cases. Fig. 4.63b presents the lateral-averaged distributions of the cooling effectiveness. It can be found that mainstream velocity profile 3 gives a lower effectiveness area near the downstream of the film hole exit in the range of x/D=0-15 approximately. The reduction implies the coolant development in spanwise direction is suppressed with velocity profile 3 boundary condition. At further downstream, the cases with velocity profile 2 and 3 overtake the baseline case with velocity profile 1 at about x/D=7.5 and 17.5.

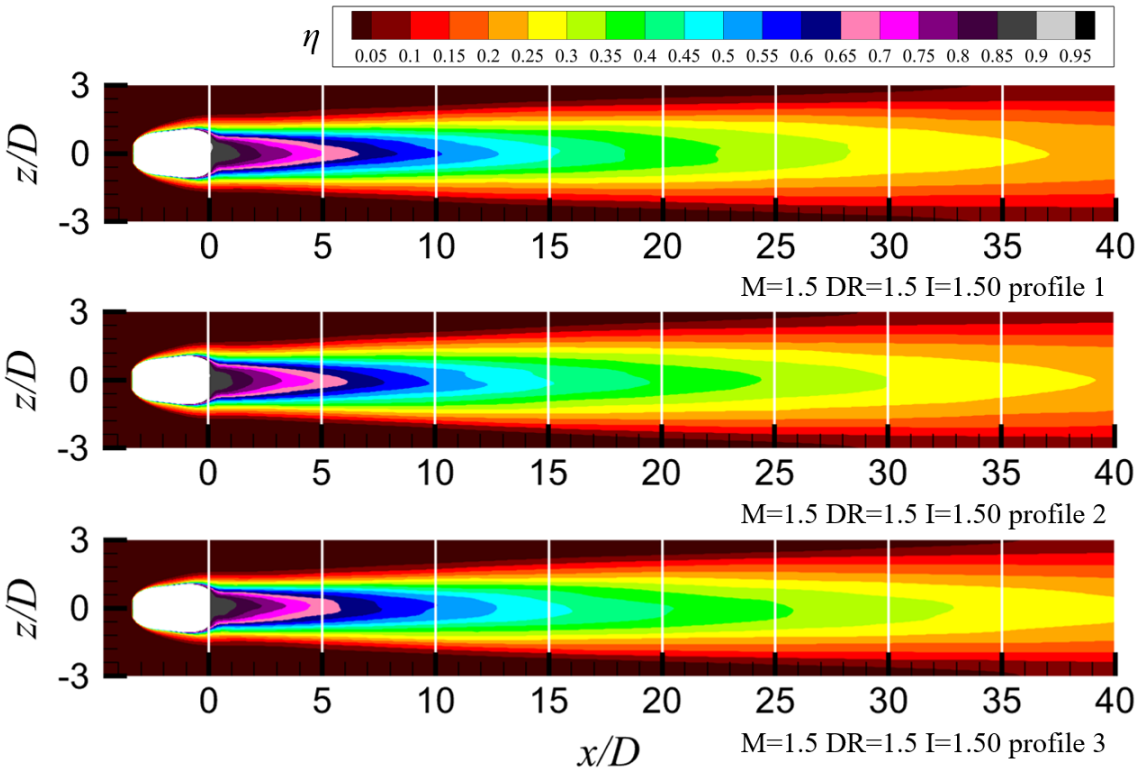

Fig. 4.62 Time-averaged film cooling effectiveness contours of the bottom surface with different mainstream inlet velocity profiles at DR=1.5 Tu=0.5%

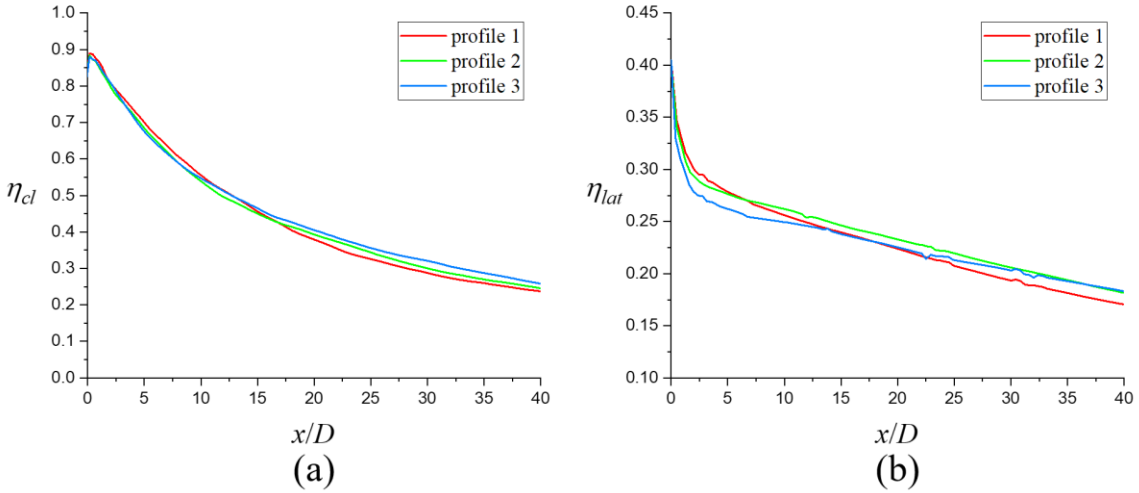

Fig. 4.63 Time-averaged film cooling effectiveness distributions with various mainstream inlet boundary conditions at DR=1.5 Tu=0.5% (a) centerline (b) lateral-averaged

Fig. 4.64 shows the spanwise distributions of adiabatic film cooling effectiveness at near field and far field. For the near field at x/D=5 of the cooling channel, velocity profile 2 and 3 conditions give a similar trend of the cooling effectiveness near the center region, while there is a rapid decay from the center to sides for profile 3 boundary condition. Far field at x/D=30, mainstream with velocity profile 3 shows higher cooling effectiveness in the center. According to the trends of the near and far fields, it can be deduced that the thicker mainstream inlet boundary layer causes the attenuation of the lateral spreading of the coolant upstream of the channel, and slightly affects the coolant development in wall-normal direction at far field.

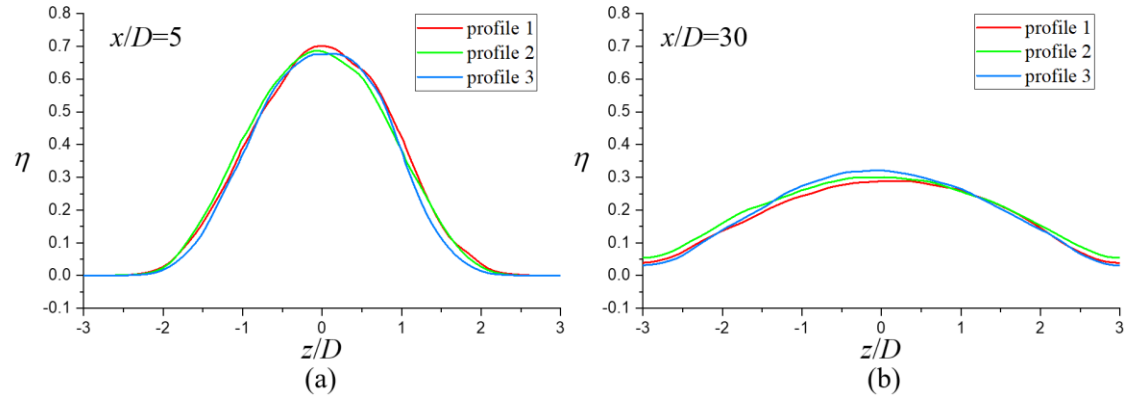

Fig. 4.64 Spanwise distributions of adiabatic film cooling effectiveness at DR=1.5 Tu=0.5% (a) near field (b) far field

With the help of the instantaneous Q-criterion iso-surface shown in Fig. 4.65, the flow visualization directly presents the vortex structures in flow field. Q value is equal to 1 for both cases. T_{RMS} reflects the mix between the coolant and the mainstream. As can be seen, the hairpin vortices develop from small scale to large scale size, lower T_{RMS} still exists at x/D=25-30 for profile 3 relative to profile 1, which means the mixing process ends further downstream for profile 3. Horseshoe vortices form at the leading edge of the shaped hole shown in the top view. From the top view of profile 1, the horseshoe vortices are generated continuously along the outer layer of the coolant until x/D=2. While for profile 3 the fitful horseshoe vortices are formed at x/D<0. Hence, the inlet boundary layer affects the formation of the horseshoe vortices in leading edge region.

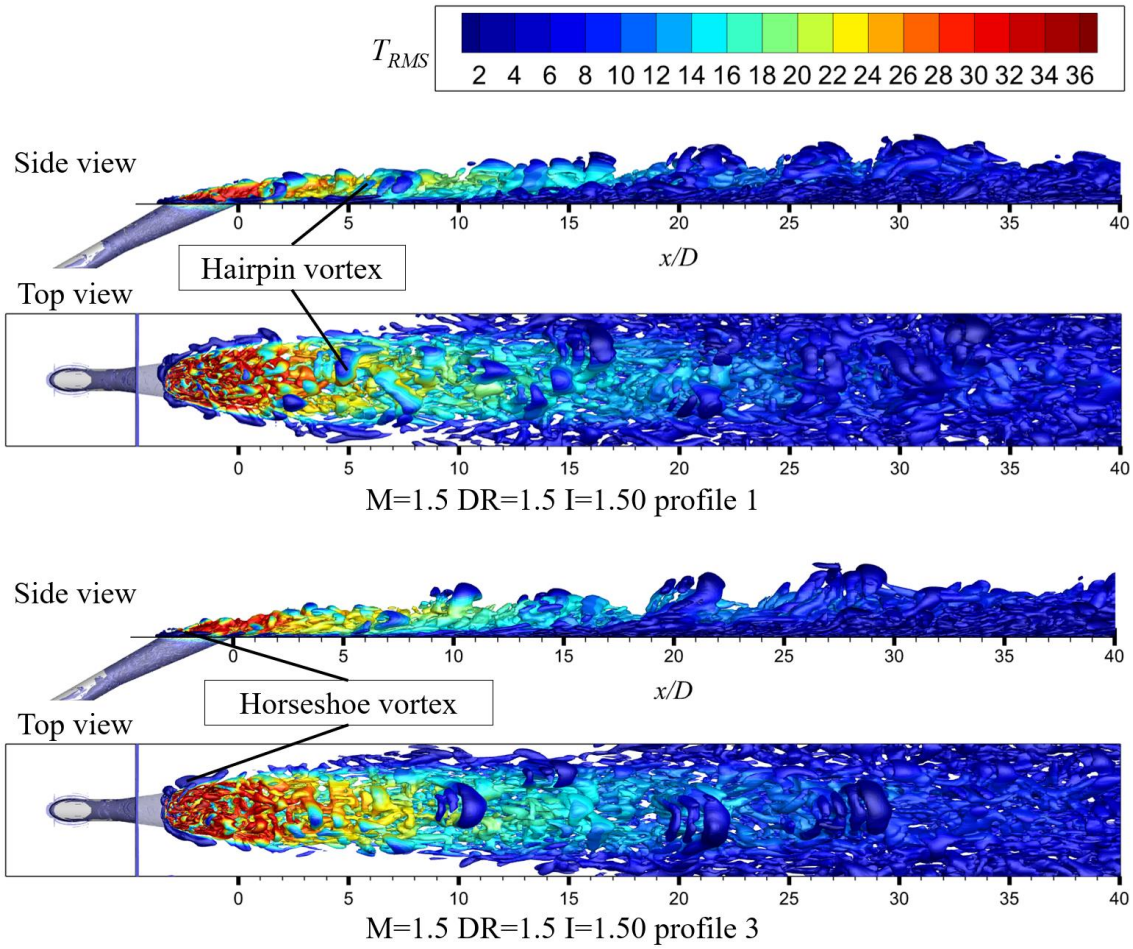

Fig. 4.65 Instantaneous Q-criterion iso-surface colored by T_{RMS} at DR=1.5 Tu=0.5%

4.4.5 Effects of the curvature on shaped film hole

Fig. 4.66 presents the schematic of shaped film hole with streamwise-curved surface. The geometrical size of the 7-7-7 shaped film hole is the same as that used in the investigation of flat bottom surface. The convex curved surface aims at studying the film hole downstream of the leading edge, as shown in Fig. 4.67. The suction side is simplified as a curved surface. In Fig. 4.66, the height of the channel remains constant at 10D, and the radius R of the curved surface is 100D, and the curvature is equal to the reciprocal of the radius R, namely 1/R. The length of the streamwise-curved surface L_{curve} is 40D. The origin of the coordinate is at the middle trailing edge of the shaped film hole exit. The mainstream inlet boundary condition is set the same as that in section 4.4.2, namely the velocity profile 1 as mentioned above.

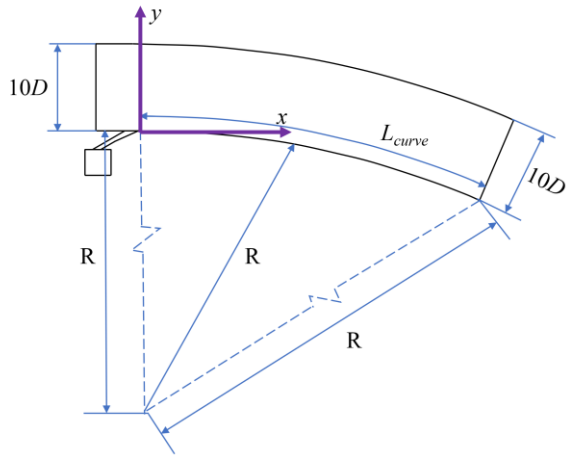

Fig. 4.66 Schematic of the shaped film hole with streamwise-curved surface

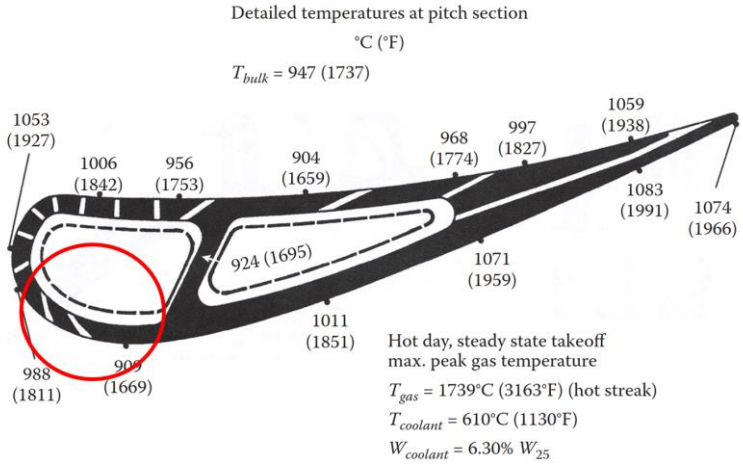

Fig. 4.67 E3 stage-1 HPT vane pitch section with temperature distribution [151]

In order to facilitate the post-processing, the x, y coordinates of the curved bottom surface, as shown in Fig. 4.69, can be converted into the flat bottom surface for the comparison by the following relationship:

$$\begin{cases} x_{transf} = \arcsin\left(\dfrac{x}{R}\right) R \ \ (x > 0) \\ y_{transf} = 0 \\ z_{transf} = z \end{cases} \tag{1.53}$$

where *R* is the radius of the curved bottom surface

The cross-section planes in the curved cooling channel, depicted in Fig. 4.75, can be converted into the plane at the same streamwise location in the straight channel with the equation 1.54.

$$\begin{cases} x_{transf} = s \\ y_{transf} = \sqrt{(x-0)^2 + (y+100)^2} - R \\ z_{transf} = z \end{cases} \tag{1.54}$$

where *s* represents the streamwise location in the channel.

For the mainstream curved cooling channel, the coordinate is transformed into straight cooling channel with following equations 1.55, as presented in Fig. 4.71.

$$\begin{cases} r = \sqrt{(x-0)^2 + (y-R)^2} & (x > 0 \ y > 0) \\ x_{transf} = \arcsin\left(\dfrac{x}{r}\right) r & (x > 0 \ y > 0) \\ y_{transf} = r - R & (x > 0 \ y > 0) \end{cases} \tag{1.55}$$

where *r* is the distance between the point in the channel and the center of the curve.

Fig. 4.68 shows the time-mean film cooling effectiveness along the centerline. The solid line denotes the curved cooling channel, and the dash line represents the original straight cooling channel. Compared with the cases with flat plate, for M=1.5-2.0 the trends of the streamwise-curved surface between *x*/*D*=0-15 show an agreement with the flat

bottom surface. While the centerline cooling effectiveness is improved at about x/D=15-40 at further downstream regions.

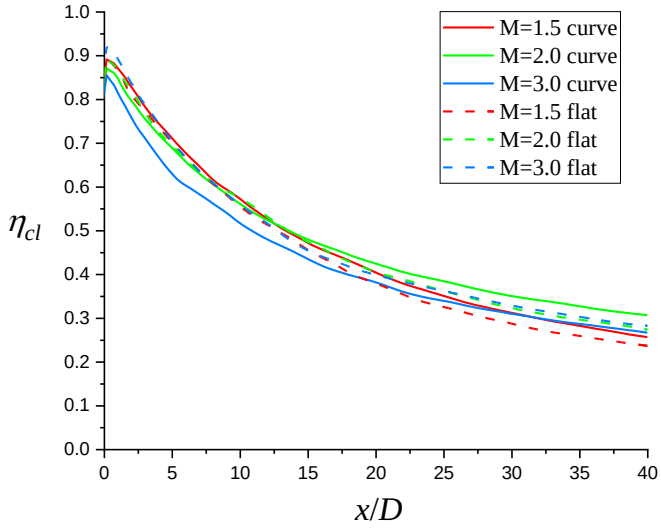

Fig. 4.68 Time-averaged centerline adiabatic film cooling effectiveness of shaped hole at DR=1.5 Tu=0.5%

Referring to Fig. 4.69, the cooling effectiveness contour presents the effects of the curved bottom surface on the effectiveness distribution. For the curved plate, the effectiveness can be sustained at further distance. And the difference of the centerline effectiveness is more clearly visible at higher blowing ratio case. From x/D=15 to x/D=40, the curved bottom surface obtains roughly a 7.3% and 7.1% increase of the centerline film cooling effectiveness for M=1.5 and M=2.0 conditions respectively. When M=3.0, the centerline cooling effectiveness begins to decay, and the decrease of the effectiveness is clearly seen at near field of x/D=0-15. It indicates that the high momentum injection enters the mainstream channel with higher velocity and cannot attach to the curved bottom surface immediately as good as the flat surface. Therefore, the film doesn't develop as good as low momentum cases. The centerline film cooling effectiveness of M=3.0 decreases by 6.3% on average in the range of x/D=0-40. Corresponding to Fig. 4.69, the lateral spreading of the coolant is insufficient especially at far field, and cooling effectiveness falls more quickly along the streamwise direction in the curved channel.

Fig. 4.70 shows lateral averaged mean film cooling effectiveness. The solid line denotes the curved cooling channel, and the dash line represents the original straight cooling channel. According to the comparison between the curved and flat plates, for

M=1.5 there is few discrepancies at near field, but a slight drop near x/D=5. Since x/D=20, the effectiveness of curved case slightly overtakes the flat case. From x/D=5 to x/D=40, the curved surface increases the lateral averaged film cooling effectiveness by about 2.7%.

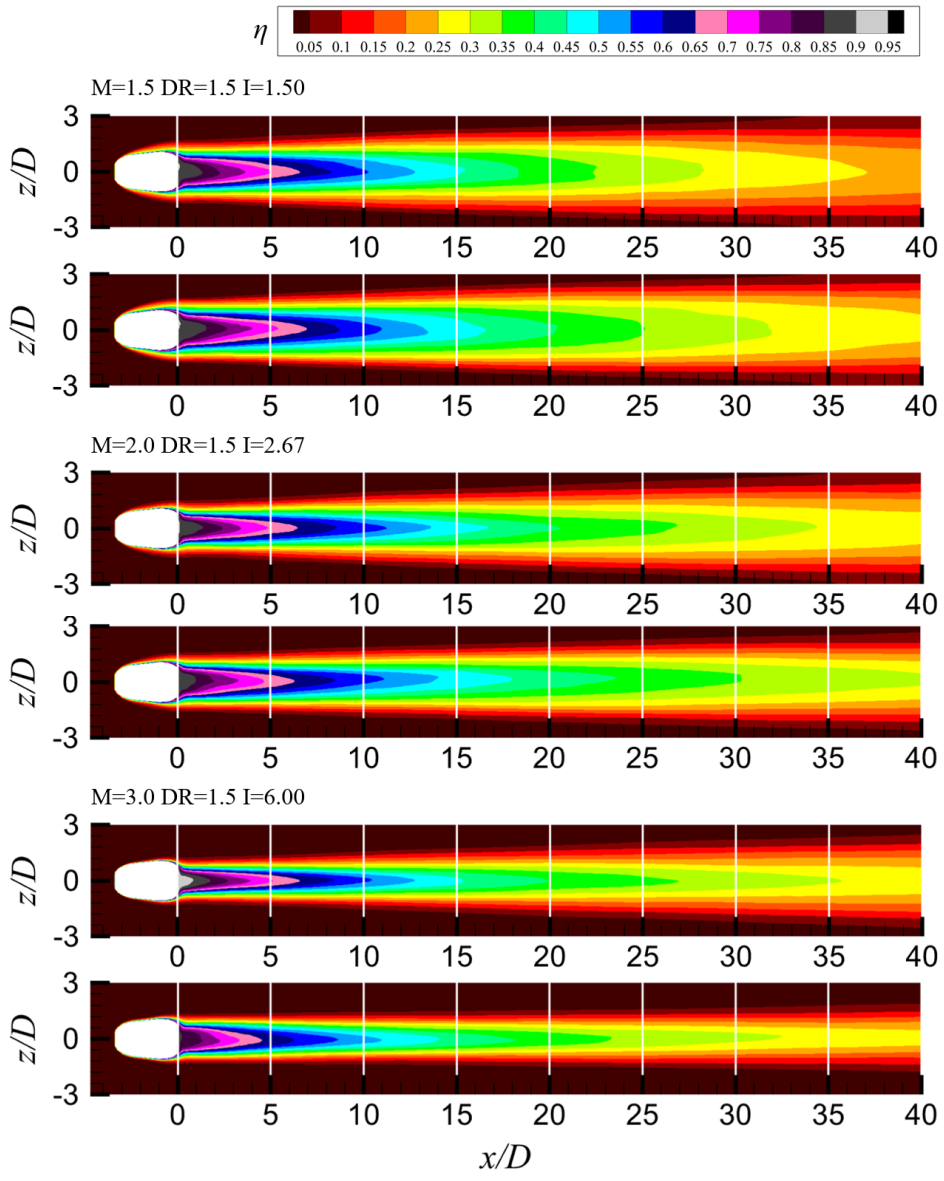

Fig. 4.69 Time-averaged film cooling effectiveness contours of shaped film hole at DR=1.5 Tu=0.5% (top row: flat surface, bottom row: curved surface)

As the blowing ratio increase, the curved case shows an obvious deterioration relative to the flat one. The lateral averaged film cooling effectiveness of the curved bottom decreases by about 7.9% at M=2.0 and x/D=5-40. Therefore, the curved surface produces more undesired effects on the cooling effectiveness at higher blowing ratio. As for M=3.0,

the lateral averaged effectiveness from x/D=5 to x/D=40 drops by 25.8%. The lateral averaged effectiveness decreases sharply from x/D=0 to x/D=15 at near field, then the decay rate becomes slow at further downstream and stabilizes at η_{lat}=0.1, which can demonstrate the lift of the coolant along the curved bottom surface. This phenomenon is consistent with the cylindrical film hole with a convex surface investigated by Ito et al. [152]. For the cylindrical film hole, the lateral averaged film cooling effectiveness with convex bottom surface is improved at lower blowing ratio of M=0.5-1.0 and DR=2.0, while the lateral averaged effectiveness begins to reduce at M=1.9 DR=2.0, compared with the flat bottom surface. Because at lower blowing ratio case, the momentum flux ratio is also smaller at the constant density ratio and the coolant jet is pushed on the bottom wall by the pressure force around the coolant as soon as it enters the mainstream cooling channel. However, when the blowing ratio increases, and the coolant is injected with high momentum, which results in the detachment from the surface. The convex curved surface is more sensitive to the momentum in the coolant, compared with the flat surface.

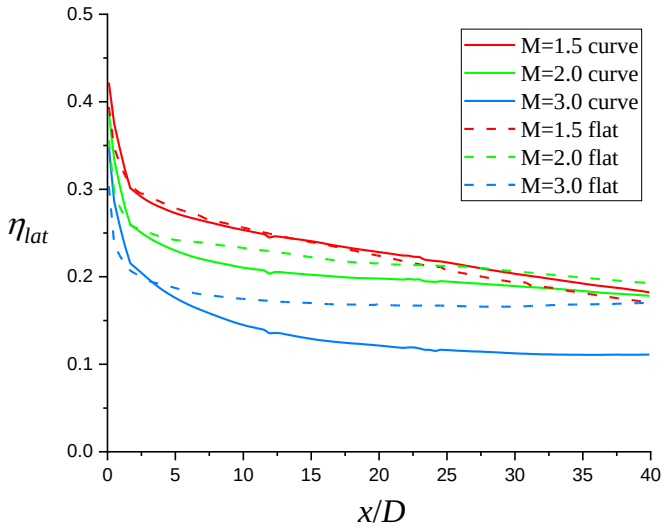

Fig. 4.70 Lateral averaged mean film cooling effectiveness of shaped hole at DR=1.5 Tu=0.5%

Fig. 4.71 and Fig. 4.72 shows the curved and transformed cooling channels with time-averaged and instantaneous and non-dimensional temperature T_{non}, after the coordinate transformation, the characteristics of the flow field can be still retained, and it also facilitates the comparison between the straight and curved channels.

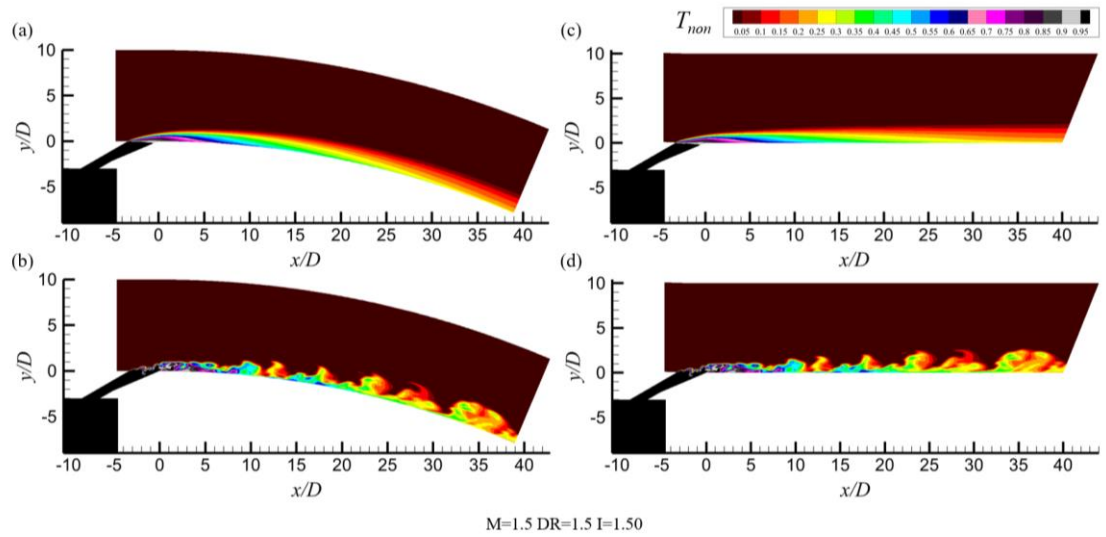

Fig. 4.71 The center plane distributions of time-averaged (top row) and instantaneous (bottom row) T_{non} (a-b) the curved cooling channel (c-d) the transformed curved cooling channel at M=1.5 DR=1.5 Tu=0.5%

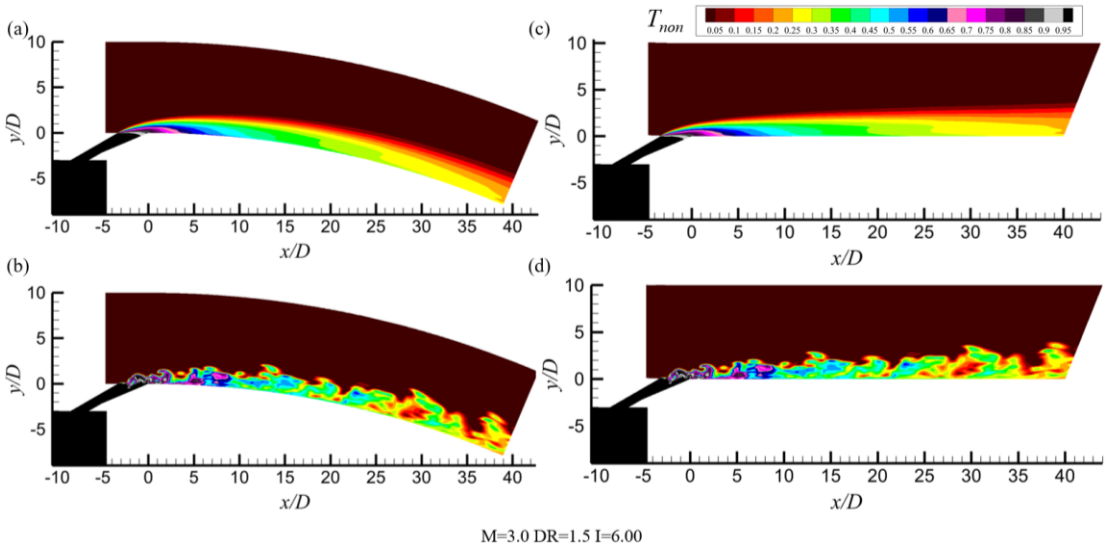

Fig. 4.72 The center plane distributions of time-averaged (top row) and instantaneous (bottom row) T_{non} (a-b) the curved cooling channel (c-d) the transformed curved cooling channel at M=3.0 DR=1.5 Tu=0.5%

Fig. 4.73 and Fig. 4.74 present the comparison between the non-dimensional temperature of the straight cooling channel and the transformed curved cooling channel. For M=1.5, the time averaged non-dimensional temperature shows similar distributions in the center cross section plane, shown in. Fig. 4.73a and Fig. 4.73c. The coolant can still attach the bottom surface at 1/100*D* curvature. In Fig. 4.73b and Fig. 4.73d, it can be clearly seen that the lower temperature coolant remains attached in the range of *x*/*D*=0-10 in curved channel. Both channels present similar T_{non} distributions near the bottom surface at

M=1.5. When M=3.0, the T_{non} distributions in the center cross section show imperceptible differences between the straight and transformed curved channels. It can be implied that no separation is generated in the convex curved channel, and the coolant is concentrated near the center plane, which results in the insufficient lateral spread for the curved channel relative to the straight channel.

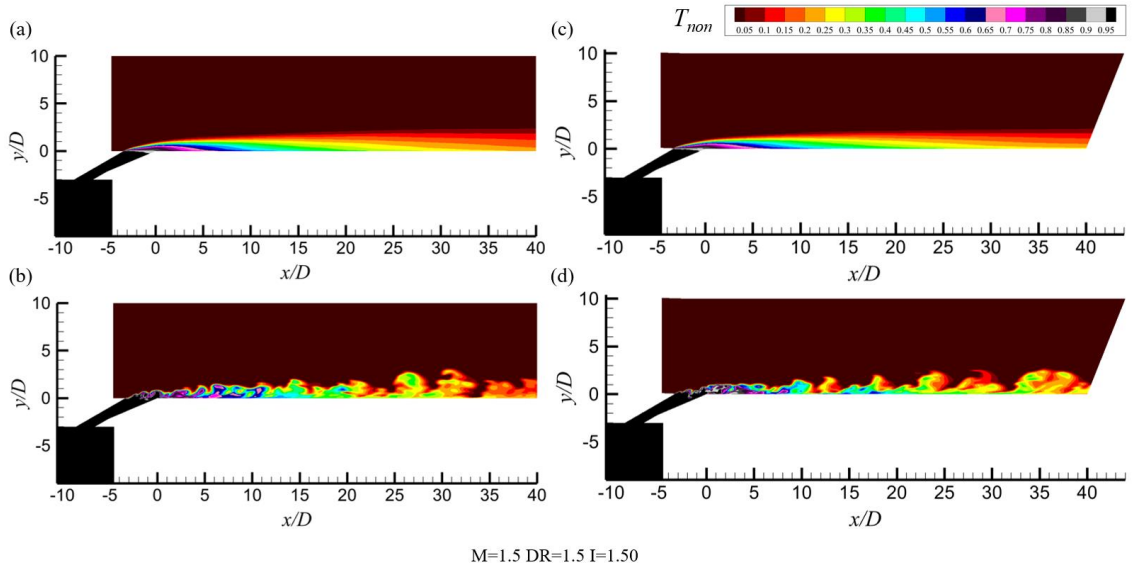

Fig. 4.73 The center plane distributions of time-averaged (top row) and instantaneous (bottom row) T_{non} (a-b) the straight cooling channel (c-d) the transformed curved cooling channel at M=1.5 DR=1.5 Tu=0.5%

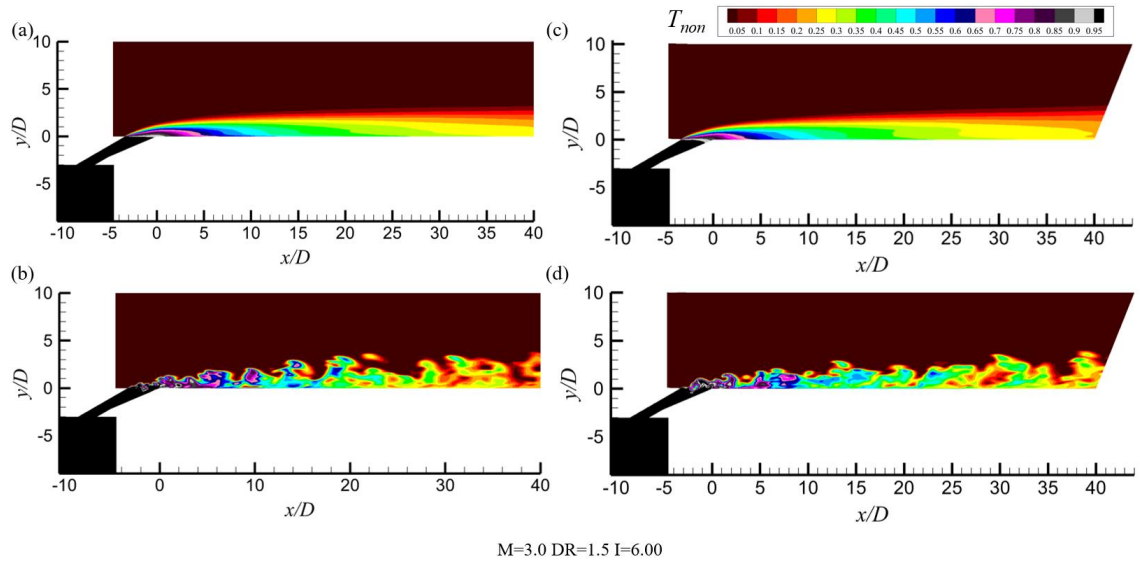

Fig. 4.74 The center plane distributions of time-averaged (top row) and instantaneous (bottom row) T_{non} (a-b) the straight cooling channel (c-d) the transformed curved cooling channel at M=3.0 DR=1.5 Tu=0.5%

Fig. 4.75 illustrates the non-dimensional temperature and the RMS of temperature distributions of the curved and the straight channels from x/D=5 to x/D=30. According to the comparison, the time averaged T_{non} and T_{RMS} show an agreement at near field. At x/D=30, the coolant shows a semiellipse-like distribution in curved channel with blue dash line, while the coolant is distributed as a triangle-like shape. The coolant covers the more areas in spanwise direction at far field at curved bottom surface. And the temperature fluctuation in the core region of the coolant is relatively larger at further downstream.

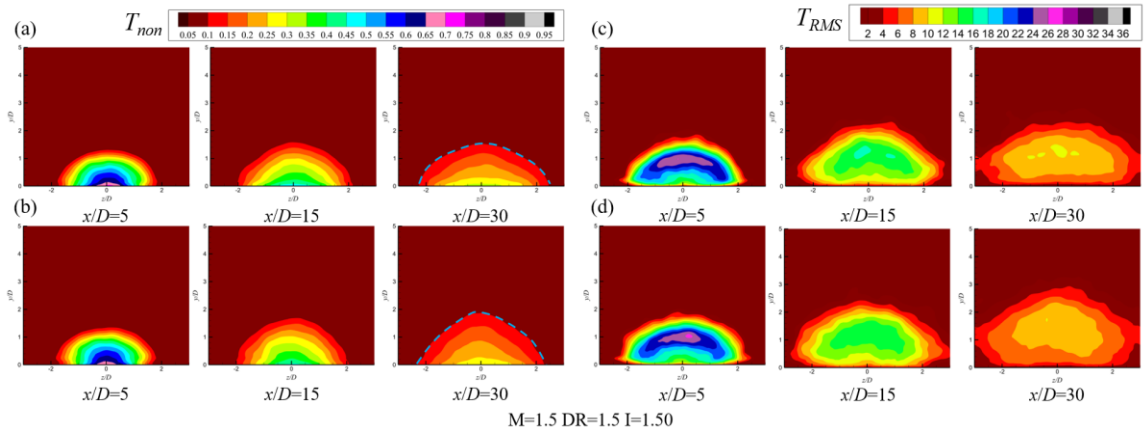

Fig. 4.75 Cross section distributions of the curved (top row) and the straight (bottom row) channels (a-b) non-dimensional temperature T_{non} (c-d) RMS of temperature fluctuation T_{RMS} at M=1.5 DR=1.5 Tu=0.5%

For M=2.0 shown in Fig. 4.76, due to the curve surface, the coolant with higher velocity shows a slight lift from the bottom surface at x/D=30, where the lift allows the high temperature mainstream to penetrate into the two sides of the coolant. Besides, from x/D=15 to x/D=30, the interface between the coolant and the mainstream is also lifted, and there is a low T_{RMS} region in the bottom center, which can be inferred that the coolant is still attached to the bottom surface and the flow field is relative stable.

For M=3.0, the comparison between the curved and straight cooling channel is depicted in Fig. 4.77. The temperature distribution in curved channel is more concentrated to the center regions, and the coolant becomes narrower in spanwise direction and higher in radial direction. As can be seen from the T_{RMS} contours, the coolant is not as stable as the straight channel at x/D=5 and y/D<1, where the coolant is strongly mixed with the mainstream directly at the trailing edge areas of the film hole exit. At x/D=30, the mainstream is drawn

by the CRVP beneath the coolant, which results in the decay of the cooling effectiveness at bottom surface.

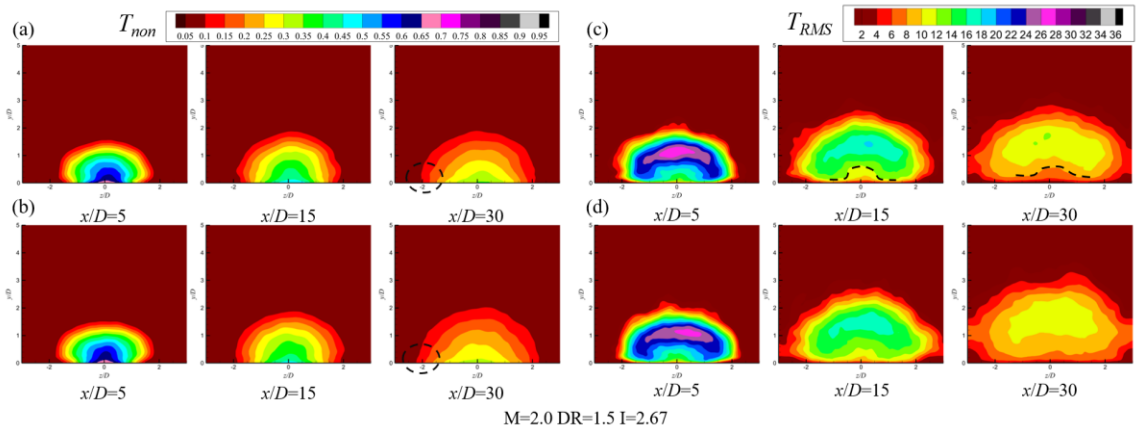

Fig. 4.76 Cross section distributions of the curved (top row) and the straight (bottom row) channels (a-b) non-dimensional temperature T_{non} (c-d) RMS of temperature fluctuation T_{RMS} at M=2.0 DR=1.5 Tu=0.5%

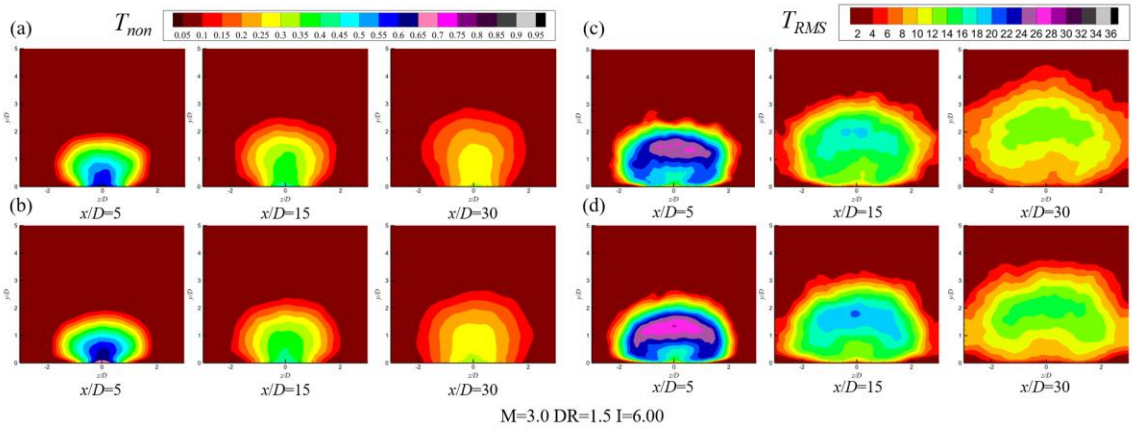

Fig. 4.77 Cross section distributions of the curved (top row) and the straight (bottom row) channels (a-b) non-dimensional temperature T_{non} (c-d) RMS of temperature fluctuation T_{RMS} at M=3.0 DR=1.5 Tu=0.5%

The non-dimensional temperature is shown in Fig. 4.78 with respect to the wall-normal direction at z/D=0. For the straight cooling channel, the ordinate represents the normal distance to the bottom surface, and for the curved cooling channel, the ordinate refers to the radial direction of the curved bottom surface. Therefore, two cases with different geometries can be compared at the same streamwise location.

For M=1.5 at the near field, the non-dimensional temperature shows similar distribution between the curved and the flat surface. As the coolant flows further downstream in curved channel, at x/D=15 the normalized temperature presents a slight drop at y/D=1-2, and the

difference becomes larger at x/D=30. From Fig. 4.68, it can be found that the cooling effectiveness of the centerline improved mildly in curved channel at further downstream at M=1.5. Thus, it can be deduced that the coolant is mixed with the mainstream quickly above the bottom surface in the curved channel, causing the decrease of the T_{non} of the coolant. Besides, the mix could be more intense along the radial direction in the curved channel at far field, which is inferred from the increasing discrepancy between the curved and flat surface at x/D=30.

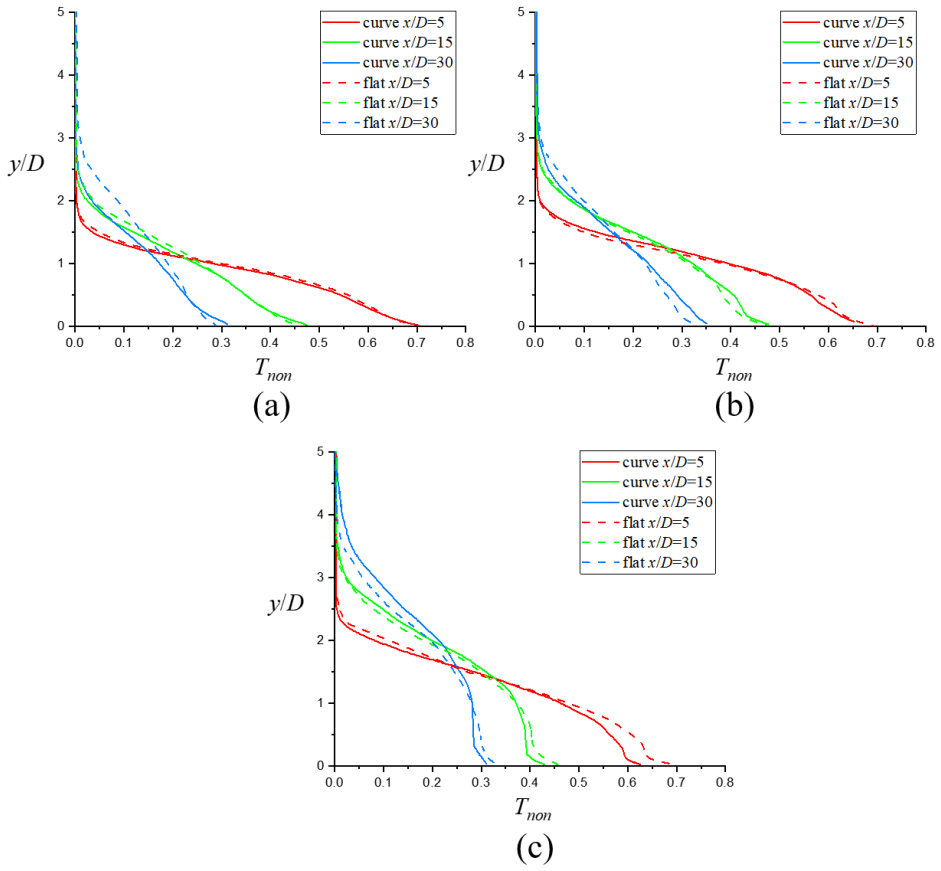

Fig. 4.78 Time averaged non-dimensional temperature at near, middle and far fields along wall-normal direction (a) M=1.5 (b) M=2.0 (c) M=3.0 at DR=1.5 Tu=0.5%

For higher blowing ratio of M=2.0, an increase of the non-dimensional temperature is found at x/D=15 and 30 near the curved bottom surface (y/D<1). While the T_{non} is lower at x/D=30 in the curved channel, compared with the straight channel. Thus, the curve shows a desired effect in near bottom wall region and an undesired effect at further location far from the bottom wall. When blowing ratio is as high as 3.0, an obvious decrease is shown at x/D=5 in the curved channel at y/D<1, and the deterioration of T_{non} is also presented at

middle and far field of the channel at near bottom surface regions. However, for the curved case, the T_{non} is improved and surpasses the straight channel when y/D is over 1. The reason may be that the curved channel leads to the lift of the coolant jet, thus the position in the radial direction is higher compared with the straight channel. Since less coolant remains near the bottom surface, the mainstream is drawn below the coolant.

There three points located at the exit of the shaped film hole to monitor the velocity variation during a period in convex curved channel. The coordinates of the three monitor points are (-2.36*D*, 0, 0.31*D*), (1.26*D*, 0, -0.35*D*) and (1.26*D*, 0, 0.35*D*). According to the relationship between the Power spectra as mean square amplitude (MSA) and the frequency shown in Fig. 4.79, the peak value of the power density on the vertical axis is corresponding to the main frequency at the monitor point in the flow field, thus the main frequencies measured at three monitor points at M=3.0 in curved cooling channel are 249Hz, 249Hz and 278Hz respectively. For the frequency of 249Hz, it is equivalent to about 40 time steps. At high frequency of 1000Hz approximately, there is an intensive oscillation. And the power spectral density shows a downward trend when the frequency is over about 300Hz.

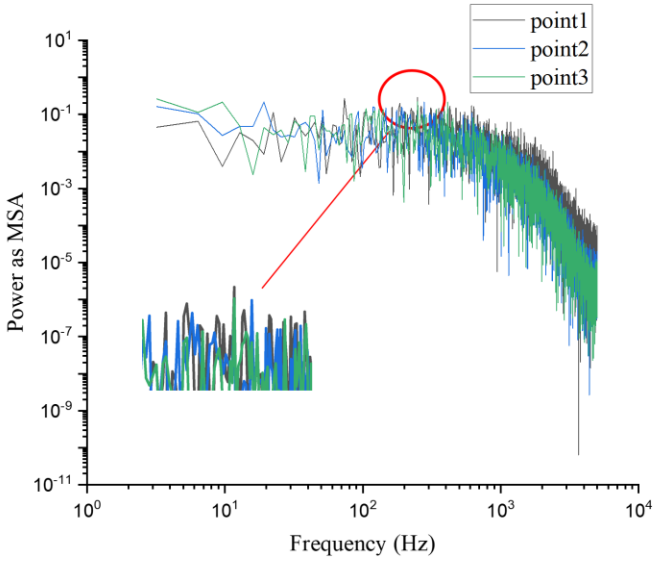

Fig. 4.79 Instantaneous velocity power spectral density (PSD) in curved channel at M=3.0 DR=1.5 Tu=0.5%

Chapter 5

Numerical simulation of NASA C3X turbine vane

It is acknowledgeable that the turbine vane operates at very high temperature conditions. And it is too expensive to implement the experiment under the realistic engine operation condition because of the test rig and equipment as well as the huge operational costs. Therefore, the low temperature measurement is commonly used aiming to obtain the non-dimensional parameters and scale to the realistic engine conditions. Thanks to the increasing popularity of the CFD tools, it is possible to simulate the high temperature engine conditions efficiently at much lower cost. In this chapter, the conjugate heat transfer simulation was implemented on the NASA C3X turbine vane.

5.1 Geometry of NASA C3X turbine vane

Fig. 5.1 presents the top view schematic of the C3X turbine van geometry from NASA. The coordinate of the vane is referred to from the public report of NASA written by Hylton et al. [81] and the details are presented in appendix B.

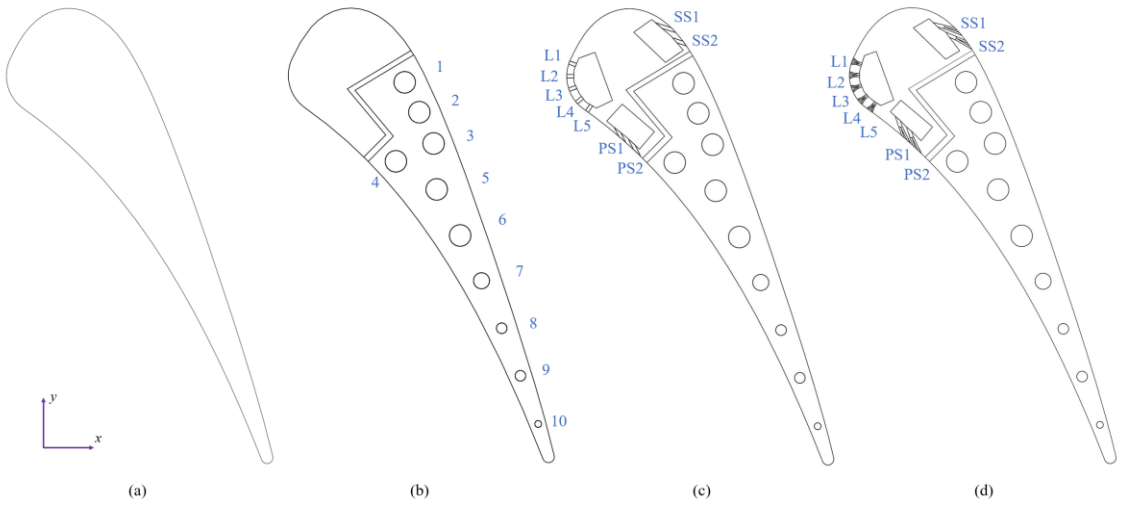

Fig. 5.1 Schematic of the C3X turbine vane (a) solid turbine vane (b) with internal cooling (b) with cylindrical film hole (c) with shaped film hole

The C3X cascade parameters are shown in Tab. 5.1. Fig. 5.1b adds the internal cooling tubes based on the solid cascade shown in Fig. 5.1a, and the inside cooling passages are numbered sequentially from 1 to 10. According to the NASA original experiment, the film cooled part was isolated from the rest of the cascade, because heat transfer was not measured. The test cascade was cut into two sections and a sealed air gap was used as a thermal barrier for preventing the heat transfer between the two sections. In the experiment, the conventional cylindrical film holes L1-L5, SS1-SS2 and PS1-PS2 were equipped at the leading edge and downstream of the suction and pressure surfaces respectively, as shown in Fig. 5.1c. The streamwise direction of the radial internal cooling tubes inside the rear part and the film cooling plenums inside the front part is from the -*z* to +*z*. In present work, the shaped film hole cascade was also tested in the simulation presented in Fig. 5.1d. The computational domain of the cascade is depicted in Fig. 5.2. One and three times of the axial chord length are determined upstream and downstream of the cascade vane for the development of the freestream and wake.

Tab. 5.1 C3X cascade geometry parameters

Parameters	Values
Stagger angle	59.89°
Flow exit angle	72.38°
Height	77.22 mm
Pitch	117.73 mm
Chord	144.93 mm
Axial chord	78.16 mm
Suction surface arc length	180.37 mm
Pressure surface arc length	139.82 mm

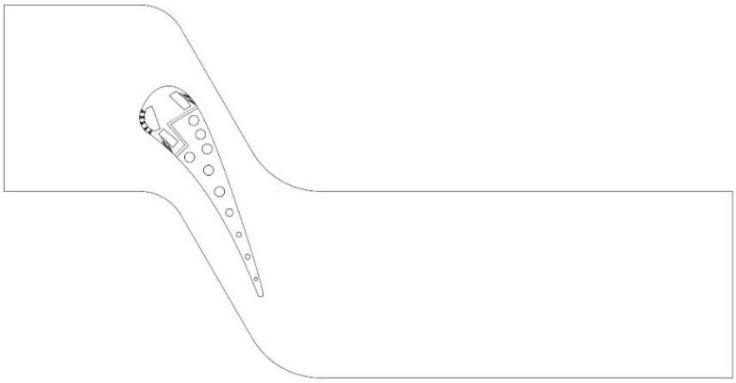

Fig. 5.2 Schematic of the cascade channel geometry

Fig. 5.3 illustrates the film hole with inclined and compound angles. The inclined angle α is defined as the angle between the axis and the *xy* plane, and compound angle β is the angle between the projection of the film hole axis on *xy* plane and the *x*-axis.

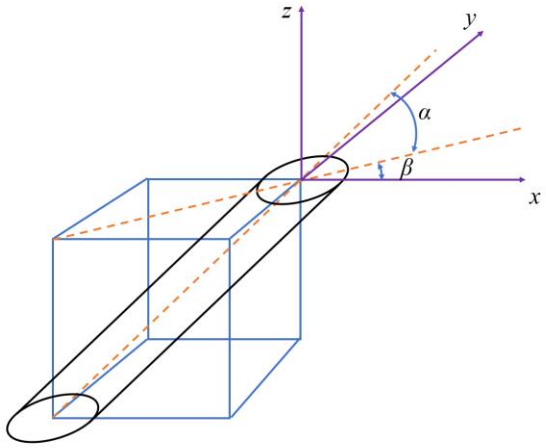

Fig. 5.3 Schematic of the film hole angles

Tab. 5.2 and Tab. 5.3 list the main geometry parameters of the cylindrical and shaped film hole structures used for the C3X cascade respectively. Since the exit area is larger than the inlet area for the laidback fan-shaped film hole due to the expansion in lateral and forward directions, the number of the shaped film hole is less than the cylindrical film hole in each row. But the diameters remain the same for both cases. The leading-edge, downstream suction-side and pressure-side film holes are pumped by three vertical plenums. The film cooling system is composed of five rows of leading-edge showerhead film holes and two rows of suction-side and pressure-side film holes downstream. The details of the film hole parameters can be found in the following tables.

Tab. 5.2 Cylindrical film hole geometry parameters

Cylindrical film hole	
Parameters	Values
Leading-edge film hole count	10+9+10+9+10 (total: 48)
Suction-side film hole count	19+19 (total: 38)
Pressure-side film hole count	19+19 (total: 38)
Leading-edge film hole	
Diameter *D*	1 mm
Length *L*	5*D*

Spacing S (distance in xy plane)	4D
Pitch P (distance in z direction)	7.5D
Inclined angle α	45°
Compound angle β	90°
Suction-side film hole	
Diameter D	1 mm
Length L	5D
Spacing S (distance in xy plane)	6D
Pitch P (distance in z direction)	4D
Inclined angle α	35°
Compound angle β	0°
Pressure-side film hole	
Diameter D	1 mm
Length L	7D
Spacing S (distance in xy plane)	6D
Pitch P (distance in z direction)	4D
Inclined angle α	20°
Compound angle β	0°

Tab. 5.3 Shaped film hole geometry parameters

Shaped film hole	
Parameters	Values
Leading-edge film hole count	9+8+9+8+9 (total: 43)
Suction-side film hole count	19+19 (total: 38)
Pressure-side film hole count	19+19 (total: 38)
Leading-edge film hole	
Diameter D	1 mm
Length L	5.8D
Spacing S (distance in xy plane)	5.5D
Pitch P (distance in z direction)	7.5D
Inclined angle α	30°
Compound angle β	90°
Suction-side film hole	
Diameter D	1 mm
Length L	5D
Spacing S (distance in xy plane)	5D
Pitch P (distance in z direction)	4D

Inclined angle α	30°
Compound angle β	0°
Pressure-side film hole	
Diameter D	1 mm
Length L	7D
Spacing S (distance in xy plane)	4D
Pitch P (distance in z direction)	4D
Inclined angle α	30°
Compound angle β	0°

5.2 Mesh and boundary conditions

The mesh was generated by the Ansys workbench meshing, as shown in Fig. 5.4. The near wall regions are refined such as the blade wall and the internal cooling passages in tubes. The external flow domain is swept with the mix of the quadrilateral and triangular face mesh types to reduce the mesh cell number and the computation time. And there is a transitional region between the solid wall and the external flow domain aiming at generating the tetrahedrons and the prism boundary layer. The solid-fluid interface between the transitional region and the solid wall is set with the coupled wall in Fluent, which allows the heat flux to pass the interface. The total mesh cells are about 28 and 44 million for the cylindrical and shaped film hole cases respectively to satisfy the requirement of y^+<1.

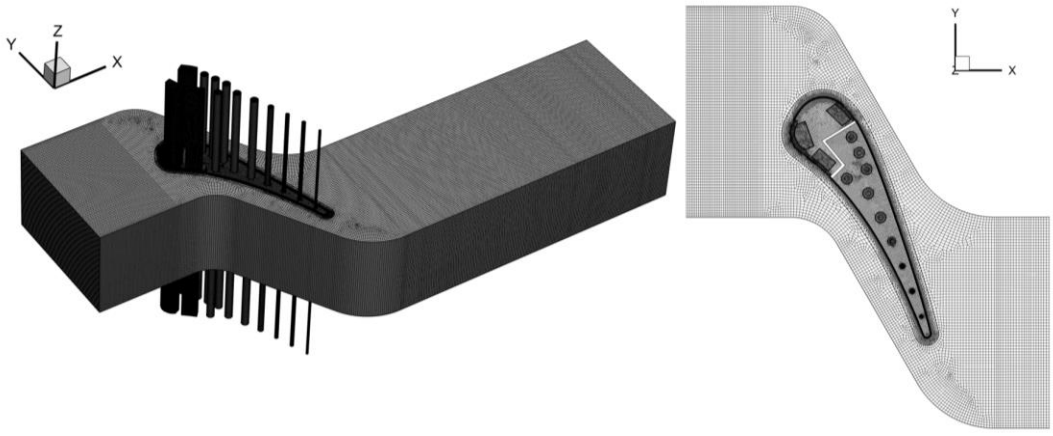

Fig. 5.4 Mesh of the computational domain of the film cooled C3X cascade

The case code 34155 in the NASA report [81] was selected as the boundary conditions. The mainstream inlet total pressure is 310,195Pa, and the mainstream outlet static pressure

is set to 215,251Pa based on the outlet Mach number Ma_2=0.75 with the following relationship:

$$\frac{P_{t1}}{P_2} = \left(1 + \frac{\gamma - 1}{2} \mathrm{Ma}_2^2\right)^{\frac{\gamma}{\gamma - 1}} \tag{1.56}$$

where γ is the heat capacity ratio. The mainstream inlet total temperature T_{t1} is specified at 701K, and the mainstream inlet turbulence intensity is set to 6.5% for both cases. The side walls are periodic. The top and bottom walls are set as slip walls because the effects of the endwall are ignored. The suction and pressure sides are no slip walls. The inlet mass flow rate of the leading-edge, suction-side and pressure-side film hole plenums are 0.0102kg/s, 0.0169kg/s and 0.0117kg/s respectively, and the outlet static pressure of the coolant plenums are prescribed at 98,584Pa, 98,584Pa and 98,763Pa. In order to make sure both cylindrical and shaped film cooling cases are equal in the mass flow rate of the coolant used for film cooling, for the case with shaped film holes, the outlet pressure of the film plenums is adjusted based on the coolant used in cylindrical film hole case.

However, the boundary conditions of the internal cooling tubes are missing, therefore, referring to the another earlier literature from NASA [82], the boundary conditions are specified as the mass flow inlet and static pressure outlet listed in Tab. 5.4. Note that since the back pressure data cannot be found, thus, 4 times of the atmosphere pressure are used as the outlet boundary condition. For the part of the LES setup, it is the same as the single hole film cooling cases above, and WALE subgrid model is used with SIMPLEC pressure-based solver.

Tab. 5.4 Boundary conditions of the internal cooling tubes

Number of tubes	Diameter mm	T_{t1} K	Mass flow rate kg/s
1	6.30	365.31	0.02110
2	6.30	365.29	0.02240
3	6.30	351.09	0.02170
4	6.30	355.05	0.02230
5	6.30	344.21	0.02260
6	6.30	383.91	0.02310
7	4.70	354.71	0.02230
8	3.10	380.76	0.00748

9	3.10	425.30	0.00469
10	1.98	467.00	0.00246

The ideal gas is set as the fluid and the stainless steel for solid vane. The density of the stainless steel is 8030kg/m^3, and the specific heat is 502 J/(kg · K). The thermal conductivity varies with the temperature as follows:

$$\lambda = 0.0115T + 9.9105 \tag{1.57}$$

5.3 Aerothermal performance of film cooled C3X vane

The film cooled NASA C3X turbine vane has been experimentally studied by several researchers, such as McClintic [153] and Dyson [154]. In terms of the numerical simulation, Jiang et al. [155] simulated the cylindrical film hole vane with mist-air as the coolant. SST *k*-ω and SST *k*-ω with γ-Re_θ transition model were tested and the results show that SST *k*-ω turbulence model with transition model reduced the errors in terms of the normalized temperature distributions on pressure and suction sides. Andrei et al. [156] also selected SST *k*-ω model to analyze the thermal performance of the unfilm cooled and film cooled C3X vanes. Gregory et al. [157] investigated heat transfer performance of VKI rotor and C3X with SST *k*-ω model in CFX. Overall, it can be found that RANS method is commonly used for the conjugate heat transfer of the film cooled C3X vane, however, according to the comparison from Dyson [154], for the thermal boundary prediction, SST *k*-ω with γ-Re_θ transition model shows the best agreement with experimental data, with 15% average error on the thermal boundary layer thickness, compared with 65% average error given by SST *k*-ω model. The accuracy of the RANS simulation still needs to be improved for the conjugate heat transfer problem, and LES is relative less investigated than RANS for the conjugate problem, thus, in this chapter LES is employed for the C3X numerical simulation.

Fig. 5.5 shows wall temperature T normalized by mainstream temperature T_∞ for the cylindrical hole film cooled C3X turbine vane at mid-span section to make the comparison between the simulation results and experimental data.

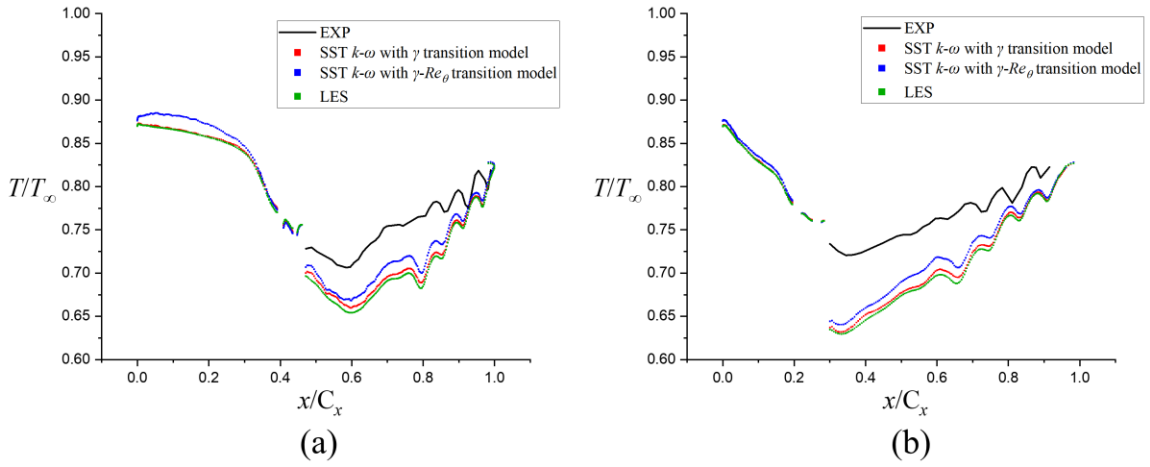

Fig. 5.5 Mid-span wall temperature normalized by mainstream temperature of the RANS, LES and experiment (a) suction side (b) pressure side

The experiment from NASA only considered the rear part of the vane downstream of the film cooling holes, so the temperature data of the leading-edge part are not measured and provided. Since the boundary condition of the internal cooling tube was not reported in the literature, the simulation near the thermal barrier is different from the experimental data. However, both simulation and experiment show an upward trend along the suction and pressure side. According to the previous publications, the turbulence model with the transition model has better capabilities to predict the film cooled turbine, therefore, LES is also compared with SST *k-ω* with *γ* transition model and SST *k-ω* with *γ-Reθ* transition model. The SST *k-ω* with *γ* transition model underestimates the wall temperature of the suction and pressure surfaces compared with the SST *k-ω* with *γ-Reθ* transition model, additionally the difference is more clearly for the pressure side. The SST *k-ω* with *γ* transition model shows a better agreement with the LES results than the SST *k-ω* with *γ-Reθ* transition model, though the normalized wall temperature is slightly higher than the LES. For the leading-edge part, the SST *k-ω* with *γ* transition model and LES almost coincide with each other on pressure and suction sides, but the SST *k-ω* with *γ-Reθ* transition model overestimates the normalized temperature than the others.

Tab. 5.5 lists the mass flow rate used for the leading-edge, suction-side and pressure-side film holes respectively.

Tab. 5.5 Mass flow rate and blowing ratio of C3X with cylindrical and shaped film holes

Position	Mass flow rate kg/s	Blowing ratio

Leading edge	0.004683966	1.0
Pressure side	0.003687655	2.0
Suction side	0.011874263	0.6

The blowing ratios at the leading edge and the pressure and suction sides are defined as equation 1.58 and 1.59.

$$\mathrm{M} = \frac{\dot{m}_c / \mathrm{A}_{in}}{\rho_\infty u_\infty} \tag{1.58}$$

$$\mathrm{M} = \frac{\dot{m}_c / \mathrm{A}_{in}}{\rho_{local} u_{local}} \tag{1.59}$$

where ρ_∞ and u_∞ denote the inlet mainstream density and velocity, and ρ_{local} and u_{local} represent the local mainstream density and velocity. The velocity at pressure side is lower than the one on suction side, thus the blowing ratio of pressure side is larger than that of the suction side.

Fig. 5.6 and Fig. 5.7 show time averaged T/T_∞ contours of the cross-sectional planes of C3X vane with cylindrical and shaped film holes by LES. Due to the thermal barrier, the rear part isn't affected by the front part. Because the boundary conditions of the radial internal cooling are identical to each other, the normalized temperature distributions are similar for the same cross-sectional planes. The coolant enters the film plenums from the bottom of the vane, thus, the coolant temperature of vane gradually increases from root to tip, and the reduced cooling effect causes the growth of the cross-sectional plane temperature of the vane.

The leading-edge region suffers from the high mainstream directly, and the cramped structure of the trailing edge limits the size of the internal cooling tube, which consequently leads to higher heat load than the middle chord region. The shaped leading-edge film holes result in a slightly lower temperature in the front part than the cylindrical film holes in root and 25% span planes. Besides, it can be found that in the regions of the suction and pressure sides downstream the film cooling holes, T/T_∞ of the cylindrical film hole case is relatively higher than the shaped film hole case, especially in the 75% span and the tip planes.

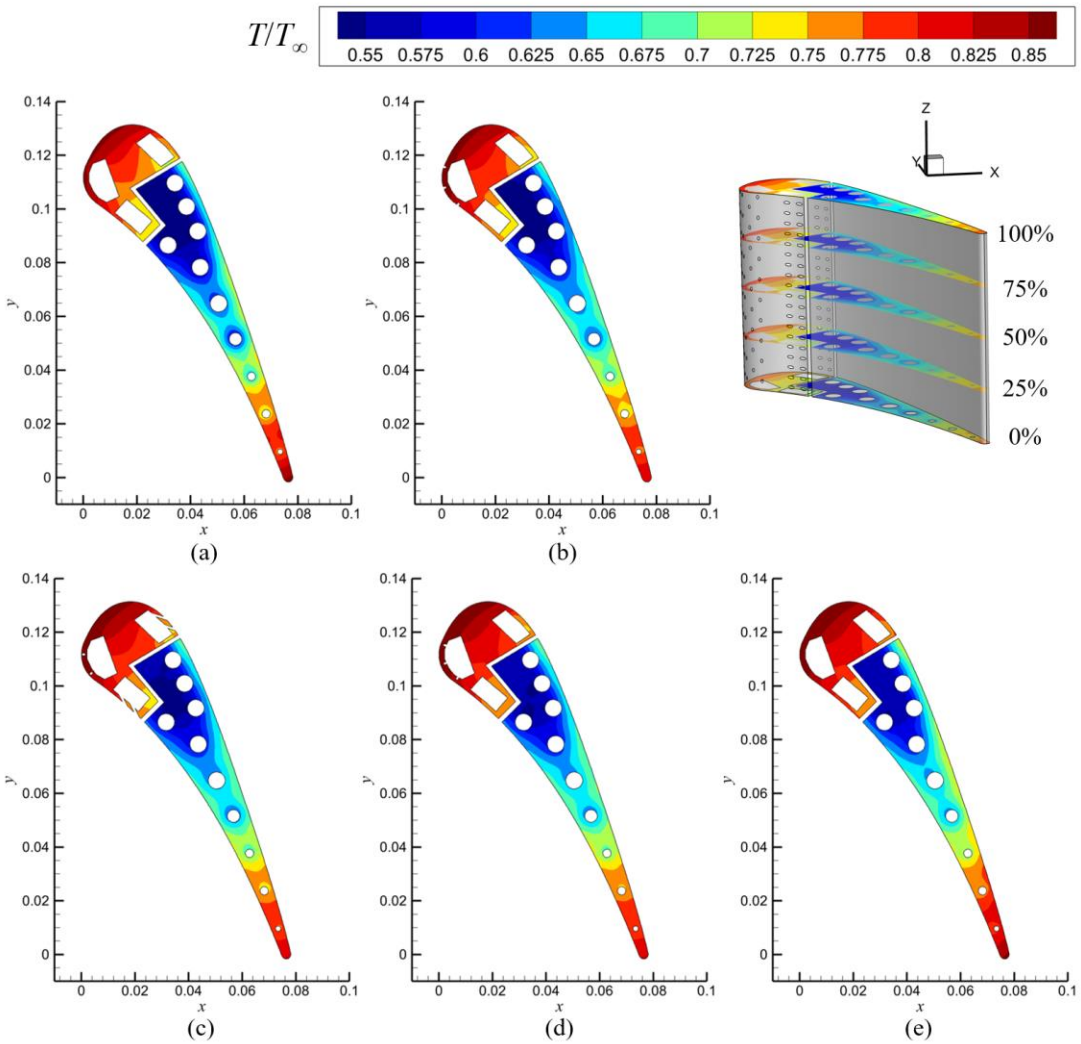

Fig. 5.6 Cross-sectional time averaged T/T_∞ contours of C3X vane with cylindrical film holes (a) root (b) 25% span (c) mid-span (d) 75% span (e) tip

Since the leading-edge region operates under high thermal load conditions, it's necessary to layout the film cooling holes at leading edge to protect the surface from the high temperature mainstream. Fig. 5.8 displays the time mean T/T_∞ distributions of cylindrical and shaped film cooling hole cases. For the cylindrical film holes, the high thermal load regions concentrated on the upper part of the surface. The temperature gradually drops downstream of the leading edge. Compared with the cylindrical film hole case, the shaped film hole provides positive effects on the leading-edge wall protection. High heat load area only occurs at the tip where T/T_∞ is over 0.87. Due to the 90° compound angle of the leading-edge film holes, L2, L3 and L4 column shaped holes cause lower T/T_∞ regions that form an inclined angle with respect to the shaped film hole axis.

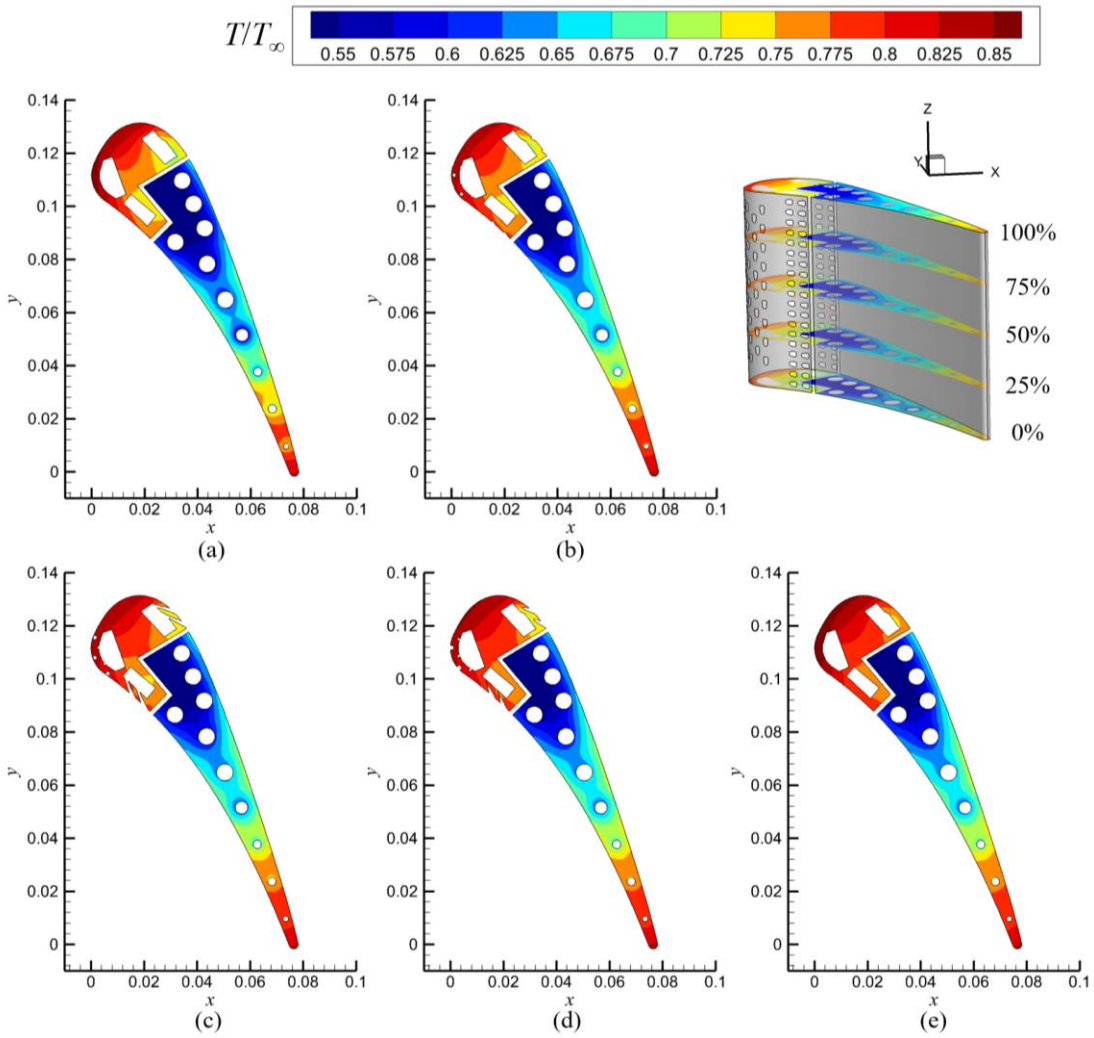

Fig. 5.7 Cross-sectional time averaged T/T_∞ contours of C3X vane with shaped film holes (a) root (b) 25% span (c) mid-span (d) 75% span (e) tip

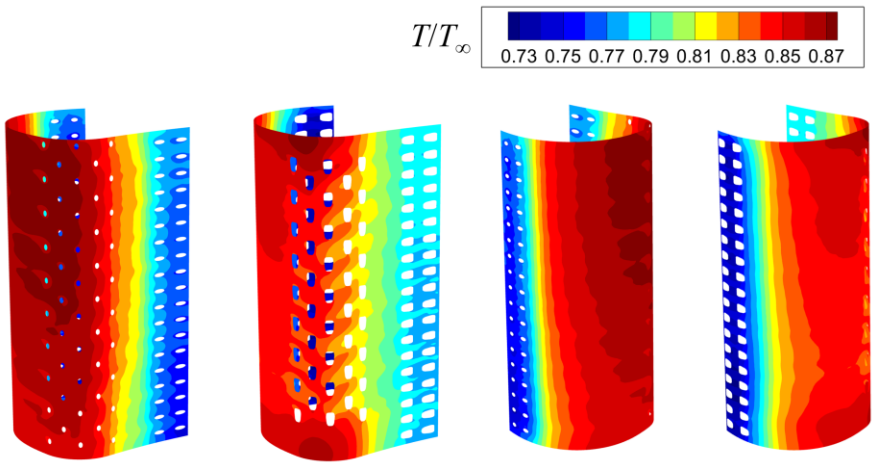

Fig. 5.8 Time averaged T/T_∞ distributions of leading-edge regions of cylindrical and shaped film cooling hole cases

Fig. 5.9 compares the time averaged normalized temperature distributions of pressure and suction sides between the cylindrical and shaped film hole cases. For both cases, the regions downstream of the film holes present remarkable low temperature on pressure and suction walls, due to the introduction of the film cooling. For the cylindrical film holes, the film cooling leads to a lower temperature area on suction side mainly from $L_{arc}/L_{arc\ max}$=0.34 to $L_{arc}/L_{arc\ max}$=0.58. Because the high velocity coolant is injected from the hole and lifted from the suction surface, the wall temperature is higher than the shaped film hole case in the near region behind the film hole. Corresponding to Fig. 5.10, the shaped film holes on suction side show better thermal performance and protection of the blade, compared with the cylindrical film holes, and the shaped film holes result in a uniform temperature distribution on suction side. With respect to the pressure side, two film hole structures provide a similar temperature distribution, whereas the shaped film holes show slightly lower temperature downstream of the film holes. At tip region the shaped film hole case can cover larger area than the cylindrical film hole case.

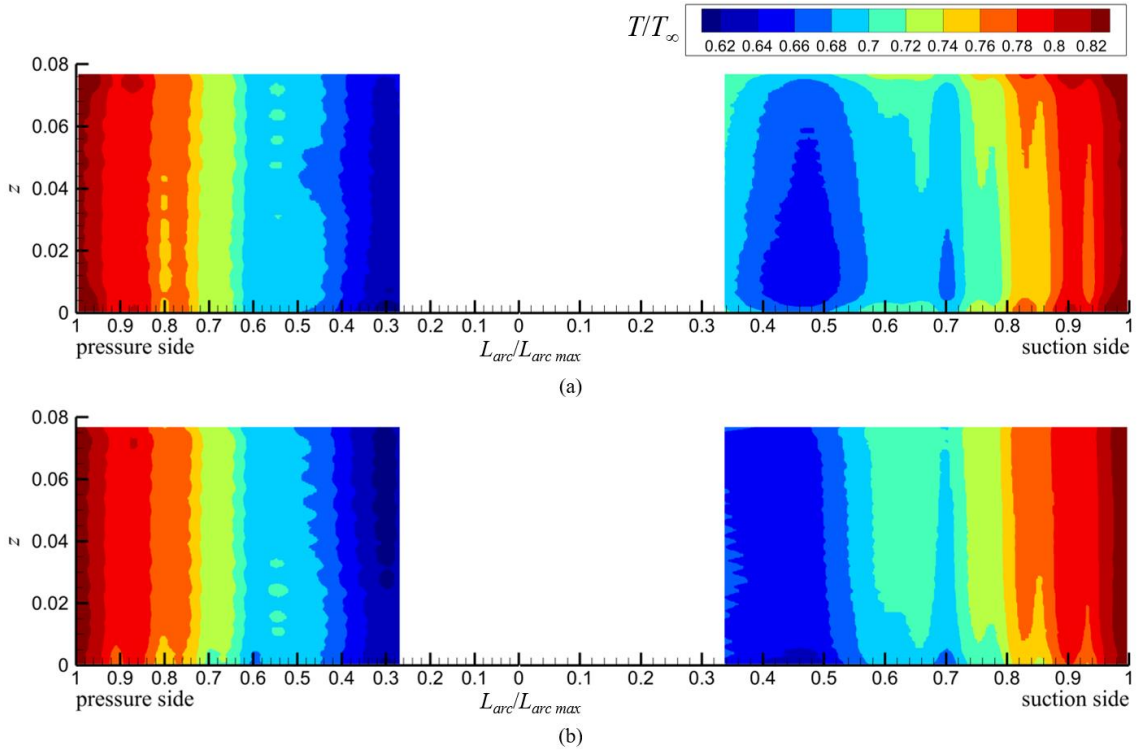

Fig. 5.9 Comparison of time averaged T/T_∞ distributions on pressure and suction sides (a) cylindrical film hole case (b) shaped film hole case

Additionally, Fig. 5.10 also illustrates the spanwise-averaged normalized temperature at leading edge. The shaped film hole reduces the maximum T/T_∞ to roughly 0.84 at x/C_x=0, comparing the maximum T/T_∞ =0.86 for cylindrical film hole case. Due to the film cooling protection for the leading-edge wall from x/C_x=-0.2-0.4, the leading-edge temperature of shaped film hole case decreases by up to 2.3%. The fluctuations occur approximately in the range of x/C_x=-0.8/-1 on suction side and x/C_x=0.7-1 on pressure side for both cases.

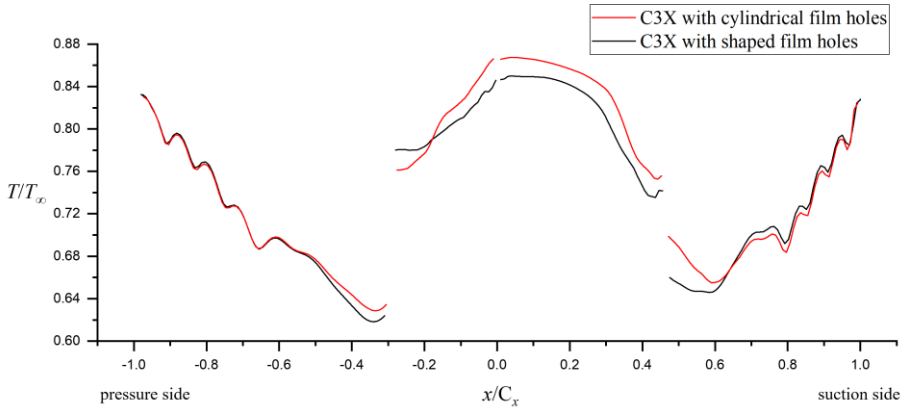

Fig. 5.10 Comparison of time averaged spanwise-averaged T/T_∞ distributions on pressure and suction sides

Fig. 5.11 illustrates the time averaged T/T_∞ distributions at various cross-sectional planes from root to tip. For the suction side, the shaped film hole case shows much better thermal performance at root and tip sections as well as the 25% span than that of the cylindrical film hole case in x/C_x=0.5-1.0, which contributes to the attachment of the injection and the lateral spreading of the coolant in shaped film hole case. For the pressure side, the normalized temperature gradually increases for C3X with cylindrical film holes from root to tip, while the T/T_∞ of C3X with shaped film holes is steadier and less affected by the internal radial cooling. In the trailing edge region, the shaped film hole case also presents lower temperature than that of the cylindrical film hole case. It can be inferred that the higher momentum coolant of cylindrical holes affects the flow field downstream of vane more relative to the shaped film hole. In the leading-edge region, the shaped hole case provides lower wall temperature at midspan and 75% span, compared with the cylindrical hole. Besides, according to Fig. 5.11a and Fig. 5.11e the temperature at tip is higher than that at root at leading edge for both cases.

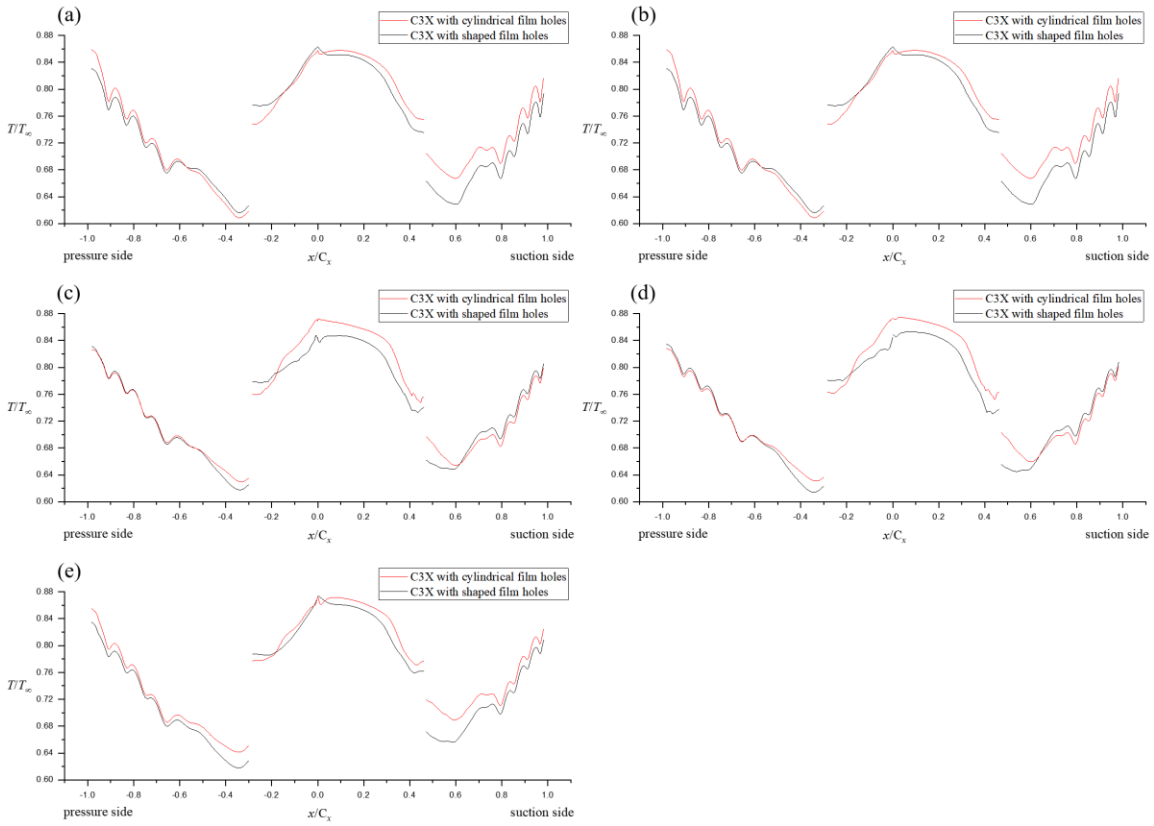

Fig. 5.11 Time averaged T/T_∞ distributions at various span (a) root (b) 25% span (c) mid-span (d) 75% span (e) tip

Fig. 5.12 presents the mean static pressure normalized by inlet total pressure. The experimental data is the case code 34000 from NASA[81], where the pressure in plenums is equal to the mainstream and no film coolant is injected from the cylindrical film holes. Comparing between the no film cooling experimental data and the simulation results of the C3X with film cooling, the p_s/p_{t1} distribution shows almost the same trend on the pressure side. The effects of the film cooling on the pressure distribution mainly consist in the suction side. The film holes are equipped between x/C_x=0.4 and x/C_x=0.5, and p_s/p_t is higher from x/C_x=0.2 to the trailing edge. The reason is due to the cooling injection, the mainstream bumps into the lower velocity coolant, the velocity is lower than the no film case and the pressure is increased clearly downstream of the film holes. Moreover, the velocity of the freestream is much higher on suction side than the pressure side, thus the deceleration effect of the flow near the wall is more obvious on suction side.

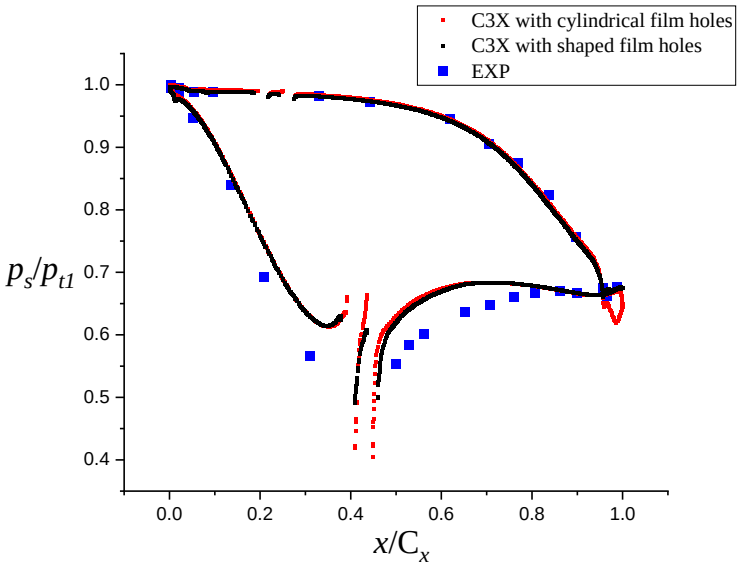

Fig. 5.12 Time averaged $p_s/p_{t\,in}$ distributions of C3X vane with cylindrical and shaped film holes

Time averaged T/T_∞ distributions at mid-span are shown in Fig. 5.13. The detailed views present the areas of the film holes on pressure side and suction sides. As the results of the simplified flat channel, the film coolant is lifted higher from the exit of the film hole into the mainstream on both pressure and suction sides for C3X with cylindrical film holes. Because of the expansion shape of the shaped film hole, the coolant jet is injected into the mainstream with lower velocity, thus can keep attached to the surface along the streamwise direction.

Fig. 5.14 depicts normalized velocity and the local streamlines at mid-span. From the cross-sectional plane, the jet normalized velocity u/u_∞ is about 3-4 at the exit of cylindrical film hole on suction side, while u/u_∞ is about 1 for shaped film hole on suction side. For the pressure side, u/u_∞ is in the range of 0.5 and 1 which is also higher than the shaped film hole. Note that a lower velocity region is formed at the expansion section of the shaped film hole, and the recirculation zone can be found. Due to the lower jet velocity from the film hole, the local mainstream near the wall is inclined to the exit of the film hole. For the cylindrical film hole, the coolant contains higher momentum at film hole exit, therefore, the injection penetrates into the local mainstream further.

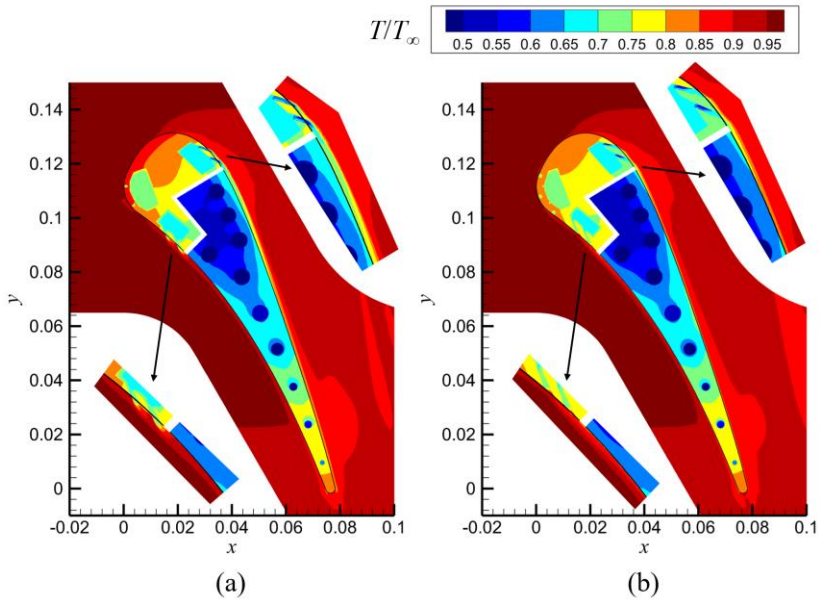

Fig. 5.13 Time averaged T/T_∞ distributions at mid-span (a) cylindrical film hole case (b) shaped film hole case

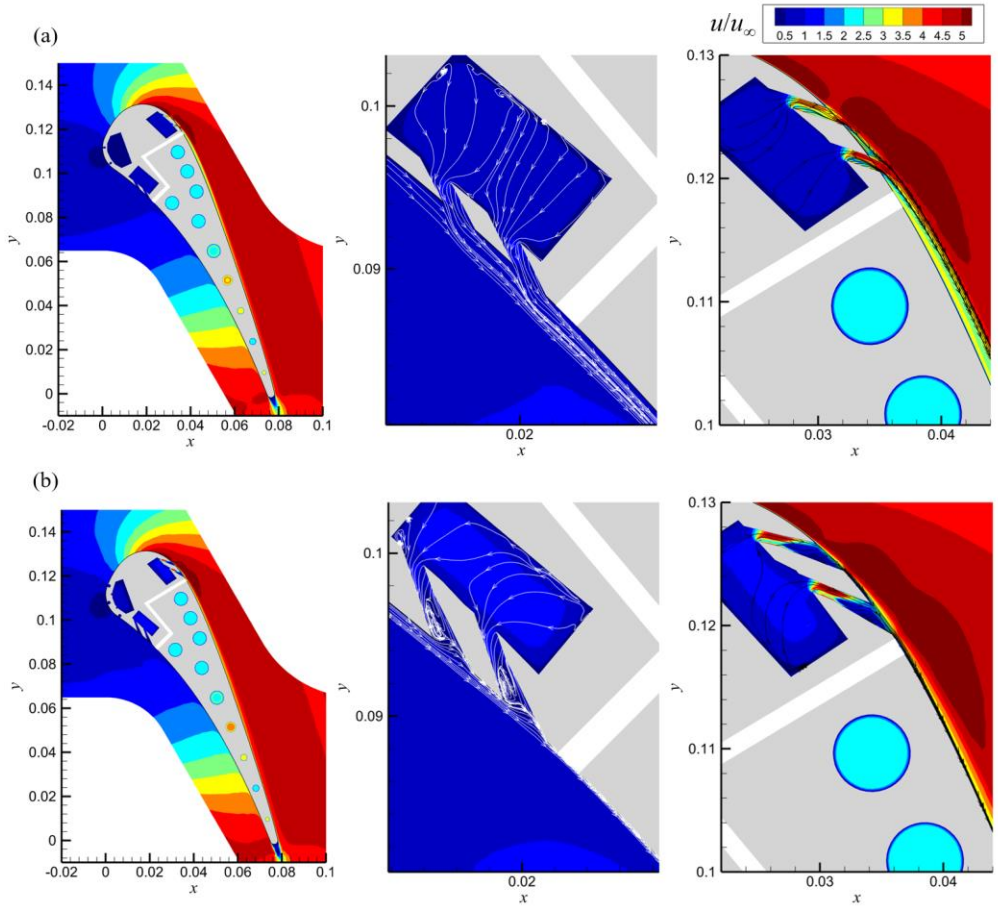

Fig. 5.14 Time averaged u/u_∞ contours and streamlines from film holes at mid-span (a) cylindrical film hole case (b) shaped film hole case

In Fig. 5.15, the velocity power spectral densities of the C3X vane are presented. Three monitor points are located downstream of the trailing edge of the vane. The main frequency is about 6,539 Hz and 17,872Hz for cylindrical and shaped film hole cases respectively. Note that an obvious peak value can be found in shaped film hole case, while for cylindrical case there is not a clear peak as the shaped hole case in Fig. 5.15(b). It could be implied that the cylindrical film hole on pressure and suction sides affects the downstream flow field and larger scale vortices are generated in the weak region. The shaped film hole causes more smaller scale vortices, and the frequency is higher with more fluctuations in the flow field downstream the cascade.

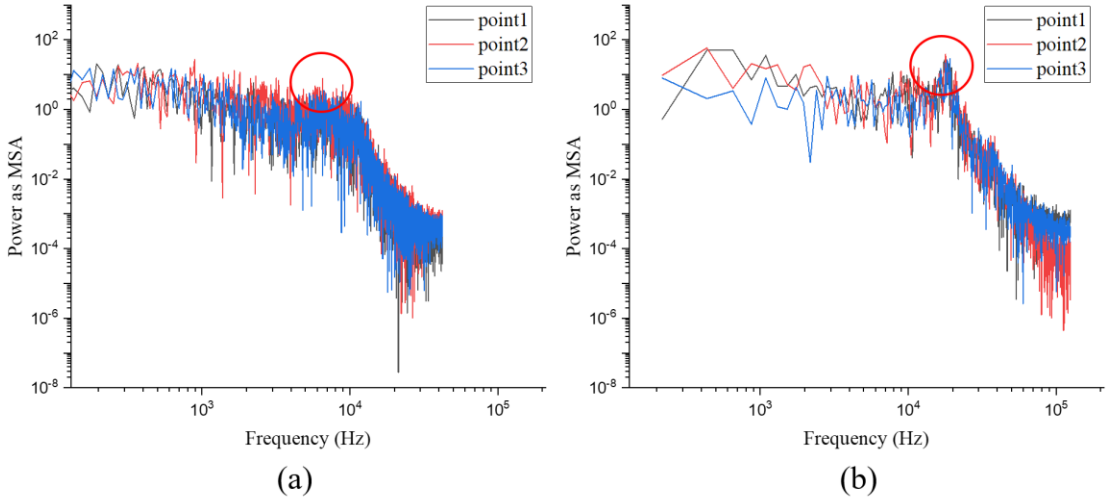

Fig. 5.15 Instantaneous velocity power spectral density (PSD) (a) cylindrical film hole case (b) shaped film hole case

Chapter 6

Conclusions

The work conducted in the PhD thesis studied the aerothermodynamics of the turbine external film cooling by numerical simulation method. Large eddy simulation was evaluated and used to reproduce the flow field of the conventional cylindrical and laidback fan-shaped film cooling hole structures and provide the details of the flow field and thermal performance. The simulation was implemented in the range of M=0.5-3.0 and Tu=0.5%-20% for the same density ratio DR=1.5. Besides, three different kinds of mainstream inlet boundary profiles were employed to investigate the effects on the cooling effectiveness. The Reynolds number based on film hole diameter D and the mainstream inlet velocity is 5,102. Additionally, C3X vane equipped with two film hole structures was investigated and analyzed by LES. The main conclusions are drawn as follows:

1. The comparison between the large eddy simulation with three different subgrid models and the RANS with various turbulent models were conducted under M=1.5, DR=1.5 Tu=0.5% conditions. Referring to the experimental data from Thole et al. [1], the average errors at x/D=0.2-32.5 are 5.9%, 3.8% and 2.6% for the Smagorinsky-Lilly, WMLES and WALE subgrid-scale models, respectively. The discrepancies of RNG k-ε, Realizable k-ε, Standard k-ω, *SST* k-ω with γ transition model and Reynolds stress model are from 23.0% to as high as 47.0%. All the RANS turbulence models overestimate the adiabatic film cooling effectiveness along the centerline of the bottom surface, wherein RNG k-ε turbulence model shows the best prediction capability though the error is still much larger than the LES results.
2. When M=1.0 and M=1.5, the shaped film hole provide the best performance at near and far field respectively. No separation occurs at M=1.5-3.0. High momentum at high blowing ratio resists the penetration of the injection into the mainstream and prolongs the mixing process to further downstream. At lower blowing ratio only anti-CRVP is formed to mitigate the trend of the coolant detachment and enhance the spreading of the coolant. At higher blowing ratio only CRVP generates and dominates the cooling

channel. Turbulent viscosities in different directions show strong anisotropy characteristics in film hole exit region.

3. The centerline and lateral-averaged film cooling effectiveness of the shaped film hole decays more markedly at higher turbulence intensity when M=1.5 and 2.0. High turbulence intensity enhances the mixing process and causes the effectiveness degradation at far field. The effects on the low blowing ratio are more serious relative to the high blowing ratio. Tu=20% results in a 13.4% and an 8.6% decrease of the area-averaged film cooling effectiveness for M=1.5 and 2.0 at x/D=0-30.
4. The inlet mainstream boundary layer affects the formation of the horseshoe vortices in leading edge region of the film hole exit. The velocity profile with thicker boundary layer ends the mixing process further downstream of the cooling channel, which leads to the slightly higher centerline cooling effectiveness. Besides, the thicker boundary layer causes the attenuation of the lateral spreading of the coolant at near field.
5. The convex curved bottom surface increases the centerline film cooling effectiveness by roughly 7.3% and 7.1% for M=1.5 and M=2.0 and decreases by 6.3% on average at M=3.0 from x/D=15 to x/D=40 where the lateral spreading of the coolant is insufficient especially at far field, and cooling effectiveness falls more quickly along the streamwise direction. From x/D=5 to x/D=40, the curved surface increases the lateral averaged film cooling effectiveness slightly by about 2.7% at M=1.5 and decreases by about 7.9% and 25.8% at M=2.0 and M=3.0 respectively. The convex curved surface produces more undesired effects on the cooling effectiveness at higher blowing ratio. The convex curved surface is more sensitive to the momentum in the coolant, compared with the flat surface.
6. Film cooled C3X vane reveals the aerothermal performance under the real engine conditions, compared with the low temperature simplified model investigation. C3X vane with shaped film holes reduces the maximum normalized temperature to 0.84 at leading edge, which decreased by 2.3% relative to the maximum T/T_∞ =0.86 of the cylindrical film hole case. The shaped film hole causes the coolant to cover more areas downstream of the pressure-side and suction-side film holes than the cylindrical film hole for the specified blowing ratio conditions, which is consistent with the results that the shaped film hole shows better cooling effectiveness at higher blowing ratio than the

cylindrical film hole downstream of the channel and the coolant is spread more sufficiently in lateral direction.

References

[1] Schroeder, R. P., and Thole, K. A., "Adiabatic Effectiveness Measurements for a Baseline Shaped Film Cooling Hole," Proc. ASME Turbo Expo 2014: Turbine Technical Conference and Exposition, American Society of Mechanical Engineers, Düsseldorf, Germany, p. V05BT13A036.

[2] Han, J. C., Dutta, S., and Ekkad, S., 2012, Gas turbine heat transfer and cooling technology, CRC Press.

[3] Boyce, M. P., 2011, Gas turbine engineering handbook, Elsevier.

[4] Clifford, R., 1985, "Rotating heat transfer investigations on a multi-pass cooling geometry," In AGARD Heat Transfer and Cooling in Gas Turbines.

[5] Ni, M., Zhu, H., Qiu, Y., Xu, D., and Liu, S., 2005, "Review of aero-turbine blade cooling technologies," Gas turbine technology, 18(4), pp. 25-33.

[6] 2011, "MHI Achieves 1,600°C Turbine Inlet Temperature in Test Operation of World's Highest Thermal Efficiency "J-Series" Gas Turbine," https://www.mhi.com/news/1105261435.html.

[7] Clarke, D. R., Oechsner, M., and Padture, N. P., 2012, "Thermal-barrier coatings for more efficient gas-turbine engines," MRS Bull., 37(10), pp. 891-898.

[8] Krishna Anand, V. G., and Parammasivam, K. M., 2021, "Thermal barrier coated surface modifications for gas turbine film cooling: a review," J. Therm. Anal. Calorim., 146(2), pp. 545-580.

[9] "Pratt & Whitney F135," https://en.wikipedia.org/wiki/Pratt_%26_Whitney_F135.

[10] Langston, L., 2018, "Single-crystal turbine blades earn ASME milestone status," Machine Design, 90, pp. 46-52.

[11] Wahl, J. B., and Harris, K., 1984, "Improved 3rd generation single crystal superalloy CMSX-4® Plus (SLS)–A study of evolutionary alloy development," Cannon-Muskegon Corporation, MI, pp. 49441-40506.

[12] Erickson, G. L., 1995, "A new, third-generation, single-crystal, casting superalloy," JOM, 47(4), pp. 36-39.

[13] Cao, Y., Tao, Z., Xu, G., Ding, S., Zhu, G., and Ji, S., 2005, Heat tranfer of aero engine, Beihang University Press.

[14] Sautner, M., Clouser, S., and Han, J. C., "Determination of surface heat transfer and film cooling effectiveness in unsteady wake flow conditions," Proc. AGARD CONFERENCE PROCEEDINGS AGARD CP, AGARD, pp. 6-6.

[15] Kan, R., 2014, "Flow and Heat Transfer Characteristics of Gas Turbine Blade Trailing-Edge Internal Cooling," Doctor, Tsinghua University.

[16] Huang, Y., Ekkad, S. V., and Han, J. C., 1998, "Detailed Heat Transfer Distributions Under an Array of Orthogonal Impinging Jets," J. Thermophys Heat Transfer, 12(1), pp. 73-79.

[17] Gao, L., 2003, "Effect of jet hole arrays arrangement on impingement heat transfer," Master, the Louisiana State University.

[18] Lee, J., Ren, Z., Ligrani, P., Fox, M. D., and Moon, H.-K., 2015, "Crossflows from jet array impingement cooling: Hole spacing, target plate distance, Reynolds number effects," Int. J. Therm. Sci., 88, pp. 7-18.

[19] Luo, L., Zhang, Y., Sunden, B., Qiu, D., Wang, S., and Zhang, X., 2020, "COMPUTATIONAL INVESTIGATION OF CURVATURE EFFECTS ON JET

IMPINGEMENT HEAT TRANSFER AT INTERNALLY COOLED TURBINE VANE LEADING EDGE REGIONS," Heat Transfer Research, 51(4), pp. 333-357.

[20] Camerlengo, G., Borello, D., Salvagni, A., and Sesterhenn, J., "Effects of Wall Curvature on the Dynamics of an Impinging Jet and Resulting Heat Transfer," Proc. Active Flow and Combustion Control 2018, Springer International Publishing, pp. 355-366.

[21] Buzzard, W., Ren, Z., Ligrani, P., Nakamata, C., and Ueguchi, S., "Influences of Target Surface Roughness on Impingement Jet Array Heat Transfer: Part 1 — Effects of Roughness Pattern, Roughness Height, and Reynolds Number," Proc. ASME Turbo Expo 2016: Turbomachinery Technical Conference and Exposition, American Society of Mechanical Engineers, p. V05AT13A003.

[22] Buzzard, W., Ren, Z., Ligrani, P. M., Nakamata, C., and Ueguchi, S., "Influences of Target Surface Roughness on Impingement Jet Array Heat Transfer: Part 2 — Effects of Roughness Shape, and Reynolds Number," Proc. ASME Turbo Expo 2016: Turbomachinery Technical Conference and Exposition, American Society of Mechanical Engineers, p. V05AT13A004.

[23] Han, J. C., Park, J. S., and Lei, C., 1984, "Heat transfer and pressure drop in blade cooling channels with turbulence promoters," No. NASA-CR-3837.

[24] Arun, K., and Prabhu, S. V., 2007, "Effect of Aspect Ratio, Channel Orientation, Rib Pitch-to-Height Ratio, and Number of Ribbed Walls on Pressure Drop Characteristics in a Rotating Channel with Detached Ribs," Int. J. Rotating Mach., 2007.

[25] Liu, Y.-H., Huh, M., Han, J.-C., and Moon, H.-K., "High Rotation Number Effect on Heat Transfer in a Triangular Channel With 45°, Inverted 45°, and 90° Ribs," Proc. ASME Turbo Expo 2009: Power for Land, Sea, and Air, American Society of Mechanical Engineers, pp. 127-138.

[26] Bagabir, A. M., Khamaj, J. A., and Hassan, A. S., 2013, "Numerical Study of Turbulent Periodic Flow and Heat Transfer in a Square Channel with Different Ribs," Journal of Applied Mathematics and Physics, 1.06, pp. 65-73.

[27] Tanda, G., 1996, "Application of optical methods to the study of convective heat transfer in rib-roughened channels," Doctor, The City University of London.

[28] Kan, R., Ren, J., and Jiang, H., "Combined Effects of Perforated Blockages and Pin Fins in a Trailing Edge Internal Cooling Duct," Proc. ASME Turbo Expo 2014: Turbine Technical Conference and Exposition, p. V05AT12A020.

[29] Roth, R., Lenk, G., Cobry, K., and Woias, P., 2013, "Heat transfer in freestanding microchannels with in-line and staggered pin fin structures with clearance," Int. J. Heat Mass Transfer, 67, pp. 1-15.

[30] Moon, M.-A., and Kim, K.-Y., 2014, "Analysis and optimization of fan-shaped pin–fin in a rectangular cooling channel," Int. J. Heat Mass Transfer, 72, pp. 148-162.

[31] Chyu, M. K., Siw, S. C., and Moon, H. K., "Effects of Height-to-Diameter Ratio of Pin Element on Heat Transfer From Staggered Pin-Fin Arrays," Proc. ASME Turbo Expo 2009: Power for Land, Sea, and Air, American Society of Mechanical Engineers, pp. 705-713.

[32] Siddique, W., Khan, N. A., and Haq, I., 2015, "Analysis of numerical results for two-pass trapezoidal channel with different cooling configurations of trailing edge: The effect of dimples," Appl. Therm. Eng., 89, pp. 763-771.
[33] Schukin, A. V., Kozlov, A. P., and Agachev, R. S., "Study and Application of Hemispheric Cavities for Surface Heat Transfer Augmentation," Proc. ASME 1995 International Gas Turbine and Aeroengine Congress and Exposition, American Society of Mechanical Engineers, p. V004T009A034.
[34] Chyu, M. K., Yu, Y., Ding, H., Downs, J. P., and Soechting, F. O., "Concavity Enhanced Heat Transfer in an Internal Cooling Passage," Proc. ASME 1997 International Gas Turbine and Aeroengine Congress and Exhibition, American Society of Mechanical Engineers, V003T09A080.
[35] Burgess, N. K., and Ligrani, P. M., "Effects of Dimple Depth on Nusselt Numbers and Friction Factors for Internal Cooling in a Channel," Proc. ASME Turbo Expo 2004: Power for Land, Sea, and Air, American Society of Mechanical Engineers, pp. 989-998.
[36] Hosseinalipour, S. M., Afkari, P., Shahbazian, H., and Sundén, B., 2019, "A numerical framework for heat transfer and pressure loss estimation of matrix cooling geometry in stationary and rotational states," Numerical Heat Transfer, Part A: Applications, 76(5), pp. 348-368.
[37] Saha, K., Guo, S., Acharya, S., and Nakamata, C., "Heat transfer and pressure measurements in a lattice-cooled trailing edge of a turbine airfoil," Proc. ASME Turbo Expo 2008: Power for Land, Sea, and Air, American Society of Mechanical Engineers, pp. 1117–1125.
[38] Metzger, D. E., Fan, C. S., and Haley, S. W., 1984, "Effects of pin shape and array orientation on heat transfer and pressure loss in pin fin arrays," ASME, Transactions, Journal of Engineering for Gas Turbines and Power, 106, pp. 252-257.
[39] Carcasci, C., Facchini, B., Pievaroli, M., Tarchi, L., Ceccherini, A., and Innocenti, L., "Heat Transfer and Pressure Drop Measurements on Rotating Matrix Cooling Geometries for Airfoil Trailing Edges," Proc. ASME Turbo Expo 2015: Turbine Technical Conference and Exposition, American Society of Mechanical Engineers, pp. V05AT11A011-V005AT011A011.
[40] Saha, K., Acharya, S., and Nakamata, C., "Heat Transfer and Pressure Drop in a Converging Lattice Structure for Airfoil Trailing Edge Cooling," Proc. ASME 2008 International Mechanical Engineering Congress and Exposition, American Society of Mechanical Engineers, pp. 1175-1184.
[41] Bu, S., Yang, L., Qiu, H., Luan, Y., and Sun, H., 2017, "Effect of sidewall slots and pin fins on the performance of latticework cooling channel for turbine blades," Appl. Therm. Eng., 117, pp. 275-288.
[42] Sun, H., Sun, T., Yang, L., Bu, S., and Luan, Y., 2018, "Effect of bleed hole on internal flow and heat transfer in matrix cooling channel," Appl. Therm. Eng., 136, pp. 419-430.
[43] Bunker, R. S., "Latticework (Vortex) Cooling Effectiveness: Part 1—Stationary Channel Experiments," Proc. ASME Turbo Expo 2004: Power for Land, Sea, and Air, American Society of Mechanical Engineers, pp. 909–918.

[44] Liu, J. H., Liu, Y. B., and Liu, L., 2018, "Film cooling modeling of a turbine vane with multiple configurations of holes," Case Stud. Therm. Eng., 11, pp. 71-80.
[45] Smith, L., Karim, H., Etemad, S., and Pfefferle, W. C., 2006, The gas turbine handbook, National Energy Technology Laboratory.
[46] Scesa, S., 1954, "Effect of local normal injection on flat-plate heat transfer," University of California, Berkeley.
[47] Seban, R. A., and Back, L. H., 1962, "Velocity and Temperature Profiles in Turbulent Boundary Layers With Tangential Injection," J. Heat Transfer, 84(1), pp. 45-54.
[48] Seban, R. A., 1960, "Heat Transfer and Effectiveness for a Turbulent Boundary Layer With Tangential Fluid Injection," J. Heat Transfer, 82(4), pp. 303-312.
[49] Seban, R. A., 1960, "Effects of initial boundary-layer thickness on a tangential injection system," J. Heat Transfer, 82(4), pp. 392-393.
[50] Eckert, E. R. G., and Birkebak, R. C., 1964, "The effects of slot geometry on film cooling," Heat Transfer, Thermodynamics, and Education, pp. 150-163.
[51] Chin, J. H., Skirvin, S. C., Hayes, L. E., and Silver, A. H., 1958, "Adiabatic Wall Temperature Downstream of a Single Tangential Injection Slot," ASME Paper(58-A), p. 107.
[52] Hartnett, J. P., Birkebak, R. C., and Eckert, E. R. G., 1961, "Velocity Distributions, Temperature Distributions, Effectiveness and Heat Transfer for Air Injected Through a Tangential Slot Into a Turbulent Boundary Layer," J. Heat Transfer, 83(3), pp. 293-305.
[53] Eckert, E. R. G., 1970, "Gas-to-gas film cooling," Journal of engineering physics, 19(3), pp. 1091-1101.
[54] Sinha, A. K., Bogard, D. G., and Crawford, M. E., 1991, "Film-Cooling Effectiveness Downstream of a Single Row of Holes With Variable Density Ratio," J. Turbomach., 113(3), pp. 442-449.
[55] Pietrzyk, J. R., Bogard, D. G., and Crawford, M. E., 1989, "Hydrodynamic Measurements of Jets in Crossflow for Gas Turbine Film Cooling Applications," J. Turbomach., 111(2), pp. 139-145.
[56] Pietrzyk, J. R., Bogard, D. G., and Crawford, M. E., 1990, "Effects of Density Ratio on the Hydrodynamics of Film Cooling," J. Turbomach., 112(3), pp. 437-443.
[57] Thole, K. A., Sinha, A., Bogard, D. G., and Crawford, M. E., 1992, "Mean temperature measurements of jets with a crossflow for gas turbine film cooling application," Rotating Machinery Transport Phenomena, pp. 69-85.
[58] Bunker, R. S., 2005, "A Review of Shaped Hole Turbine Film-Cooling Technology," J. Heat Transfer, 127(4), pp. 441-453.
[59] Gritsch, M., Schulz, A., and Wittig, S., 1998, "Adiabatic Wall Effectiveness Measurements of Film-Cooling Holes With Expanded Exits," J. Turbomach., 120(3), pp. 549-556.
[60] Treager, I. E., 1979, Aircraft gas turbine engine technology, McGraw-Hill.
[61] Kim, Y. W., Downs, J., Soechting, F. O., Abdel-Messeh, W., Steuber, G., and Tanrikut, S., 1995, "A summary of the cooled turbine blade tip heat transfer and film effectiveness investigations performed by Dr. DE Metzger," J. Turbomach., 117(1), pp. 1-11.

[62] Kim, Y. W., and Metzger, D. E., 1995, "Heat Transfer and Effectiveness on Film Cooled Turbine Blade Tip Models," J. Turbomach., 117(1), pp. 12-21.
[63] Bunker , R. S., Bailey, J. C., and Ameri, A. A., 1999, "Heat Transfer and Flow on the First-Stage Blade Tip of a Power Generation Gas Turbine: Part 1—Experimental Results," J. Turbomach., 122(2), pp. 263-271.
[64] Kwak, J. S., and Han, J. C., "Heat Transfer Coefficient and Film-Cooling Effectiveness on the Squealer Tip of a Gas Turbine Blade," Proc. ASME Turbo Expo 2002: Power for Land, Sea, and Air, pp. 1073-1082.
[65] Mhetras, S., Yang, H., Gao, Z., and Han, J.-C., "Film-Cooling Effectiveness on Squealer Rim Walls and Squealer Cavity Floor of a Gas Turbine Blade Tip Using Pressure Sensitive Paint," Proc. ASME Turbo Expo 2005: Power for Land, Sea, and Air, American Society of Mechanical Engineers, pp. 397-408.
[66] Ahn, J., Mhetras, S., and Han, J. C., 2005, "Film-Cooling Effectiveness on a Gas Turbine Blade Tip Using Pressure-Sensitive Paint," J. Heat Transfer, 127(5), pp. 521-530.
[67] Yan, X., Huang, Y., and He, K., 2018, "Effect of ejection angle and blowing ratio on heat transfer and film cooling effect on a winglet tip," Int. J. Heat Mass Transfer, 125, pp. 357-374.
[68] Yan, X., Huang, Y., and He, K., 2017, "Investigations into heat transfer and film cooling effect on a squealer-winglet blade tip," Int. J. Heat Mass Transfer, 115, pp. 955-978.
[69] He, K., Li, J., and Yan, X., 2018, "Numerical investigations into heat transfer and film cooling effect on a transonic blade endwall," Appl. Therm. Eng., 129, pp. 934-952.
[70] He, K., 2017, "Investigations of film cooling and heat transfer on a turbine blade squealer tip," Appl. Therm. Eng., 110, pp. 630-647.
[71] Dunn, M. G., and Stoddard, F. J., 1979, "Measurement of Heat-Transfer Rate to a Gas Turbine Stator," Journal of Engineering for Power, 101(2), pp. 275-280.
[72] Takeishi, K., Matsuura, M., Aoki, S., and Sato, T., 1990, "An Experimental Study of Heat Transfer and Film Cooling on Low Aspect Ratio Turbine Nozzles," J. Turbomach., 112(3), pp. 488-496.
[73] Friedrichs, S., Hodson, H. P., and Dawes, W. N., "Distribution of Film-Cooling Effectiveness on a Turbine Endwall Measured Using the Ammonia and Diazo Technique," Proc. ASME 1995 International Gas Turbine and Aeroengine Congress and Exposition, American Society of Mechanical Engineers, V004T09A001.
[74] Satta, F., and Tanda, G., 2015, "Effect of discrete-hole arrangement on film-cooling effectiveness for the endwall of a turbine blade cascade," Appl. Therm. Eng., 91, pp. 507-514.
[75] Lynch, S. P., and Thole, K. A., 2017, "Heat Transfer and Film Cooling on a Contoured Blade Endwall With Platform Gap Leakage," J. Turbomach., 139(5).
[76] Mensch, A. E., and Thole, K. A., 2016, "Effects of non-axisymmetric endwall contouring and film cooling on the passage flowfield in a linear turbine cascade," Exp. Fluids, 57(1).
[77] Kercher, D. M., 2000, "Turbine Airfoil Leading Edge Film Cooling Bibliography: 1972–1998," Int. J. Rotating Mach., 6(5), pp. 313-319.

[78] Hanus, G. J., and L'Ecuyert, M. R., 1977, "Leading-Edge Injection for Film Cooling of Turbine Vanes," J. Energy, 1(1), pp. 44-49.
[79] Kim, Y. J., and Kim, S. M., 2004, "Influence of shaped injection holes on turbine blade leading edge film cooling," Int. J. Heat Mass Transfer, 47(2), pp. 245-256.
[80] Elnady, T., Hassan, I., Kadem, L., and Lucas, T., 2013, "Cooling effectiveness of shaped film holes for leading edge," Exp. Therm Fluid Sci., 44, pp. 649-661.
[81] Hylton, L. D., Nirmalan, V., Sultanian, B. K., and Kaufman, R. M., 1988, "The effects of leading edge and downstream film cooling on turbine vane heat transfer," No. ALLISON-EDR-13481.
[82] Hylton, L. D., Mihelc, M. S., Turner, E. R., Nealy, D. A., and York, R. E., 1983, "Analytical and Experimental Evaluation of the Heat Transfer Distribution over the Surfaces of Turbine Vanes," No. NAS 1.26:168015.
[83] Goldstein, R., Eckert, E. R. G., Eriksen, V. L., and Ramsey, J. W., 1970, "FILM COOLING FOLLOWING INJECTION THROUGH INCLINED CIRCULAR TUBES," Israel journal of technology, 8(1-2), pp. 145-154.
[84] Pietrzyk, J. R., Bogard, D. G., and Crawford, M. E., 1989, "Effects of Density Ratio on the Hydrodynamics of Film Cooling," p. V004T008A018.
[85] Abhari, R. S., and Epstein, A. H., 1994, "An Experimental Study of Film Cooling in a Rotating Transonic Turbine," J. Turbomach., 116(1), pp. 63-70.
[86] Doorly, J. E., and Oldfield, M. L. G., 1986, "New Heat Transfer Gages for Use on Multilayered Substrates," J. Turbomach., 108(1), pp. 153-160.
[87] Oldfield, M. L. G., Bryanston-Cross, P. J., Nicholson, J. H., and Scrivener, C. T. J., 1986, "A study of passage flow through a cascade of turbine blades using image plane holographic interferometry," In AGARD Advanced Instrumentation for Aero Engine Components 12 p (SEE N87-21170 14-31.
[88] Blair, M. F., and Lander, R. D., 1975, "New Techniques for Measuring Film Cooling Effectiveness," J. Heat Transfer, 97(4), pp. 539-543.
[89] Eberly, M. K., 2012, "Time-resolved Studies of High Density Ratio Film-cooling Flows," Master, The Pennsylvania State University
[90] Gregory, J. W., Asai, K., Kameda, M., Liu, T., and Sullivan, J. P., 2008, "A review of pressure-sensitive paint for high-speed and unsteady aerodynamics," Proceedings of the Institution of Mechanical Engineers, Part G: Journal of Aerospace Engineering, 222(2), pp. 249-290.
[91] McLachlan, B. G., and Bell, J. H., 1995, "Pressure-sensitive paint in aerodynamic testing," Exp. Therm Fluid Sci., 10(4), pp. 470-485.
[92] Zhang, L., Baltz, M., Pudupatty, R., and Fox, M., "Turbine Nozzle Film Cooling Study Using the Pressure Sensitive Paint (PSP) Technique," Proc. ASME 1999 International Gas Turbine and Aeroengine Congress and Exhibition, American Society of Mechanical Engineers, p. V003T001A057.
[93] Wang, N., Zhang, M., Shiau, C.-C., and Han, J.-C., "Film Cooling Effectiveness From Two-Row of Compound Angled Cylindrical Holes Using PSP Technique," Proc. ASME Turbo Expo 2018: Turbomachinery Technical Conference and Exposition, p. V05CT19A003.
[94] Li, X., Qin, Y., Ren, J., and Jiang, H., "Algebraic Anisotropic Turbulence Modeling of Compound Angled Film Cooling Validated by PIV and PSP Measurements,"

Proc. ASME Turbo Expo 2013: Turbine Technical Conference and Exposition, p. V03BT13A028.
[95] Ravelli, S., Casarsa, L., and Barigozzi, G., 2019, "Numerical evaluation of showerhead film cooling aerothermal performance on a first-stage vane," Int. J. Therm. Sci., 141, pp. 171-186.
[96] Ravelli, S., and Barigozzi, G., 2019, "Numerical evaluation of heat/mass transfer analogy for leading edge showerhead film cooling on a first-stage vane," Int. J. Heat Mass Transfer, 129, pp. 842-854.
[97] Abdeh, H., Barigozzi, G., Ravelli, S., and Rouina, S., 2020, "A Parametric Investigation of Vane Showerhead Film Cooling by Pressure-Sensitive Paint Technique," J. Turbomach., 142(3).
[98] Drost, U., Bölcs, A., and Hoffs, A., "Utilization of the Transient Liquid Crystal Technique for Film Cooling Effectiveness and Heat Transfer Investigations on a Flat Plate and a Turbine Airfoil," Proc. ASME 1997 International Gas Turbine and Aeroengine Congress and Exhibition, American Society of Mechanical Engineers, p. V003T009A006.
[99] Lutum, E., von Wolfersdorf, J., Semmler, K., Dittmar, J., and Weigand, B., 2001, "An experimental investigation of film cooling on a convex surface subjected to favourable pressure gradient flow," Int. J. Heat Mass Transfer, 44(5), pp. 939-951.
[100] Barigozzi, G., Franchini, G., and Perdichizzi, A., "The Effect of an Upstream Ramp on Cylindrical and Fan-Shaped Hole Film Cooling: Part II — Adiabatic Effectiveness Results," Proc. ASME Turbo Expo 2007: Power for Land, Sea, and Air, American Society of Mechanical Engineers, pp. 115-123.
[101] Satta, F., and Tanda, G., 2014, "Measurement of local heat transfer coefficient on the endwall of a turbine blade cascade by liquid crystal thermography," Exp. Therm Fluid Sci., 58, pp. 209-215.
[102] Chen, P., Wang, L., Li, X., Ren, J., Jiang, H., and Simon, T., 2020, "Enhancement of Film Cooling Effectiveness Using Dean Vortices," J. Turbomach., 142(1).
[103] Li, Y., Zhang, Y., Su, X., and Yuan, X., 2018, "Experimental and numerical investigations of shaped hole film cooling with the influence of endwall cross flow," Int. J. Heat Mass Transfer, 120, pp. 42-55.
[104] Sreedharan, S. S., and Tafti, D. K., "Effect of Blowing Ratio in the Near-Stagnation Region of a Three-Row Leading Edge Film Cooling Geometry Using Large Eddy Simulations," Proc. ASME Turbo Expo 2009: Power for Land, Sea, and Air, American Society of Mechanical Engineers, pp. 213-224.
[105] North, G. R., Pyle, J. A., and Zhang, F., 2014, Encyclopedia of atmospheric sciences, Elsevier.
[106] Rozati, A., and Tafti, D. K., 2008, "Large-eddy simulations of leading edge film cooling: Analysis of flow structures, effectiveness, and heat transfer coefficient," Int. J. Heat Fluid Flow, 29(1), pp. 1-17.
[107] Li, W., Shi, W., Li, X., Ren, J., and Jiang, H., "Large Eddy Simulation of Axial and Compound Angle Holes With Varying Hole Length-to-Diameter Ratio," Proc. ASME Turbo Expo 2017: Turbomachinery Technical Conference and Exposition, American Society of Mechanical Engineers, Charlotte, North Carolina, USA, p. V05AT12A004.

[108] Zamiri, A., You, S. J., and Chung, J. T., 2020, "Large eddy simulation of unsteady turbulent flow structures and film-cooling effectiveness in a laidback fan-shaped hole," Aerosp. Sci. Technol., 100, p. 105793.
[109] Muldoon, F., and Acharya, S., 2006, "Analysis of k and epsilon Budgets for Film Cooling Using Direct Numerical Simulation," AIAA Journal, 44(12), pp. 3010-3021.
[110] Muldoon, F., and Acharya, S., "Direct Numerical Simulation of a Film Cooling Jet," Proc. ASME Turbo Expo 2004: Power for Land, Sea, and Air, American Society of Mechanical Engineers, pp. 461-473.
[111] Muldoon, F., and Acharya, S., 2009, "DNS study of pulsed film cooling for enhanced cooling effectiveness," Int. J. Heat Mass Transfer, 52(13), pp. 3118-3127.
[112] Fu, W.-S., Chao, W.-S., Tsubokura, M., Li, C.-G., and Wang, W.-H., 2018, "Direct numerical simulation of film cooling with a fan-shaped hole under low Reynolds number conditions," Int. J. Heat Mass Transfer, 123, pp. 544-560.
[113] Cao, L., Tang, X., Zhang, Y., Xue, M., Li, A., Gai, Q., and Liu, F., 2006, "Progress of Advanced Near Net- Shape InvestmentCasting Technology of Superalloys," JOURNAL OF AERONAUTICAL MATERIALS(03), pp. 238-243.
[114] Xu, L., Bo, S., Hongde, Y., and Lei, W., 2015, "Evolution of Rolls-royce Air-cooled Turbine Blades and Feature Analysis," Procedia Eng., 99, pp. 1482-1491.
[115] Wassell, A. B., and Bhangu, J. K., "The Development and Application of Improved Combustor Wall Cooling Techniques," Proc. ASME 1980 International Gas Turbine Conference and Products Show, American Society of Mechanical Engineers, p. V01AT01A066.
[116] Frasier, D. J., 1999, "Single-cast, high-temperature thin wall structures having a high conductivity member connecting the walls and methods of making the same," Allison Engine Company, Inc., Indianapolis, Ind.
[117] Helmink, R. C., 2012, "Evaluation technique for bonded, dual wall static and rotating airfoil materials," Rolls-Royce North American Technologies, Inc., Indianapolis, IN(US).
[118] F.BROWN, S., 1990, "21st century hot jet engines," Popular science, pp. 87-89.
[119] Thomas, M., Helmink, R., Frasier, D., Whetstone, J., Harris, K., Erickson, G., Sikkenga, S., and Eridon, J., 1994, "Allison manufacturing, property and turbine engine performance of CMSX-4 single crystal airfoils," Materials for advanced power engineering, Part II, pp. 1075-1098.
[120] "Thermal barrier coating," https://en.wikipedia.org/wiki/Thermal_barrier_coating.
[121] Bennett, T. D., and Yu, F., 2005, "A nondestructive technique for determining thermal properties of thermal barrier coatings," J. Appl. Phys., 97(1).
[122] Sahith, M. S., Giridhara, G., and Kumar, R. S., 2018, "Development and analysis of thermal barrier coatings on gas turbine blades – A Review," Mater. Today:. Proc., 5(1, Part 3), pp. 2746-2751.
[123] Anderson, J. D., Degrez, G., Dick, E., and Grundmann, R., 2009, Computational fluid dynamics: an introduction, Springer.
[124] Launder, B. E., and Spalding, D. B., 1972, "Lectures in mathematical models of turbulence."
[125] Yakhot, V., and Orszag, S. A., 1986, "Renormalization group analysis of turbulence. I. Basic theory," J. Sci. Comput., 1(1), pp. 3-51.

[126] Wang, F., 2004, Analysis of computational fluid dynamics: CFD principle and application, Tsinghua University Press.
[127] Shih, T.-H., Liou, W. W., Shabbir, A., Yang, Z., and Zhu, J., 1995, "A new k-ϵ eddy viscosity model for high reynolds number turbulent flows," Comput. Fluids, 24(3), pp. 227-238.
[128] Wilcox, D. C., 1998, Turbulence modeling for CFD, DCW industries La Canada, CA.
[129] Inc., F., 2017, "ANSYS Fluent Theory Guide."
[130] Smagorinsky, J., 1963, "General circulation experiments with the primitive equations: I. The basic experiment," Mon. Weather Rev., 91(3), pp. 99-164.
[131] Deardorff, J. W., 1970, "A numerical study of three-dimensional turbulent channel flow at large Reynolds numbers," J. Fluid Mech., 41(2), pp. 453-480.
[132] Zhang, Z., Cui, G., and Xu, X., 2008, Large eddy simulation of turbulence theory and applications, Tsinghua University Press.
[133] Garnier, E., Adams, N., and Sagaut, P., 2009, Large eddy simulation for compressible flows, Springer Science & Business Media.
[134] Fawcett, R. J., Wheeler, A. P. S., He, L., and Taylor, R., 2011, "Experimental Investigation Into Unsteady Effects on Film Cooling," J. Turbomach., 134(2).
[135] Gritsch, M., Colban, W., Schär, H., and Döbbeling, K., 2005, "Effect of Hole Geometry on the Thermal Performance of Fan-Shaped Film Cooling Holes," J. Turbomach., 127(4), pp. 718-725.
[136] Kraichnan, R. H., 1970, "Diffusion by a Random Velocity Field," The Physics of Fluids, 13(1), pp. 22-31.
[137] Smirnov, A., Shi, S., and Celik, I., 2001, "Random Flow Generation Technique for Large Eddy Simulations and Particle-Dynamics Modeling," J. Fluids Eng., 123(2), pp. 359-371.
[138] Eberly, M. K., and Thole, K. A., 2013, "Time-Resolved Film-Cooling Flows at High and Low Density Ratios," J. Turbomach., 136(6), p. 061003.
[139] Mensch, A., and Thole, K. A., 2013, "Overall Effectiveness of a Blade Endwall With Jet Impingement and Film Cooling," J. Eng. Gas Turbines Power, 136(3).
[140] Burd, S. W., and Simon, T. W., 1999, "Measurements of Discharge Coefficients in Film Cooling," J. Turbomach., 121(2), pp. 243-248.
[141] Liu, C.-l., Ye, L., Zhu, H.-r., and Luo, J.-x., 2017, "Investigation on the effects of rib orientation angle on the film cooling with ribbed cross-flow coolant channel," Int. J. Heat Mass Transfer, 115, pp. 379-394.
[142] Saumweber, C., Schulz, A., and Wittig, S., 2003, "Free-Stream Turbulence Effects on Film Cooling With Shaped Holes," J. Turbomach., 125(1), pp. 65-73.
[143] Lumley J, L., 1967, "The structure of inhomogeneous turbulent flows," Atmospheric Turbulence and Radio Wave Propagation, pp. 166-178.
[144] Haven, B., Yamagata, D., Kurosaka, M., Yamawaki, S., and Maya, T., "Anti-kidney pair of vortices in shaped holes and their influence on film cooling effectiveness," Proc. ASME 1997 International Gas Turbine and Aeroengine Congress and Exhibition, American Society of Mechanical Engineers.
[145] Wang, C., Sun, X., Fan, F., and Zhang, J., 2020, "Study on trench film cooling on turbine vane by large-eddy simulation," Numerical Heat Transfer, Part A: Applications, 78(7), pp. 338-358.

[146] Hunt, J. C., Wray, A. A., and Moin, P., "Eddies, streams, and convergence zones in turbulent flows," Proc. Publication: Studying Turbulence Using Numerical Simulation Databases, 2. Proceedings of the 1988 Summer Program.
[147] Yu, F., 2020, "Improvements to Turbulence Models for Better Simulations of Film Cooling Flow Field and Heat Transfer," Doctor, The Pennsylvania State University
[148] Polanka, M. D., 1999, "Detailed film cooling effectiveness and three component velocity field measurements on a first stage turbine vane subject to high freestream turbulence," Doctor, The University of Texas at Austin.
[149] Thole, K. A., Bogard, D. G., and Whan-Tong, J. L., 1994, "Generating high freestream turbulence levels," Exp. Fluids, 17(6), pp. 375-380.
[150] Bons, J. P., MacArthur, C. D., and Rivir, R. B., 1996, "The Effect of High Free-Stream Turbulence on Film Cooling Effectiveness," J. Turbomach., 118(4), pp. 814-825.
[151] Halila, E., Lenahan, D., and Thomas, T., 1982, "Energy Efficient Engine," General Electric Company, pp. NASA CR-167955.
[152] Ito, S., Goldstein, R. J., and Eckert, E. R. G., 1978, "Film Cooling of a Gas Turbine Blade," Journal of Engineering for Power, 100(3), pp. 476-481.
[153] McClintic, J. W., 2013, "Experimental investigation of overall effectiveness and coolant jet interactions on a fully cooled C3X turbine vane," Master, The University of Texas at Austin.
[154] Dyson, T. E., 2012, "Experimental and computational investigation of film cooling on a large scale C3X turbine vane including conjugate effects," Doctor, The University of Texas at Austin
[155] Jiang, Y., Zheng, Q., Dong, P., Yao, J., Zhang, H., and Gao, J., 2015, "Conjugate heat transfer analysis of leading edge and downstream mist–air film cooling on turbine vane," Int. J. Heat Mass Transfer, 90, pp. 613-626.
[156] Andrei, L., Andreini, A., Facchini, B., and Winchler, L., 2014, "A Decoupled CHT Procedure: Application and Validation on a Gas Turbine Vane with Different Cooling Configurations," Energy Procedia, 45, pp. 1087-1096.
[157] Laskowski, G. M., Tolpadi, A. K., and Ostrowski, M. C., "Heat Transfer Predictions of Film Cooled Stationary Turbine Airfoils," Proc. ASME Turbo Expo 2007: Power for Land, Sea, and Air, American Society of Mechanical Engineers, pp. 475-485.

Acknowledgements

How time flies, I have spent three years studying for my Ph.D degree in Italy since 2018. At the end of the thesis, I would like to sincerely thank all the members of the group in Genova. Firstly, a massive thanks to my supervisor Professor Pietro Zunino, a really nice and knowledgeable tutor. It is a great honor for me to have the rare opportunity studying and working in such a beautiful and charming coastal city Genova in my twenties. In addition, special thanks to my co-supervisor: Prof. Francesca Satta, a very patient and friendly teacher who provides me with various methods and suggestions for the turbine cooling investigation, and the CFD expert Professor Dario Baris who is very keen to answer my countless questions and teaches me a lot about the CFD knowledge. And many thanks to Prof. Marina Ubaldi, Prof. Daniele Simoni, Prof. Davide Lengani, Dr. Matteo Dellacasagrande, Prof. Yigang Luan and Dr. Yonglei Qu for giving me lots of useful suggestions and ideas for my thesis. Also, many thanks to Dr. Yue Yin for helping me implement the simulation with the server remotely. Honestly speaking, I couldn't have done it without you and your help. Last but not least, I would like to thank my parents who always support me no matter what decisions I have ever made. I really appreciate it. All good things must come to an end, it is hard to say goodbye to my tutors, my colleagues and my friends, and it is so lucky for me to meet you. Though the study in Genova is complete, the unforgettable experience will always remain in my mind. Hope to see you guys again someday in either Italy or China.

Appendix A

Matlab code for calculating the lateral-averaged film cooling effectiveness used in current work:

```
clc
clear all;

u_e = 10 ;  % freestream velocity
nn
%%%%%%%%%%%%%%%%%%%%%%%%%%%%%%%%
% data format of myfile.csv
%
% Slice: X=0.890099  %The location in streamwise direction
% 0.895641,         %Cooling effectiveness in lateral direction
% 0.893102,
% 0.891074,
% 0.863468,
% …
%
% Slice: X=1.28515
% 0.889171,
% 0.886363,
% 0.88183,
% 0.876051,
% …
%%%%%%%%%%%%%%%%%%%%%%%%%%%%%%%%

%% read csv file
filename= './myfile.csv';     %modify the filename?
fileID = fopen(filename,'r');
formatSpec = '%s';
delimiter = ',';
startRow = 0;  % remove headerlines
dataArray = textscan(fileID, formatSpec, 'Delimiter', delimiter, 'HeaderLines',startRow,
'ReturnOnError', false);
%%% Close the text file.
fclose(fileID);
%%% Allocate imported array to column variable names
eff = dataArray{:,1};
eff1 = str2double(eff); % remove text in eff

%% create rownum, find the row number that include 'Slice'
head = contains(eff,'Slice');   % find rows in the file that include 'Slice'
```

```
m=1;
for n=1:length(eff)

   if head(n,1)==1
      rownum(m,1) = n;
      slice(m,1) = eff(n,1);
      m=m+1;
   end
end

rownum(m,1)= length(eff1)+1;  %add another row in rownum to prevent the error of the
length in the array

%% calculate lateral-averaged effectiveness
for n=1:length(rownum)-1
   %calculate lateral-averaged effectiveness
   mmstart=rownum(n,1)+1;
   mmend=rownum(n+1,1)-1;
   mm=eff1(mmstart:mmend,1);
   lat_ave(n,1)=mean(mm);

   %x_D localtion
   x_D_temp = regexp(slice,'[+-]?\d+\.?\d*','match');
   x_D(n,1)= str2double( cell2mat(x_D_temp{n,1})  );
   n=n+1;
end

%% output
output = [x_D lat_ave];
output_reorder = sortrows(output,1,'ascend'); % sort the results
```

Matlab code for calculating the area-averaged film cooling effectiveness used in current work:

```
clc
clear all;

temp_m=295; % temperature of mainstream K
temp_c=196.67; % temperature of coolant K

%%%%%%%%%%%%%%%%%%%%%%%%%%%%%
% data format of bottom_temp.txt
% cellnumber,x-coordinate,y-coordinate,z-coordinate,mean-temperature,face-area-magnitude
%       1,-3.415333573E-03, 5.998569697E-11,-3.255467396E-03, 2.027899073E+02, 3.573482146E-08
%       2,-3.048207844E-03, 8.389963169E-10,-3.125978401E-03, 2.023562417E+02, 3.557121583E-08
%       3,-3.599772230E-03,-6.698518962E-10,-3.461643355E-03, 2.275538539E+02, 8.639939936E-08
%       4,-3.119922942E-03, 5.789327698E-11,-3.253350267E-03, 2.275250037E+02, 3.746010803E-08
%       …
%%%%%%%%%%%%%%%%%%%%%%%%%%%%%


%% read csv file
filename= './bottom_temp.txt';     %modify filename???
fileID = fopen(filename,'r');
formatSpec = '%f%f%f%f%f%f';
delimiter = ',';
startRow = 1;  % remove headerlines
dataArray = textscan(fileID, formatSpec, 'Delimiter', delimiter, 'HeaderLines',startRow, 'ReturnOnError', false);
%%% Close the text file.
fclose(fileID);
%%% Allocate imported array to column variable names
num = dataArray{:,1};
coord_x = dataArray{:,2};
coord_y = dataArray{:,3};
coord_z = dataArray{:,4};
temp = dataArray{:,5};
area = dataArray{:,6};

%% set region x/D=0-30
m=1;
for n=1:length(num)
```

```
    if ( coord_x(n,1)>0.00775*0 && coord_x(n,1)<0.00775*30 )
    rownum(m,1)=n;
    m=m+1;
    end
    n=n+1;
end

%% calculate effectiveness in each cell
for n=1:length(rownum)
    row=rownum(n,1);
    eff(row,1)=(temp(row,1)-temp_m)/(temp_c-temp_m);

end

%% calculate area-averaged effectiveness
area_total=0;
int_eff=0;
for n=1:length(rownum)
    row=rownum(n,1);
    area_total=area_total+area(row,1);
    int_eff=int_eff+eff(row,1)*area(row,1);
end

eff_area_ave=int_eff/area_total;
```

Appendix B

The coordinate of NASA C3X turbine vane is shown in Tab. 6.1.

Tab. 6.1 NASA C3X turbine vane coordinate

Position number	Suction side		Position number	Pressure side	
	x cm	y cm		x cm	y cm
1	0.1097	11.6548	1	7.4849	-0.0617
2	0.3894	12.189	2	7.3188	0.3559
3	0.7658	12.6764	3	7.1483	0.7737
4	1.2723	13.0233	4	6.9736	1.1895
5	1.8743	13.1376	5	6.795	1.6035
6	2.4707	12.9939	6	6.6116	2.0155
7	2.9835	12.6538	7	6.4237	2.4254
8	3.3985	12.1976	8	6.2309	2.8329
9	3.7376	11.6817	9	6.0328	3.238
10	4.0272	11.1364	10	5.8296	3.6406
11	4.2885	10.5766	11	5.6203	4.0401
12	4.5326	10.0094	12	5.4051	4.4364
13	4.7648	9.4369	13	5.1834	4.829
14	4.987	8.8605	14	4.9548	5.2177
15	5.2019	8.2814	15	4.7191	5.602
16	5.411	7.7003	16	4.476	5.9817
17	5.6157	7.1176	17	4.2248	6.3563
18	5.8171	6.5336	18	3.9654	6.7249
19	6.016	5.9487	19	3.6975	7.0874
20	6.2126	5.3632	20	3.4204	7.443
21	6.4074	4.7767	21	3.1339	7.7909
22	6.5997	4.1897	22	2.8374	8.1308
23	6.7894	3.6015	23	2.5314	8.4615
24	6.9756	3.0122	24	2.2149	8.7826
25	7.1575	2.4221	25	1.8885	9.0935
26	7.3335	1.8301	26	1.5519	9.3932
27	7.5024	1.2357	27	1.2052	9.6815
28	7.6624	0.6391	28	0.8494	9.9578
29	7.8115	0.0411	29	0.4999	10.2116
30	7.8161	-0.0053	30	0.3848	10.3035

31	7.8082	-0.0516	31	0.2822	10.4094
32	7.7879	-0.0935	32	0.1938	10.5273
33	7.7572	-0.1288	33	0.1212	10.6556
34	7.718	-0.1542	34	0.065	10.792
35	7.6736	-0.1681	35	0.0264	10.9342
36	7.6269	-0.1699	36	0.0063	11.0802
37	7.5816	-0.1587	37	0.0046	11.2278
38	7.5408	-0.1356	38	0.0216	11.3741
39	7.5077	-0.1026	39	0.0569	11.5171